Investigation of Growth, Electrical and Opto-electronic Transport in Nanowires of Charge Transfer Complexes

Thesis submitted for the degree of
Doctor of Philosophy (Science)

in

Physics (Experimental)

by

Rabaya Basori

Department of Physics
University of Calcutta
April 2015

To my Family

Acknowledgments

Though only my name appears on the cover of this dissertation, a great many people have contributed to its production. I owe my gratitude to all those people who have made this dissertation possible and because of whom my graduate experience has been one that I will cherish forever.

First, I would like to express my special appreciation and thanks to my advisor **Prof. A. K. Raychaudhuri** for his worthwhile guidance, support, inspiration and stood by me throughout the entire process of completing my PhD at *S N Bose National Centre for Basic Sciences, Kolkata, India*. I have been amazingly fortunate to have an advisor who gave me the freedom to explore on my own, and at the same time the guidance to recover when my steps faltered. His patience and support helped me overcome many crisis situations and finish this dissertation. I am incredibly grateful for all I have received over these years.

I wish to express my sincere thank to Prof. T. Saha Dasgupta, Prof. Ranjan Chaudhuri, Prof, A. K. Mukhopadhyay and others for representing physics in an easy way during my course work. I also want to thank Dr. M. Kumar, Dr. S. K. Pal for effective discussions of my work. Special thanks to Dr. T. P. Sai to introduce with the initial experimental work of my thesis. I am grateful to Prof. K.S. Narayan from JNCASR and Dr. A. Sinha from Bose Institute to give me the opportunity to do experiments in their lab for a short period of time.

I feel pleasant being a member of the New Nano Lab for the friendly and healthy academic environment with an essence of family life. I would like to thank Kaustuv da who make the lab environment easy for me from the beginning and help me to improve my work with effective suggestion. He help me in learning electron beam lithography, FIB and other experimental techniques. Thanks to Sudeshna di with whom I can easily discuss my academic as well as personal matters. She never said 'no' whenever I asked for help from her and she always tries to give her best. I gratefully acknowledge Sudeshnadi, Shahnewazda and Rajibda for introducing me with C++ programming. I would like to thank Barnalidi for her support and suggestions. I would like to thank Manotoshda, Rajeshda, Bipulda, Pobitrada, Anindyadi, Sabyasachi, Rishi, Ravindra, Shaili, Bhivuti, Jasashree, Subarna, Putul for their support and help whenever it needed. I spend a nice time with all of them them in the lab.

I am also thankful to the technical staff Joy, Shaktida, Piyali, Surajitda, Deepankarda, Urmi, Amit and others. I would like to thank the people of administrative, engineering, computer, library, electrical, instrumentation, workshop, canteen, cleaner, security guards and other supporting staff of SNBNCBS for their timely help and also for their the day-to-day activities in the centre.

Apart from the lab members, I am deeply grateful to one of my best friends *Urbashi*. She was the only one in the centre who is always beside of me in all my good and hard time unconditionally. We not only take part in academic discussions, but can share everything with each other. I will miss the time I spend with her in the rest of my life. Lots of thank to my friend Jagadish for his support. Thanks Tanmoy for introducing me with Full Prof software. I am also thankful to Nasim, Suvankar, Saikat, Washey Injamum for providing me scientific papers and other utilities whenever I asked. I will always be happy remembering my all other friends.

My acknowledgements will never be completed without the special mention of my friend *Md. Wali*

Hossain without the support, encouragement and unconditional help of whom it was not possible for me to enter into my dream world of scientific research. He not only spend his precious time for assisting me, but also make me strong and independent. I would like to thank Mubarak uncle, Wahida aunt and each and every member in their family for their support and love.

Words are not enough to express my sincere gratitude to my respected teacher *Mr. Abul Kalam Azad*. Without the support, inspiration and guidance of him it is not possible to achieve MSc degree for me. He and his wife always support and suggest in every crucial steps of my life. I convey my sincere gratitude to Ashit sir and Golam Robbani sir for their inspiration.

Most importantly, none of this would have been possible without the love and patience of my family. 26 alphabet is not enough to thanks my parents. They have been a tremendous source of support and encouragement throughout my life. I shall always miss my father's presence at every step in rest of my life. My deepest gratitude to my brother *Imdadul* to fulfil my wishes as much as he can. Words are not sufficient to express my sincere thanks to all my brothers and sisters who always ready to sacrifice anything for me. I would like express my sincere thanks to my brother in laws, sister in laws and my nice and nephews for their love and support. I love and adore them for their constant support and being patient for the work I did. My dissertation is a tribute to all of them.

Rabaya Basori
Kolkata, India
April, 2015

List of Publications

Published

1. **Rabaya Basori**, K. Das, P. Kumar, K. S. Narayan and A. K. Raychaudhuri
   Large photoresponse of Cu:7,7,8,8-tetracyanoquinodimethane nanowire arrays formed as aligned nanobridges
   Appl. Phys. Lett., 102 (6), 061111-4 (2013).

2. **Rabaya Basori** and A. K. Raychaudhury
   Role of Contact and Contact Modification on Photo-response in a Charge Transfer Complex Single Nanowire Device
   Nano-Micro Lett. 6(1), 63-69 (2014).

3. **Rabaya Basori**, K. Das, P. Kumar, K. S. Narayan and A. K. Raychaudhuri
   Single CuTCNQ charge transfer complex nanowire as ultra high responsivity photo-detector
   Optics Express 22(5),4944-4952 (2014).

4. **Rabaya Basori** and A. K. Raychaudhuri
   Graphitic oxide induced enhanced electrical conductance in Cu:TCNQ nanorod film
   Accepted in **IEEE Explore.**

Ready for submission

1. **Rabaya Basori** and A. K. Raychaudhuri
   Modification of temperature and bias dependent conductance of a charge transfer complex nanowire grown with an electric field from vapor phase

2. **Rabaya Basori**, M. Kumar and A. K. Raychaudhuri
   Resistive switching mechanism in a single Cu:TCNQ nanowire

3. **Rabaya Basori** and A. K. Raychaudhuri
   Electric field assisted growth of Cu:TCNQ nanowires.

List of Abbreviations

TCNQ	Tetracyanoquinodimethane	Z	Degree of charge transfer
CT	Charge Transfer	I	Current
EBL	Electron Beam Lithography	V	Voltage
FEB	Focused Electron Beam	A	Ampere
FIB	Focused Ion Beam	K	Kelvin
AFM	Atomic Force microscopy	T	Temperature
NPGS	Nano Pattern Generating System	FEG	Field Emission Gun
XRD	X-Ray Diffraction	R	Resistance
FTIR	Fourier Transform Infra-Red	Ω	Ohm
TEM	Transmission Electron Microscope	ρ	Resisvity
DEP	Dielectrophoretic	G_0	Linear Conductance
MSM	Metal-Semiconductor-Metal	I_{Ph}	Photo-current
MSM	Metal-Insulator-Metal	$\Re$	Responsivity
GO	Graphitic Oxide	G	Photo-conductive gain (in Chapter 6)
PMMA	Poly(methyl methacrylate)	R_c	Contact resistance
HRS	High Resistive State	R_s	Sample resistance
LRS	Low Resistive State	ξ_0	Coherence length
EDL	Electric Double Layer	L_t	Tunneling length
FET	Field Effect Transistor	FBGFET	Floating Back-gate FET
SEM	Scanning Electron Microscope	h	Plank's Constant
CDW	Charge Density Wave	k_β	Boltzmann Constant
PVD	Physical vapor Deposition	eV	Electron-volt
NW	Nanowire	nm	Nanometer
SNW	Single Nanowire	E_g	Pinning gap
LUMO	Lowest Unoccupied Molecular Orbitals	g_E	Density of state
HOMO	Highest Occupied Molecular Orbitals	E_F	Fermi energy
VRH	Variable Range Hopping	E_{th}	Threshold field
I_DS	Source-Drain Current	V_{DS}	Source-Drain Voltage
I_G	Gate Current	V_g	Gate voltage
I_{ill}	Illuminated-current	I_{dark}	Dark-current
V_{SET}	Set voltage	V_{RESET}	Reset voltage
ϕ	Barrier height	Γ	Tunneling rate
τ	Carrier life-time	τ_t	Carrier transit-time
l	Nanowire length	d	Nanowire diameter
μC	Micro Coulomb	nC	Nano Coulomb
σ	Electrical conductivity	S	Siemens
e	Electronic charge	$\mu-$m	Micro-meter
α	Inverse localization length	C-Pt	Carbon-Platinum

Contents

List of Figures

List of Tables

Chapter 1

Introduction

One dimensional nanostructures have attracted considerable recent attention due to their special properties, which make them important in basic scientific research and also in potential technological applications [1]. A good deal of current research in science and technology of nanowires (NWs) is being directed mainly towards the synthesis and characterization of one dimensional nanoscale materials for new types of electronic, optical and magnetic devices and understanding of their physical behaviour.

1.1 Charge transfer complex

This thesis addresses an important specific sub-area in the broad field of NWs, namely NWs of charge-transfer (CT) complexes. Molecular CT complexes are electron-donor-electron-acceptor complexes, characterized by electronic transition(s) to an excited state in which there is a partial transfer of electronic charge from the donor to the acceptor moiety. During interaction between donor and acceptor, charge is redistributed inside the compound. In this process, the donor is oxidized by loosing charge and acceptor is reduced. TTF:TCNQ (Tetrathiafulvalene-Tetracyanoquinodimethane), Cu:TCNQ (Copper-Tetracyanoquinodimethane) are such examples of CT complexes. Figure 1.1 (upper frame) shows the CT between single molecule of donor TTF, acceptor TCNQ and the CT complex TTF:TCNQ after transferring charge. Lower frame of Fig. 1.1 shows stacking of TTF:TCNQ molecules, which consist of a quasi-one-dimensional, chain-like arrangement of the TTF and TCNQ [2]. The field of charge-transfer organic conductors has been the object of rapidly growing research activity for its unconven-

tional physical properties, which includes a variety of phase transitions including such phenomena as Peierls transition and CDW transition. Organic molecules can show many remarkable properties, say for example, electrical conductivity changes arising from excitation using radiation sources such as light or even simple polymerisation of organic units. These materials not only show considerable interests in fundamental research for their unconventional physical properties, but also for potential applications. In the context of the demand for information storage, CT complexes show excellent potential for application. Materials which exhibit switching with hysteresis can be used to make memory devices. Charge-transfer complexes are such a material having switching with hysteresis. These CT complexes are known to have high electrical conductivity and in this thesis we find that the material also has a high optical conductivity. A specific feature of these electronic materials is their low dimensionality, which is due to the particular chain like molecular architecture of these organic conductors. Organic semiconductors are currently investigated as an alternative to inorganic (metal-oxide) resistive-state switching material for non-volatile memory applications like non-volatile Random Access Memory (RAM) [3, 4]. High electrical conductivity, low dimensionality and switching property will make the material suitable for high density device integration in future technology.

1.2 Cu:TCNQ as charge-transfer complex

A charge-transfer complex (or CT complex) or electron-donor-acceptor complex is an association of two or more molecules, or different parts of one large molecule, in which a fraction of electronic charge is transferred between the molecular entities. TTF:TCNQ, Ag:TCNQ, Cu:TCNQ are common examples of CT complex [2, 3]. In this thesis, we have only focused on Cu:TCNQ. In this material Cu acts as the metallic donor and TCNQ as the organic acceptor. The donor molecule possesses a low ionization potential, whereas the acceptor molecule has a strong electron affinity. But, as individuals, both types of molecules (or atoms) are charge neutral. When donor and acceptor interact, the charge is redistributed in the compound. The donor species are oxidized by loosing charge and the acceptor species are reduced. The degree of this charge transfer is abbreviated as Z and adopts values $0 < Z < 1$; $Z = 0$ represents no charge transfer, while $Z = 1$ stands for a complete charge transfer from donor to acceptor. Depending on the conditions, this transfer results in partially occupied atom or molecule

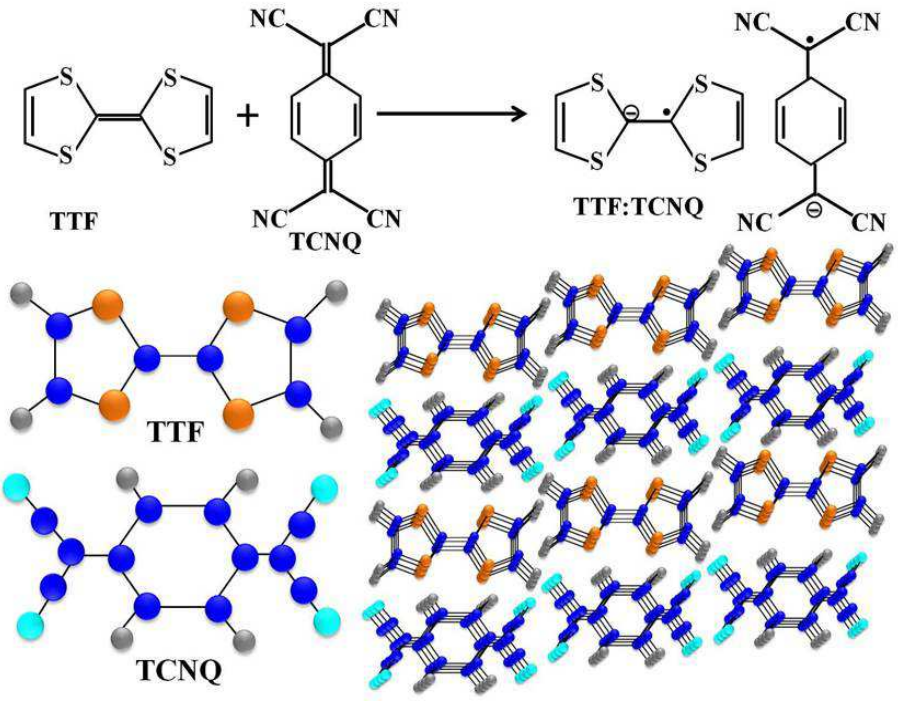

Figure 1.1 (Upper frame) The charge transfer between single molecule of TTF (donor), TCNQ (acceptor) and the CT complex TTF:TCNQ after transferring charge. (Lower frame) Stacking of TTF:TCNQ molecules in 3D [2].

orbitals which influence different properties of the material.

In organics, homonuclear molecular chains are bonded only by van der Waals force; whereas in CT complexes, additional Coulomb force and dipole induced force also take part in inter-molecular bonds. Depending on these forces CT complex can be categorized in to strong and weak complexes. In molecules of weak CT complexes electron shells are fully occupied and hence degree of charge transfer Z between donor (D) and acceptor (A) is only marginal in the ground state, but can be much larger in the excited state. In this complexes, molecules are stacked alternatively ($D^+A^-D^+A^-D^+A^-$...) and has lower electrical conductivity. TTF:TCNQ is an example of weak CT complex [5, 6]. In contrast, strong CT complexes display a strong ionic character and this is due to a large charge transfer Z between donor and acceptor, even in the ground state. In this complexes, molecules are stacked separately ($D^{+Z}D^{+Z}D^{+Z}A^{-Z}A^{-Z}A^{-Z}$...) and has higher electrical conductivity. More precisely, strong CT complexes can be classified into different ionic types depending on the radical ion salts used for CT complex [7]. First one is, radical ion source, where both ionized molecules (donor and acceptor) are radicals i.e. with unpaired electrons or open electron shell configuration. Therefore, both molecules

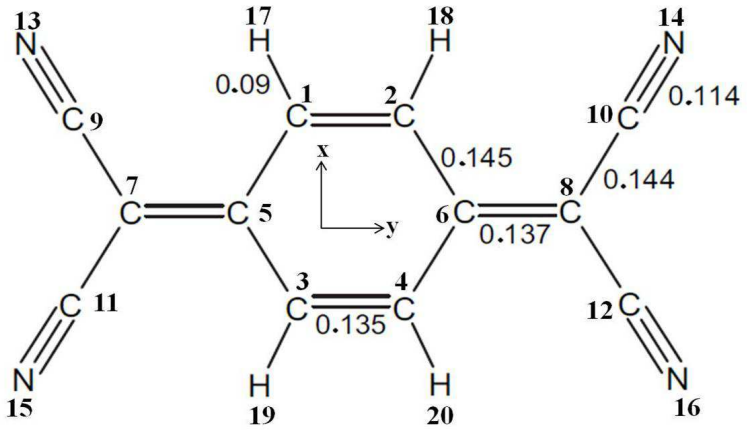

Figure 1.2 Chemical structure of the TCNQ molecule. The numbers denote the molecular bond lengths in nm calculated by Long et al [10].

possess an electron spin. The second one is radical cation source, where only the cation is a radical. In this case, the anion possesses a fully occupied electron shell and therefore no electron spin. The third one is radical anion source, where only the anion is a radical. In this case, the cation possesses a fully occupied electron shell and therefore no electron spin. $Cu^{+}TCNQ^{-}$ is an example for an anion radical salt [8].

TCNQ (7,7',8,8'-Tetracyano- 1,4-quinodimethane) is an organic compound with IUPAC name (Cyclohexa-2,5-diene-1,4-diylidene)-dimalononitrile. The base of this molecule is the chemical compound 1,4-Benzoquinone with the formula $C_6H_4O_2$. This organic six-membered ring compound is the oxidized derivative of 1,4-hydroquinone. In the TCNQ molecule the oxygen is substituted by four cyano C≡N (or nitrile) groups at the carbon positions 7,7',8,8' with chemical formula $C_{12}H_4N_4$. Structure of TCNQ is shown in Fig. 1.2. The electrons are localized in the benzene ring, which means that the molecule has no aromatic character. The TCNQ molecule acts as an acceptor and by accepting electrons, it is transformed from the quinoide to a conjugated system with a favorable energetic configuration [9]. TCNQ has monoclinic crystal structure [10]. The perpendicular distance between the planes of adjacent molecules within a given stack is 3.45 Å, only about 0.1Åmore than that in graphite. In TCNQ crystals, molecules are connected by weak van der Waals force which allows for an overlapping of the $\pi-$orbitals of neighbouring TCNQ molecules in the stack. This configuration is responsible for a good conductivity along the stack direction.

To increase the conductance of TCNQ, metal-TCNQ had been synthesized [9]. There are two

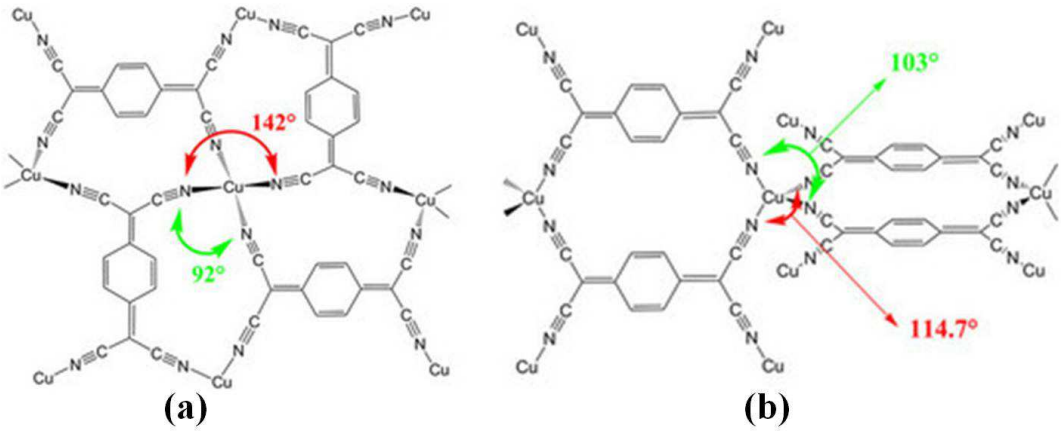

Figure 1.3 Schematics of (a) Phase-I and Phase-II of Cu:TCNQ molecular complex. Reprint with permission from [12].

different deposition methods described for Cu:TCNQ thin films and NWs. One is a wet chemical process, which is based on a spontaneous electrolysis technique [8]. A copper electrode is cleaned in order to remove a possible oxide layer and then immediately dipped into a saturated solution of TCNQ in acetonitrile. On contact with the solution, a direct oxidation reaction between Cu and TCNQ takes place [11, 12, 13] and the form of reaction is: $(Cu^0) + (TCNQ^0) \rightarrow (Cu^+TCNQ^-)$. Another is physical vapor deposition (PVD) method. In this method, TCNQ and Cu is thermally co-evaporated onto a substrate in high or ultra-high vacuum; or TCNQ is thermally evaporated on a Cu layer. Cu layer is need to be activated thermally in order to accelerate the diffusion of Cu into the TCNQ layer and trigger the above stated reaction. Depending on the synthesis process and growth parameters Cu:TCNQ has two phases: Phase-I with tetragonal (a = 3.887 Å, b = c = 11.266 Å, β= 90^o V = 493.5 Å^3) and Phase-II with monoclinic (a = 5.3337 Å, b = 5.3312 Å, c = 18.875 Å, β= 94.036^o, V = 535.38 Å^3) crystal structure [11]. A simple schematic view of the two different structures is shown in Fig. 1.3. The structures of both phases are based on the repeat pattern of a four-coordinate Cu ion ligated to the nitrile groups of separate TCNQ, but spatial arrangement of TCNQ molecule is different in two phases. The first difference is the relative orientation of TCNQ moieties around the Cu atoms. In Phase-I, neighbouring TCNQ molecules are rotated 90^o with respect to one another, but all are in the same plane. In this phase, a Cu atom is coordinated with four nitrogen atoms of neighbouring TCNQ molecules and N-Cu-N angles are 92^o and 142^o respectively, as shown in Fig. 1.3(a) [11]. In contrast, Phase-II displays a different structure where an infinite number of TCNQ molecules are oriented in the same

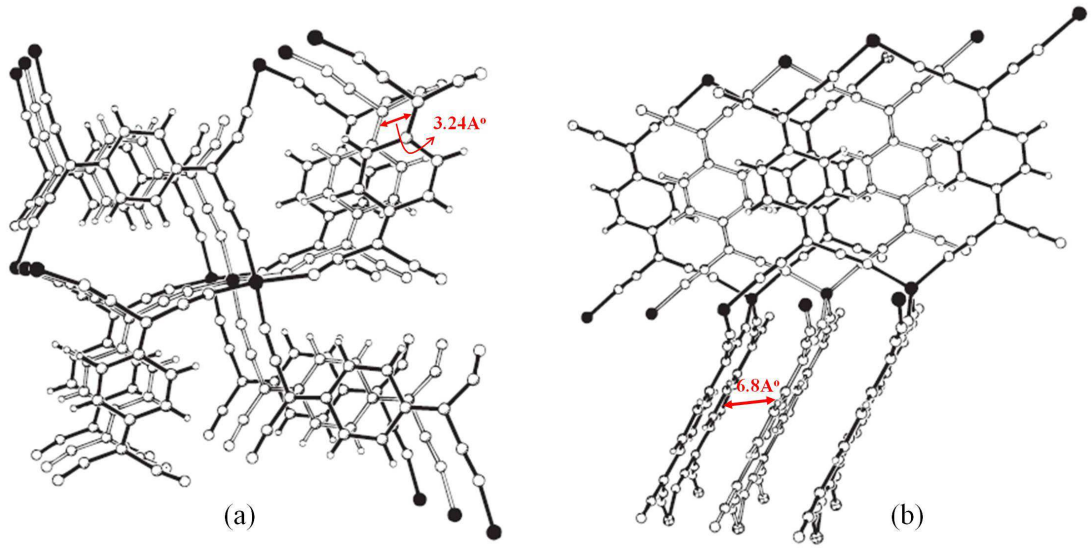

Figure 1.4 Schematics of interpenetration network of (a) Phase-I and (b) Phase-II of Cu:TCNQ molecular complex. Copy right with permission from [11].

direction, but in two perpendicular planes. In this case, N-Cu-N angles are 103^o and 114.7^o respectively (Fig. 1.3(b)). The second major difference concerns the type of interpenetration of the networks. In Phase-I, the two independent networks result in a columnar stack of TCNQ molecules with the closest distance being 3.24 Åas shown in Fig. 1.4(a). This distance allows for a $\pi - \pi$ orbital stacking. In sharp contrast, the interpenetration in Phase-II does not bring the two independent networks together. The TCNQ rings are in fact out of alignment and no $\pi - \pi$ stacking occurs as shown in Fig. 1.4(b). In this case, the closest distance between parallel TCNQ units in the same network is 6.8 Å.

The conductivity of CT complexes is directly dependent on the crystal structure [14]. CT complexes with an alternative stacking of donor and acceptor molecules ($D^+A^-D^+A^-D^+A^-$....) exhibit low conductivity values. This is due to a complete charge transfer from donor to the neighbouring acceptor molecules:

$$D + A \rightarrow D^+ + A^- \tag{1.1}$$

In this case, a further charge transfer is energetically disadvantageous because to ionize the donor and acceptor molecules further, the molecules need to overcome high ionization potential:

$$D^+ + A^- \rightarrow D^{2+} + A^{2-} \tag{1.2}$$

Therefore, high conductivity values are only possible in CT complexes with separated stacks of donor

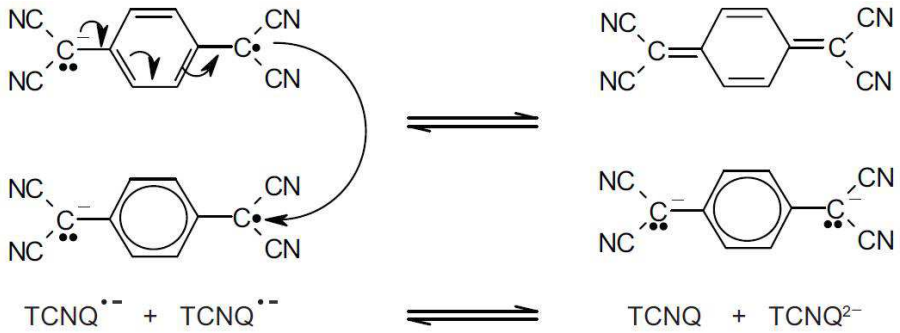

Figure 1.5 Ionization of CT complex with complete charge transfer (Z=1). Reprint with permission from [14].

and acceptor molecules ($D^{+Z}D^{+Z}D^{+Z}A^{-Z}A^{-Z}A^{-Z}$....). Although, this kind of stacking is necessary, but not sufficient condition to get high conductivities.

The degree of charge transfer Z also has a decisive influence on conductivity in this kind of systems. For example, the acceptor molecule TCNQ is negatively ionized for Z = 1. Charge transfer within a TCNQ stack in this case would occur by the conversion of two $TCNQ^{-}$ anions to a neutral TCNQ molecule and a $TCNQ^{2-}$ dianion as shown in Fig. 1.5. This dianion configuration is energetically unfavourable due to the high Coulomb potentials. Hence, a charge transfer of Z = 1 results at maximum in conductivity values typically for semiconductors.

On other hand, CT complexes with separated stacks of donor and acceptor molecules and partial charge transfer Z display the highest conductivity values. In this case, the charge transfer occurs as follows:

$$\begin{aligned} D + D^{+} &\rightarrow D^{+} + D \\ A + A^{-} &\rightarrow A^{-} + A \end{aligned} \tag{1.3}$$

One ionized and one neutral molecule are converted to a neutral and an ionized molecule. Therefore, charge can be transported without the presence of high energy barriers. Conversion of ionized molecules are shown in Fig. 1.6. The distance between the single acceptor or donor molecules is also important for the conductivity. Short distances allow a better overlap of occupied and unoccupied orbitals and increase the conductivity.

The above discussed conductivity mechanism, which is constrained in the direction along the stacks of the $\pi-$electrons of the molecules, is the dominating cause for the conductivity in a CT complex

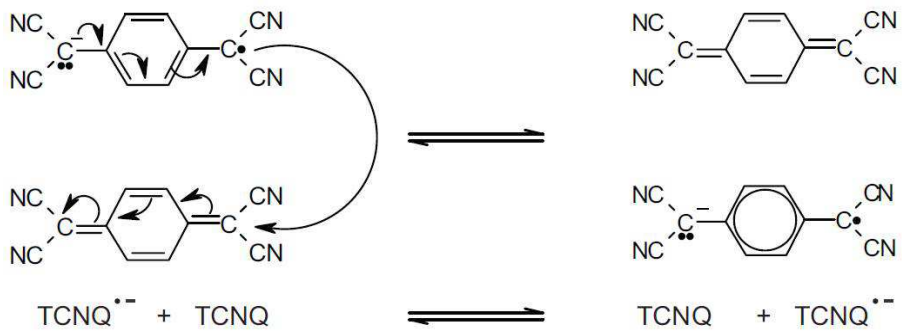

Figure 1.6 Ionization of CT complex with partial charge transfer (Z<1). Reprint with permission from [14].

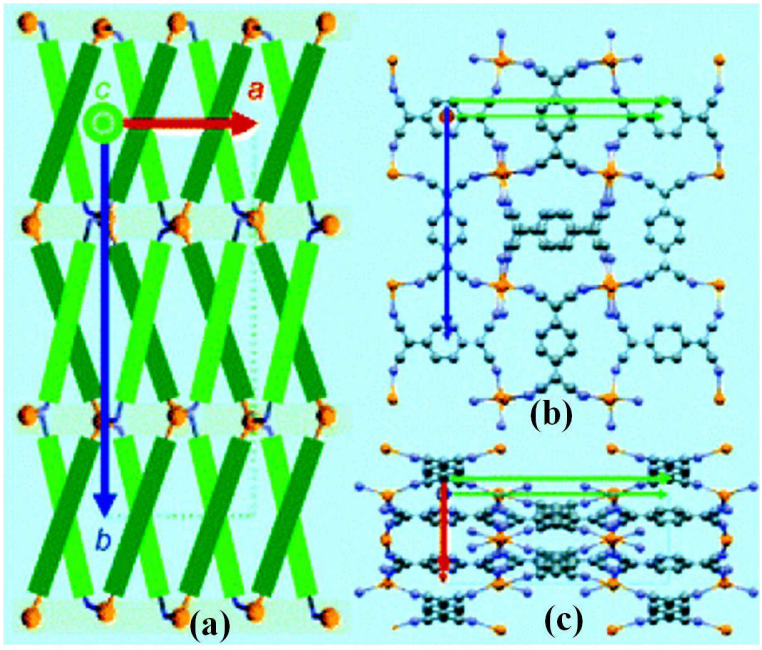

Figure 1.7 (a) Schematic of $\pi - \pi$ stacking. Stacking in (b) Phase-I and (c) Phase-II of Cu:TCNQ. Reprinted with permission from [15].

like Cu:TCNQ. In addition, a charge transport is also possible between the single stacks. In single crystals of Cu:TCNQ CT complex, Cu^{+} and $TCNQ^{-}$ form discrete columnar stacks in a face-to-face configuration with strong overlap in the $\pi-$system as shown in Fig. 1.7 [15]. The *a* axis is suitable for $\pi-$stacking and it changes along the stacking axis (1 0 0), but not perpendicular to it as shown in Fig. 1.8. Charge transfer occurs between the central Cu atoms and the N atoms of the nitrile groups of TCNQ which generally depends on their band structure as represented in Fig. 1.8. The band structure of Cu:TCNQ in high impedance state is shown in Fig. 1.8(a) [16]. a' band of Cu:TCNQ largely made

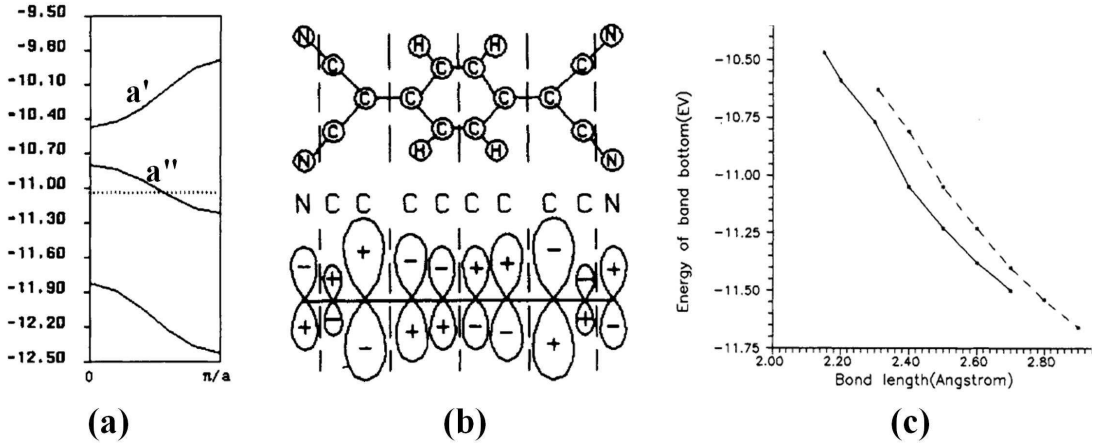

Figure 1.8 (a) Band diagram of Cu:TCNQ. Stacking in (b) Phase-I Cu:TCNQ and (c) Energy change of band bottom. Solid line is the energy of a' band of Cu-TCNQ; dashed line is the energy of a' band of Ag-TCNQ. Reprinted with permission from [16].

up of 4s orbital of Cu ([Ar]$3d^{10}4s^1$), while a'' bands are mainly composed of $\pi-$ orbitals or lowest unoccupied molecular orbitals (LUMO) of TCNQ. The overlapping of neighbouring $\pi-$ orbitals of TCNQ is shown in Fig. 1.8(b). Fermi level of the compound is -11.06 eV as shown by the dotted line in Fig. 1.8(a) and cross the a'' bands. During conduction, carrier migration of Cu:TCNQ mainly depends on the overlapping of $\pi-$ orbitals and at the Fermi level d^2E/dk^2 being positive, it is reasonable to consider that carriers are electrons. It has to be mentioned that *s* orbitals of Cu and $\pi-$ orbitals of TCNQ forms bonding about the Fermi level and anti-bonding above the Fermi level [16]. The gap between a' and a'' is ~ 0.33 eV. Molecular arrangement beings unfavorable to a'' orbitals of TCNQ, a'' bands appear to be narrow. Hence, electron have to overcome high-energy barrier during migration and as a result conductivity become low. Application of bias bring enormous change in conductivities and charge transfer. The energy of a' band is inversely proportional to bond length of Cu-N as shown in 1.8(c) and charge transfer decreases as bond length increases. When applied field across Cu:TCNQ exceeds threshold field, electrons in the a'' band starts to jump to a' band i.e. anti-bonding orbitals of Cu-N. This transition makes the Cu-N bond weak and increase the bond length, resulting decrease in the energy of a' band. Therefore, more electron can jump from a'' to a' bands; in other words more electron will fill the anti-bonding orbitals of Cu-N which make the bonds so weaker that Cu and N can separate easily. As a result, a' band becomes conducting, with the Fermi level down to -11.6 eV and increase the conductivity of Cu:TCNQ [16]. Thus, a good conductivity based on a $a' - a''-$band is

possible for Phase-I CT complexes. In this thesis, most of the work has been performed with Phase-I Cu:TCNQ NW with $\pi-$stacking, responsible for high electrical conductance.

1.3 Review of electrical transport in Cu:TCNQ

Basic reason of relatively higher conductance of Phase-I crystal structure of Cu:TCNQ compared to that of Phase-II has already been discussed in the previous subsection. Heintz et al. measured the conductivity properties of Cu:TCNQ for the two crystallographic phases [11]. They used pressed pellets. These measurements revealed semiconducting properties for both systems. Phase-I displayed a room-temperature conductivity of 2.5×10^{-1} S/cm. In contrast, Phase-II is a very low conductivity semiconductor with a room temperature conductivity of 1.3×10^{-5} S/cm. Temperature dependent conductivity is shown in Fig. 1.9. The band gaps estimated from temperature dependence of conductivity were 0.137 eV and 0.332 eV for Phase-I and Phase-II respectively. One problem for the measurement on pressed pellet of an anisotropic materials that they do not give proper numbered values.

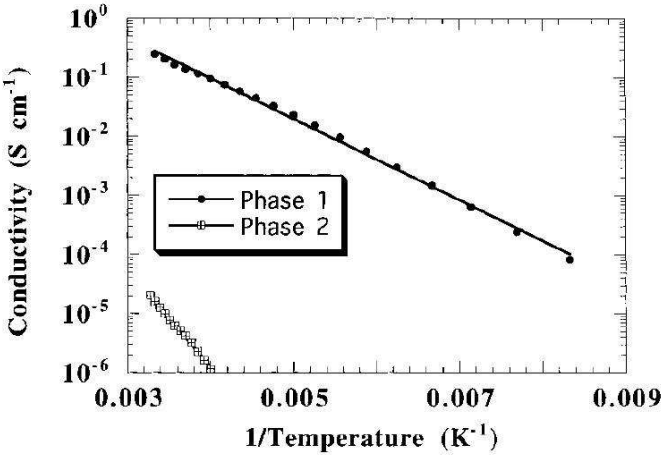

Figure 1.9 Plots of conductivity σ (S cm^{-1}) versus temperature for bulk Cu:TCNQ Phase-I and Phase-II measured on pressed pellets. Reprinted with permission from [11].

Zhou et al. [17] investigated the temperature and bias voltage dependent electrical transport properties of in situ fabricated Cu:TCNQ NW. They have synthesized Cu:TCNQ NW laterally on e-beam lithographically pre-defined electrodes of Cr-Cu/Au on 500nm Si/SiO_2 substrate by physical vapor deposition method and an SEM image of the device is shown in Fig. 1.10(a). They found that at low bias, conductance and current exhibit a power-law dependence on temperature and bias voltage,

Table 1.1 Reviews of electrical transport in Cu:TCNQ

Reference	Sample form	Temperature range (K)	Basic observation
[11]	Bulk Cu:TCNQ (pressed pellet)	300-120	Measured electrical conductivity both for Phase-I and Phase-II which show semiconducting nature. Phase-I higher conductivity than Phase-II. Conductivity of Phase-II and Phase-I close to electrical properties in 'unswitched' and 'switched' state of Cu:TCNQ.
[17]	Nanowire array (Au-Cu/Cu:TCNQ/Au)	330-105	Nanowires are quasi-1D systems with large number of nearly independent conducting channel in parallel. power law dependence indicates the existence of Coulomb interaction in the NW.
[18]	Nanowire array (Au/Cu:TCNQ/Al)	300-85	Quadratic dependence of I-V indicates the characteristic of space charge limited current. Temperature dependent conductance fit well with Arheneous model, indicating activated transport.

respectively. They explain the data by a theoretical model of nearly independent parallel chains of quantum dots created by randomly distributed defects. Fig. 1.10(b) shows the temperature dependence of the conductance G as determined by measuring the dc I-V characteristic and taking the slope at zero bias for three representative devices. They have observed nonmetallic behavior (dG/dT $>$0) over the entire temperature range measured (330 K to 105 K), with the conductance decreasing by three orders of magnitude upon cooling. The data failed to fit with simple activation or 3-D variable range hopping (VRH) model and only supported by 1-D VRH model. With further decrease of temperature, the conductance becomes immeasurably small possibly due to Coulomb blockade effects at very low temperature. Fig. 1.10 (c) showed power law dependence of conductance G as ($G \propto T^{\alpha}$), whereas Fig. 1.10(d) log-log plot of I-V curves at different temperatures. A transition between Ohmic ($I \sim V$) and power-law behavior ($I \sim V^{\beta+1}$) was observed as V increases. Power-law behavior has been observed in various 1D systems, different inorganic NW including conducting polymers [19, 20]. The power-law

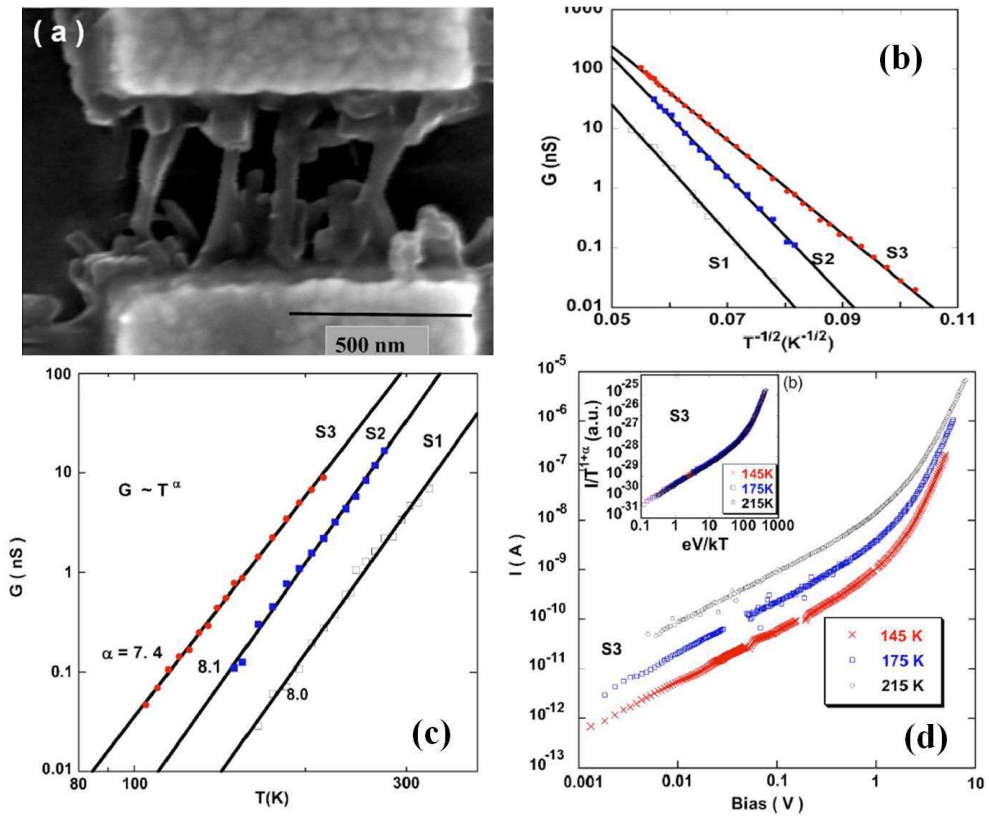

Figure 1.10 (a) SEM micrograph of Cu:TCNQ NW device. (b) Low bias conductance of three Cu:TCNQ NW devices (symbols) and fits (solid lines) to the 1D variable range hopping model (c) Low bias conductance vs T for the same Cu:TCNQ NW devices, solid lines are fits to the power law, G∝T^{α}. (d) I-V data taken at different temperatures. All curves show a change from linear response ($\beta \sim 0$) to power-law dependence at a temperature dependent high bias voltage. Inset: $\frac{1}{T^{\alpha+1}}$ determined from the I-V data plotted against eV/k_{β}T. Reprinted with permission from [17]

temperature dependence and 1D VRH behavior in the Cu:TCNQ NWs attributed to the transitional parameter range between VRH and weakly coupled quantum dots. When the power-law behavior in the I-V characteristic failed to explain in the context of the standard VRH model, the experimental results agreed with the 1D quantum dot chain model indicating that the Coulomb interactions in the Cu:TCNQ NWs cannot be neglected. They have also pointed out that the Cu:TCNQ NWs in the devices behaves like quasi-1D systems with a large number of nearly independent 1D conducting channels in parallel. Therefore, mesoscopic fluctuations that would normally obscure the power-law behavior in strictly 1D wires are averaged out in the NW device. Table 1.1 gives an overview of reported temperature dependent electrical transport measurement on Cu:TCNQ.

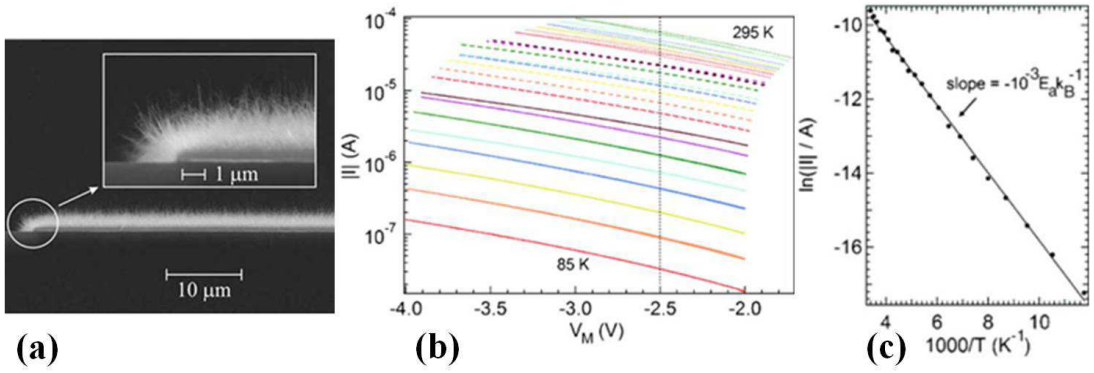

Figure 1.11 (a) Cross-sectional SEM micrograph of a 50 μm Au line with Cu:TCNQ NWs. (b) log$|I|$-V curves of 200×200 μm^2 Au/Cu:TCNQ/Al memory in on state at different temperatures; voltage scan: -2 to -4 V and back applied to the memory element with R=10 kΩ, and (c) corresponding ln$|I|$-T^{-1} plot at -2.5 V across the memory element. Copyright with permission from [18]

Muller et al. [18] also measured the electrical transport of Cu:TCNQ NW film in the form of Au/Cu:TCNQ/Al crossbar array in switched state using Au as bottom and Al as top electrode. Nanowire film were synthesized by PVD method. SEM micrograph of the device is shown in Fig. 1.11(a). Investigation of the current transport in the ON state of Cu:TCNQ was realized by temperature dependent measurements. After switching the device to the ON state, scan from 0 to -7 V and back (at 295 K), voltage sweeps between -2 and -4 V were applied to the memory element in series with a load resistor of 10 kΩ at temperatures ranging from 295 K down to 85 K (with 10 K steps) as shown in Fig. 1.11.(b). A ln$|I|$ verses T^{-1} plot (Fig. 1.11.(b)) results in a straight line from which an activation energy E$_g$ ∼0.08

Table 1.2 Comparative study of conductivity in Cu:TCNQ

Device structure	Conductivity (S/cm)	Reference
Pellet (Phase-I)	2.5×10^{-1}	[11]
Pellet (Phase-II)	1.3×10^{-5}	[11]
Single NW	1.34×10^{-4}	[22]
Single NW	1.67×10^{-2}	[23]
Nanowire film	2×10^{-1}	[24]

eV has been calculated using the Arrhenius equation. The thermally activated conduction in the ON state of Au/Cu:TCNQ/Al memories confirms that the material Cu:TCNQ behaves like a semiconductor,

which indicates that the current in the ON state is not simply due to conduction by metallic filaments, or tunnel transport, unlike what is observed for polymer-based metal/polymer/metal cells [21]. Table 1.2 summarises the comparative study of conductivity of Cu:TCNQ that has been reported or calculated from the data provided by different groups. The table shows that there are variations in the data. The highest in single NW is around 1.67×10^{-2} S/cm. The cause of variation can be that most of these reported experiments have undefined Z (extent of charge transfer) and also they used 2-probe measurements that may have contribution from contacts.

1.4 Review of resistive switching in Cu:TCNQ

Cu:TCNQ CT complex material is mostly known for its electrical resistive state switching property. This material generally shows bipolar resistive state switching i.e. RESET condition occur for opposite polarity of SET condition. Details of resistive switching is explained in chapter 5.

Knorr et al. [25] has investigated bipolar resistive switching of Cu/Cu:TCNQ/Al film cross-junctions in both vacuum and different gas environments as shown in Fig. 1.12. Although switching was reproduced in ambient atmosphere, but it was reversibly suppressed in well-degassed samples in vacuum and in dry N_2. The device switches to OFF state currents in ambient air when approximately $+2.6$ V bias was applied to the Al electrode at low voltage sweep rates. OFF-switching at constant bias was accelerated in humid and oxygen-rich atmospheres. They suggest that resistive switching occurs in a hydrated native alumina layer at the Cu:TCNQ/Al interface that grows in thickness during exposure to ambient humidity: ON state switching occurred by electrochemical metallization of free Al and/or Cu ions and OFF-switching by anodic oxidation of the Al electrode and previously grown metal filaments.

Muller et al. [26] had also observed bipolar switching in a device consisting of Cu/Cu:TCNQ/Al cross bar memory arrays. Cu:TCNQ films were prepared by vapor phase reaction of Cu and TCNQ. 200 μm wide and 100 nm thick Al top electrode lines were then deposited in a cross bar geometry using lithographic process. Fig. 1.13(a) and (b) shows the cross-section and top view of the device respectively. Fig. 1.13(c) shows the SEM image of the Cu:TCNQ film formed on 50 μm wide Cu lines.

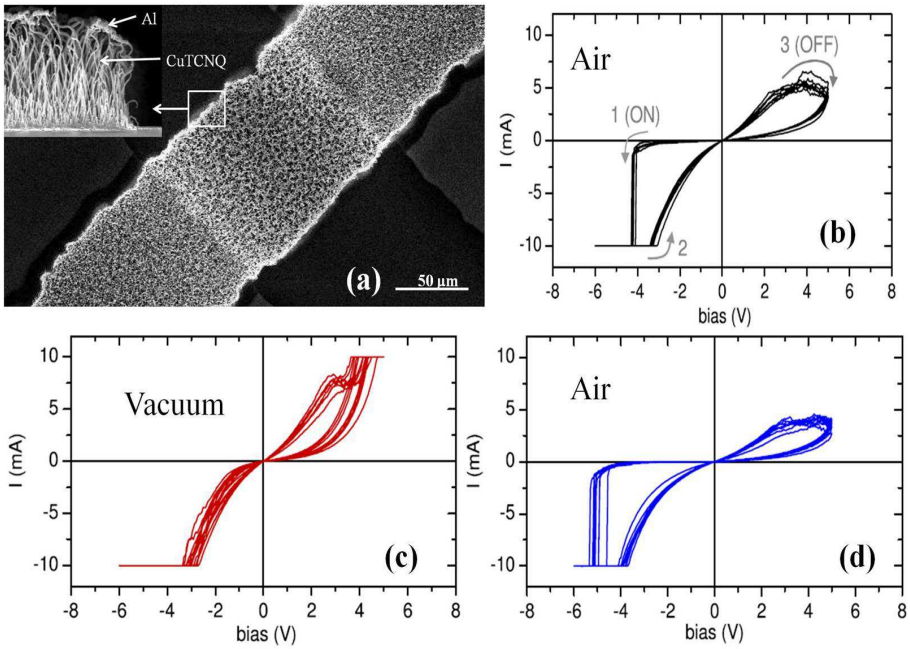

Figure 1.12 (a) Cross-sectional SEM micrograph of a 50 μm Au line with Cu:TCNQ NWs. (b) log|I|-V curves of 200×200 μm^2 Au/Cu:TCNQ/Al memory in on state at different temperatures; voltage scan: -2 to -4 V and back applied to the memory element with R=10 kΩ, and (c) corresponding ln|I|-T^{-1} plot at -2.5 V across the memory element. Reprinted with permission from [25]

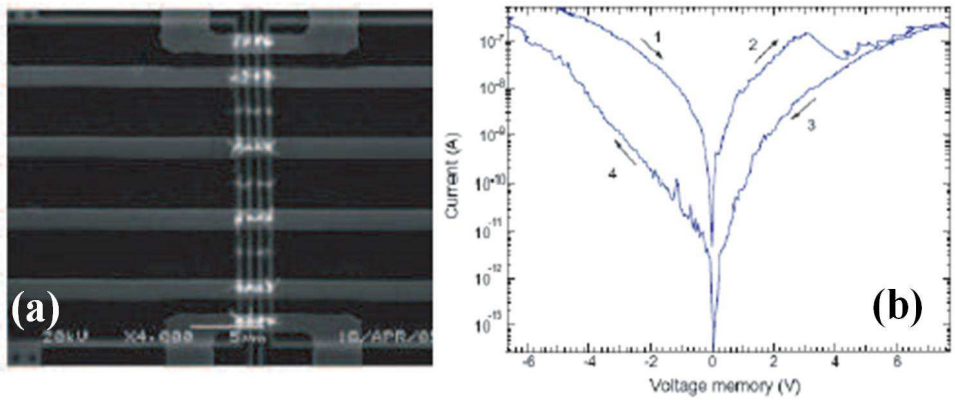

Figure 1.13 (a) SEM image of electrodes after Cu:TCNQ growth and deposition of top Al contacts in test structure for integration in the CMOS backend-of-line scheme. (b) log| I |-V curve of a Cu:TCNQ memory element. Reprinted with permission from [26].

Fig. 1.13(d) shows the log| I |-V curves of a Cu:TCNQ memory element (50 μm × 200 μm) taken with a load resistor of 22 kΩ. The ON/OFF current ratio is about 10. In first few cycles of voltage sweeps the ON/OFF current ratio was about 150, which then reduced to a lower value on repeated cycling.

Nanodevice prototypes with electrical switching characteristics based on a Cu:TCNQ NW array

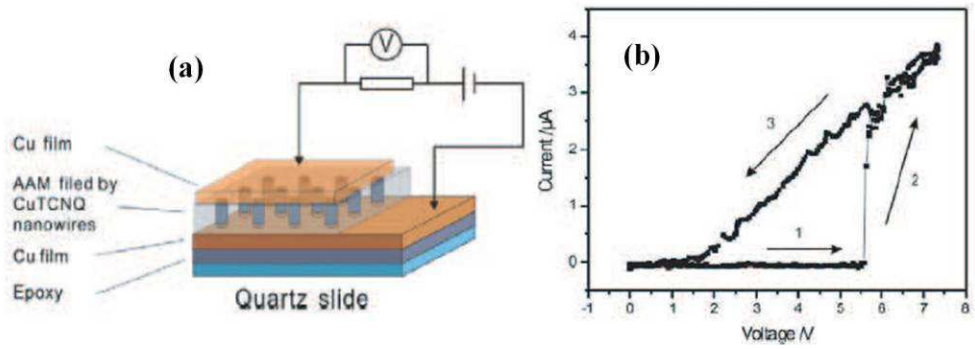

Figure 1.14 (a) Schematic of the measurement circuit on the device of Cu:TCNQ NWs grown in an anodic alumina membrane (AAM). (b) I-V characteristics of Cu:TCNQ NWs. Reprinted with permission from [27].

were fabricated by Shen et al. and reproducible electrical switching and memory effects were observed by Shen et al. [27]. They have used anodic alumina membranes (AAMs) of 60 nm and 200 nm pore diameter and 10 μm thickness for synthesizing Cu:TCNQ NWs. 1 μm thick film of Cu was coated on one side of AAM by thermal evaporation and then the Cu side of the AAM was stuck to a quartz substrate with a epoxy. Using electrodeposition a small amount of Cu was deposited at the bottom of the membrane. Then the membrane was exposed to TCNQ vapor in a vacuum furnace for the formation of Cu:TCNQ NWs. After that Cu was further deposited on top of Cu:TCNQ for top electrode. Fig. 1.14(a) schematically represents electrical circuit configuration of the NW device on AAM template. I-V characteristics of Cu:TCNQ NWs is shown in Fig. 1.14(b) for positive half of the applied bias. 1.0 MΩ resistor in series with the sample was used to control current through the NW. Nanowire device exhibits the same for negative polarity of the applied bias i.e. the device performed unipolar switching (Transition from high to low and low to high resistive state for same polarity of the applied bias.) In this device configuration, top and bottom electrodes were of Cu. Symmetric electrode configuration is the probable reason for unipolar switching. The ON/OFF ratio for switching reaches 10^4.

Xaio et al. [28] have fabricated planar Cu:TCNQ NW devices. On a SiO_2/Si substrate multilayered electrodes of Ti/Au/Cu/Au (70 nm Ti/Au, 50 nm Cu and 100 nm Au) were fabricated using e-beam lithography with varying electrode gaps. In this device configuration, the Cu electrode is sandwiched between two Au electrodes, so that only side wall of Cu electrode is exposed. Cu:TCNQ NW was then synthesized on this patterned device as shown in Fig. 1.15(a). As synthesized NW device was used to measure I-V. The I-V curves exhibit reversible hysteretic switching and memory behavior. As the

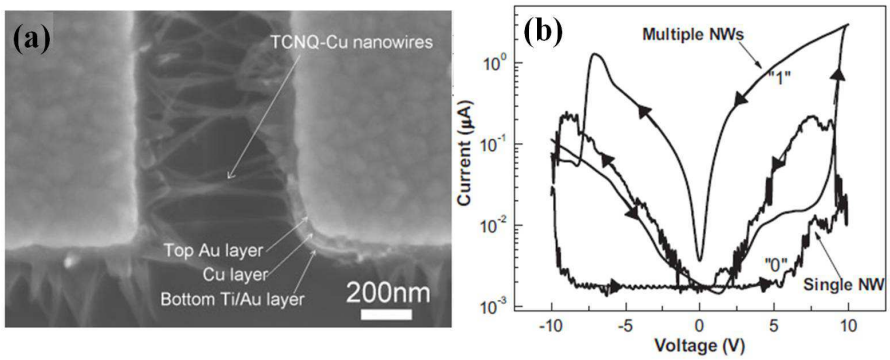

Figure 1.15 (a) SEM image of the Cu:TCNQ NW bridging electrode structure. (b) Typical room temperature I-V characteristics of a single Cu:TCNQ and multiple NWs bridging between electrodes indicating a reversible bistable switching behavior. The arrows show the voltage sweep directions. Reprinted with permission from [28].

voltage bias is increased from 0 to $+10$ V, the current increases monotonically at low biases until a sudden jump in current is observed at a positive threshold voltage (V_T) of approximately $=7$ V. The Cu:TCNQ NW remains in the high-current state as the voltage bias is increased to $+10$ V and while the voltage is lowered from $+10$ to 0 V. In contrast, the Cu:TCNQ NW remains in the low-current state if the bias is not allowed to exceed this threshold voltage as shown in Fig. 1.15(b).

Zheng et al. [23] fabricated a single NW device and observed electrical resistive state switching. Cu:TCNQ NWs were synthesized by a method that combine physical and chemical vapor deposition techniques as shown in inset of Fig. 1.16(a). In order to measure the I-V properties of individual Cu:TCNQ NW, synthesized NWs were separated from the substrate by ultrasonication in alcohol. The suspension was then deposited onto a silicon chip capped with a layer of 200-500 nm SiO_2. Photolithography was employed to form a square electrode array which consisted of 10 nm of Ni and 100 nm of Au, as can be seen in Fig. 1.16(a). Individual NW with good contacts on both ends were then located using SEM as shown in Fig. 1.16(b). The sample for measurement was 400 nm in diameter and the spacing between the two electrodes was 2.1 μm (Fig. 1.16(b)). When the voltage applied to the device was increased to the threshold voltage of 34 V, the current rapidly increased, indicating the sample transfer from a high-resistance to a low-resistance state. After the voltage was swept down to 0 V, the sample turned back to high-resistance state. The NW resistance in the high-resistance state and low-resistance state was approximately 10 GΩ and 2.83 MΩ, respectively. The actual ON/OFF resistance ratio for switching reaches 4 orders as can be seen in the logarithmic plot for I-V in inset

of Fig. 1.16(c). Threshold voltage of switching was found to have linear dependence of NW length as shown in Fig. 1.16(d), indicating the local field dependence of the phase transition. They have proposed field driven solitions transportation model to explain switching, which is basically based on self multiplication of the charge carriers. At low electric fields, most of these charged defects present in the CT complex NW are not free to move, but are thought to be spatially confined by a three-dimensional electrostatic potential [29]. These charged defects are either thermally excited or introduced during the crystal growth process. When the magnitude of the electric field is increased, these charges are driven into motion by a field-assisted dissociation mechanism. Further dissociation of charges goes on with increasing field, leading to a self-multiplication of current at sufficiently high fields and results in switching. Lowering of electric field make the charge carrier immovable bringing the system to high resistive state.

Except threshold voltage other important parameter of switching is reproducibility and endurance

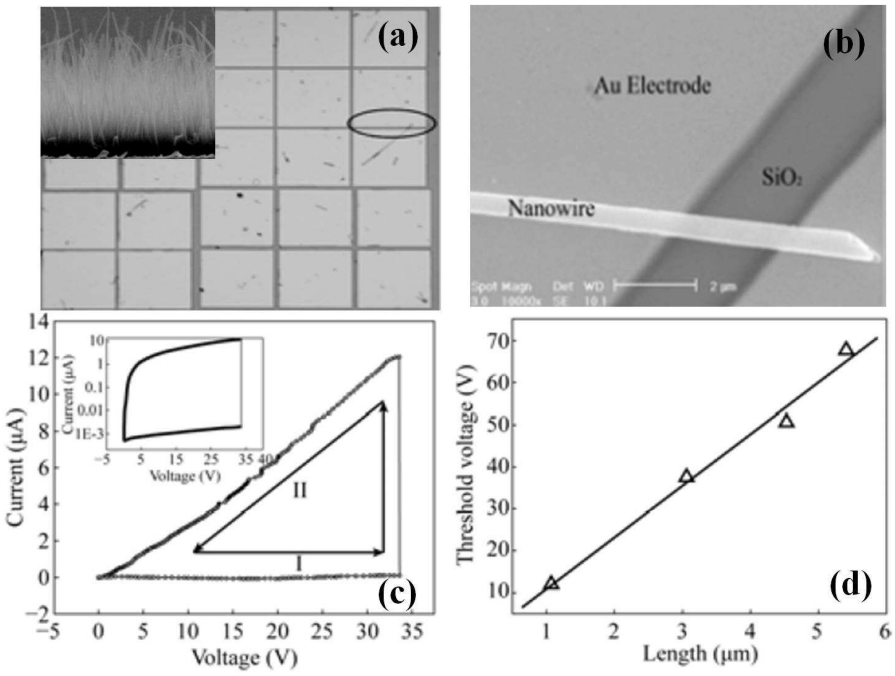

Figure 1.16 (a) Optical image of Ni/Au pads array, (b) SEM image showing one NW in contact with two pads. (c) I-V characteristics of individual Cu:TCNQ NW, and the arrow demonstrated the sequence of applying the voltage. State I and II indicated the electrical 'OFF' and 'ON' states, respectively. (d) The spacing between the two electrodes versus the switching threshold. Reprinted with permission from [23].

which determines how many times the device can be used to write and erase while using the material

in memory device. Muller et al. reproduces the switching property successfully in Cu/Cu:TCNQ/Al cross-point cell arrays devices for many times. Fig. 1.17(a) represents the log$|I|$-V curves for an Au/Cu:TCNQ/Al memory curves, recorded during 10000 write-erase cycles with ON and OFF threshold voltages in Fig. 1.17(b) [33]. Fig. 1.17(c) represents the retention measurement of the ON (write) and OFF state (erase) of the Ag/Ag-TCNQ/P4PMS (50 nm)/Ag device by another group [34]. They have applied a voltage pulse of $\pm$4 V to write (ON) or erase (OFF) the states of the device, followed by a read out of the states of the device by a -0.5 V read pulse. Current as a function of time is compared in Fig. 1.17(c) in the two cases.

Along with the material property of switching, electrode material is also important to achieve high endurance, switching speed, retention time, and ON/OFF current ratio. table 1.3 represents comparative study of resistive switching in CT complex materials, where SNW refers to 'single nanowire' and that of ANW for 'array of nanowire'.

Table 1.3 Comparative study of resistive switching in CT complex materials

Reference	Nanowire Diameter (nm)	Device Structure	Maximum Device Current	Switching Characteristics	
				ON/OFF ratio	V_{Th}
[28]	20	Cu:TCNQ SNW	0.25 μA	10	7
[23]	400	Cu:TCNQ SNW	12 μA	10^4	34
[27]	60-200	Cu:TCNQ ANW	4 μA	6×10^3	5.5
[30]	50	Cu:TCNQ ANW	1 μA	20	7
[31]	80	Ag:TCNQ SNW	0.12 μA	10^4	7.5
[32]	60	Au:TCNQ SNW	0.27 nA	10	8.5

1.4.1 Resistive switching model in MSM or MIM devices

Devices based on a metal-insulaotr-metal (MIM) or metal-semiconductor-metal (MSM) cell are usually called resistance switching RAM, or resistive-RAM (ReRAM). The letter 'M' in the abbreviation MIM is not restricted to metals, but refers to any reasonably good electron conductor, and is often different for the two sides. The 'insulator' or 'semiconductor' in these structures is often an ion-conducting material.

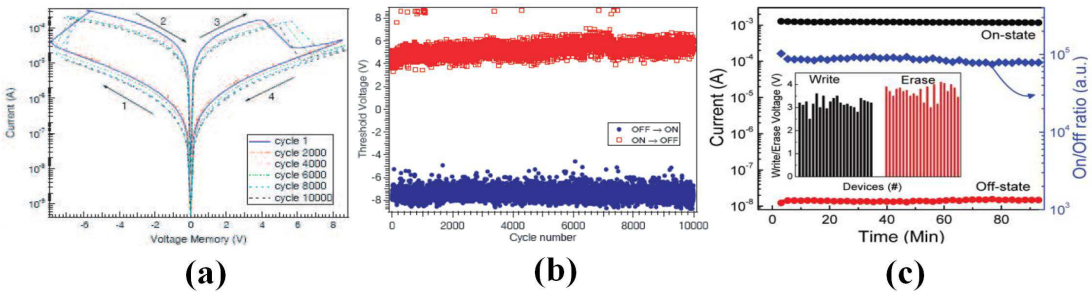

Figure 1.17 (a) Log| I |-V curves for an Au/Cu:TCNQ/Al memory recorded during 10000 write/erase cycles. (b) Threshold voltages for ON and OFF switching of the measurement series as function of the cycle number. Reprinted with permission from [33]. (c) Data retention measurement of the ON (write) and OFF state (erase) of the Ag/Ag-TCNQ/P4PMS (50 nm)/Ag device. Absolute values of current are plotted for comparison. The high and low conducting states were induced by -4 and +4 V (each of 10 s width), respectively, and probed by using -0.5 V. The ratio between the on and OFF-state currents (ON/OFF ratio) are shown on the right axis. The inset shows the write/erase voltage variation from a number of Ag/Ag-TCNQ/P4PMS (50 nm)/Ag devices. Reprinted with permission from [34]

.

There are a number of models proposed to explain switching in MIM or MSM device. Cu/Cu:TCNQ/Al or Au/Cu:TCNQ/Au configurations as discussed from reported data are assumed to be MSM configuration as Cu:TCNQ behaves like a semiconductor. Different groups proposed different models to explain switching in Cu:TCNQ.

Billen et. al. [35] proposed a model to explain bipolar switching in Cu:TCNQ by redox-reaction. Bipolar switching results observed in Cu/Cu:TCNQ/M (M= Al and Yb) memory elements in a device (200 μm$\times$200 μm) connected with a load resistance R=10 kΩ is shown in Fig. 1.18 (a) and (b) for different top metal electrode configuration in different atmosphere. Both devices performed switching only in ambient atmosphere but not in inert atmosphere or vacuum, leading to a conclusion that switching is possible only when an easily oxidized electrode is used that is actually exposed to an oxidizing ambient. In this case, the device shows high resistive state (HRS) to low resistive state (LRS) transition at a threshold voltage of 7-8 Volt. The HRS originates from insulating interfacial layer between NW and top contact. To elucidate the LRS, they have recorded thermal image within 3 min during which -2 V square waves at a frequency of 1 Hz was applied and found local hot spots appeared at several places on the cross-point (Fig. 1.18(c)), which was a clear indication for inhomogeneous current distribution attributed to electrical conduction through conductive channels inside the oxide/hydroxide layer at the

Cu:TCNQ/Al interface. Then, they proposed a model for the resistance switching of Cu:TCNQ that is compatible with all above findings. Fig. 1.18(d) and (e) schematically represents the mechanism. The $Cu^{+}TCNQ^{-}$ salt acts as source of monovalent Cu^{+} cations. These ions migrate through a thin

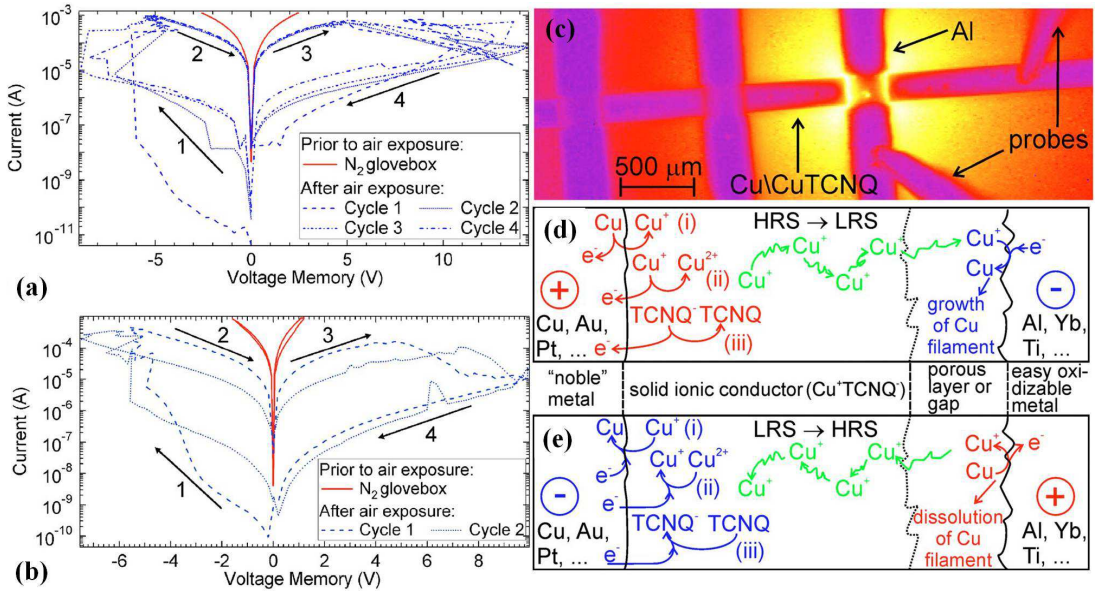

Figure 1.18 Log $|I|$-V curves of Cu/Cu:TCNQ/M memory elements (200×200 μm, load resistor R=10 kΩ measured) in N2 filled glovebox directly after M (100 nm) top contact deposition, and after air exposure, (a) M=Al, voltage scan $0 \rightarrow -15 \rightarrow +15 \rightarrow 0$ V, and (b) M=Yb, voltage scan $0 \rightarrow -10 \rightarrow +10 \rightarrow 0$ V. (c) Thermal image showing local hot spots (yellow) for the LRS of a Cu/Cu:TCNQ/Al memory. (d) and (e) Proposed switching mechanism; Oxidations are shown in red, reductions in blue, and migration of Cu+ in green. Reprinted with permission from [35].

porous oxide/hydroxide layer at the Cu:TCNQ/oxidizable electrode interface through the gap between the Cu:TCNQ and the probe needle or scanning tunneling microscope (STM) tip and are electrochemically reduced to metallic Cu when the electrode (probe needle or tip) is polarized sufficiently negatively, with respect to the other electrode (Fig. 1.16(d)). The process continues with time and finally one or more conductive filaments bridge over the porous layer or the gap. They form conductive filaments that lower the resistance of the porous oxide layer, thus, bringing the memory to the LRS. By reversing the polarity the metallic Cu is electrochemically oxidized into Cu+ cations and the filament(s) dissolves, leading to the HRS (Fig. 1.18(e)).

Recent reports suggest that the transition from Phase-II to Phase-I may be the reason of switched low resistive ON state from high resistive OFF state as shown in Fig. 1.19 by Fernandez et al. [12].

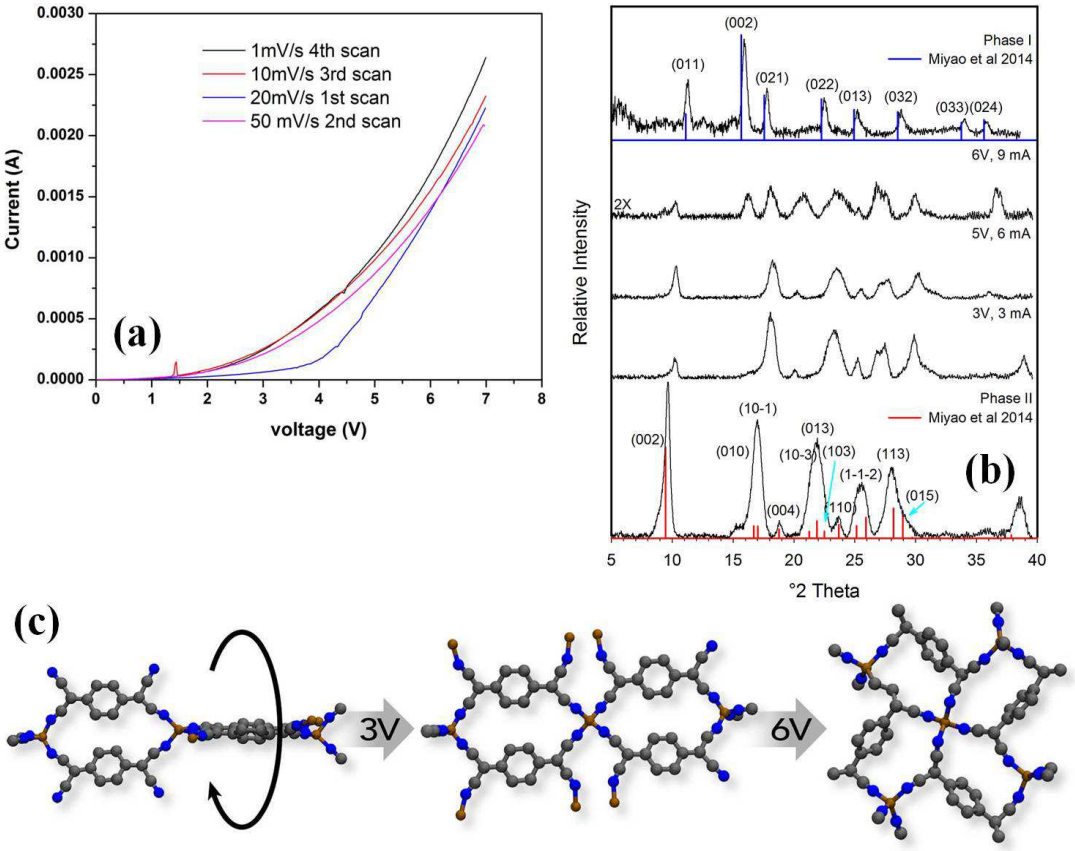

Figure 1.19 (a) DC current-voltage plot showing bistable switching in a 10 μm thick Cu:TCNQ Phase-II film placed between two electrodes in a sandwich structure. Each new scan was performed after a relaxation period of about a minute. (b) XRD spectra of Cu:TCNQ as a function of voltage showing the reflection planes for both phases, Phase-I and Phase-II. (c) Single crystal structure of Cu:TCNQ 'OFF 'state Phase-II (left) transitioning to a proposed new 'ON'state Phase-III (center) at 3 V followed by a transition to Phase-I at 6 V. Reprinted with permission from [12].

Although the authors do not show switching as shown in other previous studies [26, 34, 35]. They have performed dc current-voltage measurement between 0 and 6 V on thin film of Cu:TCNQ which shows conductivity comparable to Cu:TCNQ Phase-II in the voltage range 0-1 V and Cu:TCNQ film goes from an 'OFF' insulating state to an 'ON' conducting state at approximately 4.5 V for first cycle and at 2.5 V for rest of the cycles irrespective of the scan rate as shown in Fig. 1.19(a). This could be due to the fact that a small fraction of the conducting phase is still present even after the applied voltage is switched-off. ON state conductivity in the voltage range of 4-6 V is equal to Cu:TCNQ Phase-I. This is due to transformation of Cu:TCNQ Phase-II at low bias to Cu:TCNQ Phase-I at high bias. To gain insight on the electrical switching mechanism, and more importantly, determine if a struc-

tural transformation on Cu:TCNQ plays a role on the electrical switching of Cu:TCNQ film materials they performed in *operando* X-ray diffraction (XRD) as a function of applied potential as shown in Fig. 1.19(b). At 0 V bias i.e. at 'OFF' state, Cu:TCNQ film shows XRD pattern of Phase-II structure, intense peaks of which are at $2\theta = 9.2^o$ (002) perpendicular to the N-Cu-N coordination mode and $2\theta = 16.8^o$ (10-1). These peaks are shifted to $2\theta = 10.3^o$ and $2\theta = 18.3^o$ with decreased intensity as sufficient bias is applied across the film. These shifted peak corresponds to (002) and (011) of Cu:TCNQ Phase-I. The decreased (002) intensity suggests a distortion of the structure such that atoms, and especially the heavier Cu atoms, are no longer aligned on planes parallel to (001). The distortion would result in deviation from the tetrahedral symmetry at the Cu positions and as a result overlapping occurs between the hybrid sp orbitals of the cyanide functionalities and the π system of the benzene rings, and Cu:TCNQ Phase-II transformed to Phase-I through an intermediate phase called Phase-III as schematically illustrated in Fig. 1.19(c).

There are some different proposed models/theories trying to explain the resistive switching in MIM or MSM devices based on electrical effects. Electronic charge injection and/or charge displacement is seen as one origin of the switching. Some uses charge-trap model which can explain the different resistance states of a MIM/MSM cell by the modification of the electrostatic barriers due to trapped charges [36]. According to this model, charges are injected by Fowler Nordheim tunneling at high electric fields and subsequently trapped at sites such as defects or metal nanoparticles in the insulator. This model was later modified in order to incorporate charge trapping at interface states, which is thought to affect the adjacent Schottky barrier at various metal/semiconducting interfaces [37].

Another category contains all MIM/MSM systems in which the resistive switching is primarily based on ionic transport and electrochemical redox-reactions. This is a research field where nanoelectronics [38] intersects with nanoionics [39]. A model of resistive switching of MIM/MSM devices based on cation migration is shown in Fig. 1.20. A solid electrolyte layer is sandwiched between the two electrodes, of which one is made of silver. During the set process (Fig. 1.20 (a)), a positive bias voltage is applied to the silver electrode and causes the oxidation of the electrochemically active electrode metal (Ag) [40]. The resulting Ag+ ions are mobile in the solid electrolyte and drift due to the electrical field towards the cathode. These cations discharge at the negative charged

Table 1.4 Reported models used to explain resistive switching in Cu:TCNQ

Reference	Basic Model	Supporting Experiment
[30]	Conductive channel formation and disruption by redox reaction	Performed local I-t measurements by approaching AFM tip on NW surface and constant voltage was applied across the tip. Stepwise current spikes indicate successive conductive channel formation during the SET process.
[42]	Conductive channels formation and disruption by redox reaction	Performed impedance spectroscopy measurement for Au and Al top electrode contact and measured dielectric constant which match to an interface layer of naturally oxidized Al between Cu:TCNQ and the Al top electrode. Presence of Al oxide at the interface indicates redox reaction at interface.
[35]	Conductive channels formation and disruption by redox reaction	Thermal images were recorded during measurement and local hot spots appeared at several places on the cross-point of NW and top contact Al electrode, which clearly indicates inhomogeneous current distribution, attributing electrical conduction through conductive channels inside the oxide/hydroxide layer at the Cu:TCNQ/Al interface. Performed Raman spectra in unswitched and switched state
[23]	Field driven solitions transportation model	No supporting experiment has been performed.
[12]	Transformation from Phase-II to Phase-I	Performed XRD at different bias.

(inert) counter electrode leads to the growth of Ag dendrites. The dendrite forms a highly conductive filament when reaching the anode. The system is then in the low resistance ON state. The reset process occurs by application of a reversed voltage. If a negative bias voltage is applied to the silver electrode, an electrochemical dissolution of the conductive bridges takes place, resetting the system

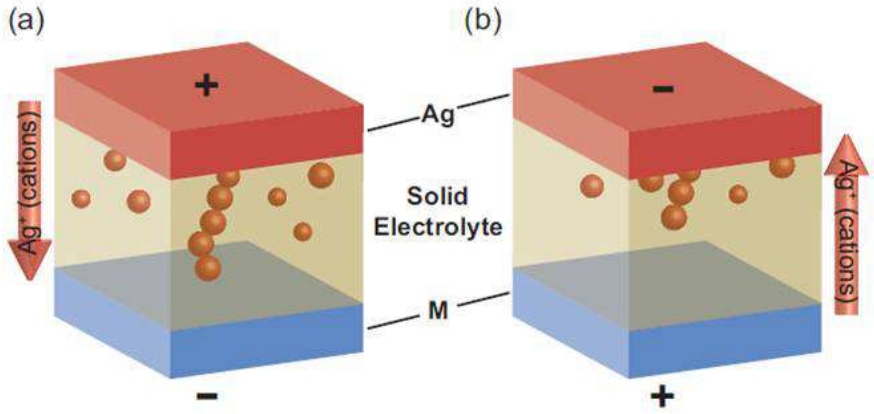

Figure 1.20 Schematics of the cation movement in a MIM/MSM device: (a) electrodeposition during set process (b) breaking of metal filaments during reset process. Reprinted with permission from [40].

into the OFF state (Fig. 1.20(b)). Copper is also often used as electrode material, due to its comparable electrochemical potential and mobility.

Most of the report of switching in Cu:TCNQ is based on the Cu filament formation and destruction by redox reaction in the NW electrode interface. Table 1.4 shows the reported switching model in Cu:TCNQ corresponding experiment to support the switching model they provided.

1.5 Opto-electronic property of Metal:TCNQ

At 1982 Potember [41] for the first time observed that semiconducting organometallic films such as Cu:TCNQ can switch between two stable states when exposed to optical radiation. Semiconducting Cu:TCNQ, are grown as polycrystalline films directly on the metallic substrates by reacting neutral TCNQ in acetonitrile solution with copper. For electrical measurements, a top Al or Cr metal electrode was deposited directly on the organic film, and contacts had been made in between top metal electrode and metallic base substrate. For the optical and electro-optical experiments, the top metal electrode was either omitted or prepared with a thickness that permitted partial transmission of optical radiation. Depending on the specific material involved, they have varied the field strength between 2×10^3 V/cm and 2×10^4 V/cm using laser source, required to cause switching transitions. They have illuminated a number of Cu:TCNQ and Ag:TCNQ specimens with the 488 and 458 nm lines from an Ar-ion laser. The effects of illumination by laser source have been observed both by Raman spectra and by electrical

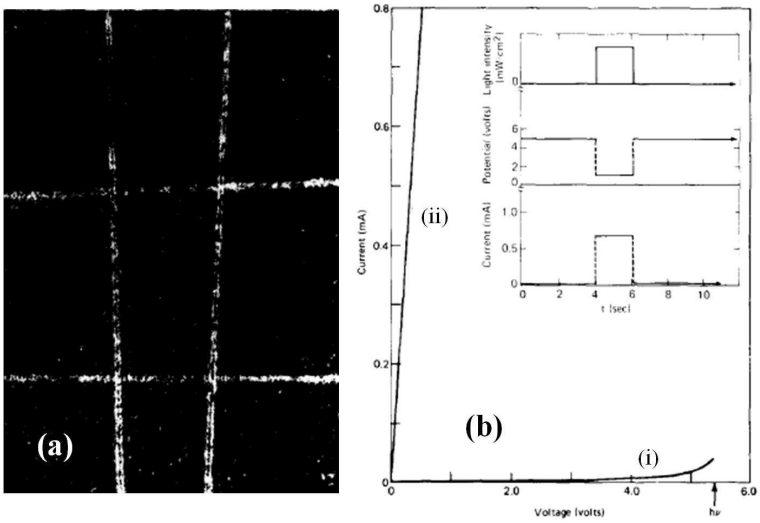

Figure 1.21 (a) High contrast pattern generated by optical beam exposure of Ag:TCNQ film. (b)Switching characteristic of Ag:TCNQ induced by application of argon laser beam showing (i) high- and (ii) low-impedance states. Inset: Time variation of current when laser beam was periodically interrupted. The laser power was 25 mW and the beam diameter was 100 μm. Reprinted with permission from [41].

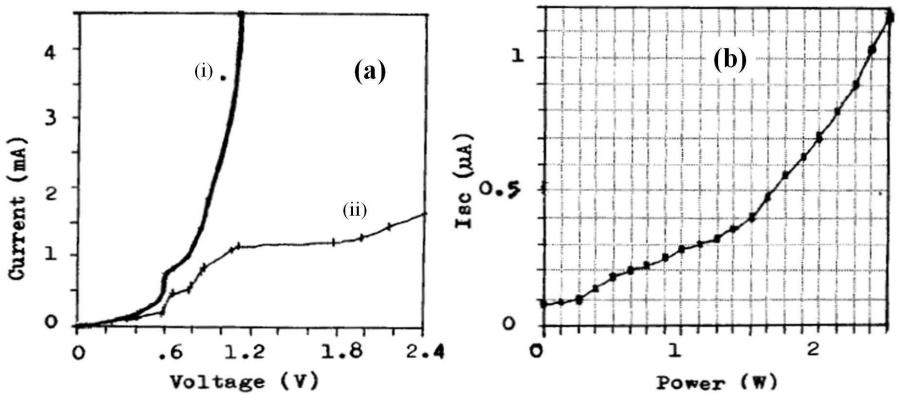

Figure 1.22 (a) VI data of Cu:TCNQ film (i) under radiation (488 nm, 2.8 W/cm^2) and (ii) in dark. (b) I_{sc} with illuminated power. Reprinted with permission from [41].

measurements made on the samples in conventional two-probe electrode configuration. Illumination creates high contrast in Ag:TCNQ film as shown in Fig. 1.21(a). I-V measurement before and after irradiation has been shown in Fig. 1.21(b).i.e. laser exposure with suitable power brings the system from high to low resistive switched state.

Gu et al.[43] also measured the current in Cu:TCNQ film in dark and under illumination as shown in Fig. 1.22(a). They carried out opto-electronic experiments in the application of Ar-ion laser at 488

nm with an effective beam diameter of 44 mm. The laser beam was focused on the Cu:TCNQ film through glass/ITO. At the same time the Cu:TCNQ film was biased with a dc electric field of $\sim$ 20 mV to 3.5 V across the Cu/Cu:TCNQ/ITO structure. With illumination, current increases over dark by 100 times (Fig. 1.22(a)). In addition they have also observed a photo-voltaic effect in the same structure. Fig. 1.22(b) demonstrates the short circuit current I_{sc} with illumination power (effective area of beam 0.61 cm^2) and the curve was almost linear. They considered that this photo-voltaic effect was due to taking shape of Schottky barrier between Cu:TCNQ and ITO. These reports confirm the opto-electronic behaviour in CT complex materials. However, these observations are relatively old and there are no recent attempts to redo these investigations so that merits of Cu:TCNQ as an opto-electronic material can be developed. In this thesis, our attempt is to focus on these and related issues.

1.6 Motivations behind the present work

Based on the preceding review we present below the main features of this thesis:

1. Most of the reports are on NW/film grown on Cu film. Very few reports are on predefined pattern. One of our aim is to control lateral growth of Cu:TCNQ NW on predefined patterns and make single NW device with variable length and diameter. The diameter and the numbers of NWs bridging/connecting the two electrodes can be controlled using the controlled evaporation rate. The applied field between predefined electrodes during NW growth also controls the diameter.

2. There are very few reports on temperature dependent electrical transport of Cu:TCNQ NW particularly at T$<$ 100 K. In this thesis, we have investigate electrical conduction of Cu:TCNQ NWs over a wide range of temperatures. We have also studied the conduction in NWs grown in presence of field and compare it with zero field grown NWs. For the first time, we have investigated the existence of charge density wave transport in Cu:TCNQ NW below a transition temperature.

3. Most of the available reports on resistive switching of Cu:TCNQ were on films and rarely on single NWs. The mechanism behind the switching is not also properly understood till now. Here, we have observed switching in a single NW and separated out the contribution of switching from the NW and that from contacts. We have also established a viable model and tried to develop a numerical analysis of the model.

4. It can be seen from the review that there are insufficient investigations on opto-electronic property of Cu:TCNQ. In this thesis, we have investigated or explored the opto-electronic property of both single and array of Cu:TCNQ NWs, in particular their performance as a photodetector.

1.7 Structure of the thesis

The thesis is framed on the following works: (1) growth and structural characterization of NWs, (2) device fabrication down to a single NW level using nanolithography processes, (3) electrical and opto-electrical investigations of a specific 1-D organic CT complex. The specific CT complex investigated in this thesis is a metal-organic Cu:TCNQ. The proper charge transfer has high densities of charge carriers in Cu:TCNQ which leads to substantial electrical conductivity and optical field-induced phase transitions. This material is well known as described before for its unique one dimensional electrical property and also a large bipolar resistive state transition when the applied bias crosses a threshold voltage [8]. This resistive switching property opens up the possibility to use this material as ReRAM. A mechanism of switching with metallic channel formation by redox reaction has been reported [35], but there are no experimental evidence for it. Few reports are on temperature dependent electrical transport of Cu:TCNQ NWs, though the actual mechanism of transport is not well explored [44, 17]. Very few works have been reported previously on CT complex material as erasable optical storage, but the detail experimental study has not been done on it. [45].

In this thesis, our main emphasis was on the issues of transport in CuTCNQ NW, which was not well studied before. Apart from that our important contribution is in finding a new effect, i.e. photo-conductivity in NW of such materials. An important new aspect of work in this thesis is to take the experimental work down to single NW level. The electrical conductivity of a single NW of Cu:TCNQ have been investigated and demonstrated the conduction mechanism in a semi-quantitative way. It has also been investigated that instead of NW arrays, whether a single NW of this CT complex can show stable and reproducible resistive switching like NW arrays. We have also looked into whether the contact electrodes plays any role in the resistive switching. To attend these queries, precise electrical and opto-electronic measurement on both single and bunches of Cu:TCNQ NWs (average diameter ranging from 10 nm to 100 nm) which were grown by vapor phase synthesis have been carried out. Directed

self-assembly of Cu:TCNQ NWs, which is an objective of the thesis, can provide controlled and unidirectional fabrication of a nanometer-sized building block of these materials. We have observed for the first photoelectrical response in the NWs of this material. Our investigations show that Cu:TCNQ CT complex material, not only have well known resistive switching behavior but also shows opt-electronic response, and the responsivity is comparable to that of the highest photo-responsive material till date. Effects of contact resistance on electrical resistive state switching and photoresponse on a single NW have also been observed.

This thesis is divided into main chapters along with summary and two appendix chapters listed below:

This thesis starts with necessary literature of the earlier work in the field of CT complexes followed by our motivation in undertaking the present work.

The 2^{nd} chapter gives a description of synthesis of Cu:TCNQ NW and characterization along with experimental set-up developed for synthesis.

The 3^{rd} chapter describes nanodevice fabrication procedure to make single NW device and experimental techniques for electrical and opto-electronic measurements.

The 4^{th} chapter reports the temperature and bias dependent electrical transport properties of array as well as single NW of Cu:TCNQ, grown without and with the application of external bias. Nanowires show a linear part of the conductance and a non-linear part beyond a threshold bias. Below 100 K, the non-linear conductance follow modified Zener tunnelling model in both types of NWs raising the possibility of charge density wave (CDW) type charge transport in the Cu:TCNQ NWs. Modified conductivity in field assisted NW over zero field grown NW have also been discussed.

The 5^{th} chapter reports a new type of unipolar resistive state (RS) switching in a single NW of Cu:TCNQ which generally shows bipolar RS switching with different electrodes configuration. This chapter also describes the effect of electrodes on switching and possible mechanism of switching supported by phenomenological model and numerical calculations.

The 6^{th} chapter describe the opto-electronic transport measurement on Cu:TCNQ NW, both in array and single, having diameter down to 30 nm with the explanation of possible reasons of current enhancement under illumination.

Last chapter is the summery and conclusions of this thesis. It describes main achievements of the

thesis and future challenges.

This thesis ends up with appendix containing two parts describing new finding in Cu:TCNQ under progress, such as enhancement of Cu:TCNQ conductance by graphitic oxide induced charge transfer, floating gate (FG) and electric double layer (EDL) FET in a single NW of Cu:TCNQ.

Chapter 2

Synthesis and Characterization

In this chapter, we have described the procedures for synthesis of Cu:TCNQ nanowires (NWs) and their characterizations. Cu:TCNQ NWs are synthesized by two different methods: Physical Vapor Deposition (PVD) and Wet Chemical method. We have also studied the field assisted growth of NW between two metal electrodes using PVD. As synthesized NWs are characterized by X-ray Diffraction (XRD), Scanning Electron Microscope (SEM), Transmission Electron Microscope (TEM) for structural and Fourier Transform Infrared Spectroscopy (FTIR) and Raman Spectroscopy for compositional characterizations. We have also described the techniques in brief followed by experimental outcomes.

2.1 Introduction

One-dimensional (1-D) nanostructures, such as wires, tubes, belts, and rods have been extensively studied for the past two decades due to their interesting and unique electronic, optical, thermal, mechanical and magnetic properties. In the early stage of this research field, novel synthetic routes and fundamental characterization were heavily emphasized. The ability to fabricate high-quality single-crystalline materials with control of diameter, length, composition, and phase enabled breakthroughs in their incorporation into useful devices. Early applications emphasized electronic and optical devices, which provided further insight and stimulus to gain a deeper understanding of the basic material properties of these structures. There are various routes to synthesize NW like physical vapour deposition (PVD), chemical vapour deposition (CVD), laser ablation, thermal annealing, vapour-liquid-solid

(VLS), chemical deposition etc. In the PVD method the source is evaporated and condensed directly onto the substrate where no catalyst is required [47]. In the CVD method, the precursor gas is delivered to the surface of the substrate, where the synthesis occurs under catalytic conditions [48]. Laser ablation method involves a target that is first thermally pressed and placed in the chamber on target plate [49]. The target is ablated under low pressure using a laser beam which condenses on the substrate catalyst. In the thermal annealing method the source material is vaporized and transported by a carrier gas to the substrate surface with a catalyst deposit [50]. The vapor condenses onto the molten catalyst and source alloy. After saturated equilibrium condition is achieved, NW grows to maintain the equilibrium in the liquid phase. In chemical method, a film coated substrate is dipped into solution of deposition material of interest, which reacts chemically in the solution to form nanostructure.

2.2 Synthesis of Cu:TCNQ Nanowires:

We have synthesized Cu:TCNQ NWs using two different methods: PVD and chemical method although most of the thesis work particularly those on single NW have been performed with NWs grown by PVD method.

2.2.1 Nanowire growth by Physical Vapor Deposition (PVD) Method:

We have used the TCNQ (7,7,8,8-tetracyanoquinodimethane) powder (purity 98 %) from Aldrich Chemical Co. and and the Copper pellets (purity 99.999 %) from Curt J. Lesker Material Group Company to grow Cu:TCNQ NWs. In PVD process, firstly Cu thin film was deposited on Si/SiO_2, Si/Si_3N_4 or glass substrate and then TCNQ was evaporated on deposited Cu film maintained at $\sim 130^oC$. TCNQ in contact with Cu reacts with it and forms Cu:TCNQ. Mechanism for the growth of Cu:TCNQ NWs can be described as follows. Initially TCNQ molecules are adsorbed by the Cu film with which it interacts forming Cu:TCNQ. Next, the incoming flux are adsorbed on these Cu:TCNQ surfaces and the electrons are transferred from the base Cu film to the adsorbed TCNQ through the Cu:TCNQ due to redox potential difference between Cu and TCNQ [51]. The TCNQ is thus oxidised to $TCNQ^-$ ion. On the other hand, since the chemical potential of Cu is different at the two ends of the Cu:TCNQ crystal with the chemical potential at the bottom end significantly higher than the chemical potential

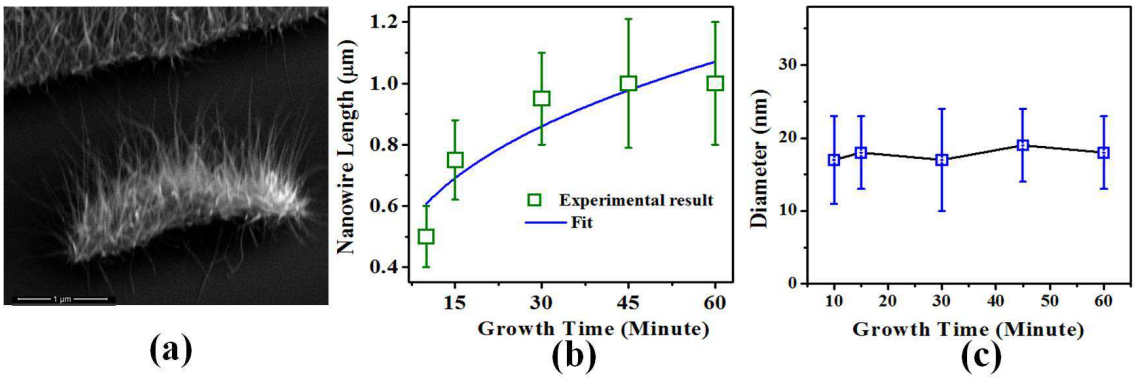

Figure 2.1 (a) SEM image of PVD grown NWs. Variation of (b) length ($l \propto \sqrt{t}$) and (c) diameter of NWs as a function of growth time for a constant evaporation rate.

at the top, Cu^+ ions migrate to the top surfaces through the Cu:TCNQ crystals formed. In NW form, the chemical potential difference is maximum between two oppositely ionised molecules and this may be the reason of NW formation of Cu:TCNQ during growth. In this process, a fractional amount of electronic charge is transferred between the acceptor and donor. Here, Cu acts as donor and TCNQ as acceptor. The formation of the NW thus involves diffusion of Cu ions. We observed that the diffusion process determines the growth rate. This also makes the charge transfer value Z less than 1. When this donor and acceptor interact, charge is redistributed in the formed NW. The reaction equation can be represented as follows:

$$Cu(solid) + TCNQ(gas) \rightarrow [Cu^+ + TCNQ^-] \leftrightarrow Cu:TCNQ \tag{2.1}$$

SEM image of synthesized NWs are shown in Figure 2.1(a). Nanowires are generally ∼10-30 nm (see Fig. 2.1(c)) in diameter and few μm in length. Diameter can be controlled by evaporation rate which is directly related to evaporation temperature and length is controlled by time of evaporation. The NW diameter becomes larger with higher temperature and higher evaporation rate [52]. For higher evaporation rate, highly energetic large amount of TCNQ molecules reach to Cu film and react with Cu to form Cu:TCNQ simultaneously on many regions of the Cu film. Many reaction regions of Cu:TCNQ molecules fused together and grew into large-diameter Cu:TCNQ NW. On the contrary, at lower temperature i.e. at lower evaporation rate, only few TCNQ molecules in vapor had enough reaction energies to form Cu:TCNQ NWs. At the low reaction temperature, the already formed Cu:TCNQ NWs prohibit TCNQ molecules to approach the Cu film and with time, reaction takes place via Cu^+ ion migration

through the already formed Cu:TCNQ NW, and hence results in thinner NW. Growth time and evaporation rate has also significant effect on dimensionality of the grown NW. Initially, length of the NWs increases with time and then it saturates. The growth being controlled by diffusion of Cu^+ ions, one would expect a reaction of $l \propto \sqrt{t}$, where l is the length of the grown NW and t is the time of growth. Diameter of the NWs is almost constant for a constant evaporation rate. Nanowire's length and diameter as a function of growth time for a constant evaporation rate is shown in Fig. 2.1(b) and (c) respectively. Slower evaporation rate gives thinner NW. Fig. 2.2(a) and (b) show SEM images synthesized with different evaporation rate. All experimental condition being constant, we can assume evaporation rate is proportional to the chamber pressure during evaporation, as higher pressure indicates more number of molecules are present in the evaporation chamber i.e. higher evaporation rate and consequently lower pressure signifies slower evaporation rate. Evaporation at 5.4×10^{-6} mbar chamber pressure gives NW diameter of $\sim 30-100$ nm, whereas NW diameter $\sim 10-30$ nm was achieved for 1.2×10^{-6} mbar chamber pressure as shown shown in Fig. 2.2(a) and (b) respectively.

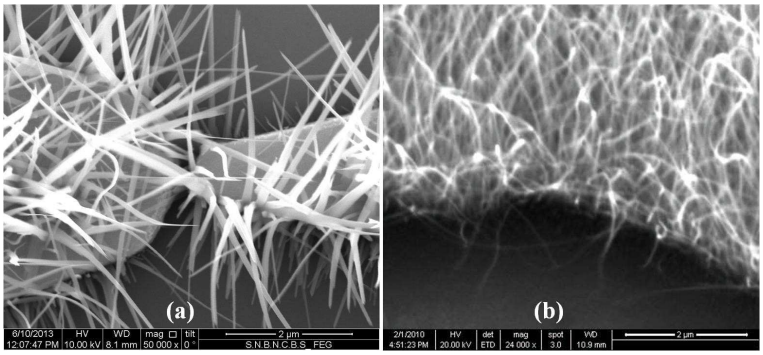

Figure 2.2 SEM image of PVD grown NWs at a constant pressure of (a) $5.4\times^{-6}$ mbar and (b) $1.2\times^{-6}$ mbar respectively. (The pressure refers to pressure during growth and not the base pressure)

2.2.1.1 Evaporation Chamber for PVD Growth:

To deposit molecular wire of CT complexes by PVD method, we have designed an evaporation chamber. Fig. 2.3(a) shows the schematic of the evaporation chamber. Most of the samples used in this thesis were synthesized in this chamber. The body of this chamber is made up of stainless steel. It consists of (i) a port connected to high vacuum turbo pumping system, (ii) another port for gas inlet/outlet, (iii) three crucibles used for Cu, TCNQ and Au or another evaporation material, (iv) six electrodes each two

are connected with one crucible to give power supply for heating the crucibles, (v) three Pt100 thermometer to measure the temperature of the crucibles, (vi) a transformer with adjustable rotor to supply power across the electrode for evaporating the materials, (vii) a sample holder mounted on a controllable rotating sample stage, (viii) a heater on top of the sample holder, (ix) a temperature controller to control the temperature of the heater, (x) a movable mechanical shutter in between crucibles and sample holder and (xi) a door containing two view ports. On the top flange, there is provision for two electrical leads for applying bias across the sample electrodes. The chamber is pumped with a Turbomolecular pump giving a base pressure of $\sim 2 \times 10^{-7}$ mbar. In this chamber three materials can be deposited consequently without braking the vacuum. To do that the sample stage can be rotated such that the sample be moved just above the required crucible. Three crucibles are connected between three sets of electrodes and the power applied between these electrodes can be controlled independently. Initially we deposit Cu on subtrates like glass or Si/SiO_2 or Si/Si_3N_4. After Cu evaporation, Cu coated substrate in the sample stage is moved to the position of the crucible containing TCNQ organic powder. Power is given to the leads of corresponding crucible to evaporate TCNQ powder. At the same time sample stage is also heated and temperature of the sample stage is controlled by the temperature controller. We generally kept the sample stage at the temperature range of 120-140^o C. TCNQ is evaporated and vapor of TCNQ comes in contact with the heated Cu film on SiO_2 substrate which results in growth of Cu:TCNQ NWs.

2.2.1.2 Field assisted growth of Cu:TCNQ NWs:

Recently there are focus on developing new techniques to control the growth of NWs on prefabricated electrodes [53, 54] using dielectrophoretic (DEP) as well as electrostatic force (EF). DEP force determines the motion of uncharged polarized particles in a non-uniform electric field [55]. Keeping in mind the above concept of DEP force, we investigated the possibility of localizing the lateral growth of Cu:TCNQ NWs bridging between two prefabricated electrodes by applying an electric field during growth. Such a field assisted procedure has been followed before for growth of NWs of charge transfer complex like TTF-TCNQ [56, 57]. However, the mechanism of field assisted growth is still not clear. We have studied the role of electric fields on growth of Cu:TCNQ NWs, where DEP [58] force takes an important part. We performed simulation to understand the effect of the EF as well as the DEP force on

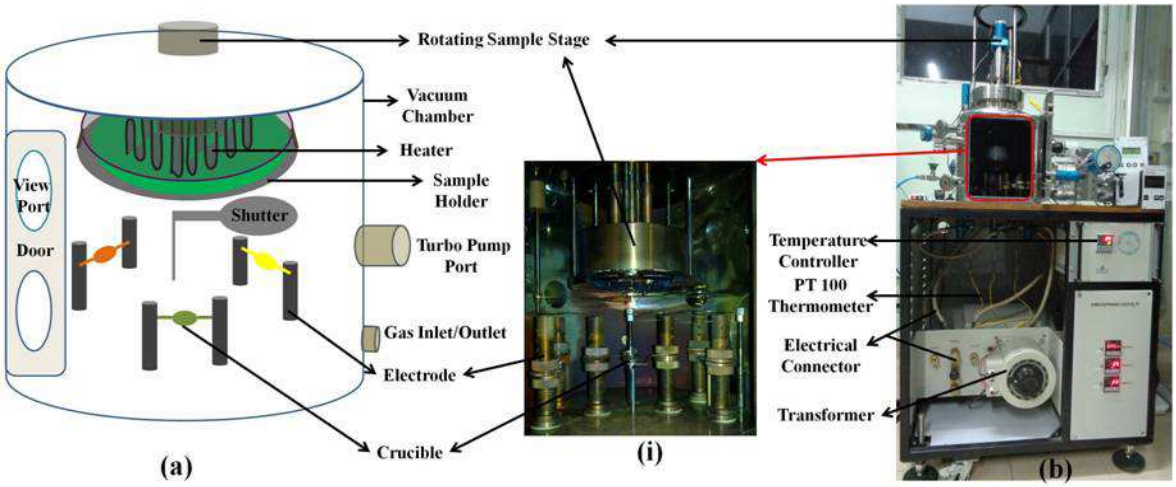

Figure 2.3 (a) Schematic of evaporation chamber. (b) Optical image of the metal-organic deposition chamber, (i) optical image of inner side of the chamber focusing crucibles and sample holder.

NWs growth. Biases of different amplitudes (0 V - 10 V) are applied between e-beam lithographically patterned electrodes of Au/Cu (top and bottom layer respectively) separated by few hundreds of nm to few μm as shown by schematic in Fig. 2.4(a) and then NWs are allowed to grow between the prefabricated electrodes with insitu applied field. This process allow us to grow NW on the substrate with a control over the diameters and the lengths of wires. SEM images of the NWs grown by applying bias from 0 to 10 volts between two electrodes are shown in Fig. 2.4(b). When the bias is more the probability of the NWs to bridge the electrodes becomes low and also the diameter of the NW decreases. Fig. 2.4(c) shows the dependence of NW diameter on growth field for a constant evaporation rate.

This controlled growth of the NWs can be explained in the framework of two co-existing forces namely Electrostatic Force (EF) and Dielectrophoretic (DEP) Force. It has been stated before that the growth occurs due to diffusion of Cu ions through growing wire. Application of a bias V between two electrodes separated by length l gives an electric field E. DEP force is the interaction of non-uniform electric field with the dipole moment induced in an object. Thus, sawtooth like geometry of our device is suitable for producing DEP force. The electric field can be defined as $E_{EF} = \frac{V}{l}$, whereas DEP force acting on cylinder (assuming NWs are cylindrical in shape) is [59], $F_{DEP} = \lambda \varepsilon_0 \varepsilon_m V_p Re\{\frac{\varepsilon_m - \varepsilon_n}{\varepsilon_m + 2\varepsilon_n}\}\nabla E^2 \approx V_p C \nabla E^2$; where, $C = \lambda \varepsilon_0 \varepsilon_m Re\{\frac{\varepsilon_m - \varepsilon_n}{\varepsilon_m + 2\varepsilon_n}\}$, V and l are applied voltage and separation between two electrodes, λ is numerical coefficient on the order of unity, ε_0,

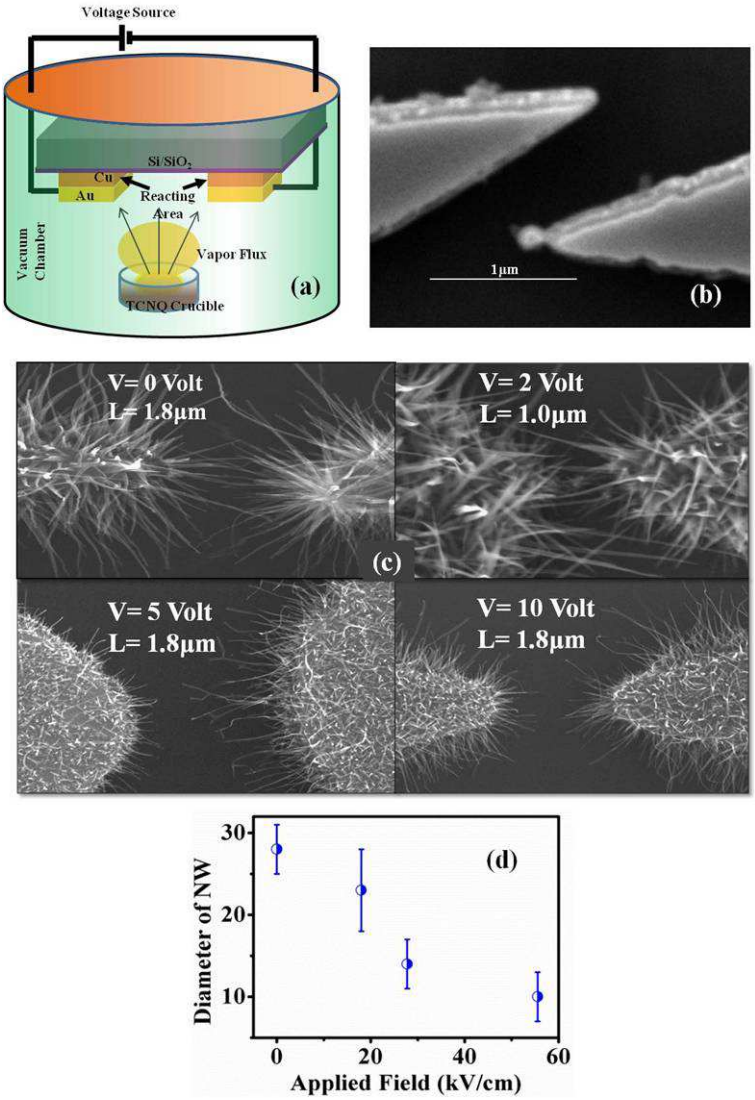

Figure 2.4 (a) Schematic representation of field dependent growth of the NWs. (b) SEM image of e-beam lithographycally fabricated Cu/Au electrode used to grow NW. (c) SEM images of NWs grown in presence of bias applied between two electrodes.(d) Dependence of NW diameter on DEP applied between two electrodes.

ε_m and ε_n are, respectively, the dielectric constant of free space, the relative dielectric constant of the suspending medium and material (Cu:TCNQ), V_p is volume of material suspended in the dielectric medium (air) which is $\pi r^2 l$, r is radius and l being length of the NW equal to the separation between two electrodes connecting the NWs. Depending on the sign of C, the DEP force propels an object towards either the EF maxima or minima. This generally used for the separation of cells or the orientation and manipulation of nanoparticles [54, 60] and NWs [61].

When bias is applied between electrodes during growth, EF is directed from positive electrode

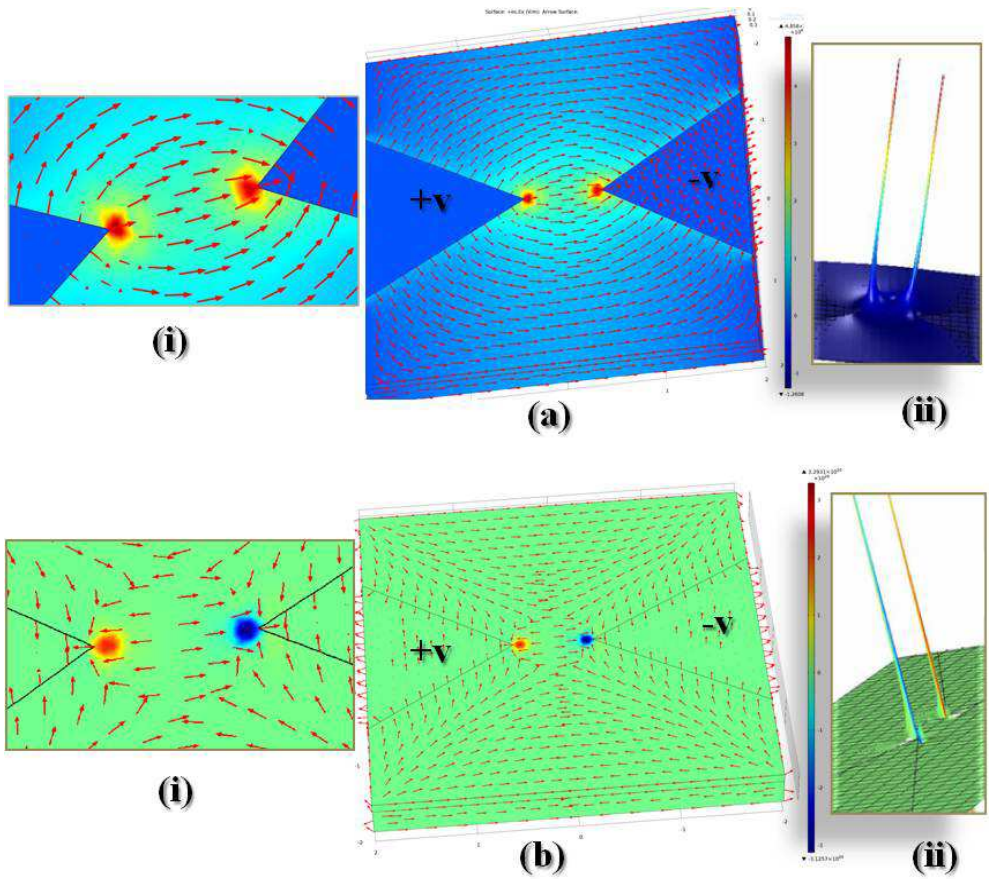

Figure 2.5 COMSOL Multiphysics Simulation of the distribution of (a) Electrostatic field and (b) Dielectrophoretic force between two metal electrodes separated by air. (i) and (ii) respectively represents magnified image of direction and height profile of the corresponding.

to negative electrode with maximum amplitude at the two tip points of the electrodes as obtained by COMSOL Multiphysics [62] simulation shown in Fig. 2.5(a). At the same time DEP force which is proportional to gradient of square of absolute value of EF is directed towards each electrode originating from middle of the electrodes gap with maximum amplitude near tip point of electrodes (Fig. 2.5(b)). At low bias, EF is stronger compared to DEP force which helps NWs to align as well as bridge between two electrodes during growth. As bias increases, DEP force dominated over EF and this DEP force pull back the NWs towards the electrodes from where NWs are growing. As a result probability of bridging NWs is decreased with increasing bias. Thus, growth and bridging is a balance between two forces dominating one over another with bias and control of NW diameter with number of NWs connecting the electrodes. SEM images in Fig. 2.4(b) and experimentally obtained results of NW diameter with different field in Fig. 2.4(c) are supported well by the simulated result in Fig. 2.5(a) and (b). By chang-

ing the applied bias between two electrodes from 0 to 10 volts and calculating corresponding DEP force at midpoint between two electrodes where DEP force is minimum, we have obtained the NW diameter for different DEP force. Simulated diameter merges well with experimentally obtained results as shown in Fig. 2.6(c). Slight deviation from experimental results is due to estimation of DEP force only without considering effect of EF on growth. Now, question arises why diameter is decreasing with increasing bias. Let's explain first the normal growth process. The growth model of Cu:TCNQ from vapor phase has not been worked out in details. In the vapor phase growth, the length grows in time following a time dependence that originates from diffusion of ionic species ($l \propto \sqrt{t}$), while the diameter does not change after initial growth period. This diameter constrained growth is very similar to growth in solution where Anodized Alumina Oxide (AAO) templates have been used to limit lateral growth. [51] In both the growth processes, two phenomena are involved after the initial nucleation phase. (See the schematic in Fig. 2.6). There is diffusion of Cu^{+1} from the Cu electrode though the growing wire (after initial nucleation phase) to the open growth face. There is also diffusion of electrons from the Cu electrode (due to redox potential) to the top growing surface, leading to oxidation of the arriving TCNQ molecules to $TCNQ^{-1}$, which then reacts with the diffusing Cu^{+1} to make the Cu:TCNQ. The efficiency of the process (ionic diffusion, as well as electron transport from Cu side to growth face) would determine the extent of the charge transfer Z. The applied field during growth can affect both the processes. This can also be explained with these two forces. As already stated that EF is in favour of NW growth and bridging. When field is applied, during the growth of Cu:TCNQ NW from positive (+ve) electrodes, Cu ions inside the NW attracted towards the negative (-ve) electrode due to the EF, whereas DEP force pull the ions toward the electrodes from middle of the electrode gap. These two forces acting on the NW are directed opposite to each other results in decreasing the NW diameter. At low bias EF dominates over DEP force which accelerates NW growth and NWs easily bridge between two electrodes. As applied bias increases, EF is suppressed by the DEP force which pulls the NWs opposite to growth direction. Due to these two opposite forces simultaneously acting on the NW creates stress along the length, favourably directed towards growth electrode of NW with increasing field and consequently diameter decreases. The process is schematically represented in Fig. 2.6(d). As the NW grows from the vapor phase with arrival of TCNQ molecules, the successive molecules due to randomization by thermal forces may not have proper alignment. Application of an EF during growth

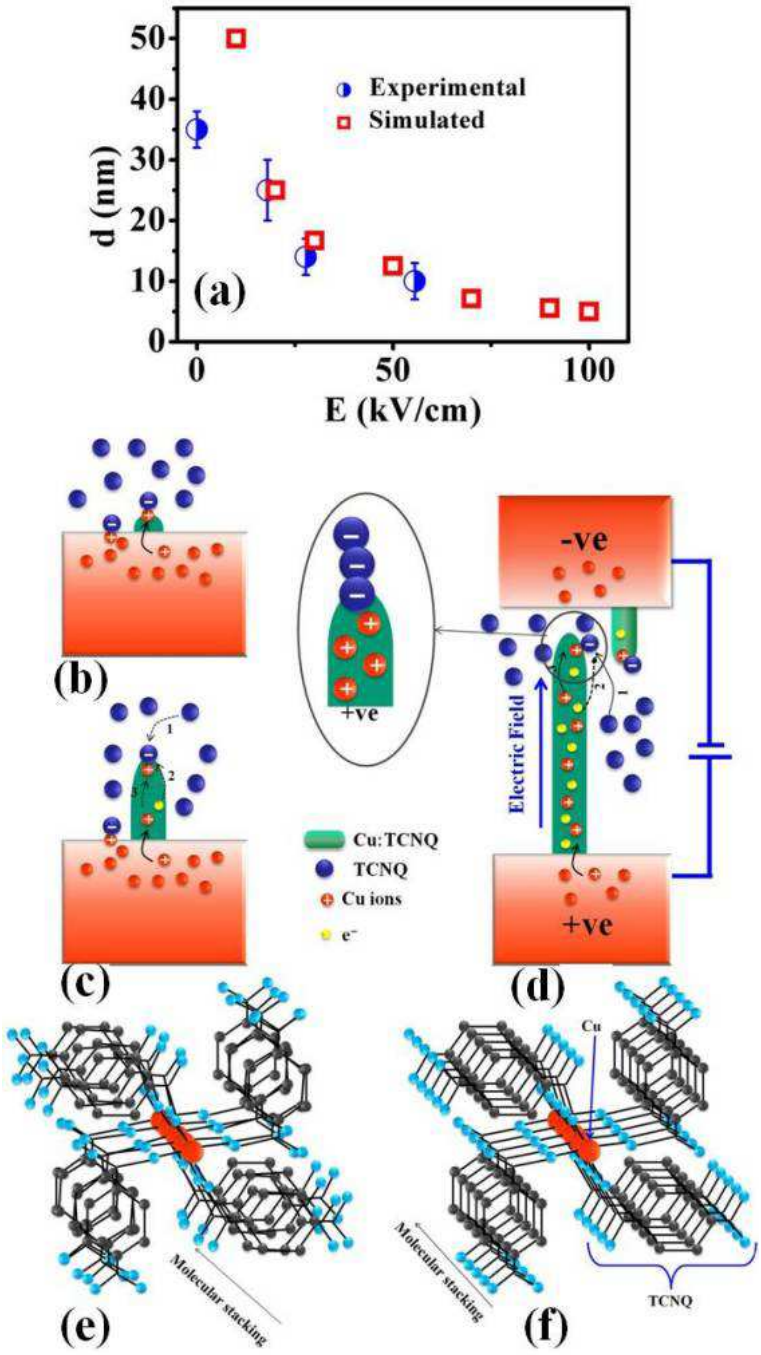

Figure 2.6 (a) Experimental (circle) and simulated (square) results of NW diameter as a function of EF applied between two electrodes. Schematic of Cu:TCNQ NW growth under externally applied field. (b) Nucleation of the ions, (c) NW growth and (d) accelerated nucleation process under field. Stacking of the Cu:TCNQ molecules during growth (e) without field and (f) with field. Field growth NW are having better $\pi - \pi$ stacking of molecules.

process will enhance the Cu ions migration from Cu electrode to the NW tip, thus facilitating the extent of charge transfer and Z enhances. We will show later on in Chapter 4 that NWs grown in an applied field have higher conductivity due to the above two effects.

2.2.2 Nanowire growth by Chemical Method:

In this method, saturated solution of TCNQ in acetronitrile with different concentration was prepared in a beaker. Cu film was made by thermal evaporation in high vacuum. Cu:TCNQ NWs and microrods are grown chemically by dipping the Cu film into TCNQ solution in acetonitrile with desired amount of time at definite temperature in air atmosphere as shown schematically in Fig. 2.7. We have used 10 mM concentration of TCNQ in acetonitrile at room temperature. Size of the nanostructures can be controlled by growth time, temperature and concentration of TCNQ solution. Depending on the growth time and temperature it may have Phase-I (tetragonal) [11, 63] or Phase-II (monoclinic) [64] crystal structure. Nanowires and microrods grown by chemical method have Phase-I structure for shorter time as shown in Fig. 2.7(b) and they grow to Phase-II structure if the growth is for longer time as shown in Fig. 2.7(c) that can be confirmed from XRD analysis as discussed later in characterization section. Growth conditions are tabulated in Table 2.1.

Table 2.1 Growth condition of chemically synthesized Cu:TCNQ NW.

Solvent	Concentration of TCNQ (mM)	Temperature (K)	Time (Minute)	Crystal Structure
Acetonitrile	10	300	0.5	Phase-I (Tetragonal)
Acetonitrile	10	370	5.0	Phase-II (Monoclinic)

2.3 Characterization

The synthesized NW samples as discussed above are mainly characterized by X-Ray diffraction (XRD), Scanning Electron Microscope (SEM), , Transmission Electron Microscope (TEM) for structural characterization, where Fourier Transform Infrared Spectroscopy (FTIR) and Raman spectroscopy were

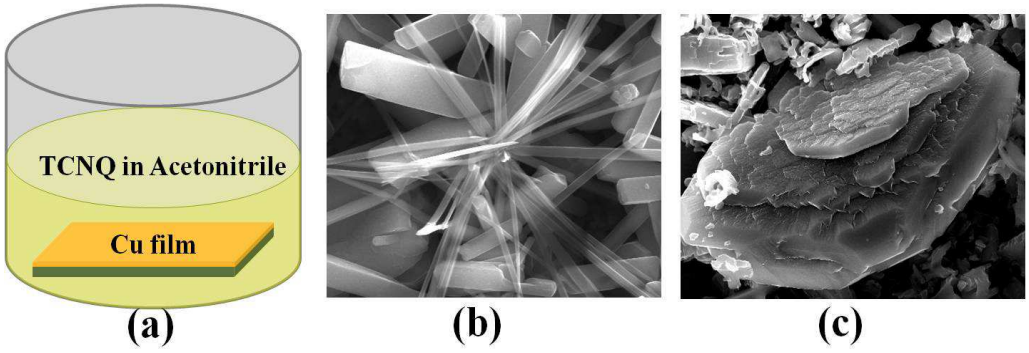

Figure 2.7 (a) Schematic of NW growth using chemical method. Chemically grown NWs and micro-rods with (b) Phase-I and (c) Phase-II.

performed for compositional characterization. The chemically synthesized Cu:TCNQ NWs are characterized in powder form. For FTIR measurement, pellets were made by embedding Cu:TCNQ powder in a matrix of IR-graded KBr and forming a pellet with pressure of ∼100 N. Nanowire dispersed on Cu grid for TEM measurement. Raman spectroscopic measurement has been performed on Cu:TCNQ NW film grown on Si/SiO_2 substrate. Here, we discuss various characterization techniques along with the basic principles and results obtained from our sample.

2.3.1 Structural Characterization

2.3.1.1 X-Ray Diffraction:

X-ray diffraction is the first step for determining the phase of any synthesized material. If the incident X-rays have the same order of wavelength as that of the atomic dimensions, then the radiations emitted by the electrons can have a definite phase relations with one another. These radiations may, therefore, undergo constructive or destructive interference producing maxima or minima in certain directions. When emitted wave differ by an integral multiple of wavelength (λ) for a certain angle it gives constructive interference scattered or emitted waves follow the Bragg's relation [65] $2d_{hkl}Sin\theta = n\lambda$ as shown in Fig. 2.8, where, n is an integer, θ is the angle of incidence and d_{hkl} is distance between two consecutive parallel planes of atom.

Fig. 2.9 shows the data taken on Cu:TCNQ NW powder grown both by PVD and chemical methods to obtain crystal structure of NWs. The structure of the NW grown with PVD method is tetragonal crystal structure having unit cell with a = 3.887 Å, b = 11.266 Å, and c = 11.266 Åand V = 493.5

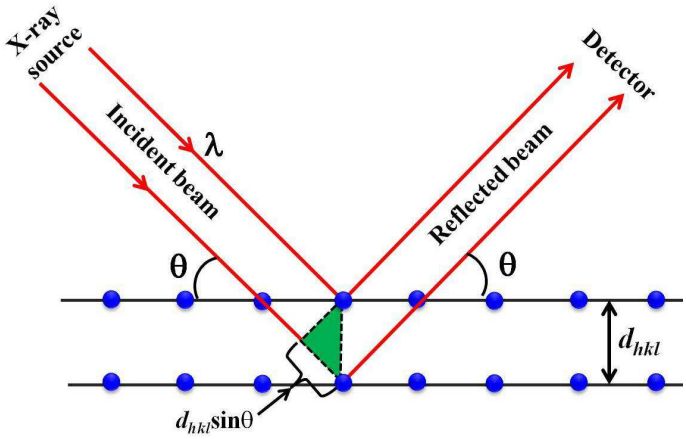

Figure 2.8 Schematic representation of Bragg's law.

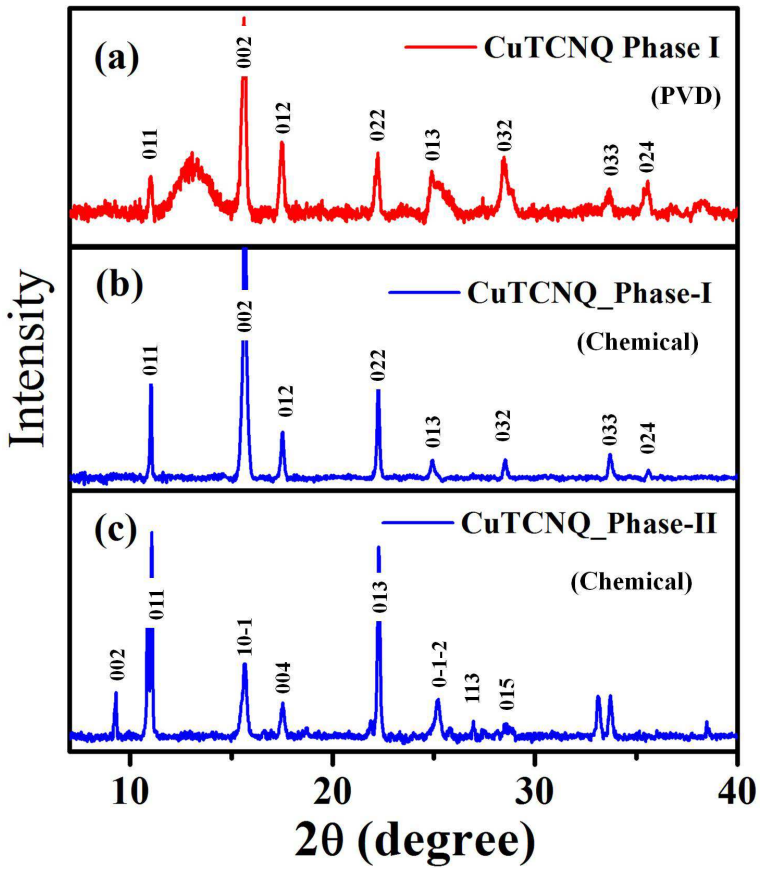

Figure 2.9 X-ray diffraction patterns of NWs grown with (a) PVD, (b) and (c) chemical methods showing Phase-I (upper and middle) and Phase-II (lower) crystal structure.

Å^3 [28] and is polycrystalline as we obtained the peak in case of polycrystalline sample with different intensities [11, 12, 52]. Both for PVD and chemically grown Phase-I crystal, the X-ray pattern show peaks at $2\theta = 10.89^o$, 15.75^o, 17.63^o, 22.48^o, 25.46^o, 28.64^o, 33.63^o and 35.59^o, corresponding planes

Table 2.2 XRD data analysis of Phase-I and Phase-II crystal structure of Cu:TCNQ.

Synthesis method	Phase-I (Tetragonal)				Phase-II (Monoclinic)			
	Unit cell	2θ	d	hkl	Unit cell	2θ (^{o})	$d(A^o)$	hkl
PVD	a = 3.887 A^o	10.89	8.1223	011				
	b = 11.266 A^o	15.74	5.6235	002				
	c = 11.266 A^o	17.63	5.0246	021				
		22.48	3.9503	022				
		25.46	3.494	013	-	-	-	-
		28.64	3.1131	032				
		33.63	2.6617	033				
		35.59	2.5195	024				
Chemical	a = 3.887 A^o	11.04	8.0047	011	a = 5.333 A^o	9.23	9.498	002
	b = 11.266 A^o	15.7	5.6377	002	b = 5.331 A^o	15.7	5.6377	10-1
	c = 11.266 A^o	17.52	5.0559	021	c = 18.875 A^o	17.57	5.0416	004
		22.23	3.9942	022	β = 94.03 ^{o}	22.32	3.9783	013
		25.0	3.5575	013		25.21	3.5284	0-1-2
		28.56	3.1216	032		27.0	3.2984	113
		33.72	2.6548	033		28.67	3.1099	115
		35.6	2.5188	024				

of which are (011), (002), (021), (022), (013), (032), (033) and (024) respectively. Crystal planes are calculated using $(\frac{b^2}{a^2})h^2+k^2+l^2=\frac{b^2}{d^2}$, where interplaner spacing $d=\frac{\lambda}{2sin\theta}$, λ being wavelength of X-ray source. We have used $Cu_{K\alpha 1}$ of wavelength 1.54056 Åat an accelerating voltage of 45kV and 40 mA current in X'Pert PRO system of PANalytical company. On the other way, chemically grown Cu:TCNQ NW shows Phase-I (tetragonal) crystal structure for shorter growth time and Phase-II (monoclinic) crystal structure having unit cell with a = 5.333 Å, b = 5.331 Å, c = 18.875 Å, β = 94.03^o, and V = 538.38 Å^3 grown for longer time period [63] at comparatively high temperature (80^{o}C). For monoclinic crystal structure the relation between interplaner spacing d and lattice parameters a, b, c and

β is $\frac{1}{d^2} = \left(\frac{1}{sin^2\beta}\right)\left[\frac{h^2}{a^2} + \frac{k^2 sin^2\beta}{b^2} + \frac{l^2}{c^2} - \frac{2hlcos\beta}{ac}\right]$. Phase-II peak at $2\theta = 9.3^o$ correspond to (002) plane, perpendicular to N-Cu-N coordination mode (see Fig. 1.3(b)). Next peak in Phase-II is located at $2\theta = 15.7^o$ correspond to (10-1) plane. Other peaks are at $2\theta = 17.57^o$, 22.32^o, 25.21^o, 27.0^o, 28.67^o, corresponding planes of which are (004), (013), (0-1-2), (113) and (015) respectively. All the experiments performed in this thesis are with NW of Phase-I crystal structure and mostly grown with *PVD* method. Experimental results for Phase-I and Phase-II structures of Cu:TCNQ are summarized in Table 2.2.

2.3.1.2 Scanning Electron Microscope

SEM [64] is most widely used form of electron microscope. It generally provides valuable information regarding the structural arrangement, size distribution of NW, shapes, spatial distributions, density, NW alignment, filling factors, etc. In SEM, stream of monochromatic electrons emitting from an electron

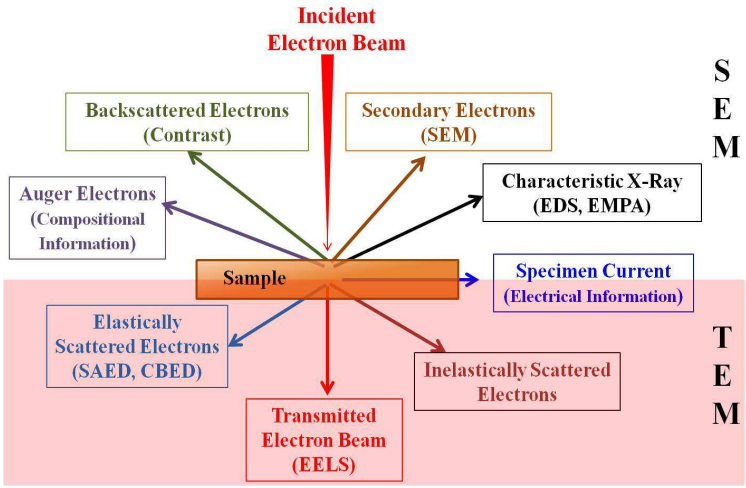

Figure 2.10 Schematic representations of the interaction of incident electron beam with specimen

gun are accelerated and focused by combination of different electromagnetic lens to form a sharply defined electron beam. This sharply defined electron beam of high kinetic energy falls on a specimen and eject electrons from the specimen due to electron-sample interaction which carry different information producing from different part of specimen as shown schematically in Fig. 2.10. Ejected signals include secondary electrons; back scattered electrons; characteristic x-rays; specimen current and transmitted electrons. Secondary electrons are produced due to inelastic scattering of electron beam with specimen

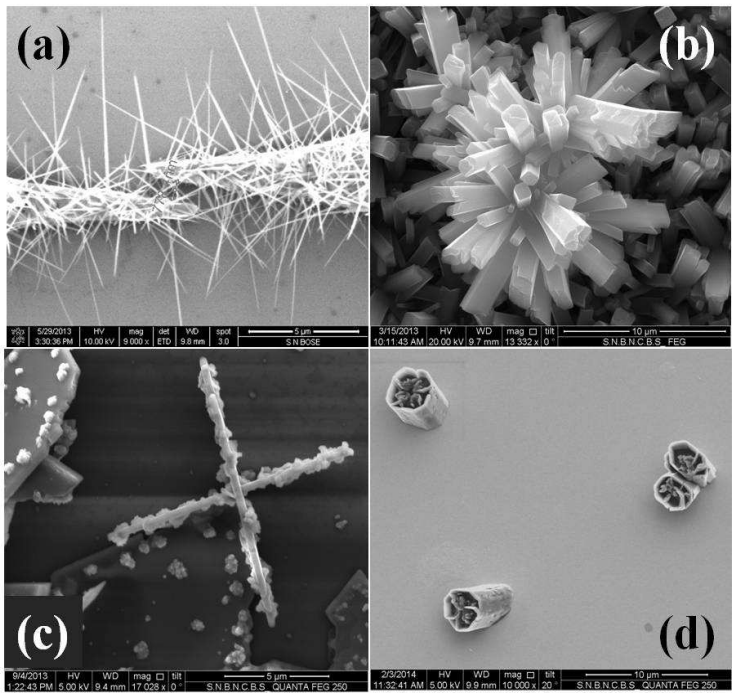

Figure 2.11 SEM micrograph of (a) PVD grown Cu:TCNQ NW (b) micro-flower of chemically grown Cu:TCNQ (c) Au nanoparticle attached on the surface of chemically grown Cu:TCNQ NW (d) chemically grown Cu:TCNQ micro pillar on Cu/Au surface.

atom and back scattered electrons are due to elastic collision. These electrons are collected by different detectors and amplified by various types amplifier, which are displayed as variations in brightness on a computer monitor. Each pixel of computer video memory is synchronized with collected signals for the position of the beam on the specimen in the microscope, and the resulting image is therefore a distribution map of the intensity of the signal being emitted from the scanned area of the specimen.

Secondary electrons and backscattered electrons are commonly used for imaging samples: secondary electrons are important for showing morphology and topography on samples and backscattered electrons are for that of illustrating contrasts in composition in multiphase samples. Backscattered electrons are part of incident beam being scattered by the atomic nucleus of the specimen, thus heavier the nucleus greater will be the backscattered electrons. This property is used to create contrast in alloys or complexes with different compositions. However, main topographical information is obtained from secondary electrons ejected from valence shells by the incident electrons. X-ray is produced by inelastic collisions of the incident electrons with electrons in discrete orbitals (shells) of atoms in the specimen. The beam current absorbed by the specimen i.e. specimen current can also be used to create

images of the distribution of specimen current.

Fig. 2.1(a) show a SEM (FEI Quanta 200) image of Cu:TCNQ NWs grown perpendicular to the substrate, and have wire diameters in the range from $\sim$10-15 nm and length $\sim$ 0.5 - 1.0 μm. Few other SEM micrograph is also shown in Fig. 2.11. Images are taken with an operating voltage of 2 - 10 kV and beam spot-size of 2-3.

2.3.1.3 Transmission Electron Microscope:

Transmission Electron Microscope (TEM) is a versatile instrument where transmitted electrons through the sample are used to collect information about internal structure of the material along with imaging [65]. In TEM, high energetic electron beam is collimated from the source and passed through a thin ($<$ 100nm) slice of specimen material and transmitted electrons are used to visualize with sub-nanometer resolution and signal is detected by the detectors. Depending on the detected signal different sample information can be achieved as listed in Table 2.2. Reflected signals are generally used to carry information in SEM and that of transmitted signals are in TEM.

In TEM, a beam of electrons condensed by the condenser lens is sent through a thin specimen, interact with it and fractional amount of beam is diffracted or scattered. The transmitted beam through the sample is focused on a back focal plane of the objective lens resulting in an electron diffraction pattern. The diffraction pattern at the back focal plane undergoes inverse Fourier Transform and magnified image is formed. Schematic of TEM is depicted in Fig. 2.12.

Depending on the nature of samples, there are some standard methods for the preparation of TEM samples. For thin film sample is prepared by cutting, mechanical grinding and polishing, dimple grinding and finally ion milling. For powder sample, the powder is diluted in alcohol or acetone and then after sonication dispersed on to a carbon coated Cu grid. The sample on Cu grid is then mounted on TEM sample holder for imaging. Different signal source from the sample carry different information as tabulated below:

Two important outcome from the sample under TEM are high resolution TEM (HRTEM) and selected area diffraction pattern (SAED) for crystal structure analysis. HRTEM image can show structures at the atomic scale, lattice fringes, and hence can be used to look at the arrangement of atoms in a crystal.

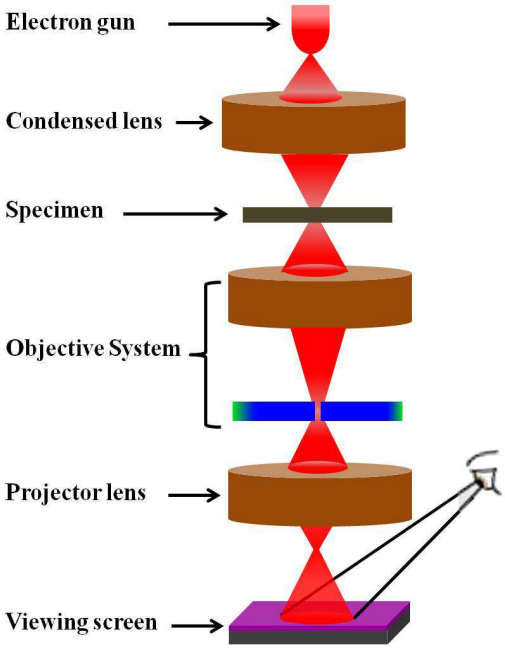

Figure 2.12 Schematic diagram of Transmission Electron Microscope.

SAED pattern can be used to obtain crystal orientation of the sample. Following is the method to index the electron diffraction pattern.

Indexing of electron diffraction pattern: Ratio-technique: From Bragg's law, $2d_{hkl}Sin\theta = \lambda$, for small diffraction angle θ, $Sin\theta \approx \theta$ and hence, $2d_{hkl}\theta = \lambda$. Again, if R be the distance of diffracted spot of interest ('B' in Fig. 2.13(b)) from the central spot ('A' in Fig. 2.13(b)) and L be the distance between screen and the sample as shown in Fig. 2.13(a) and (b) then, $tan2\theta = \frac{R}{L} \approx$ (for small angle of diffraction). Thus, $Rd_{hkl} = L\lambda$, or,$R = L\lambda(\frac{1}{d_{hkl}})$. Thus, one can write, $\frac{d_1}{d_2} = \frac{R_2}{R_1}$. If the camera constant ($L\lambda$) is known, one can easily determine the interplaner spacing.

Let's consider (hkl) value of the central spot 'A' is known. To index for the other spot we can follow the procedure: **(1.)** Choose one spot to be the origin and measure R_1. **(2.)** Measure the spacing of a second spot R_2. **(3.)** measure angle ϕ between R_1 and R_2. **(4.)** Prepare a table giving the ratios of the spacings of permitted diffraction planes in the known structure. **(5.)** take measured ratio R_2/R_2 and locate a value close to this in the table. **(6.)** Assign more widely-spaced plane (lower indices) to the shorter R value. **(7.)** Calculate angle between pair of planes of the type one have indexed. If measured ϕ agrees with one of possible value in the table, accept indexing. if not, revisit the table and select another possible pair of planes.

Table 2.3 Source of signal from a sample in an electron microscope

Signal Source	Information
Secondary Electrons	Morphology and topography of the specimen SEM
Backscattered Electrons	Qualitative idea atomic number and topographical information by illustrating contrasts in composition in multiphase samples SEM
Auger Electrons	Surface sensitive compositional information
Characteristic X-Ray	Energy Dispersive Spectroscopy (EDS) and Electron Probe Micro-Analysis (EMPA)
Elastically Scattered Electrons	Crystal structure from selected area electron diffraction (SAED),Sample thickness, symmetry determination and small change in lattice parameter (0.1%) from Convergent Beam Electron Diffraction (CBED)
Transmitted Electron Beam	Structural and chemical information (EELS)

Another way to index different plane is measuring the distance of diffracted spot from central. For spot patterns, the distance R of diffracted spot from central spot is measured from SAED patterns. This represents reciprocal of the distance of interplaner spacing (d_{hkl}). Match this interplaner spacing d_{hkl} with d_{hkl} value of permitted diffraction planes from XRD analysis and this will give the (hkl) value for that particular spot in SAED pattern. Fig. 2.14(a) shows a TEM image of a single NW connected between two electrodes fabricated in Si_3N_4 membrane. TEM image of s single strand of Cu:TCNQ NW dispersed on a TEM grid is shown in Fig. 2.14(b) taken in FEI TECNAI F20ST system. Fig. 2.14(c) is HRTEM image of the same. Fringes in HRTEM image indicates the crystalline nature of the material, diffraction pattern of which is shown in Fig. 2.14(d). We have followed the second procedure to index the SAED patterns of Cu:TCNQ as shown in lower inset. HRTEM can show structure at the atomic scale, lattice fringes and hence can be used to look at the atomic arrangement in the crystal.

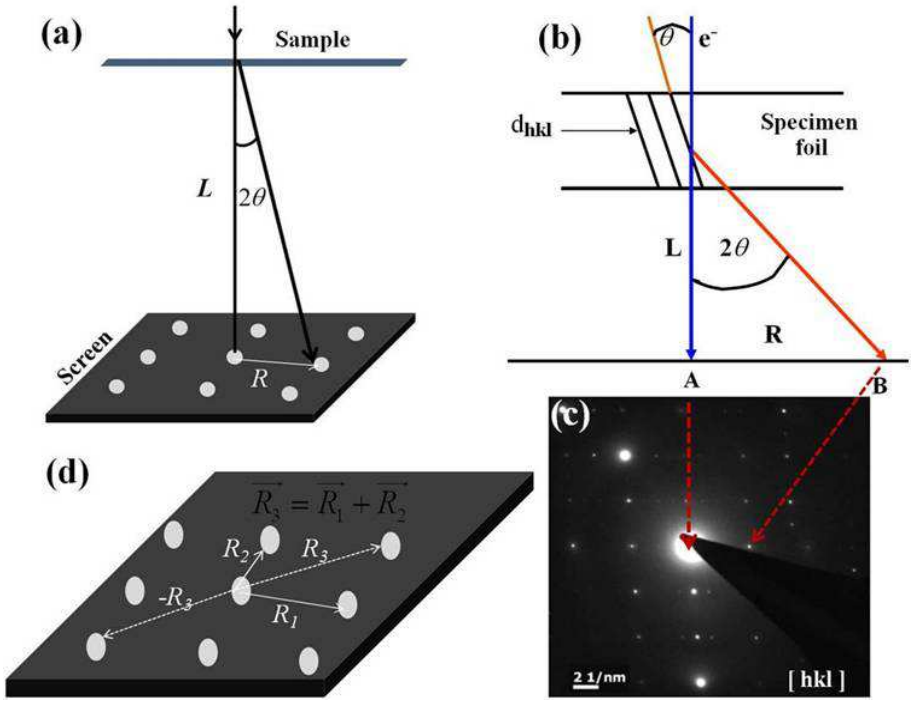

Figure 2.13 Schematics of (a) camera length in presence of imaging lenses, (b) geometry for electron diffraction producing SAED pattern, (c) SAED pattern of a Cu:TCNQ single NW in reciprocal lattice plane, (d) [hkl] indexing by vector addition.

2.3.2 Compositional Characterization

The $\hbar\omega$ vibrational spectroscopy methods namely FTIR (Fourier Transform InfraRed) and Raman spectroscopy were used separately to study shift in C≡N stretching mode of TCNQ when it forms a charge transfer salt with Cu. C≡N stretching mode is affected by the state of oxidation of TCNQ. It is a very important characterization technique because from the shift of C≡N stretching mode one can estimate Z, the measure of charge transfer.

2.3.2.1 FTIR Spectroscopy:

FTIR stands for Fourier Transform Infra-Red, and which is the preferred method of infrared spectroscopy [66]. In infrared spectroscopy, when IR radiation is passed through a sample some of the infrared radiation is absorbed by the sample and some of it is passed through (transmitted). The resulting spectrum represents the molecular absorption and transmission. The absorption peaks corresponding to the frequencies of vibrations of the atoms, creates a molecular fingerprint of the sample such that no

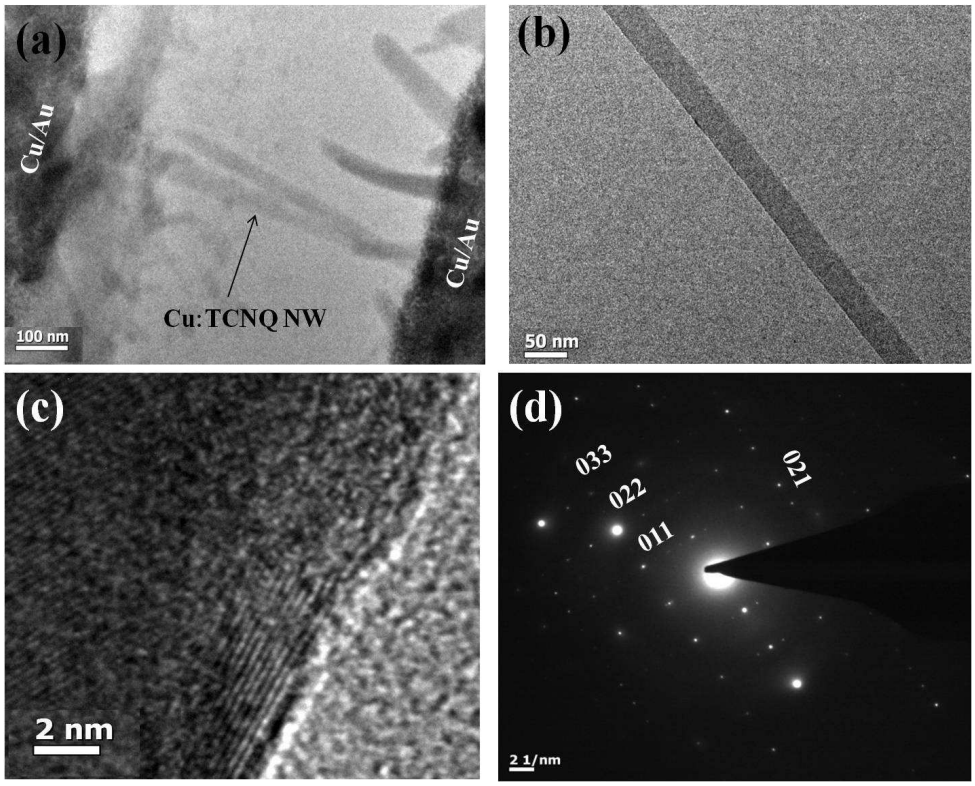

Figure 2.14 (a) TEM image of a single Cu:TCNQ NW of diameter 30 nm grown in between two electrodes of Cu/Au in Si_3N_4 membrane. (b) TEM image of a single strand of Cu:TCNQ NW dispersed on a TEM grid. (c) High resolution TEM (HRTEM) image of the corresponding NWs. (d) Selected area electron diffraction (SAED) pattern of the same.

two unique molecular structures produce the same infrared spectrum. It is schematically represented in Fig. 2.15.

Typically IR-graded KBr or NaCl are used as substrates in FTIR spectroscopy since they do not create any background. For powdered samples KBr or NaCl along with the sample materials are crushed and mixed and then cast as a pellet to study the absorption spectra. For materials which can be sublimated, they are deposited as thin films on KBr or NaCl pellets and then studied. FTIR can also be taken by drop casting the material along with a non hygroscopic solvent on to the pellet of KBr or NaCl and the solvent is dried off before obtaining the spectra. In our case we have made pellet of Cu:TCNQ NW powder on a KBr substrate and obtained the FTIR spectra.

Infrared spectroscopy is a useful tool for characterizing TCNQ materials, in particular for discerning the oxidation state of the molecule in its charge transfer salts [67, 68]. FTIR for TCNQ as well as Cu:TCNQ were performed over the range $4000-400$ cm^{-1}, because the absorption radiation of most

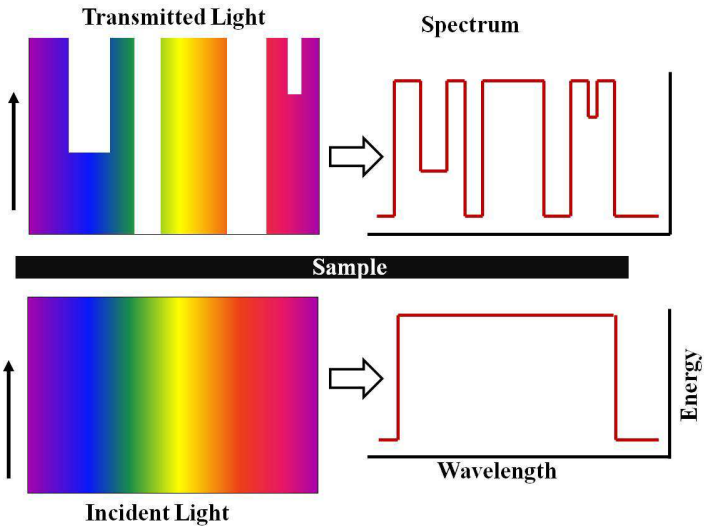

Figure 2.15 Schematic representation of spectrum formation in FTIR spectroscopy.

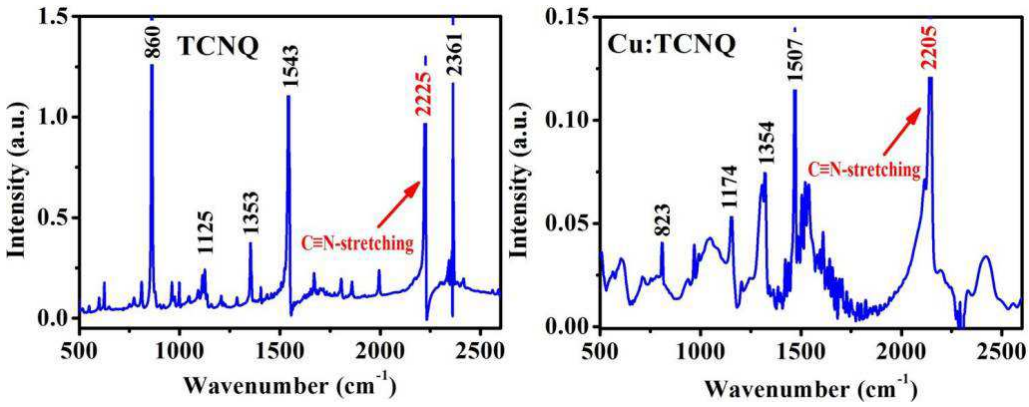

Figure 2.16 FTIR spectra of TCNQ and Cu:TCNQ. C≡N stretching mode of neutral TCNQ is at 2229 cm^{-1} and after formation of Cu:TCNQ it is at 2205 cm^{-1}.

organic compounds and inorganic ions is within this region. As stated before we use this technique to find the degree of charge transfer (Z) which determines the amount of charge transfer between acceptor and donor kind of molecular species in the CT complex material. The shift in the frequency in the vibrational spectra for neutral molecule (TCNQ) to that of ionized molecule ($TCNQ^{-}$) is used to determine the degree of charge-transfer. Fig. 2.16 shows FTIR (JASCO FT/IR-6300 company) spectra of TCNQ and Cu:TCNQ. C≡N stretching mode of neutral TCNQ is at 2229 cm^{-1}. As the Cu:TCNQ complex forms, due to the interaction between the electrons with the vibrational modes of TCNQ, the peak of neutral TCNQ shifts to 2205 cm^{-1}. This shift depends on the amount of charge-transfer between Cu and TCNQ.

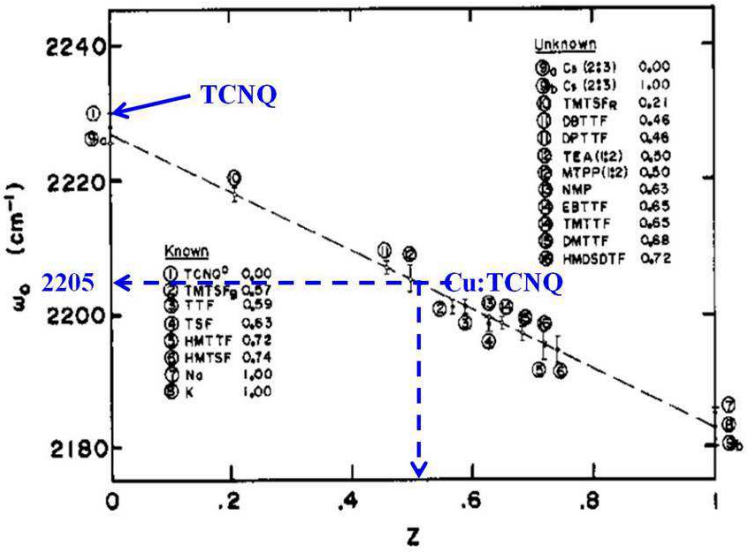

Figure 2.17 Frequency of C≡N stretching mode as function of the degree of charge-transfer (Z). Reprinted with permission from [69]. Copyright (1981) American Chemical Society.

There is no direct way to estimate the degree of charge-transfer from the observed spectra. Chappell et al. [69] have studied vibrational spectra of many TCNQ based charge-transfer salts, whose degree of charge transfer was independently known and created a calibration plot between the degree of charge-transfer Z and the observed frequency peak for the TCNQ as shown in Fig. 2.17. In Fig. 2.17 is reproduced from [66]. From Fig. 2.16 it can be seen that the C≡N stretching mode shows a peak at 2205 cm^{-1}, whereas for neutral TCNQ this mode should be observed at 2229 cm^{-1}. The estimated charge-transfer for the grown Cu:TCNQ by using the plot given in Fig. 2.17 is Z≈ 0.51%. Thus, Cu:TCNQ is formed by fractional amount of charge transfer between donor Cu and acceptor TCNQ.

2.3.2.2 Raman Spectroscopy:

Raman spectroscopy is a spectroscopic technique based on inelastic scattering of monochromatic light, usually from a laser source. In inelastic scattering, the frequency of photons of monochromatic light changes upon interaction with a sample. Photons of the laser light are absorbed by the sample and then re-emitted. Frequency of the reemitted photons is shifted up or down in comparison with original monochromatic frequency, which is called the Raman effect. This shift provides information about vibrational, rotational and other low frequency transitions in molecules. Raman spectroscopy

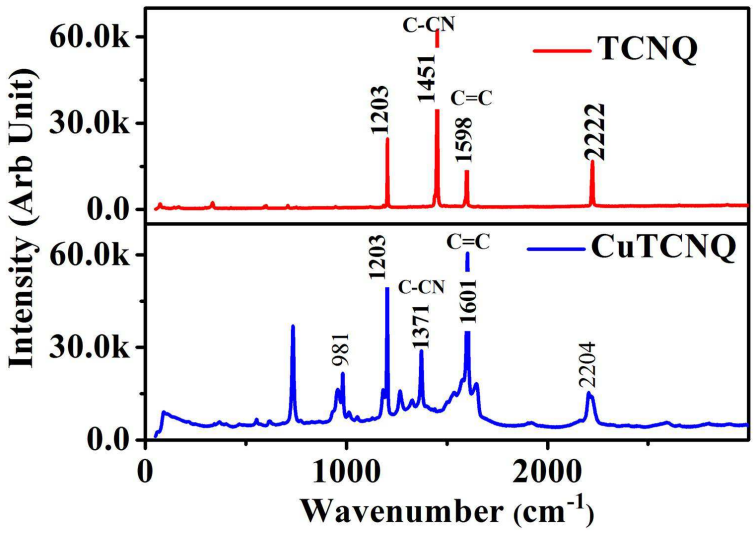

Figure 2.18 Micro Raman Spectra of TCNQ and Cu:TCNQ.

is an important characterization tool often used as supportive to infrared spectroscopy. Raman Spectroscopy is used for chemical identification, characterization of molecular structures, study of bonding in molecules, and in many more applications.

A micro-Raman set-up has been used to fetch local information of the samples down to an area of 1 micron spot thus having an advantage of doing a Raman mapping. It was used to confirm the formation of Cu:TCNQ, which was deposited on to Cu substrates by vapor phase deposition method. No other special sample preparation methods are required. Micro Raman spectroscopy is a very useful tool for studying centrosymmetric compounds such as TCNQ based charge-transfer compounds.

As from the experimental data in Fig. 2.18, C−C≡N stretching mode of neutral TCNQ is at 1451 cm^{-1}. After formation of Cu:TCNQ, stretching mode is shifted to 1371 cm^{-1} due to charge transfer from Cu to TCNQ [70]. To calculate the charge transfer between donor Cu and acceptor TCNQ, we have focused on C≡N stretching mode, one of the Raman active mode of TCNQ. From Raman spectroscopic measurement, we found that the C≡N stretching mode which is at 2222 cm^{-1} for neutral TCNQ, shifted to 2204 cm^{-1} after formation of Cu:TCNQ. Degree of charge transfer from shift in frequency of C≡N stretching mode [69] is $\approx$ 51% (using calibration curve as shown in Fig. 2.17), which is almost same as the Z obtained from FTIR spectroscopic measurement. Incomplete charge transfer in between Cu and TCNQ obtained both from FTIR and Raman measurement give us a possibility of high electrical conductivity in formed Cu:TCNQ compound.

2.4 Conclusion

Nanowires of Cu:TCNQ were grown using PVD and chemical method. Structural characterizations of the NWs were performed by XRD, SEM and TEM. For PVD growth we obtain only Phase-I crystalline structure while for chemically grown NWs both Phase-I and Phase-II are obtained. FTIR and Raman spectroscopic study indicate formation of Cu:TCNQ with incomplete charge-transfer of $\approx 51\%$. We also grow NWs by PVD method within prefabricated electrodes and applying field between them. The field assisted growth has been simulated considering both electrostatic and dielectrophoretic forces.

Chapter 3

Device fabrication and measurement techniques

In this chapter, we have discussed different nanofabrication techniques used to integrate nanodevices for measurements. By the word 'device' we imply NWs connected to 2 or 4 electrodes that are needed for electrical measurements. Fabrication of nanodevice from the synthesized and characterized nanowires (NWs) is an important aspect of this thesis. Most of the processes followed were developed during the thesis work and thus forms an important work development of this thesis. Devices used for measurements are mainly fabricated by electron and ion beam lithography process. We have also discussed the experimental techniques which have been set up and used to measure the electrical transport i.e. current-voltage or resistance at different temperature as well as measurement of transport under illumination. The measurement setups were automated by GPIB interfacing with C^{++} programming for data acquisition.

3.1 Introduction

In modern field of science and technology, along with bio, nano is the most popular scientific prefix. Working at the nanoscale enables us to understand and utilize the unique physical, chemical, mechanical, and optical properties of materials that naturally occur at that scale. Challenges in nano technology include the integration of nano structures and nano materials into or with macroscopic systems that

can interface with users. To understand the physical behaviour in nanoscale, nanodevices have to be interfaced with macro electronic systems which is possible through various nanofabrication processes. Photo, electron and ion beam lithography are some most used fabrication processes. Use of lithography for device fabrication opens the field not only for novel fabrication schemes, but the incorporation of diverse material systems into the field of nanodevice. In this thesis, our goal is to investigate the transport and opto-electronic phenomena of the Cu:TCNQ at nanoscale, particularly at the level of a single NW. So, various nanodevices have been fabricated according to the experimental requirement. We will also discuss an important specific sub-area i.e. different methods of nano fabrication along with experimental techniques developed and used for measurement.

3.2 Lithography processes:

Lithography is a process by which a defined pattern is transferred to a substrate. Common example of lithography is a printer. Fabrication of device structures having dimensions coming down to micron or even nanometer size needs sophisticated lithography techniques. First of all, it is necessary to produce patterns on a wafer corresponding to features of the nanodevice or circuitry. This may be done by one of the so-called nanolithography techniques which includes *photo lithography*, *electron beam lithography* (EBL), *ion beam lithography* etc. In this chapter, we will focus mainly on *electron* and *ion beam lithography* techniques which were mostly used for device fabrication.

3.2.1 Electron beam lithography:

When electron beam is used to write and transfer a pattern, it is called electron beam lithography or e-beam lithography. In this case, a focused beam of electrons is scanned using a pattern generator software on a surface covered with an electron sensitive film called *resist*. Exposure of electron beam changes the solubility of resist and as a result selective exposed or unexposed area of resist can be removed from the substrate by immersing it in a solvent called *developer*. Electron beam is capable of writing a pattern of line width $\sim$sub-10 nm.

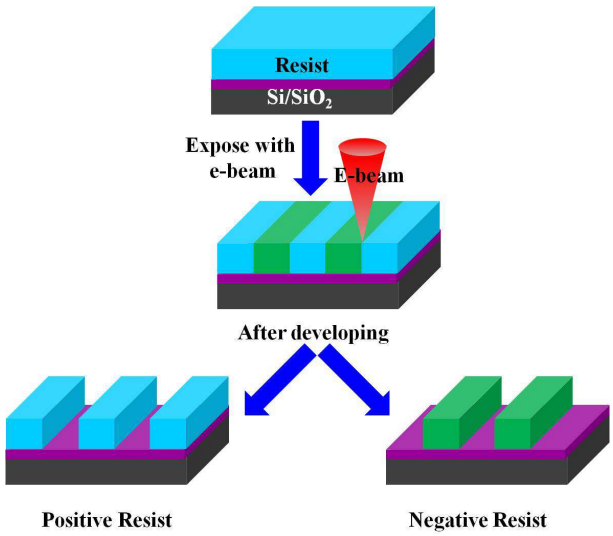

Figure 3.1 Schematic representation of positive and negative resist.

3.2.1.1 Resist:

Resist is basically a polymer. Thin layer of resist is used to transfer pattern on a substrate onto which it is deposited. Resist sensitive to e-beam is called e-beam resist. PMMA (Polymethyl methacrylate), HSQ (Hydrogen silsesquioxane) etc. are the resist used for EBL. Depending on the solubility of resist in the developer after exposing with e-beam it is of two types: *positive* and *negative*. In this thesis work PMMA has been used as an e-beam resist.

If the area of the resist exposed by electron-beam is removed when immersed in developer solution then it is called ***positive resist***. Exposure of e-beam changes the chemical structure and breaks the chain of the polymer resist so that it becomes more soluble in the developer solution. PMMA is an example of positive e-beam resist. In this thesis work, we have used positive e-beam resist resist as we used lift-off process to create metal electrodes/interconnects.

If unexposed area of the resist is removed by the developer then it is called ***negative resist***. Exposure of e-beam changes the chemical structure of the polymer resist in such a way that e-beam makes the bond stronger between two consecutive molecules of polymer chain such that the exposed regions becomes stable and insoluble in the developer solution, whereas unexposed area can easily dissolve into the developer. HSQ is an example of negative e-beam resist. Effect of e-beam exposure on positive and negative resist is schematically represented in Fig. 3.1.

3.2.1.2 Developer:

After exposing with e-beam, depending on the nature of resist exposed or unexposed resist can be removed with a solution called developer. Developer is different for different resist. For removing PMMA, IPA:MIBK (volume ratio = 3:1) is used as a developer where IPA stands for isopropyl alcohol and MIBK is methyl isobutyl ketone. Patterns created after developing the sample in developer is schematically shown in Fig. 3.1.

3.2.1.3 EBL system:

For our work we used a Scanning Electron Microscope (SEM) with a Field Emission Gun (FEG) equipped with a beam blanker that turns the e-beam 'on' and 'off' during raster scan. The electron source of the SEM is used for writing patterns as shown in Fig. 3.2(a). The photograph of our SEM converted EBL system is shown in Fig. 3.2 (b). Electron column typically consists of an electron gun - a source of producing electron beam, two or more lenses to condense the beam, scan coils for deflecting the beam, a blanker for turning the beam on and off, a stigmator for correcting any astigmatism in the beam and finest focusing of the sample, apertures to help in defining the beam, alignment systems for centering the beam in the column, and finally, an electron detector for focusing and locating marks on the sample. Let's briefly discuss the function of each element forming the electron column.

Electron gun: Electron gun materials are chosen in such a way that electron can easily emit from the material surface by heating or applying sufficiently strong electric field so that electrons get sufficient energy to overcome the work function or tunnel barrier of the material. There are two types of electron gun source: *thermionic gun* and *field emission gun*.

In *thermionic gun*, electrons are emitted from a heated filament and then accelerated towards an anode. In this type of gun, the filament is made from a high melting point material of relatively low work function in order to emit many electrons easily. Common example of thermionic gun material is Tungsten, Lanthanum hexaboride etc. Source of electrons generally used in SEM is tungsten filament for its high melting point and low work function (4.5 eV). Tungsten emits electrons $\sim$2700 K (melting temperature 3695 K) without melting or evaporating at comparatively low vacuum. But, main drawback of this electron source is its low brightness and large energy spread for its high operating temperature. To overcome this problem tungsten tip is coated with thin layer of zirconium oxide which reduces the

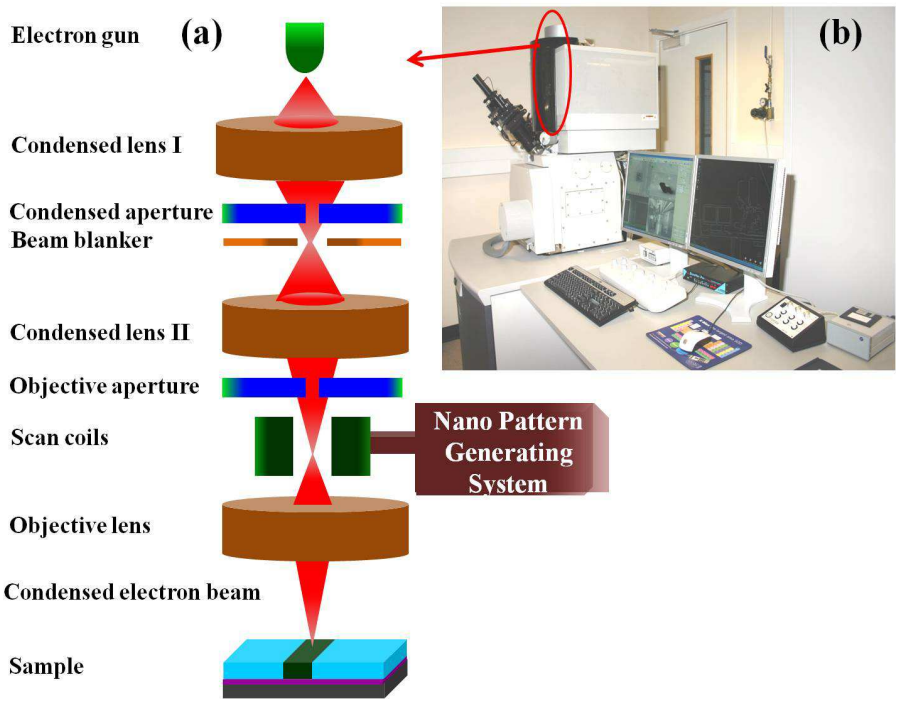

Figure 3.2 (a) Schematic illustration of electron beam column. (b) Electron beam lithography system.

work function of tungsten and continuously refill the materials evaporated from the tungsten gun. After coating tungsten tip with zirconium oxide operating temperature of tungsten reduces from 2700 K to 1800 K.

In *field emission gun*, a very strong electric field is used to extract electron from a material filament. In order to get high field strength with low applied bias, field emitting tips are made sharp. This is done by etching a single crystal tungsten wire to a needle point and welded to a hairpin filament in such a way that emitting region can be less than 10 nm. This gives a much higher brightness than thermionic gun, but requires very good vacuum.

Condenser lenses: Two or more lenses are used in e-beam lithography system or TEM. Its function is to control the beam spot size and beam convergence. Condenser lens I create a demagnified image of the gun crossover and control the minimum spot size obtained in the rest of the condensed system. Condensed lens II affects the convergence of the beam at the sample and control diameter of the illuminated area of the sample.

The pattern generator hardware uses *Scanning coils* to scan electron beam that falls on the sample.

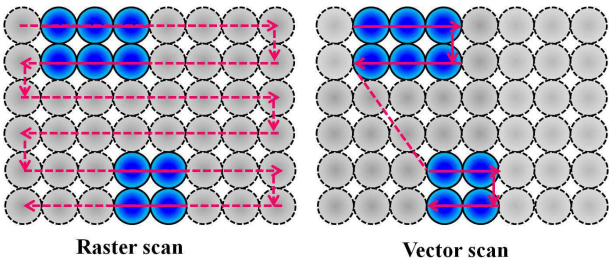

Figure 3.3 Schematic representation of raster and vector scan.

A brief description of scanning is given below.

Scanning coils controls the deflection of e-beam. Deflection of the e-beam is used to scan the beam across the surface of the sample. Scanning action is usually accomplished by energizing electromagnetic coils arranged in sets consisting of two pairs, one pair each for deflection X and Y directions. Scanning action is produced by altering the strength of the current in the scan coils as a function of time, so that the beam is moved through a sequence of positions on the specimen. Depending on the sequence of scanning it is of two types: raster and vector scanning. In raster scanning the beam is swept across the entire surface, pixel by pixel, with the beam being turned on and off according to the desired pattern. In vector scanning the beam jumps from one patterned area to the next, skipping unwanted areas.

An important hardware of the scan control as well as pattern generation is the *Beam Blanker*, described briefly below.

In both vector and raster scan, the electron beam is turned off between the designed pattern areas to be scanned. This is done by a beam blanker which deflects the electron beam far away from the optical axis of e-beam so that the beam will not reach the specimen. This is accomplished by applying an electric field to the plates perpendicular to the optical axis. The plates are connected to a blanking amplifier with a fast response time. To turn the beam off, a voltage is applied across the plates which sweep the beam off axis until it is intercepted by a downstream aperture. If possible, the blanking is arranged to be conjugate so that, upto first order, the beam at the target does not move while the blanking plates are activated. Otherwise, the beam would leave streaks in the resist as it was blanked.

Another important hardware of the SEM that is often used for pattern generation is the *Stigmator*. A stigmator is a special type of lens used to compensate for imperfections in the construction

and alignment of the EBL column. These imperfections can result in astigmatism, where the beam focuses in different directions at different lens settings; the shape of a nominally round beam becomes oblong, with the direction of the principal axis dependent on the focus setting. Possible causes of astigmatism are: (a) Asymmetry of the electromagnetic field on the beam path due to manufacturing imperfection, which deviates the lenses and the pole piece from the rotational symmetry. (b) Contamination in the optical column. Such astigmatism is corrected by a special astigmatism corrector called stigmator. Stigmators may be either electrostatic or magnetic and consist of four or more poles (eight is typical) arranged around the optical axis. When the electron currents are applied to the respective condenser lens coils, they generate magnetic fields, which will be added vectorially resultant as a field. By applying this electrically created astigmatism vertically in the direction of the intrinsic astigmatism of the electron-optical system, the effects of the two astigmatisms cancel each other, thus eliminating any astigmatism from the electron-optical system. The stigmator cancels out the effect of astigmatism, forcing the beam back into its optimum shape. For producing well defined patterns in EBL, this is an important connection that is needed.

3.2.1.4 Nano Pattern Generating System (NPGS)

NPGS is nano pattern generating system software mainly used by the researchers to generate nano size pattern for electron beam lithography. The objective for NPGS is to provide a powerful, versatile and easy route to use system for doing advanced e-beam lithography or ion beam lithography using a commercial SEM, Scanning Transmission Electron Microscope (STEM), Focused Ion Beam (FIB), dual beam i.e. microscope containing both electron and ion beam. SEM conversion kit sold by J.C.Nabity Lithography Systems (NPGS) both with FEI Quanta 200 and FEI HELIOS 600 systems for e-beam lithography was used to generate nanodevices for my research work. A block diagram overview of NPGS/SEM hardware is shown in Fig. 3.4. The bold arrows (blue colour) shows the XY scan interface between the software and the scan coils of the SEM system, as well as the connection between the SEM and an external picoammeter (some SEM system have built-in picoammeter). Thin solid arrows show the SEM's blanker and the blanking output from NPGS, and also the image signal that is sent from the SEM to the NPGS hardware. Optional connections are shown with dashed lines.

We are using NPGS containing DesignCAD 2000 in FEI Quanta 200 and DesignCAD 2008 in

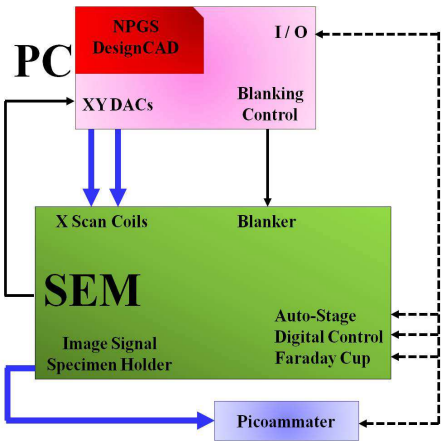

Figure 3.4 Block diagram of NPGS hardware connected to SEM system.

FEI HELIOS 600 microscopic system to design pattern to be transferred to the substrate. The NPGS uses a 16 bit multifunction board to generate the X and Y beam deflections and to program a second board which provides the signals for blanking control. The software converts the pattern designed by DesignCAD to an executable run file which generates the required signals through the NPGS card for deflecting the beam from one shape to another in the writing field. A unique feature of the NPGS is that the user has control over the exposure-spot spacing in X and Y directions, allowing the critical dimensions to be patterned more accurately. For writing a pattern user has also control on line spacing between two scanning line, dose, beam current with which pattern has to be exposed and also some extent of magnification. Patterns drawn by DesignCAD are designed in different drawing layer and/or different colour. This gives an almost unlimited number of exposures conditions within a single layer. The exposure condition is the amount of charge that falls on the PMMA (resist). The control of the expose condition avoids under or over exposure of resist. Dose can be given as area dose (μC/cm^2), line dose (nC/cm) or point dose (fC) depending on the designed pattern. Beam current and dose is related as $D * A = I * t$, where A is dimension (area or length) of the pattern, D is dose, I is beam current and t is exposure time. Beam current is controlled by the spot size i.e. size of the beam hitting the sample. Thus, spot size will be small with highest possible accelerating voltage and lowest beam current. Fig. 3.5 shows the plot of spot size vs beam current.

A general process flow for obtaining an EBL patterned sample is shown in Fig. 3.7. According to the user requirement, CAD design is used to draw a detailed design and converted to the proper EBL

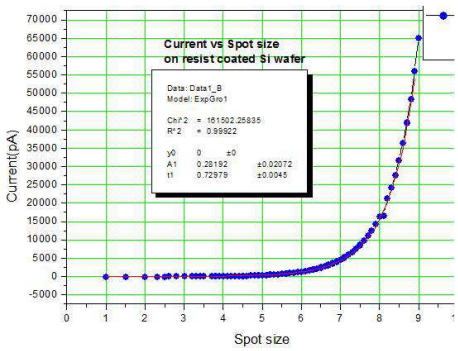

Figure 3.5 Plot of beam current with spot size.

system compatible format (e.g. DC2 file). Next, correction is made through EBL software which takes consideration of proximity effect and finally compile to a machine-executive file. After loading the sample, machine calibration is down automatically to check the electron gun, column alignment and calibrate the writing field, beam current and adjust the beam focus and astigmatism. Finally, exposure can be applied followed by developing to obtain the desired patterns.

3.2.1.5 The steps for generating EBL and transferring it to a substrate:

The general procedure followed in EBL process is described below which is also schematically shown in Fig. 3.7:

1. ***Substrate cleaning:*** The substrates used for e-beam lithography are initially cleaned by boiling them at 70^o C for 15 minutes each in trichlorethylene, acetone and methanol and followed by standard RCA (RCA stands for Radio Corporation of America, an electronics company) cleaning, where the substrates are boiled in 1:1:6 volume ration of NH_4OH:H_2O_2:DI water at 70^o C for 30 minutes. The substrates are then rinsed in DI water and again boiled in 1:1:6 (volume ration) of H_2SO_4:H_2O_2:DI water at 70^o C for 30 minutes followed by rinsing in DI water. Before using, the substrates are ultrasonicated in acetone and isopropyl alcohol and dried in flow of nitrogen gas.

2. ***Resist coating:*** Both single and bi-layer resist coated sample can be used for e-beam writing. For single layer, resist is coated on the sample with PMMA 350K at rpm 3000 for 40 second and then baked on a hotplate at 180^oC for 2 minutes. But, user generally prefer bi-layer resist coating. In this case a high molecular weight resist (950K PMMA) is spun on top of a slightly more sensitive bottom layer of low molecular weight resist (350K PMMA) i.e. single layer coated sample. In this PMMA

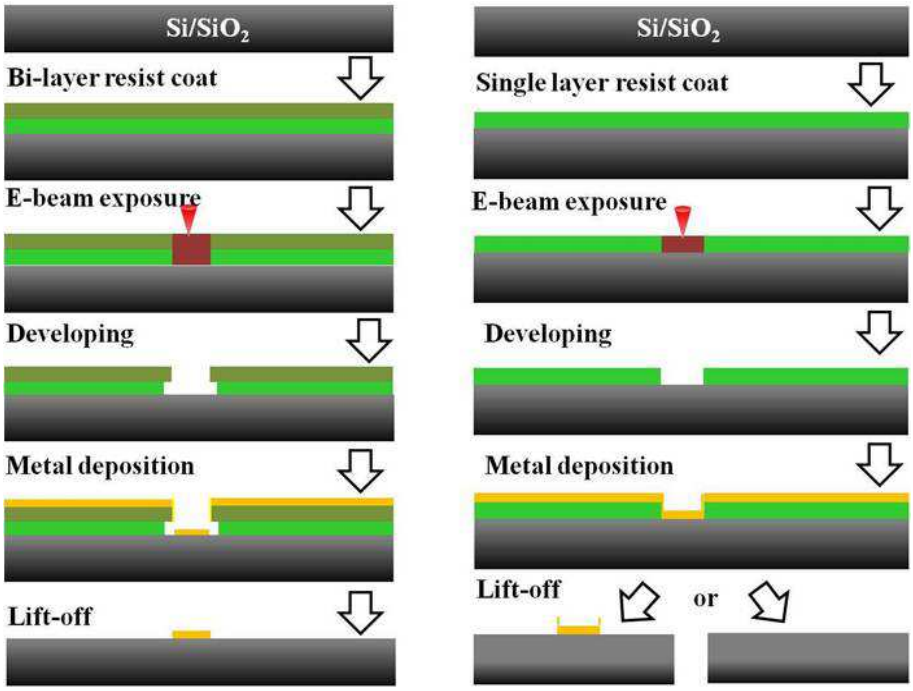

Figure 3.6 Schematic showing lift-off process in bi-layer and single layer resist coating.

950K is coated at rpm 6000 for 40 second and baked at 120^{o}C for 1 hour. Now, the sample is ready for writing with e-beam. Main advantage of bi-layer over single layer is that during developing, bottom layer being more sensitive compared to top layer it creates a under-cut as shown in Fig. 3.6 (left frame), which isolate the deposited metal from resist and lift-process occurs successfully. On the other hand, single layer resist coat does not create any under-cut and hence there is a possibility of pulling out the deposited metal from the substrate during lift-off as shown in Fig. 3.6 (right frame).

3. ***Pattern writing:*** Resist coated sample is mounted on SEM sample stage. Desired pattern are created by NPGS software and written the pattern by e-beam on resist coated substrate by control of scan and beam blanker. Large patterns are generally divided into layers so that different patterns can be written with different beam exposures. Generally larger patterns are written with area dose (μC/cm^2) and higher current, whereas smaller patterns are with line dose (nC/cm) and lower current. We generally use 300 μC/cm^2 area dose and 2 nC/cm line dose.

4. ***Developing:*** After exposing the patterns with e-beam, the substrate is then developed in an e-beam developer (MIBK:IPA=1:3) for $\sim$ 10 seconds, and then cleaned in IPA and dried with nitrogen gas flow. Developer will remove the e-beam exposed area of resist. Developing rate is faster in lower molecular

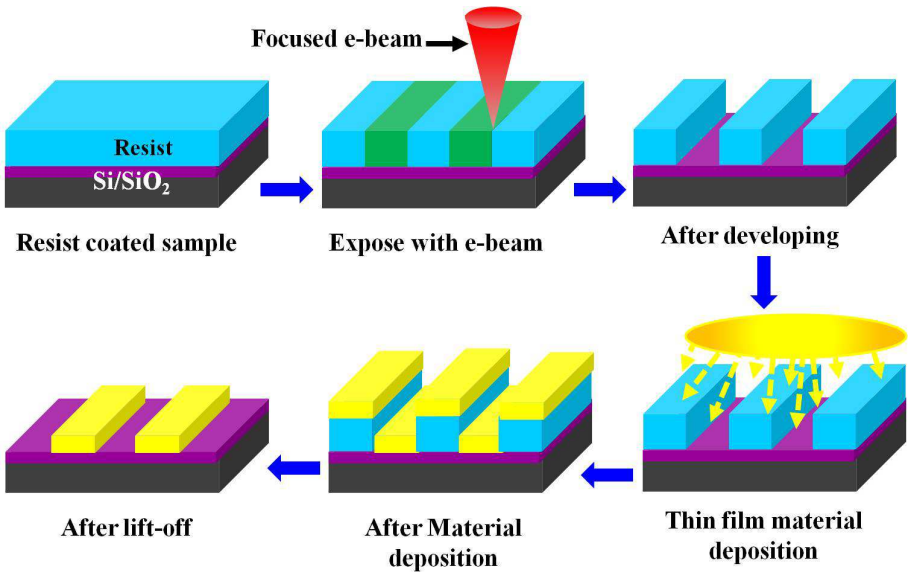

Figure 3.7 Flow chart of EBL process.

weight resist (PMMA 350K) compared to the higher molecular weight material (PMMA 950K) and hence a undercut profile is obtained as shown in Fig. 3.6 (left frame).

5. ***Metal deposition and lift-off:*** After the patterns are developed, the active material or the metals for contacts are deposited in a high vacuum chamber. The deposited material thickness has to be atleast one-third of the bottom layer resist thickness for successful lift-off. In high vacuum, metal is deposited onto the developed substrate. [Multilayer films can be deposited according to user requirement.] Metal coated sample is then immersed in acetone. This removes the remaining resist along with film on top of resist except the film in contact of the substrate after deposition which created pattern written in NPGS. This process is called 'Lift-off'. The undercut profile, obtained by bilayer lithography helps immensely in obtaining lift-off easily and consistently. For making electrical contacts we use a thin layer of Cr or Ti (about 10 nm) for adhesion of deposited metal Cu on to the SiO_2 based substrate. This is followed by Au evaporation of $\approx 50 - 100$ nm.

3.2.2 Focused ion beam lithography

Focused ion beam (FIB) is a powerful tool for maskless and resistless lithography to fabricate structures and devices in the micro and nanometer scales. In this process, a metal is directly deposited onto a

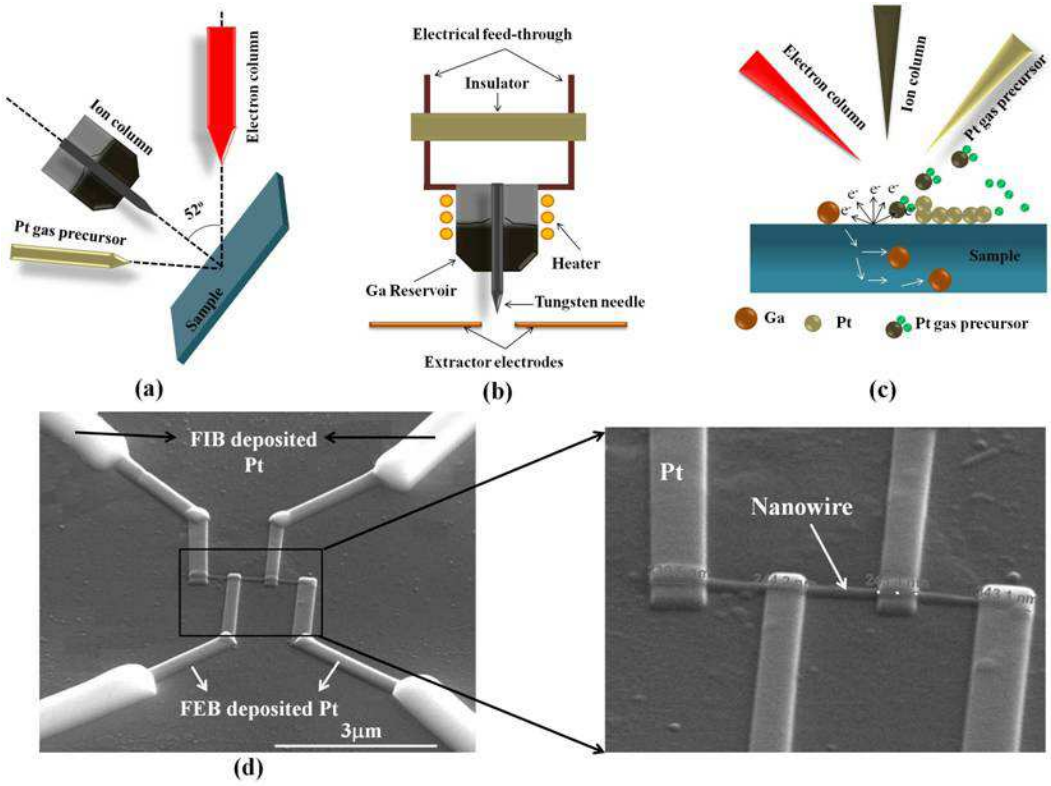

Figure 3.8 Schematic of (a) typical dual-beam column configuration, a vertical electron column with a tilted ion column, (b) Gallium ion source, (c) Platinum deposition using FEB. Sample is tilted at 52^o to make the sample surface normal to ion column. (d) SEM images of single NW device connected with FEB (near the NW) and FIB (far from the NW) deposited Pt.

cleaned wafer from a precursor and it does not need any use of resist. The instrument used in this work is having dual beam sources: one source is a field emission electron gun (SEM source) and another is a FIB (Gallium ion) source. We use the SEM for EBL process as described earlier. The FIB source is aligned at an angle of 52^0 with the SEM source as shown in Fig. 3.8(a). Combination of these two sources offers lots of advantages in nano fabrication as well as sample identification. SEM column is used for sample inspection and imaging at high resolution of specific features without the risk of sample damage. On other hand, ion source is used to deposit metal and cutting/milling. Ga is the most commonly used ion source for FIB instruments for its low melting points, volatility, vapor pressure and excellent mechanical, electrical, and vacuum properties. Schematic diagram of Ga ion source is shown in Fig. 3.8(b). This ion beams are accelerated, collimated and focused by a series of apertures and electrostatic lenses on to the sample. Both electron and ion beam are used according

to the requirement to deposit Platinum (Pt). The Pt deposition is achieved by the electron/ion beam assisted decomposition of methylcyclopentadienyl platinumtrimethyl $(CH_3)_3(CH_3C_5H_4)Pt$, which is a metal-organic gas precursor for Pt metal. It is inserted near the sample through gas injecting nozzles. Fig. 3.8(c) shows the schematic of platinum deposition using FIB. During Pt deposition using FIB column sample is tilted at 52^o opposite to FIB column to make the sample surface vertical to ion column. But, for FEB deposition we don't need to tilt the sample-stage as its surface is vertical to electron column normally. Electron/Ion bombardment on the sample create lots of secondary electrons which collide and dissociates the precursor gas and separate Pt from carbon based precursor. Pt formed by decomposition of precursor is then deposited onto the surface of substrate and gaseous residues are pumped out. Deposition can also be done by bombarding the sample with electron beam. Beam current and voltage has to be chosen in such a way that we can achieve sharp patterns with maximum concentration of metallic fraction. Placing the sample in a certain angle, imaging and deposition can be demonstrated simultaneously. Ionic mass being larger, ion beam momentum is much higher compared to electron beam which may cause the sample to be damaged, but the deposition process is quicker. On the other hand, only electron beam assisted Pt deposition takes longer time for the whole process. Thus, to avoid the sample from direct ion bombardment we always prefer electron beam assisted deposition near the sample and ion beam deposition far away from it which save the sample from damage as well as make the whole process comparatively quicker. Fig. 3.8 shows am SEM image of a single NW device connected with Pt using both FEB (near the sample) and FIB (far from the sample) source. For e-beam deposition we have used 86 pA beam current and 30 kV accelerating voltage, whereas ion beam deposition has been done with accelerating voltage of 15 kV and beam current of 43 pA.

3.3 Device Fabrication

The device fabrication in this thesis extensively uses e-beam and ion-beam lithography. E-beam lithographic patterns are generated using NPGS software. Depending on the experimental requirements we have fabricated NW devices with two different approaches: *top-down* and *bottom-up* approach. Before proceeding nano-pattern generation with these two approaches, large external contact electrodes have been made using hard mask or photo lithography processes. In hard mask lithography, cleaned sub-

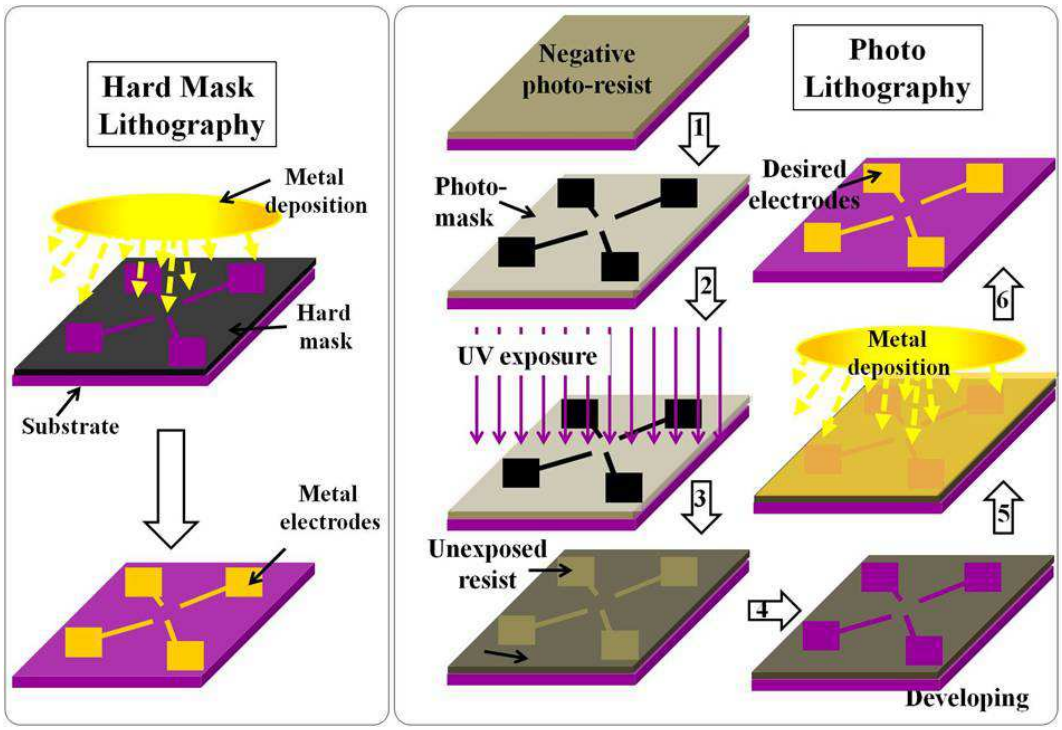

Figure 3.9 Schematic representation of external electrode fabrication by hard mask and photo lithography.

strate is covered with a hard mask which is a hard plate of metal or Si with windows of desired pattern and then metal is deposited on the substrate through the mask as shown in Fig. 3.9. On the other way, in photo lithography a photoresist coated sample is exposed to UV-light after covering with photo-mask. UV-light exposed sample is then developed and metal is deposited followed by lift-off as shown in Fig. 3.9. Photo-lithography is similar to EBL process. In this process UV-light is used to expose resist instead of e-beam in case of EBL.

Fig. 3.10 is the flow chart that represents how do one use these patterned substrate for NW connection.

3.3.1 Top-down approach (Attaching contacts to prefabricated wires →*Ex-situ fabrication*):

In top-down approach, to make single NW device, first large area electrodes of Cr/Au (10/200nm) for external electrical connections, are made by photo and e-beam lithography on a silicon chip capped with a layer of 300 nm SiO_2 or Si_3N_4 as shown schematically by step (i) in Fig. 3.11(a) (for details

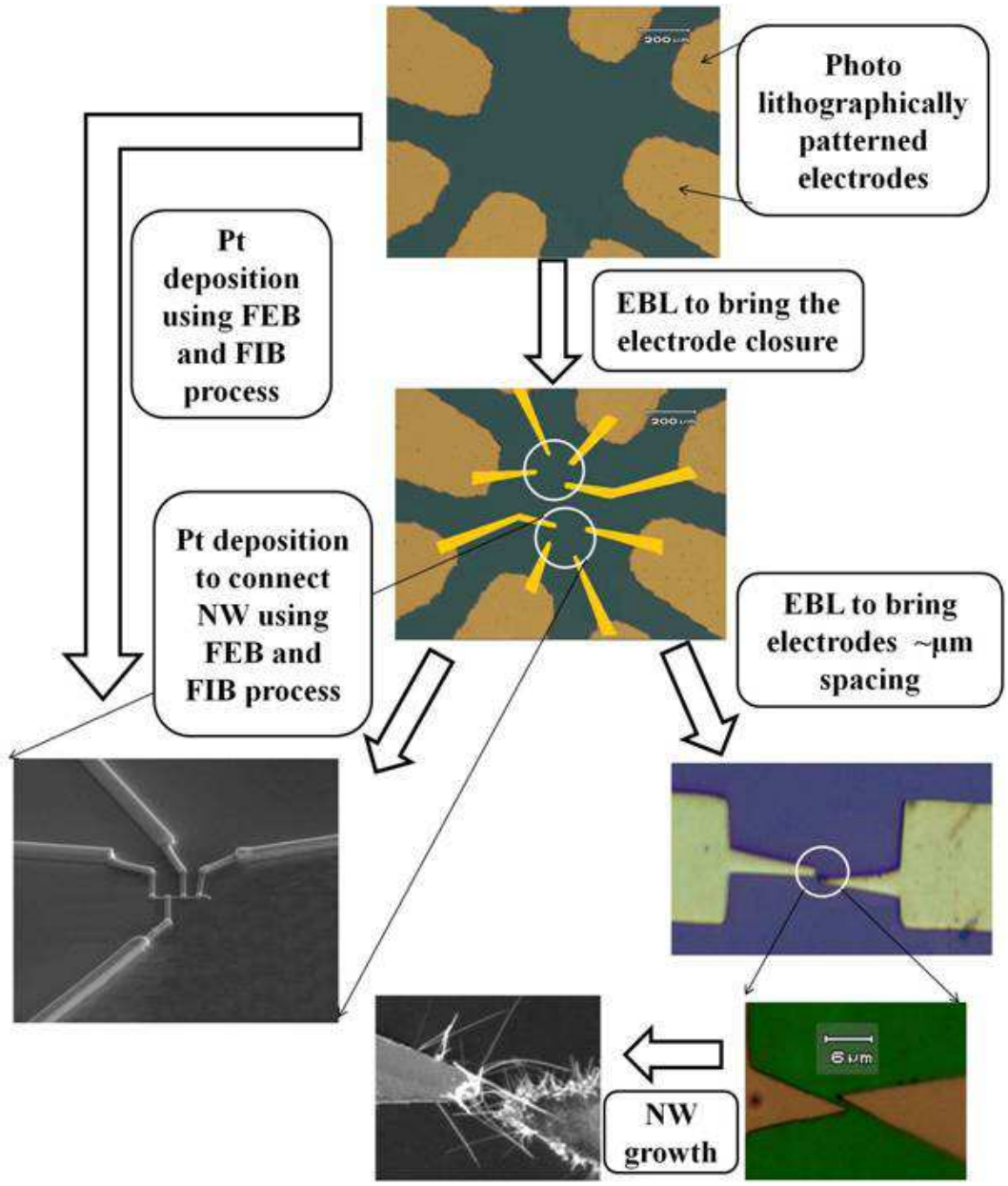

Figure 3.10 Flow chart of making contact to a single NW.

refer Fig. 3.9). Synthesized NWs are separated from the substrate by ultrasonication in alcohol. The suspension is then dispersed onto the wafer containing pre-fabricated large electrodes of Cr/Au (step (ii) in Fig. 3.11 (a)). A single isolated NW is then identified by the SEM. It is then connected with pre-fabricated external Au electrodes by a combination of both FIB and FEB deposited Pt (step (iii) in Fig. 3.11) as described in FIB/FEB lithography section. FEB deposition is done over the NWs to avoid wire damage due to ion exposure. SEM images of two single NW devices made by top-down

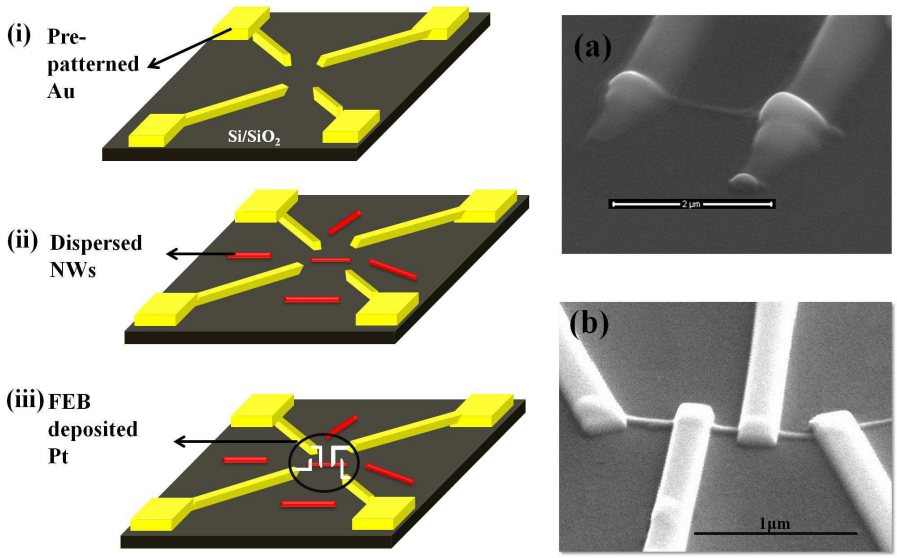

Figure 3.11 Schematic representation of device fabrication by top-down approach with SEM image of two and four probe configuration.

approach in two and four probe configuration are shown in (a) and (b) of Fig. 3.11. In this case we use the word 'Ex-situ' fabrication because the NW is synthesized outside the lithography system. For this type of fabrication, EBL can also be used to deposit contacts by lift-off. However, the Cu:TCNQ NWs being metal-organic material they dissolve in solvent used for EBL process. This necessarily bound us to direct deposition by using FIB/FEB process.

3.3.2 Bottom-up approach (Growing NWs on predefined patterns →*In-situ fabrication*):

In bottom-up approach, first predefined electrodes of Cu/Au (Au on top of Cu is deposited to limit the vertical growth of the NW from Cu) with sub-micrometer separation is made by electron beam lithographic process (describe in section 3.2.1.5) as an extension of hard-mask or photo-litho patterns and then NWs are grown on these pre-patterned Cu electrodes by PVD method. Bottom-up process to connect NWs is schematically represented by steps (i) and (ii) in Fig. 3.12. In this process, direction of NW growth can be controlled by depositing bilayer of two different metals in different angle during metal deposition, where upper layer will be non-reactive stable metal like Au from which TCNQ does not grow into NWs. Fig. 3.12(a) shown SEM image of NW device grown in Cu electrodes while that of Fig. 3.12(b) shows the same for dual layer metal (Au on top of Cu) for lateral growth. Fig. 3.12(c) shows

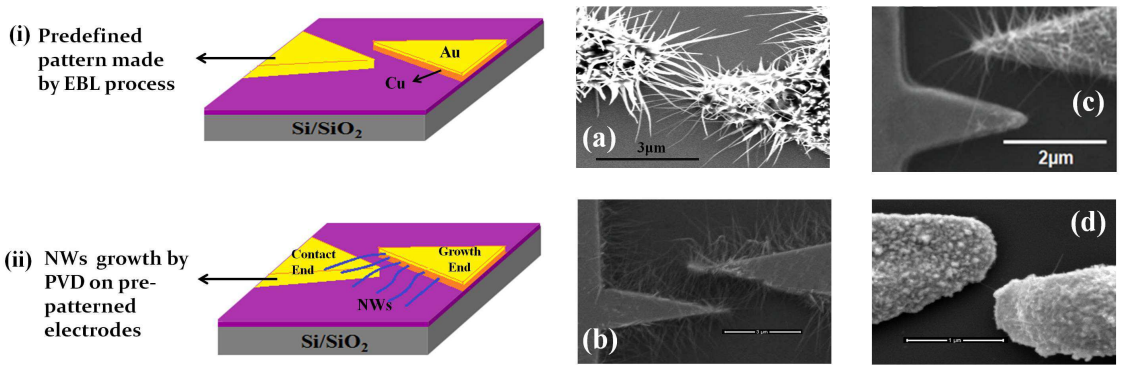

Figure 3.12 Schematic representation of device fabrication by bottom-up approach. SEM image of NWs grown by bottom-up approach (a) from prefabricated Cu electrodes, (b) lateral growth of NWs from side wall of prefabricated Cu/Au electrodes, (c) controlled unidirectional growth of NWs, (d) single NW of diameter 10 nm connected between two Cu/Au electrodes separated by 200 nm.

unidirectional growth of NW from Cu bridging Au electrode which is done by angular deposition of Au on top of Cu. Nanowire length and diameter can also be controlled by controlling electrode separation, time of NW growth and evaporation rate as discussed in chapter 2 (section 2.2). Fig. 3.12(d) shows a single NW device of diameter $\sim$10 nm and length $\sim$200 nm. Main advantage of this process is that since the device architecture and electrode can be fabricated before the growth of NWs. As a result, NWs will not suffer deterioration due to post treatment. For the same reason this fabrication process is called in-situ fabrication. The nanobridge arrays fabricated here being electrically connected to leads, allow direct use as a nanodevice without any additional steps and electrical/opto-electronic measurements can be made.

3.4 Experimental Techniques

The temperature dependent electrical and opto-electronic transport measurements were performed both with DC and AC measurement techniques using standard two probe (or pseudo four probe) and four probe electrode configurations. Schematics of DC and AC measurement set-ups are shown in Fig. 3.13 and Fig. 3.15 respectively. In four probe configuration, outer probes were used to supply current and inner two probes were to measure voltage drop across the sample. In two probe configuration, measurement was done with the same probes used for sourcing. Different probe configurations are shown in lower left of Fig. 3.13. We have measured $I-V$ and $R-T$ in single and array of NW both in cryogenic

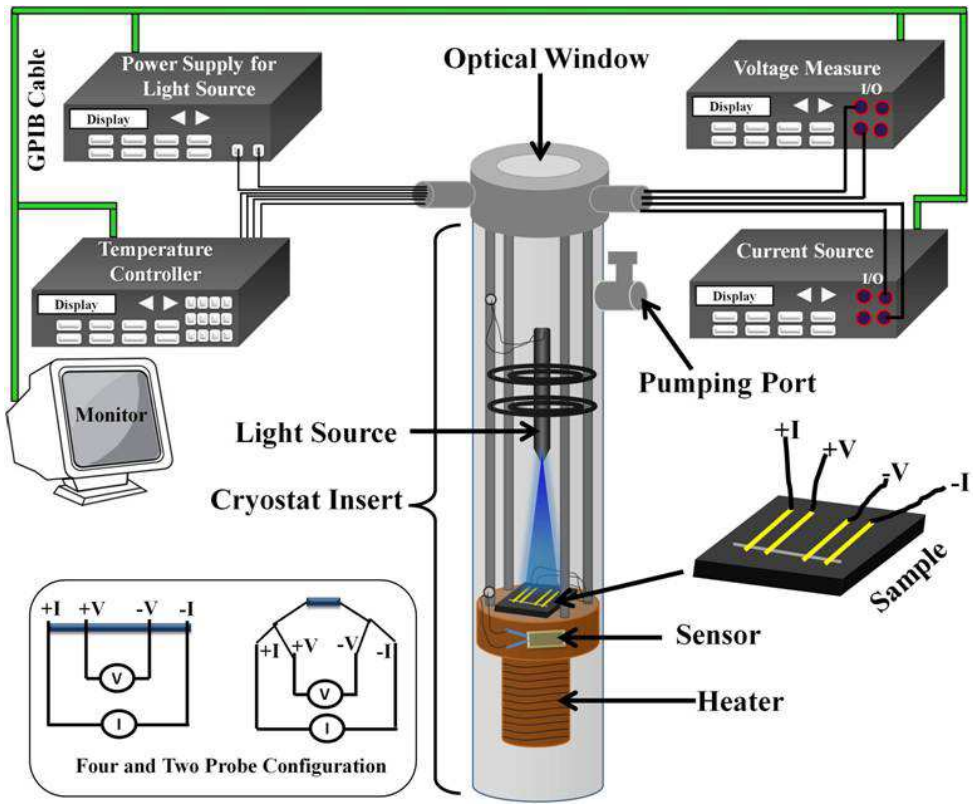

Figure 3.13 Home made cryogenic setup for temperature dependent electrical and opto-electronic measurement. (Lower left) Four and two (pseudo four) probe configuration for electrical measurement.

and cryogen-free variable temperature insert in the temperature range of 3K to 300K. In the cryogenic system, temperature range of measurement was from 300K to 80K and liquid nitrogen was used for cooling the sample stage. In the cryogen-free system, measurement has been performed in a wide range of temperature from 300K to 4K where helium gas is used for sample stage cooling.

We have designed and made a cryogenic system in our laboratory. The cryogenic system contains (a) a sample stage for mounting the sample, (b) a vacuum jacket to keep the sample stage thermally isolated from the outer atmosphere, and (c) liquid nitrogen reservoir to cool the sample down to 77K. Fig. 3.13 shows our cryogenic set-up. Sample stage was made of Cu bar. A heater of resistance 50 Ω made of manganin wire was mounted just beneath the sample mounting stage to heat the sample. A Pt100 [71] thermometer was mounted close to the sample to get the sample temperature with minimum loss. We have made an arrangement also for in-situ light illumination on the sample stage to perform opto-electronic measurement at low temperatures. Sample can be illuminated by putting the illumina-

tion source inside the cryogenic sample stick as shown in Fig. 3.13 or by putting the light source outside the system and illuminating the sample via an optical window (quartz) at the top of the sample stick. There are 14 electrical connections in the sample holder; 4 for connecting the sample, 4 for temperature sensor (Pt100), 2 for heater, 2 for applying gate bias across the sample, and 2 for supplying power to the laser source for illumination. Illumination power can be varied by varying bias applied across the laser source. Electrical wires in the sample holder are fitted inside the sample rods through Teflon strip (to avoid body short) and are connected to external instruments via two 8-pin vacuum feed-through. Heater and sensor are connected to a Lake Shore 340 temperature controller and laser source to a power supply. Source meter and piccoammeter was used to perform electrical measurements. Measurement set-ups are automated by GPIB (General Purpose Interface Bus) interfacing using C^{++} programs.

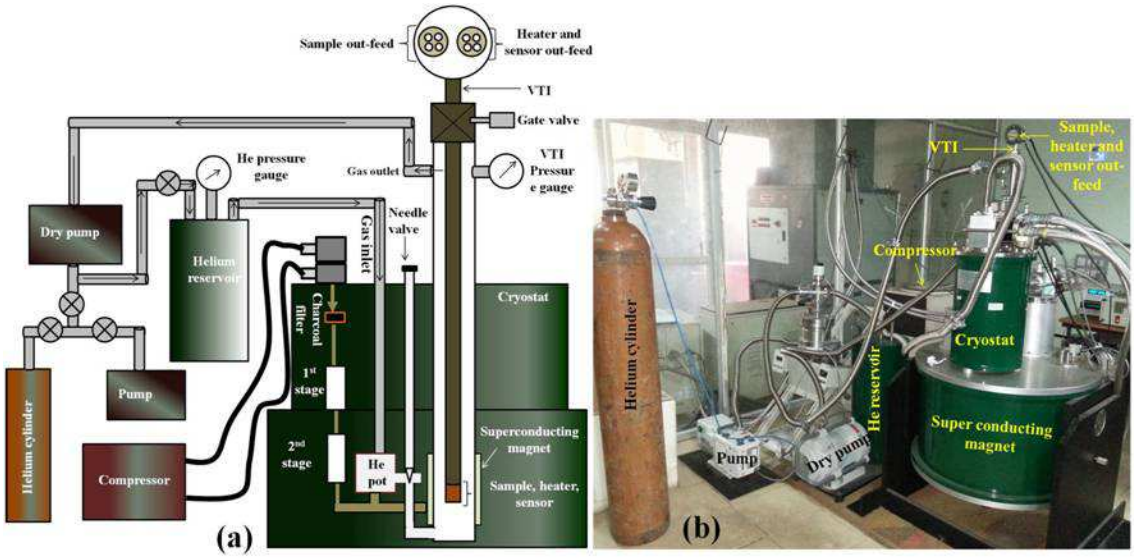

Figure 3.14 (a) Schematic of cryogen-free VTI system. (b) Photograph of the whole system.

For low temperature measurements upto 4 K, we have used commercially available cryogen-free variable temperature insert (CFVTI) produced by *Cryogenic Limited*. The system uses a single two-stage Gifford McMahon cryocooler to produce temperatures around 4 K at the second stage, which enables operation of VTI between 4 K and room temperature. Main components of VTI cryogenic system are (i) a cryostat (which is basically a vacuum insulated chamber to support and thermally isolate the VTI and superconducting magnet), (ii) a superconducting solenoid magnet, (iii)cryocooling system (vacuum pumping system, helium gas flow system and compressor) (iv) a variable temperature

insert, and (v) a sample stick containing calibrated cernox^{TM} [72] temperature sensor, heater, sample mounting stage along with electrical wires for connections. Schematic view along with an photograph of the CFVTI system is shown in Fig. 3.14. Outer body of the VTI is made up of aluminium alloy and that of sample column is from stainless steel. First stage of the cryocooler is made radiation shield by polished cooper to make superinsulation between room temperature outer world and the shield. Cooling is done by a two-stage cryo-cooler by circulating helium gas as indicated by arrow in Fig. 3.14(a). The cryo-cooler cold head is fitted on top plate of the cryostat. The compressor is connected to a high pressure host. First stage cools the radiation shield around the lower temperature part of the system. Second stage cools the magnet as well as sample stage. In operation, the 1st stage cools the system to 35 - 40 K and below 4.2 K in the 2nd stage. The system is only operated under vacuum condition (except helium gas in the reservoir).

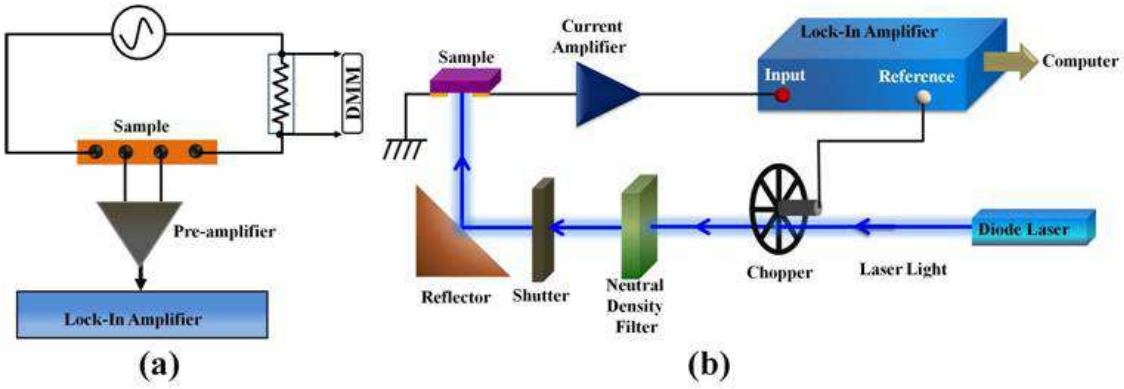

Figure 3.15 (a) Basic principle of AC resistance measurement. (b) Opto-electronic measurement set-up for AC measurement.

3.4.1 Electrical measurement

The resistance of the Cu:TCNQ NW samples as a function of temperature was measured with two different approaches:

(a) By passing a constant current through the sample and measuring the voltage drop across the sample. Resistance was calculated from the applied current and measured voltage drop.

(b) By measuring $I-V$ at different constant temperature. Resistance at each temperature was calculated from the slope of $I-V$ curve of the corresponding temperature. Combination of resistance at each temperature forms the R-T curve.

To measure the electrical properties, source meter (Keithley SM-2410, SM-2400) [73] was used for both voltage and current source and picoammeter (Keithley 6485), digital multimeter (Keithley DMM-2000) were used to measure current and voltage respectively across the sample and Lakeshore (Model 340) [74] was used to control temperature both in four probes and two probe configurations in DC techniques. To observe resistive state switching, $I-V$ measurement has been performed in two probe configuration using voltage as source and current as measured quantity.

AC measurement techniques was used to measure electrical property of few single NW devices with lower diameter to avoid measurement using high current and the problem of thermo emf. arising due to temperature gradient across the sample. In AC technique one can use very low signal to excite the sample and thermo emf problem can be avoided. In this technique a low frequency AC current is passed through the samples and voltage drop corresponding to the excitation frequency was measured by phase sensitive detection technique. A schematic view of the measurement is shown in Fig. 3.15 (a) and (b).

3.4.2 Opto-electronic measurement

Opto-electronic measurement have been performed using both AC and DC measurement techniques. Zero bias photo-current $I_{Ph}(V=0)$ of the single and array of NW was taken using Lock-In-Amplifier. The photo-current was directly put into the current amplifier input of the lock-in which has sensititvity < 0.5 pA current gain. Schematic diagram of the measurement of the zero bias photo-response with lock-in amplifier is shown in Fig. 3.15(b). The term zero bias current is used because no bias has been applied to measure the photo-current. The illumination was turned 'ON' and 'OFF' mechanically by a shutter when data (shown in chapter 6) was taken. In this case a laser source of wavelength 405 nm has been used as source of illumination. Power of the laser light is controlled by neutral density filter. Power of the illuminated light falling on the sample is measured by putting a power-meter in place of the sample. By measuring the total illuminated area on the sample and power of illumination, we have calculated the power density of illumination. Nanowire dimension being known, we can easily estimate the power falling on the NW. During DC measurement, we have used Horiba Jobin-Yvon Fluorolog-3 spectrofluorimeter for sample illumination. An optical image of the set-up along with optical layout of illumination source is shown in Fig. 3.16 (upper frame). A continuous source of light

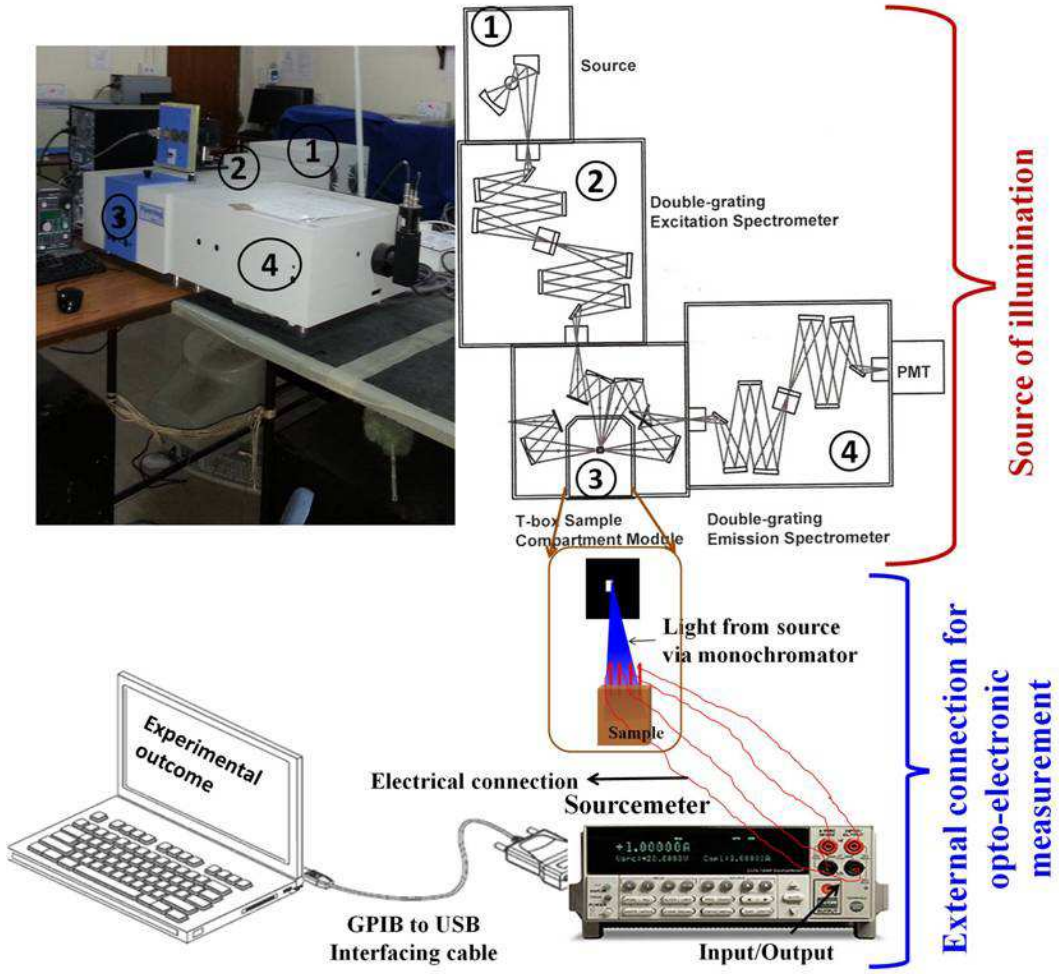

Figure 3.16 Opto-electronic measurement set-up for DC measurement. (Upper left frame) Optical image of the set-up Horiba Jobin-Yvon Fluorolog-3 spectrofluorimeter. (Upper right frame) Optical layout of the same. (Lower frame) External electrical connection for taking data.

(150-Watt ozone-free xenon arc lamp) illuminated onto an excitation monochromator, which selects a band of wavelengths. This monochromatic excitation light is directed onto the sample. If the sample emits luminescence, it is directed into emission monochromator which select a band of wavelengths and shines them into a detector. Although for our measurement emission is not an important part. The spectral response and $I-V$ curves were recorded using a source meter (Keithley SM-2400) as a voltage source and a picoammeter (Keithley 6485) to measure current. Lower frame in Fig. 3.16 illustrates the external electrical connection for the opto-electronic measurements. We have measured $I-V$ and $I-t$ in dark and after illuminating the sample with monochromatic light of various wavelength. Power

falling on the sample for the xenon source has been calibrated using the known power for laser source. Let us consider, $I_L(V=0)$ is the zero bias photo-current for illumination power of P_L in laser source, and $I_X(V=0)$ is zero bias photo-current in xenon lamp source. Thus, illumination power P_X corresponding to $I_X(V=0)$ is calculated from $\frac{P_L}{P_X} = \frac{I_L(V=0)}{I_X(V=0)}$, or $P_X = \frac{P_X}{P_L} I_L(V=0)$. Experimental results has been discussed elaborately in chapter 5.

3.5 Conclusion

In this chapter, we have discussed different lithography techniques and fabrication method to integrate single and NW array device. Experimental techniques for electrical and opto-electronic measurement have also been discussed.

Chapter 4

Temperature dependent electrical transport in Cu:TCNQ nanowire

In this chapter, we have reported the temperature and bias dependent electrical transport properties of array as well as single nanowire (NW) of Cu:TCNQ, laterally connecting two electrodes ($\sim 1\mu m$ gap) with and without the presence of external electric field applied between the electrodes during growth. Temperature and bias dependent electron transport of these bridged NW devices has been investigated down to 40K with the aim to probe the effect of temperature, applied bias and applied field during growth on transport of Cu:TCNQ. It has been found that the NWs show a linear part of the conductance and a non-linear part beyond a threshold bias. The field applied during growth affects both the parts. Below 100 K, the bias dependent conductance with threshold can be fitted to a modified Zener tunnelling model in both types of NWs raising the possibility of charge density wave (CDW) type charge transport in the Cu:TCNQ NWs. It has been proposed that the enhancement of the conductance in Cu:TCNQ NWs when the growth is performed in an applied field occurs due to better charge transfer as well as more ordered arrangements of TCNQ stacks. That modified the parameters related to the linear as well as non-linear conductance.

4.1 Introduction

Investigations of electronic transport in ultrafine metal and semiconductor NWs have been a topic of considerable current interest [75, 76, 77]. Important parameters that determine the transport properties of NW are material composition, growth condition, crystal quality, NW diameter etc. [78, 79]. In this chapter, we investigate an interesting possibility whether application of electric field during growth can influence the electrical conductivity of the NW when they are grown from a vapor phase. This question becomes particularly relevant because there are attempts to use electric field assisted growth/alignment as a tool to assemble NWs into large scale circuits [53, 54, 57]. Particularly, in the context of semiconductor NWs like Si or Carbon nanotube, it has been established that an applied field can produce an alignment field (due to large anisotropy in polarization) that can overcome the randomizing effect of the thermal vibrations [80, 81, 82]. We address here the issue whether the applied field, in addition to alignment, can also 'tailor' its properties, particularly its electrical transport. The work reported here was done in specific context of a charge transfer complex NW for reasons elaborated below. However, it may be seen that this may have a general applicability for growth of NWs of similar such systems. While electric field assisted growth in charge transfer complex have been reported before, [57] mainly to align and make NWs grow as bridges between two electrodes with micron or sub-micron gap. The possibility that such a growth process can actually lead to control/modification of physical properties have not been reported before.

Low dimensional systems are found to be more sensitive to certain lattice driven instabilities which depends on temperature and affects the physical as well as thermodynamical properties of these systems [57, 83, 84].

Peierls instability [85] is one of such instabilities occurring in these kind of systems. According to Peierls assumption, when atoms in a one-dimensional chain of regularly spaced atoms are moved slightly closer to one of its neighbors in same direction, periodicity of this chain will be distorted. This will reduce the translational symmetry and introduce a new gap in the density of states at a point in k space corresponding to that periodicity as represented in Fig.4.1. This change in lttice periodicity leads to modulation in electron density created in the distorted chain is known as CDW (see Fig.4.1(c) and (d)). The distorted structure will have a lower total electronic energy than the undistorted structure

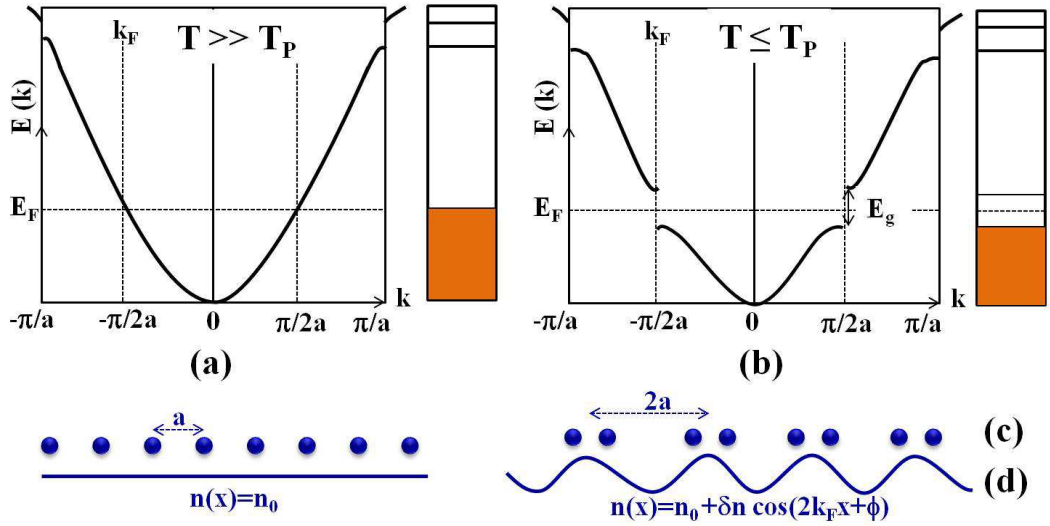

Figure 4.1 Electron dispersion and band pattern of one-dimensional molecular system: (a) metallic state and (b) insulating state produced by Peierls transition. E(k) is the energy of the conduction electrons, k their wavevector, n(x) the electron density in the metallic state. E_g is energy gap at $k=k_F$ created due to Peierls transition. (c) Static distortion of the lattice and (d) charge-density wave as a result of distortion. δn is the amplitude of the density modulation. Copyright with permission from [86].

which tends to dimerize and a gap would appear at the Fermi energy (see Fig.4.1), and thus the system would become an insulator. This distortion will occur only when the reduction in electronic energy in the distorted lattice must be greater than the increase in elastic energy associated with the structural bonds between atoms in the chain. At higher temperature increase in elastic energy is less than the reduction in electronic energy and electrons easily get excited across the gap which prohibit to create distortion in the lattice chain. When temperature is reduced below Peierls transition temperature (T_P), increase in elastic energy crosses the value of decrease in electronic energy creating a gap at the Fermi surface. TTF:TCNQ CT complex exhibits CDW transport below a transition temperature [57]. We find that in NW of Cu:TCNQ there is evidence of such CDW below 100K as seen from transport data elaborated below.

The work reported here was carried out in NWs of the charge transfer complex Cu:TCNQ with diameters in the range ≈20 30 nm and length of ≈1μm. The NWs were grown from vapor phase as nanobridges between prefabricated electrodes with and without an electric field applied between them (see Fig. 4.2). We investigated the electrical conduction over a wide temperature range (40 K to 300 K) and find that there are substantial differences between wires that are grown with and without an electric

field. The NWs show a large component of non-linear transport beyond a threshold field, which is also strongly temperature dependent. We found that for T$<$100K, the non-linear component of the conduction resembles that of a CDW transport. In this temperature range the bias dependent conductance can be well fitted to a modified Zener Tunneling model developed for CDW transport [83, 84]. The applied field during growth also modifies the non-linear component of the conductance including the threshold for the non-linear transport. These aspects have not been reported before in such charge transfer complex NWs like Cu:TCNQ and also raises the possibility of such investigations in other organic charge transfer complexes.

Cu:TCNQ has attracted wide attention both as a system of basic physics interest in context of charge transport in qausi-1 dimensional conductors and also because of its potential applications in non volatile electrical memory, [8, 13] humidity sensors [87] and high responsivity photo-detector [88] etc. This has been studies in Chapter 1. However, most of the work done on this charge transfer complex material has been concentrated on electrical resistive state switching [8, 13, 35]. In Cu:TCNQ charge (electron) transfer occurs from the donor Cu (that oxidizes to Cu^{+}) to the acceptor TCNQ moity. In this complex, the structure has an important role to play. Cu:TCNQ can grow into two phases [11]. Phase-I with a distorted Tetrahedron of four nitrogen atoms around the metal (Cu) shows higher conductivity. While, in the lower conductivity Phase-II the metal coordination is more tetrahedral. These arrangements alter the packing and orientations of the quinoid ring of TCNQ which in turn affect the conductivity. This makes Cu:TCNQ as an attractive Metal Organic Framework (MOF) system. Growth of Cu:TCNQ crystals from solution by electro-crystallization using different potentials have shown that one may obtain different morphology of the conducting Phase-I Cu:TCNQ [11]. There are interesting report of reducing TCNQ by photochemical reaction leading to formation of metal-TCNQ complexes [89, 90]. Very recently, it has been shown that the change of conductivity of Cu:TCNQ by an applied field (post-synthesis) can be linked to structural changes [12]. The above discussion shows that electric field can act as a tool to alter the structure and electrical properties in Cu:TCNQ. However, it has never been investigated whether application of the electric field during growth, particularly in a vapour phase, can alter its conductivity. The present investigation addresses this particular issue. We also discuss the likely mechanisms that lead to the property modifications.

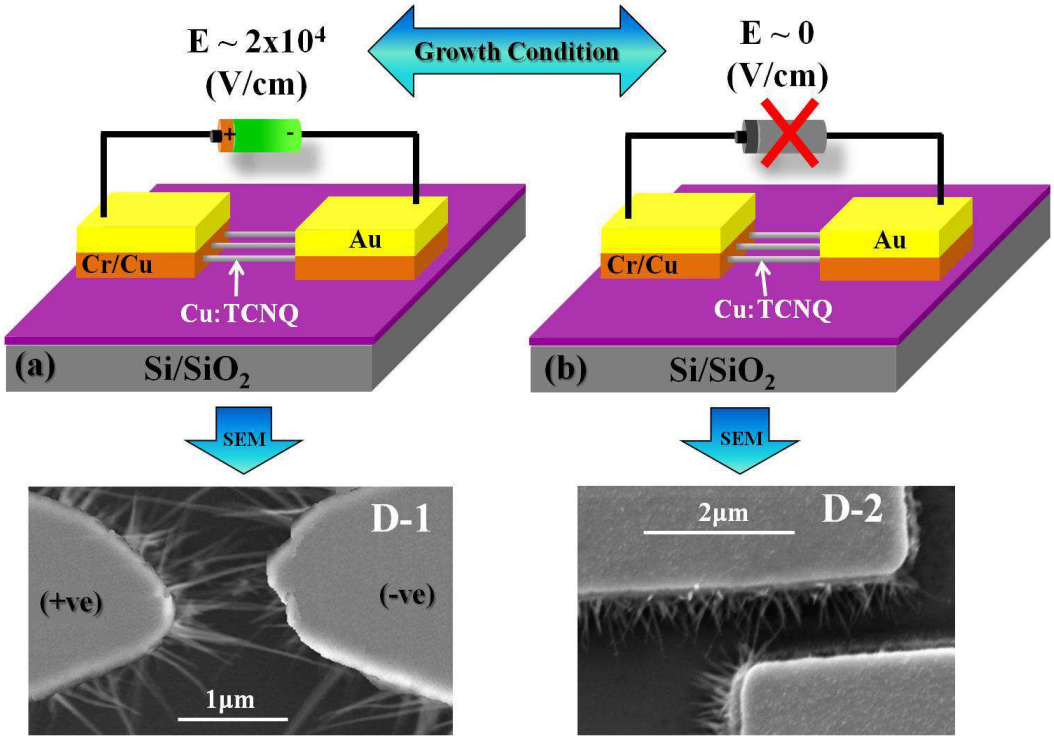

Figure 4.2 Schematic of the device for inplane growth of Cu:TCNQ NW within prefabricated pads (a) with and (b) without field. SEM images of Cu:TCNQ NWs corresponding to the growth conditions are represented by arrows.

4.2 Sample preparation in pre-defined electrodes

The NW growth process was carried out using vapor phase growth on e-beam lithographically made predefined electrodes. This process gives well defined NWs with much less diameter. Another important advantage is that one can have the growth as a nanobridge that connects two prefabricated contact pads which allows us to carry out electrical experiments without any post-growth processing or lithographic processes. Also, NWs do not suffer deterioration due to post treatment.

Fabrication process for nanobridges of Cu:TCNQ that join two prefabricated contact pads are described briefly below. Electrodes (pads) consist of three layers. The tri-layer (Au/Cu/Cr) pads were fabricated using electron beam lithography and lift-off with thermal deposition of a 10 nm Cr (adhesion layer), 50 nm of Cu (growth layer), and 100 nm of Au (protection layer) on oxidized Si wafers with 300 nm of thermal SiO_2. The typical gap between pads was $\sim 1\mu$m. The Cu:TCNQ NWs grow by the reaction of TCNQ vapor with the Cu layer in the electrodes via a vapor-solid reaction [91]. TCNQ vapor was created by resistive heating of TCNQ at around 120^0C. We made two types of samples.

During growth, for one sample an electric field (E$= 2 \times 10^4$V/cm) was directly applied between the pads. This sample is marked as D-1. If the electric field strength is too high the wires which bridge the electrode gap can get damaged, due to the high current passing through them, as also been observed by Sakai et al [56]. For the other sample no bias was applied during growth. The NWs grown with a zero field is marked as D-2. Fig. 4.2 demonstrate the schematic of NW growth condition and SEM images of the corresponding devices of a real system used for measurements. The NWs grow to bridge the electrodes through the sidewalls of the Cu layer. Generally the growth is stopped as soon as few NWs connect the bridge as determined by finite current between the electrodes. The nanobridges so formed have typically 2-5 NWs of Cu:TCNQ of very similar diameter ($\approx 20-30$nm). The Cu:TCNQ NWs grown by this method consist of more conducting Phase-I Cu:TCNQ, [11] as confirmed by XRD, TEM and FTIR. From the FTIR data and the observed shift in the -CN- stretching band we obtain average charge transfer value (Z) of $\approx$0.6 for the Cu:TCNQ NWs grown by vapor phase. It can be seen below that NWs grown in presence of field has good enough stacking sequence that one can observe the onset of Peierls Transition and CDW transport below the transition as will be discussed below.

4.3 Electrical transport measurements

In the nanobridges since wires are connected to electrodes one can directly make measurements of $I-V$ curves. The bias dependent conductance $G(V)$ was obtained by differentiating the $I-V$ curves numerically ($G(V) = \frac{dI}{dV}$). The measurements were done using a Source-meter (Keithley SM 2400) in a variable temperature insert in a Closed Cycle Refrigerator (VTI cryogenic) down to 40K. The measurements were performed for T $\geq$ 40 K temperature because below that temperatures the nanobridges are prone to mechanical failure. The nanobridges withstand thermal cycling reproducibly in the temperature range of 40 K to 300 K.

4.4 Experimental results

An assortment of the $I-V$ characteristics of both the NW samples were measured over the temperature range 40 to 300 K are shown in Fig. 4.3. The data are plotted in log-scale (current axis) to accentuate the current in the low bias region. The figure shows that the natures of transport in the two types of

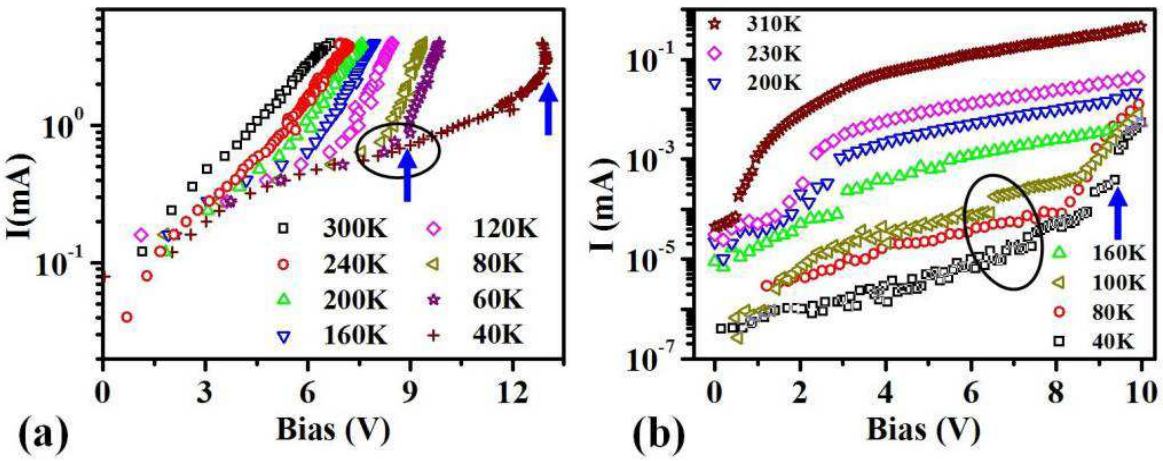

Figure 4.3 I-V data at different temperatures of NWs grown (a) with field, E$\sim 2\times10^4$ V/cm and (b) without field, E$\sim$ 0 V/cm. The V_{th} for temperatures T $<$ 100 are marked by arrows.

NWs are somewhat different. The field grown NWs have higher conductance. The NWs show linear (symmetric) $I-V$ curves at low bias but beyond a threshold voltage V_{th} the $I-V$ curves become strongly non-linear. The extent of non-linearity is also different in the two NWs. The $I-V$ data taken at different temperature show that there is a change in the conductance behaviour below 100 K where it becomes strongly non-linear and the threshold becomes more pronounced (Data highlighted by a circle). We show below that the strongly non-linear behavior may be related to CDW type transport.

The non-linear character of the transport beyond a threshold bias can be seen more clearly in the bias dependence of the conductance (G) as shown in $G-E$ curves in Fig. 4.4. The data shown have been scaled by the number of bridging wires in the nanobridge so that the value of the conductance G represents the conductance value of a single NW. It can be seen from the data that the conductance of the wires grown in presence of the electric field (sample D-1) is larger by few orders compared to that of NW's grown by the same method but with zero field (sample D-2). The bias dependent G taken at different temperatures also show that the nature of dependence of G on E change for T$<$100 K. We will discuss this issue in details later on.

We also note that while both the NWs show semiconducting behaviours and the conductance G reduces on cooling, the reduction is much stronger for the zero field grown NWs. In case of the field grown sample D-1, the reduction on cooling is rather shallow. The limiting low bias conductance $G_0(G_0 = \frac{dI}{dV}$ for $V \to 0$) for the zero field grown sample at room temperature is $\approx 5\mu$S so that $\frac{G_0}{e^2/h}$ is $\approx$1/8, signi-

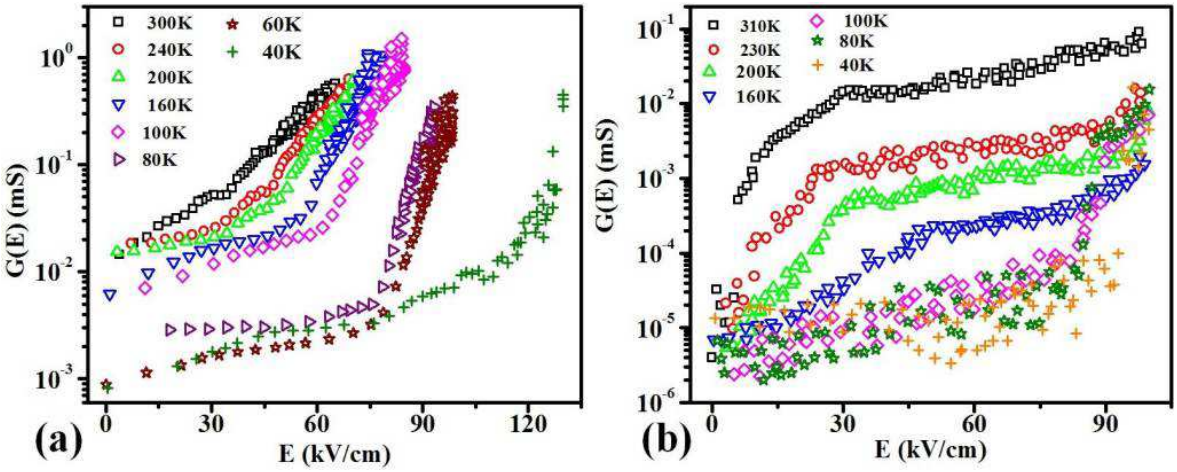

Figure 4.4 Bias dependent conductance G=dI/dV of NWs grown (a) with and (b) without field. The value of G has been scaled by number of wires to obtain the conductance of a single NW.

fying that the NW strands are deep into the insulating state justifying a substantial reduction of G_0 on cooling. However, for the NW's grown in field at room temperature $\frac{G_0}{e^2/h} \leq 1$. Thus the NW strands grown in a field are on the verge of undergoing an insulator-metal transition. The application of field thus drives the NW's close to the transition boundary.

We have observed resistive state switching in Cu:TCNQ NW at a field of E$\sim 1.4 \times 10^5$ V/cm. Since the phenomenon of switching is not within the scope of the chapter, we kept the bias voltage below that value. However, even in that bias scale we observe a strong dependence of $G(E)$ on bias field E and existence of a threshold bias for non-linear conduction. (Note: The onset of non-linearity is distinct from switching). The thresholds in both the samples are enhanced as the temperature of measurement is reduced. We will do quantitative analysis of the non-linear part of the data later on.

The results presented above clearly show that when an electric field is applied to the NWs during growth, the conductivity of the NWs so grown get strongly modified. The modification occurs in the conductance, temperature dependence and also in the non-linear part of the conductance. The experiment establishes the enabling role of the applied electric field during growth. It can thus act as a tool to control the resulting conductance of the NWs. The fact that the experiments were carried out in a nanobridge enabled us to reach conclusion about the conductance change at the level of a single NW is important. Experiments carried out on a bundle or a film of such NWs would not have allowed us to reach a clean conclusion.

4.5 Discussion

4.5.1 Analysis of the conductance data with linear and non-linear part

The observed conductances of both the NW samples, contain a linear part (bias independent conductance) and a strong non-linear part when the applied bias crosses a threshold. One of the models that has been proposed for such one-dimensional system is formation of Luttinger liquid; when the temperature is not too low, function $I(V,T)$ is predicted to behave approximately as one of the two power laws: $I \propto VT^{\alpha}$ at low bias and $I \propto V^{\beta+1}$ at high bias [17] usually with $\alpha \gg \beta$. There are reports that non-linear conduction in Cu:TCNQ may be following such relation [17]. This was based on data taken over the T range of 330 K to 105 K [17]. We find that on extending the data to lower temperature this does not remain valid. Instead there is signature of clear threshold for transport and the bias dependent G both the NW samples show behavior that is different from that expected for a Luttinger liquid.

One of the mechanism that can give rise to non-linear transport with a threshold is CDW transport. In a related system of charge transfer complex TTF:TCNQ there is clear signature of CDW transport in bulk single crystals [92], films [93, 94], as well as in NWs [57]. In such a system the CDW transport occurs due to Peierls transitions in TTF and TCNQ stacks below 50K. The NWs of TTF:TCNQ in which such a CDW transport observed were grown from vapor phase between prefabricated contact pads, as has been done here [57, 95]. Though no CDW type transport or Peierls transition in Cu:TCNQ has been reported till date, we investigated whether the non-linear transport can be described by such a scenario. Since the conductivity of Cu:TCNQ was not measured below 100 K before, it may be that such a phenomena was not observed or reported.

The transport in the Cu:TCNQ NWs have a linear part G_0 and a bias dependent non-linear part which we write as:

$$G(E) = G_0 + G_1 f(E) \tag{4.1}$$

Where E is the field (=$\frac{V}{d}$, d = electrode separation, which is $\sim 1\mu$m in our case), G_1 is a measure of the weight of non-linear part described by the function $f(E)$. We find that for higher temperatures T>

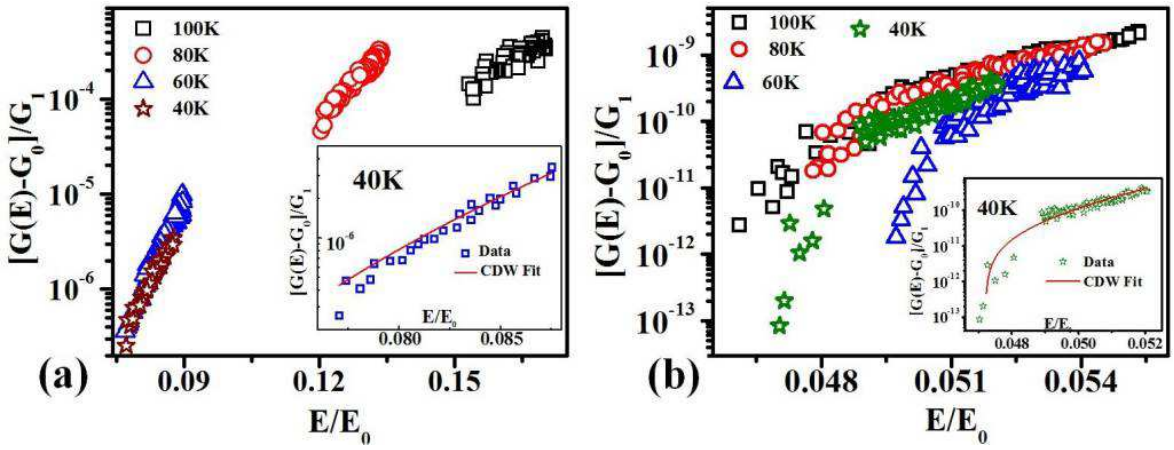

Figure 4.5 The non-linear part of conductivity for the NWs grown (a) with and (b) without field as different temperatures fitted to the modified Zener tunneling relation. Inset in (a) and (b) indicates the CDW fit at 40K.

100 K, in both the samples the functional dependence of $f(E)$ can be described by a power law such that:

$$f(E) = (E - E_{th})^{\gamma} \tag{4.2}$$

Where both E_{th} as well as γ in both the samples have a shallow rise on cooling with E_{th} and γ values lying in the range 30 - 40 kV/cm and 2.5 - 3 respectively. However, below 100 K, there is a distinct change in the threshold dependent conduction and the bias dependence of G can be better fitted with a modified Zener model developed for CDW transport [83, 84]. For CDW system that shows non-linear transport with threshold the function $f(E)$ can be modelled by modified Zener model [84] as:

$$f(E) = \left(1 - \frac{E_{th}}{E}\right) exp\left(-\frac{E_0}{E}\right) \tag{4.3}$$

Where E_{th} is the threshold field and E_0 is a scale of field for tunneling across a pinning gap for the CDW. The fit to the data to Eqn.4.3 have been shown for the data at 40K for both the samples in the inset of Fig. 4.5, where we show the value of the scaled function $\frac{G(E) - G_0}{G_1}$ vs the ratio $\frac{E}{E_0}$. Fig. 4.5 shows all the data for both the samples below 100 K plotted in the scaled curves. It can be seen that for both the samples, a functional form given by Eqn.4.3 remains valid. Linear conductance G_0 for the whole temperature range (300 K - 40 K) is shown in Fig. 4.6. The parameters of the fit namely G_1, E_{th}

and E_0 are shown in Fig. 4.8 as a function of temperature (below 100 K).

A number of observations can be noted from Fig. 4.8, that reflect both the similarity and differences between the two NW samples. It is also interesting that in both the samples, the non-linear conduction (with threshold) for $\leq$100 K, can be described by the Eqn.4.3. Though there is a qualitative similarity between the parameters of the non-linear conduction in the two samples, there are important quantitative differences between the two set of parameters belonging to the two samples. It need to be emphasized that though the non-linear conduction in both the samples follow Eqn.4.3, which is associated with CDW transition, we are not in a position to firmly claim that the non-linear conduction so observed indeed originate from CDW related phenomena. However, it need to be pointed out that charge transfer complexes containing TCNQ moiety, like TTF:TCNQ that has similar structure like that of Cu:TCNQ forms a CDW system due to Peierls transitions on the TCNQ and TTF stacks at 54K and 38K respectively [57]. Such a transition has also seen in TTF:TCNQ NWs grown by similar methods including electric field assisted growth. Thus there does exist a possibility of a Peierls transition in the TCNQ stacks in Cu:TCNQ leading to formation of CDW. This, however, would need independent support from temperature dependent structural data.

4.5.2 Linear conductance and the temperature dependent resistivity

The values of the field independent conductivity G_0 differ significantly in the two samples. This is shown in Fig. 4.6(a). Near room temperature the field grown wires (D-1) have a conductivity that is about one order more than that of the zero field grown NWs (D-2), as stated before. However, due to steep temperature dependence of the more insulating NWs in D-2, G_0 of the two differ by nearly 2 orders at 100 K. There are also certain qualitative observations that can be seen in the temperature dependences of the G_0 of the two NWs. The G_0 decreases from 300 K down to 250 K region for both the samples, although steeper for the zero field grown NW. However, there is a temperature independent plateau in both the samples below 220 K region down to about 125 K where they again show a gradual decrease on cooling (see Fig. 4.6 and Fig. 4.7). From the conductance G_0 we obtain the resistivity ($\rho = \frac{A}{G_0 l}$, A=area, l=length of NW). We find that ρ shows activated behavior following a variable range hopping (VRH) relation for a disordered 1-dimensional system [17, 96, 97]:

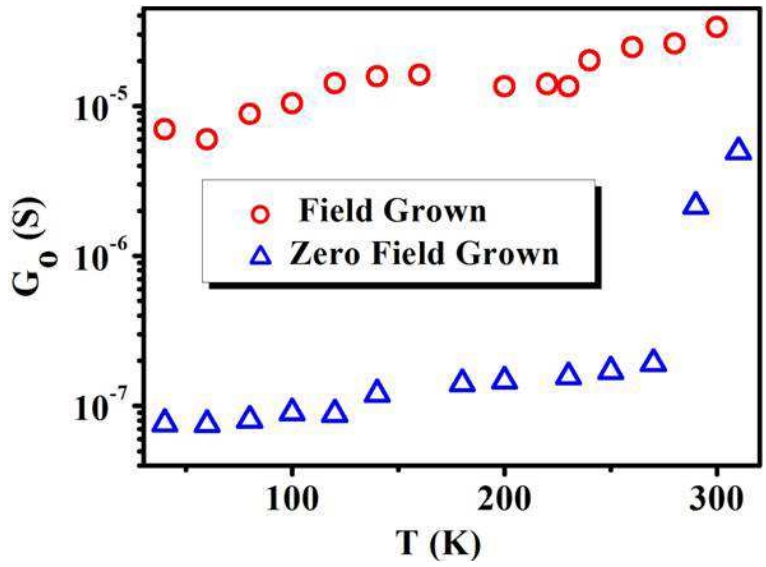

Figure 4.6 Temperature dependence of the linear conductance G_0 (calculated from the slope of linear region of $I-V$) for field grown and zero field grown NW.

$$\rho(T) = \rho_0 + exp\left(\frac{T_0}{T}\right)^{1/n} \tag{4.4}$$

Where T_0 is the energy scale for the hopping. And the exponent $n = d+1$, d being the dimensionality. For 1-dimensional system like the one being investigated expected n=2. The value of T_0 is related to the inverse localization length (α) and the width of distribution of site energies ($\pm\Delta$) so that $T_0 \sim \frac{a\alpha\Delta}{k_B}$

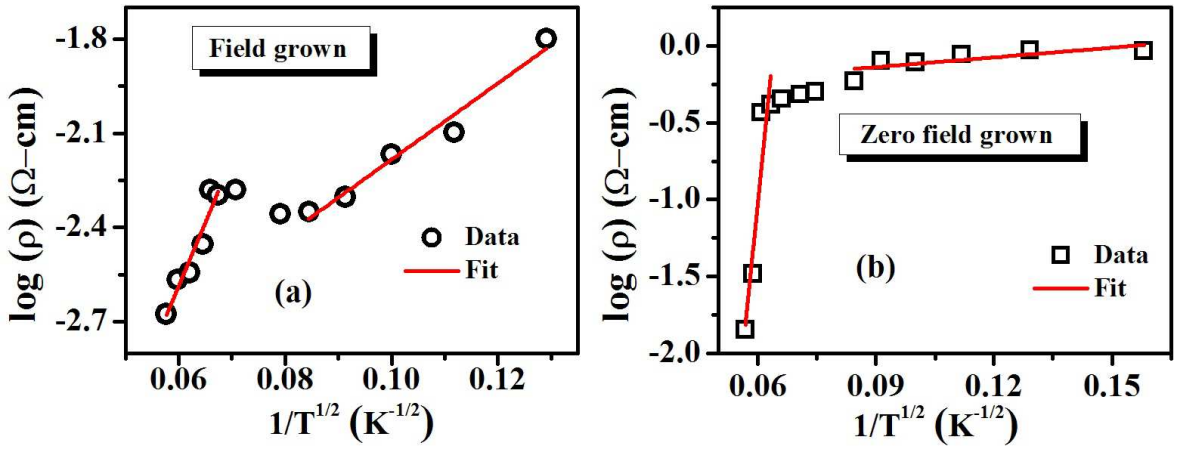

Figure 4.7 Temperature dependent resistivity fitted with VRH model in (a) field grown and (b) zero field grown NWs at low bias (linear region) defined as ρ =A/($G_0 l$), where A is the area and l is the length of the NW.

, a being the interatomic distance. The fit to the above Eqn.4.4 was done in two distinct temperature

ranges of resistivity data for both the NWs as shown in Fig. 4.7. The fit parameters are given in Table 4.1. There are two distinct temperature regions in both the samples. The higher temperature range starts at T$>$ 200 K. For both the samples the low temperature region starts below ≈120 K where the VRH model is not well fitted for both the samples (see fitted parameter in table 4.4). In that temperature range, instead of hopping CDW transport takes part in conduction. In the high temperature region the value of T_0 reduce from 6300 K (≈ 520 meV) in D-2 to around 1625 K (≈ 135 meV) in D-1. The reduction of the value of T_0 in the field grown sample points to reduction in disorder. Reduction of the disorder will enhance the localization length so that α decreases leading to decrease in T_0. The inference that we can obtain from the data is that on application of the electric field during growth, the order in the TCNQ is enhanced. We will see below that it likely arises from increasing the order in stacking of the TCNQ.

At temperatures below 100 K the G_0 appear not to follow any well defined temperature relation. A fit to Eqn.4.4 (Fig. 4.7) shows very low value of T_0 as given in Table 4.1 particularly for the zero-field grown sample. Such a behavior may arise from additional channels of conduction like tunneling that takes over when other channels of conduction freeze out.

Table 4.1 Fitted parameters for VRH model using Eqn.4.4

Synthesis Condition	High Temperature Region		Low Temperature Region	
	ρ_0 ($\Omega-$cm)	T_0 (K)	ρ_0 ($\Omega-$cm)	T_0 (K)
Field grown	1.05×10^{-3}	1625	2.35×10^{-2}	147
Zero field grown	6.69×10^{-7}	6300	0.72	5

4.5.3 Parameters of non-linear conductance with threshold

The non-linear part of the conductance, whose weight we measure by G_1, show strong rise on cooling. The parameters for fit to the modified Zener model (Eqn. 4.3) E_0 and E_{th} both show an enhancement on cooling. This is indeed a new observation. For the zero field grown sample (D-2), G_1 changes by nearly one order on cooling from 100 K to 40 K tending to a temperature independent value at lower T. In the same region, the G_1 for the field grown NWs (D-1) changes steeply by around 2 orders. Interestingly,

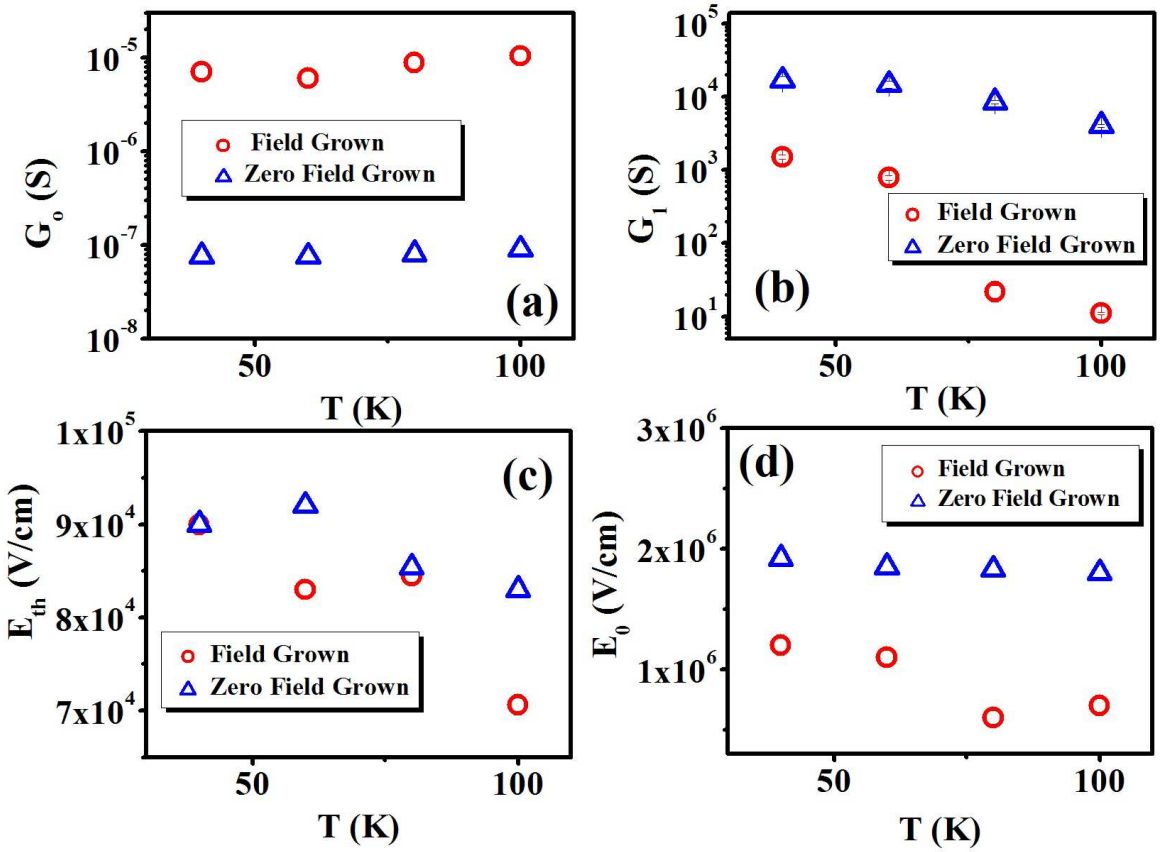

Figure 4.8 Temperature dependence of the parameters (a)G_0, (b) G_1, (c) E_{th} and (d) E_0 (below 100 K) as obtained from the fit to modified Zener tunneling relation.

the value of G_1 for D-1 stays smaller than that of D-2, which is opposite to what has been seen for G_0 which is distinctly higher for the field grown sample D-1.

The existence of a distinct threshold field is seen in both the samples and E_{th} enhances on cooling. Interestingly, the value of E_{th} for the samples are very close. Enhancement of E_{th} on cooling has been observed in other systems also that show CDW type transition [57].

The parameter E_0 shows somewhat larger fit noise. However it also increase on cooling for both the samples, more steeply for the field grown sample. For the zero-field grown sample E_0 is larger and has a relatively shallow T dependence.

It will be worthwhile to compare the parameters E_0 and E_{th} seen for the Cu:TCNQ with those observed in NWs of a system like TTF:TCNQ that are known to show Peierls transitions. The value of the ratio $\left(\frac{E_0}{E_{th}}\right)$ is an important parameter and gives the ratio of the tunneling length $L \propto \sqrt{t}$ to the

coherence length of the CDW system ξ_0 $\left(\frac{E_0}{E_{th}} = \frac{L_t}{\xi_0}\right)$. The value of the ratio is around $\approx$ 2-5 for clean CDW systems like $NbSe_3$ [98]. For NWs like TTF:TCNQ is $\approx$ 10 at low temperatures. For the field grown Cu:TCNQ NWs, at 40 K the ratio is 10 while it is $\approx$20 for the zero field grown NWs. The fields $E_0 \sim \xi_0^{-1}$ and $E_{th} \sim L_t^{-1}$. Since for both the NW's E_{th} are nearly same, the larger value of the ratio for the zero-field grown sample most likely arises due to smaller coherence length ξ_0. The coherence length ξ_0 is $\propto E_g^{-1}$ where E_g is the pinning gap of the CDW. The application of the field, if it leads to better alignment of the TCNQ stacks can lead to reduction of E_g and hence an enhancement of ξ_0 and a smaller E_0. The smaller value of the field E_0 in the field grown sample, thus may justified within the frame work of a CDW transport.

To conclude this part we observe, whatsoever, be the origin of the strong non-linearity, it is present in both samples but it is affected by the field applied during growth. The strong non-linearity appears to follow the transport behavior of a CDW system .

4.5.4 Suggested scenario for effect of applied electric field during growth leading to change in conductivity of NW

In Cu:TCNQ there are two distinct factors (they may be interconnected) that can alter its conductivity. First is the alignment in stacking of the TCNQ molecules and second is the degree of charge transfer (Z). It is thus likely that any modification of one or both of the above will lead to a change in the conductivity of the charge transfer complex. Based on this we propose the following likely scenario for our observation that the growth of the Cu:TCNQ NW in an electric field enhances its conductivity.

The growth model of Cu:TCNQ from vapor phase has not been worked out in details. In the vapor phase growth, the length grows in time following a time dependence that originates from diffusion of ionic species (Length $\propto \sqrt{t}$), while the diameter does not change after initial growth period. This diameter constrained growth is very similar to growth in solution where Anodized Alumina Oxide (AAO) templates have been used to limit lateral growth [51]. In both the growth processes two phenomena are involved after the initial nucleation phase as already discussed in Chapter 2. (See the schematic in Fig. 2.6). There is diffusion of Cu^+ from the Cu electrode though the growing wire (after initial nucleation phase) to the open growth face. There is also diffusion of electrons from the Cu electrode (due

to redox potential) to the top growing surface, leading to oxidation of the arriving TCNQ molecules to $TCNQ^{-1}$, which then reacts with the diffusing Cu^{+1} to make the Cu:TCNQ. The efficiency of the process (ionic diffusion, as well as electron transport from Cu side to growth face) would determine the extent of the charge transfer Z. The resulting conductivity would also critically depend on the alignment of the TCNQ stacks in the growing NWs. The applied electric field during growth can affect both the processes.

Application of an electric field during growth process will enhance the Cu ions migrate from Cu electrode to the NW tip, thus facilitating the extent of charge transfer and Z enhances. In general the Cu:TCNQ NW grown have $Z \approx 0.55 - 0.65$. We have shown the a small increment in Z using such materials as Graphitic Oxide can lead an enhancement in conductivity by an order of magnitude [99]. Thus an enhanced Z, enabled by the applied electric field during growth can increase the conductivity in the field grown wire substantially as observed.

As the NW grows from the vapor phase with arrival of TCNQ molecules, the successive molecules due to randomization by thermal forces may not have proper alignment. This lack of proper alignment would lead to improper arrangements of TCNQ stacks which will lead to lower conduction even if the grown wires have predominantly Phase-I. Application of the electric field, due to highly anisotropic polarizability (as in TCNQ molecule) can lead to a torque that will align the arriving TCNQ molecules leading to proper stackings. This has been seen in growth of carbon nanotubes from vapor phase [100]. The enhancement in the order of stacking will enhance the conductivity and will also increase the coherence length ξ_0 if the transport is by CDW. The scenario suggested above, though qualitative, can explain the observation that field applied during growth can indeed change the conductivity of the NW.

4.6 Conclusion

In conclusion, we have shown that application of electric field during vapor phase growth can be a viable tool to enhance/modify the conductivity of NWs. The electrical conductances of the NWs (measured) down to 40K shows a strong non-linear conductance which has a well defined threshold for T$\leq$ 100 K. The non-linear conductance was found to follow a modified Zener tunneling model proposed

for CDW transport. Such an observation was not made before in Cu:TCNQ and opens up the possibility of new investigation of CDW in this system.

The application of the field during growth enhances significantly the linear part of the conductance and for a single NW grown in field the conductance is close to $\frac{h}{e^2}$, the boundary of insulator-metal transition. The parameters of the non-linear conductance also change when the wire is grown in an electric field.

We proposed a scenario for the field growth condition where the applied field helps diffusion of Cu ions from Cu to the growing face leading to enhanced charge transfer leading to enhanced linear conductivity. The field applied during growth has been proposed to improve the stacking of the $TCNQ$ moiety leading to enhancement of conductance and also change in parameters of the non-linear conduction. Though the experiment has been done in context of a charge transfer complex NW, the concept may have applicability in growth of other semiconducting NWs.

Chapter 5

Resistive state switching in a single Cu:TCNQ nanowire

In this chapter, we have reported a new type of unipolar resistive state (RS) switching in a single NW of Cu:TCNQ which generally shows bipolar RS switching. Electrical characteristic of a single Cu:TCNQ NW devices with symmetric (C-Pt/Cu:TCNQ/C-Pt) and asymmetric (Cu/Cu:TCNQ/C-Pt) electrodes are studied at room temperature. Both the devices show unipolar switching with high ON/OFF resistance ratio and low threshold voltage when only Pt electrode is positive bias. We explain the switching by a phenomenological model along with numerical analysis, which is based on two aspects: (a) the switching phenomena is predominantly controlled by the change at the contact which we establish through a simple MSM type device model and (b) the transport through the contact region as well as through the body of the NW is localized in nature controlled by hopping/tunneling type process. We obtain semi-quantitative agreement with the experimental data.

5.1 Introduction

Recent technologies are trying to accumulate millions of information in a single chip [101, 102] of size as small as possible and single semiconducting NW having memory effect [103, 104, 105, 106] is a best choice. Materials which exhibit hysteresis or switching like behaviour can be used to make memory devices. Now, compatibility (quality) of a material to be used as memory device can be

determined by its ON/OFF current or resistance ratio, threshold voltage, cycling endurance, data densities, writing/erasing time etc. For rapid advances in information technology one need materials that have capacity to be display non-volatile memory effect with high ON/OFF current ratio, large cycling endurance and low threshold voltage to make low power consuming memory devices with long lifetime [107]. A resistive random access memory (ReRAM) cell is a capacitor like structure composed of insulating or semiconducting transition metal oxides [108] or organic compounds [8, 18] sandwiched between two metal electrodes that exhibits reversible resistive state (RS) switching on applying electric field. This kind of behaviour is shown with a layer, where ionic transports due to redox reaction can be used for making the switch ON and OFF [21]. Two terminal semiconductor sandwich structures with metallic electrodes are potentially ideal since its size can be made very small. The key feature of this two-terminal memory device is the ability to switch the resistance of the device simply by applying a voltage or a current pulse.

Organometallic compounds such as Ag:TCNQ, Cu:TCNQ are well known materials for their non-volatile electrical bipolar RS switching [8, 18]. Lots of work have been done on electrical RS switching of charge transfer complex materials like Cu:TCNQ NW array [8, 18, 28, 30, 35] with high threshold voltage and small ON/OFF ratio, where they have used Al_2O_3 layer (responsible for switching) as top electrode in a device of Cu:TCNQ NW array grown from Cu film. There are some reports on RS switching in a single NW of Cu:TCNQ [23, 28] connected between two Au electrodes. Many models have been proposed to explain the switching mechanism. Those are the formation of conductive filamentary path by redox reaction [8, 18, 28, 30, 35] and tunnelling of carrier between crystalline defects [23] which has already been discussed in Chapter 1. In general, the different resistance states are induced by the formation or dissolution of a highly conductive path, i.e., filament, into a poorly conductive medium. However, no experimental evidence or comprehensive theoretical model has so far been proposed in support of these scenario.

In chapter 4, we have discussed about temperature dependent electrical transport in Cu:TCNQ NW. In this chapter, we present a detailed study about a specific property - electrical resistive switching of Cu:TCNQ with different diameter (<100 nm). There are few essential points which this chapter attempt to address: (a) observation of unipolar resistive switching in a single Cu:TCNQ NW which generally

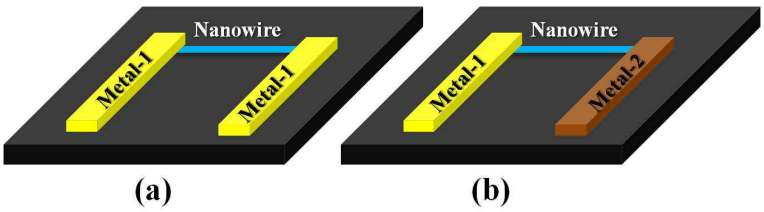

Figure 5.1 Schematic of (a) symmetric (metal-1/NW/Metal-1) and (c) asymmetric (Metal-1/Cu:TCNQ/Metal-2) electrode configuration.

show bipolar switching, (b) a phenomenological model to explain possible reason of switching including role of electrodes to perform unipolar and bipolar switching property, and also (c) analyse the experimental results under the framework of MSM (metal-semiconductor-metal) model to investigate the reason of switching which has not been done before. We have observed switching in single NW devices both with symmetric and asymmetric electrode configuration. Here, symmetric and asymmetric contact electrodes indicate the two connecting electrodes having same and different metal composition respectively. A schematic view of symmetric and asymmetric electrode configuration is shown in Fig. 5.1(a) and (b). We have also explained the possible reason of switching by the development of a basic model with several controlling parameters which are relevant to all the experimental results reported here. In the model, we have also investigated the effect of electrodes on switching and investigated that switching (unipolar or bipolar) depends on the nature of electrodes connecting the NW.

5.2 Fabrication of devices

Nature of electrodes is a crucial parameter in switching and hence device fabrication is an important part in this work [109, 110]. We performed electrical RS switching measurements in two types of single NW devices: symmetric electrode devices (device with same types of electrodes) and asymmetric electrode devices (device with different types of electrodes). Devices S-1 and S-2 (NW diameter $\sim$ 90nm and $\sim$ 65nm respectively) are having symmetric but Schottky type electrode configuration connected with FEB deposited Pt. On the other hand, device A-1 (NW diameter $\sim$ 70nm) is having asymmetric (one electrode with Ohmic and another with Schottky type) electrode configuration. Table 5.1 summarise dimensions of different devices used for measurements.

Devices with symmetric and asymmetric electrode configuration are made from two different

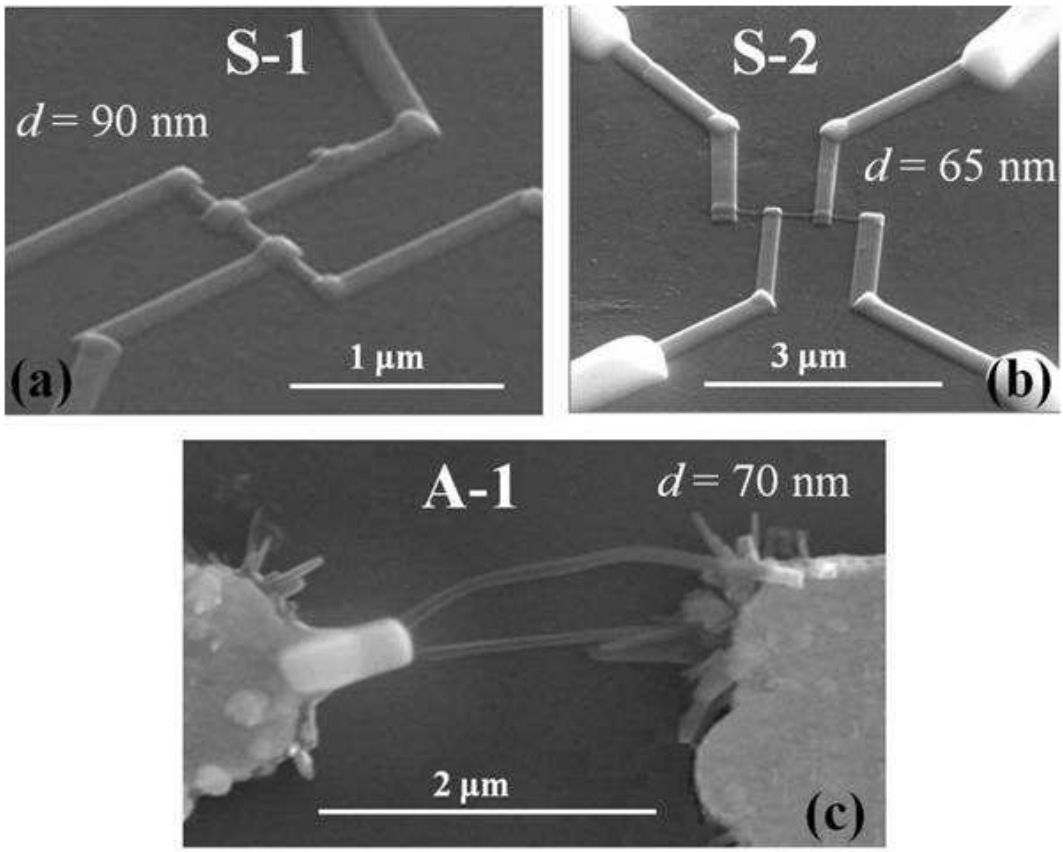

Figure 5.2 SEM image of PVD grown Cu:TCNQ NW devices having (a)−(b) symmetric (C-Pt/Cu:TCNQ/C-Pt), and (c) asymmetric (Cu/Cu:TCNQ/C-Pt) electrode configuration.

approaches- which we categorize as *top-down* and *bottom-up*. Although these processes have already discussed in Chapter 3, we will give an overview of the two process for quick reference.

5.2.1 Fabrication of symmetric electrode device

We have used *top-down* approach to construct device with symmetric electrode configuration. S-1 and S-2 are two single NW devices of different diameters with symmetric electrode configuration. SEM images of the single NW devices are shown in Fig. 5.2(a) and (b). The NWs are connected with lithographically prepatterned Au electrodes by FEB deposited Pt at low deposition current and field to avoid any structural or physical property change in the NW. For attaching leads for the measurements, synthesized NWs are separated from the substrate by ultrasonication in ethanol and then dispersed on Si_3N_4 (300 nm thick)/Si (insulating) substrate containing pre-fabricated Ti/Au electrodes made by hard mask lithography which are used as contact pads. The operation of attaching leads to individual

NWs was done in a dual beam machine FEI HELIOS 600. The wires were imaged during fabrication, using FE-SEM (Field-Emission Scanning Electron Microscope). After selection of a single NW four leads were then connected using Pt electrodes deposited by the electron beam of the FE-SEM at a voltage of 15 kV and deposition current of 90 pA using the precursor Methylcyclopentadienyl platinum trimethyl $(CH_3)_3(CH_3C_5H_4)$ Pt. The important factor that we note is Pt electrodes grown by Focused Electron/Ion beam deposition is a composite of amorphous carbon (C) and Pt. The amorphous carbon is the majority phase in which the Pt is dispersed. For sake of this identification we call the electrode C-Pt. The as prepared 4-probe single Cu:TCNQ NW devices denoted as device S-1 and S-2 connected by FEB deposited Pt with prefabricated Ti/Au symmetric electrodes is shown in Fig. 5.2(a) and (b). Final device configuration is thus 'C-Pt/Cu:TCNQ/C-Pt'. In this case, devices are said to be symmetric as all the electrodes are made of same material (C-Pt contact). Two consecutive probes in the single NW device were used for RS switching measurements with voltage as source and current as measured parameters.

Table 5.1 Electrode configuration and dimension of the devices

Device	Electrode Configuration	Dimension	
		Length (μm)	Diameter (nm)
S-1	Symmetric (C-Pt/Cu:TCNQ/C-Pt)	1.5	90
S-2	Symmetric (C-Pt/Cu:TCNQ/C-Pt)	2.5	65
A-1	Asymmetric (Cu/Cu:TCNQ/C-Pt)	1.9	70

5.2.2 Fabrication of asymmetric electrode device

We have used *bottom-up* approach to construct device with asymmetric electrode. To construct device A-1 with asymmetric electrodes required patterns of Cu/Au with sub-micrometer gap are made by e-beam lithographic process on an insulating substrate of Si/Si_3N_4. First, a thick layer of Cu ($\sim$ 50nm) is deposited onto substrate and then in order to laterally limit the growth of Cu:TCNQ NWs to the sides of the electrodes, an additional thick Au layer ($\sim$ 100 nm) is deposited on top of Cu to prevent the TCNQ vapor from reacting with the upper surface of the Cu layer. Metal evaporation was done in such a way that NWs grown from Cu (bottom electrode) of Cu/Au one electrode connect Au (top electrode)

of another electrode. Free ends of the NWs are anchored to Au with FEB deposited Pt and final device with configuration 'Cu/Cu:TCNQ/C-Pt' is thus obtained. SEM image of the NW device (diameter $\sim$ 70nm and length 1.9 μm) directly integrated into prefabricated device architecture marked as A-1 is shown in Fig. 5.2(c). In this case, device is said to be asymmetric as growth end of the NW is pure Cu which acts as Ohmic and free end anchored with C-Pt as contact with barrier. Slower reaction rate at low temperature for short time can give single NW connecting between two electrodes. The lateral bridging growth method used in this case is for the directed assembly and integration of Cu:TCNQ nanobridges into pre-specified locations on different substrates, eliminating the need for subsequent assembly processes.

5.3 Types of resistive switching

Resistive switching refers to the physical phenomena where a dielectric suddenly changes its (two terminal) resistance under the action of an electric field or current. A schematic of switching is shown in Fig. 5.3 When a certain voltage or current is applied across the device, it goes from high resistance (OFF) state to the low resistance (ON) state by application of a threshold voltage called SET voltage (V_{SET}) at certain polarity, whereas for same or opposite polarity of SET voltage the system returns to its high resistive or OFF state and the corresponding voltage is called reset threshold voltage (V_{RESET}). Depending on the polarity of SET and RESET voltage, resistive switching can be classified into two categories:unipolar and bipolar [38]. .

5.3.1 Unipolar switching

Unipolar devices are switched from the high resistance (OFF) state to the low resistance (ON) state (SET operation) by application of a threshold voltage (SET). The electrical current must be limited to a compliance current (CC) during the set process in order to prevent the device from instantly returning to the OFF state, or even worse the possible memory cell destruction. This is due to the fact, that the SET and RESET state can take place at the same polarity. The reset operation occurs at a higher current and a lower voltage than the set threshold voltage. Schematic diagram of unipolar switching is shown in Fig. 5.3(a).

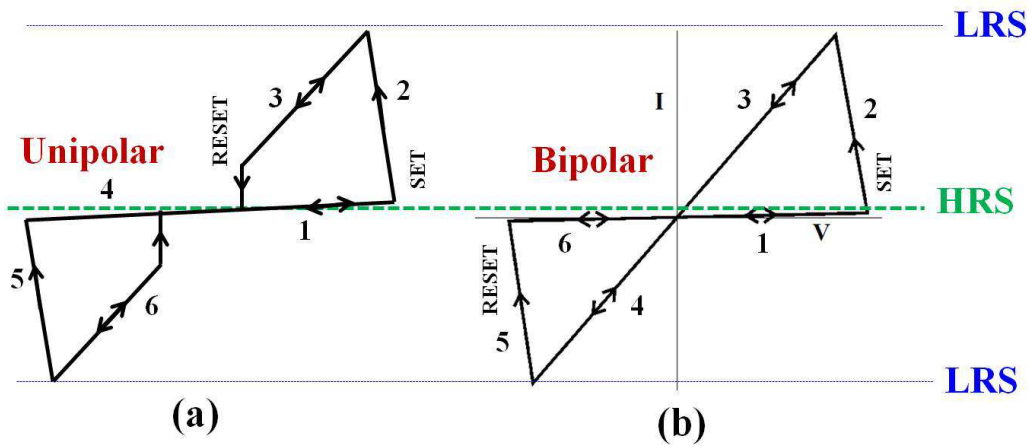

Figure 5.3 Schematic representation of (a) unipolar and (b) bipolar electrical resistive switching. HRS indicates for High Resistive State, and that of LRS is for Low Resistive State. Copyright from [4]

5.3.2 Bipolar switching

Bipolar devices are switched from the high resistance (OFF) state to the low resistance (ON) state by application of a threshold voltage. The current is often limited by a current compliance during the ON switching operation in order to prevent a possible memory cell destruction. The RESET operation takes place at the opposite polarity by application of a different threshold voltage. The MIM or MSM structure of the system must have some asymmetry (different electrode materials, electroforming step, etc.) in order to show bipolar switching behavior. Schematic diagram of bipolar switching is shown in Fig. 5.3(b).

5.4 Switching in symmetric electrode configuration

The $I-V$ curves for device S-1 and S-2 as plotted in Fig. 5.4 were obtained by sweeping up and down a dc voltage, between -5 V to +5 V. The curve shows typical unipolar resistive switching characteristics at a threshold voltage V_{SET} ~3.36 V. (V_{SET} and V_{RESET} indicates the threshold voltages when the system goes from OFF to ON and again returns from ON to OFF state respectively). Initially NW device was in HRS (high resistive state) or OFF state. With increasing bias current increases (arrow '1') and when voltage reaches the threshold V_{SET}, Cu:TCNQ NW rapidly switches from a OFF state or High Resistive State (HRS) to ON state or Low Resistive State (LRS), indicated by the sudden increase of

current in the circuit (arrow '2'). Even though current compliance (CC) was set to 100μA and 10 k Ω load resistor was placed in series with the sample to protect against current burst, but the device reaches to the compliance limit of the SourceMeter when it goes to LRS as shown in Fig. 5.4. When applied bias is reduced, current is also reduced (arrow '3') and system again turned back to its HRS from LRS with the voltage of same polarity but less than threshold voltage which is V_{RESET} $\sim$0.5V (arrow '4'). In this process SET and RESET process occurs for same polarity of applied bias and hence we may call it shows unipolar switching. The same electrical behaviour is also observed under reversed polarity of applied bias but with lower ON/OFF ratio, although the electrodes are symmetric. Slight change in ON/OFF ratio in positive and negative polarity may be due to difference in contact area of deposited C-Pt with the NW at the two ends, which acts as an important factor in switching and is discussed later. Besides, the Cu:TCNQ NW switching device exhibited reproducibility. We have collected data continuously for 24 hours. Fig. 5.5 shows switching data for 450 successive cycles. At the end of large cycle, they may stored charge in the device, as shown in shift of zero for the data after 450^{th} cycle in Fig. 5.5 (c).

5.5 Switching in asymmetric electrode configuration

We have observed switching on another NW device (A-1) having asymmetric electrode configuration (Cu/Cu:TCNQ/C-Pt), one of which is purely Ohmic and another is Schottky type as shown in Fig. 5.2(c). The $I-V$ curve as obtained from the measurement is shown in Fig. 5.6. This device also shows unipolar resistive switching and goes from HRS to LRS at threshold voltage of $V_{SET} = 3.5$ V (arrow '2'). Reverse state occurs at V_{RESET} $\sim$0V. In this case RS switching is observed only in one polarity i.e. when Pt anchored electrode of the NW is in negative polarity w.r.t. the other electrode. No switching is observer in inert atmosphere or in vacuum. It is noted from Fig. 5.6 that device with Ohmic and Schottky contact exhibits switching for one polarity of applied bias only. Possible reason of switching is the barrier height reduction due to metallic channel formation in between the interface of NW and electrodes which is elaborated later. In device A-1, one electrode being Ohmic this end does not exhibit any switching and current is also comparable to the switched state of the Schottky contact end. Thus, both the device shows RS switching at lower threshold voltage compared to other

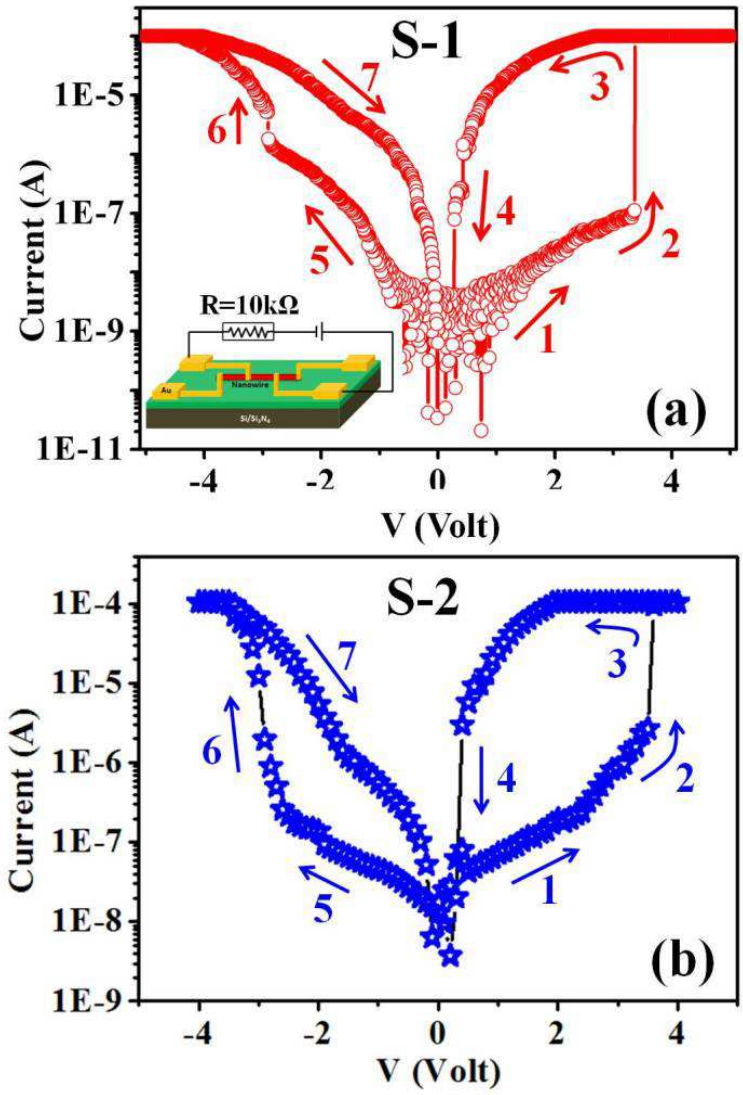

Figure 5.4 Log $|I| - V$ curves of Cu:TCNQ single NW devices with diameter (a) 90 nm and (b) 65 nm, connected with FEB deposited C-Pt in C-Pt/Cu:TCNQ/C-Pt symmetric electrode configuration. Series load resistance R = 10 kΩ and measurement has been performed in air (inset in (a)).

reported devices of Cu:TCNQ array [18, 35, 45] or single NW [23]. Thus, from the results of devices with symmetric and asymmetric electrodes it is clear that nature of electrodes take an important part in RS switching of the NW which is explained below with a theoretical model.

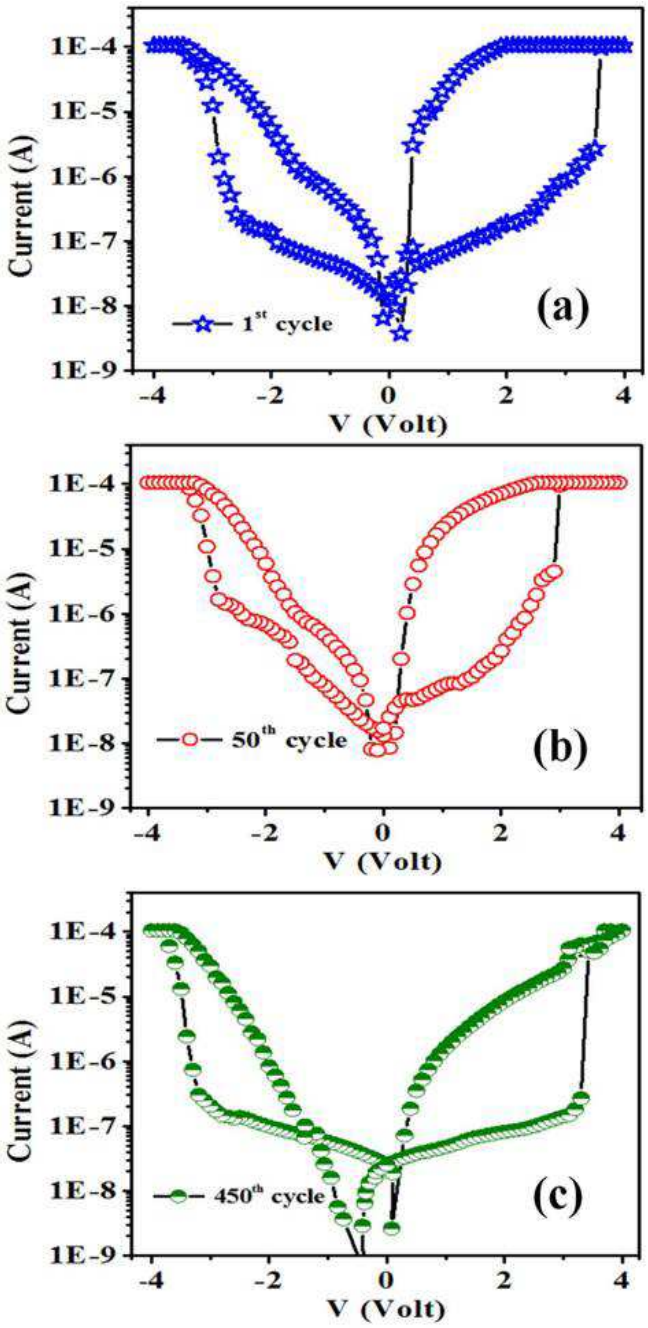

Figure 5.5 Log $|I| - V$ curves of Cu:TCNQ single NW device with large number oc successive cycles, (a) 1^{st}, (b) 50^{th} and (c) 450^{th} cycles respectively.

5.6 Analysis of switching data using MSM device model

The device of Cu:TCNQ NWs that exhibit unipolar switching are 2-terminal devices with two metallic electrodes (M) connecting the semiconductor (S) NW. Thus, 2-terminal devices can be thought of

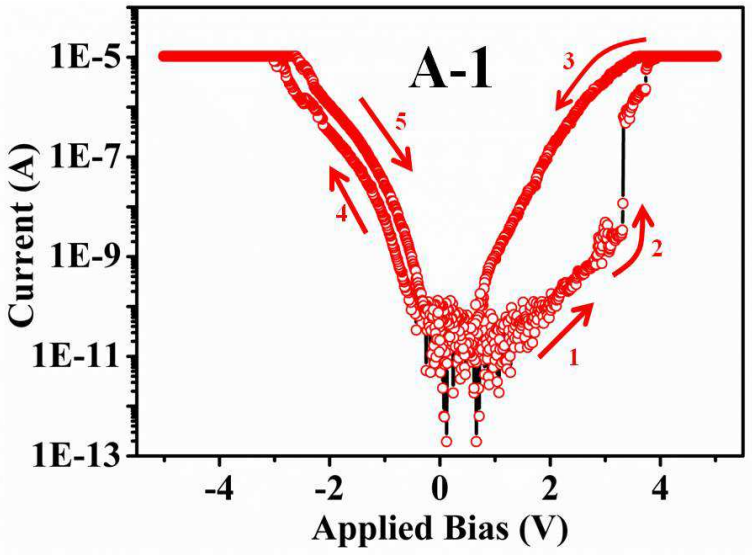

Figure 5.6 Log $|I| - V$ curves of two parallely connected NWs of Cu:TCNQ in Cu/Cu:TCNQ/C-Pt asymmetric electrode configuration measured in air.

as MSM devices [109, 112]. We have used such a device model configuration to analyse the opto-electronic data given in Chapter 6. Analysis of the switching data using MSM model has not been done before. We show that the model gives us a clear indication of the source of the large switching from a HRS to a LRS. The model allows us to separate out how much of the transition occurs due to the changes at the contact resistance and how much actually occurs due to change in the material resistivity. In case of bipolar switching, the phenomena widely studied in Cu:TCNQ, and in the model the switching mechanism have been proposed based mainly on modification at the contact [25, 26, 35]. However, it has never been established how much of the switching (with memory) is due to contributions from contact and how much is due to change in resistance of the bulk of the NW. The analysis based on MSM device elaborated below allows us to separate out the two contributions. We show that the unipolar switching reported here has contributions from both the processes with the dominant contribution arising from contact modifications.

The MSM device model has been developed for a semiconductor device with two Schottky type barriers at the contacts. For the Cu:TCNQ NWs we take the two contacts as two regions with barriers that allow transport with an applied bias. Strictly, the contacts on the Cu:TCNQ are not a conventional Schottky type contacts (contacts with sharp barrier). Nevertheless, it can be reasonably assumed that there is a contact with barrier so that a Schottky type model can used to get information on relevant pa-

rameters. The MSM model thus uses a back to back Schottky contacts connected by the NW resistance (R_s). This makes one of the contacts forward biased and other reversed biased, which exchange when the bias polarity is reversed. The switching will change R_s as well as the contact resistance (R_c) at the ends. The R_c for a given bias polarity will be determined principally by the barrier of the reversed junction of the two contacts. The model below allow us to estimate the changes in the effective contact barrier at the switching as well as the contact resistance R_c. We follow-up this device model analysis with a phenomenological model that allows us to capture the physical process that leads to the contact modification.

The MSM model gives the following equation for the I-V curve as [113]

$$I(V) = I_0 \exp\left(\frac{qV'}{\eta kT} - 1\right) \frac{\exp\left(\frac{-q(\phi_1+\phi_2)}{kT}\right)}{\exp\left(\frac{-q\phi_2}{kT}\right) + \exp\left(\frac{-q\phi_1}{kT}\right)\exp\left(\frac{qV'}{\eta kT}\right)} \tag{5.1}$$

where, $V' = V - IR$, R being the series resistance, and ϕ_1 and ϕ_2 are the barrier heights associated with two contacts (M's) in forward and reverse bias respectively, k being Boltzmann constant and η is ideality factor of a diode. I_0 is current flow across the metal-semiconductor interface by thermionic emission in both direction leads to a form for I_0 as

$$I_0 = A^* T^2 exp\left(\frac{-\phi}{kT}\right) \tag{5.2}$$

ϕ being barrier height in the metal-semiconductor interface, A^* is Richardson constant and T is temperature. Illumination can reduce barrier height ($\phi's$) by metallic channel formation in the interface region between NW and contact, leading to sharp jump in current enhancement. η generally lie between 1 - 2 for an ideal Schottky diode, although during MSM fitting using equation 5.1, we find somewhat high value of η. High η value arises because the contact we are working with is not an ideal Schottky contact.

The fits to the MSM model are shown in Fig. 5.7 for the three devices studied. Two of the devices are symmetric type (S-1 and S-2) with NW diameters 90 nm and 65 nm respectively. A-1 is the asymmetric device with NW diameter of 70 nm. Though the sample S-1 and S-2 are symmetric, the contacts are found to have different barrier heights and contacts leading to different ON/OFF ratio for the two polarities. Likely reason for this differences will be discussed later on. As can be seen from

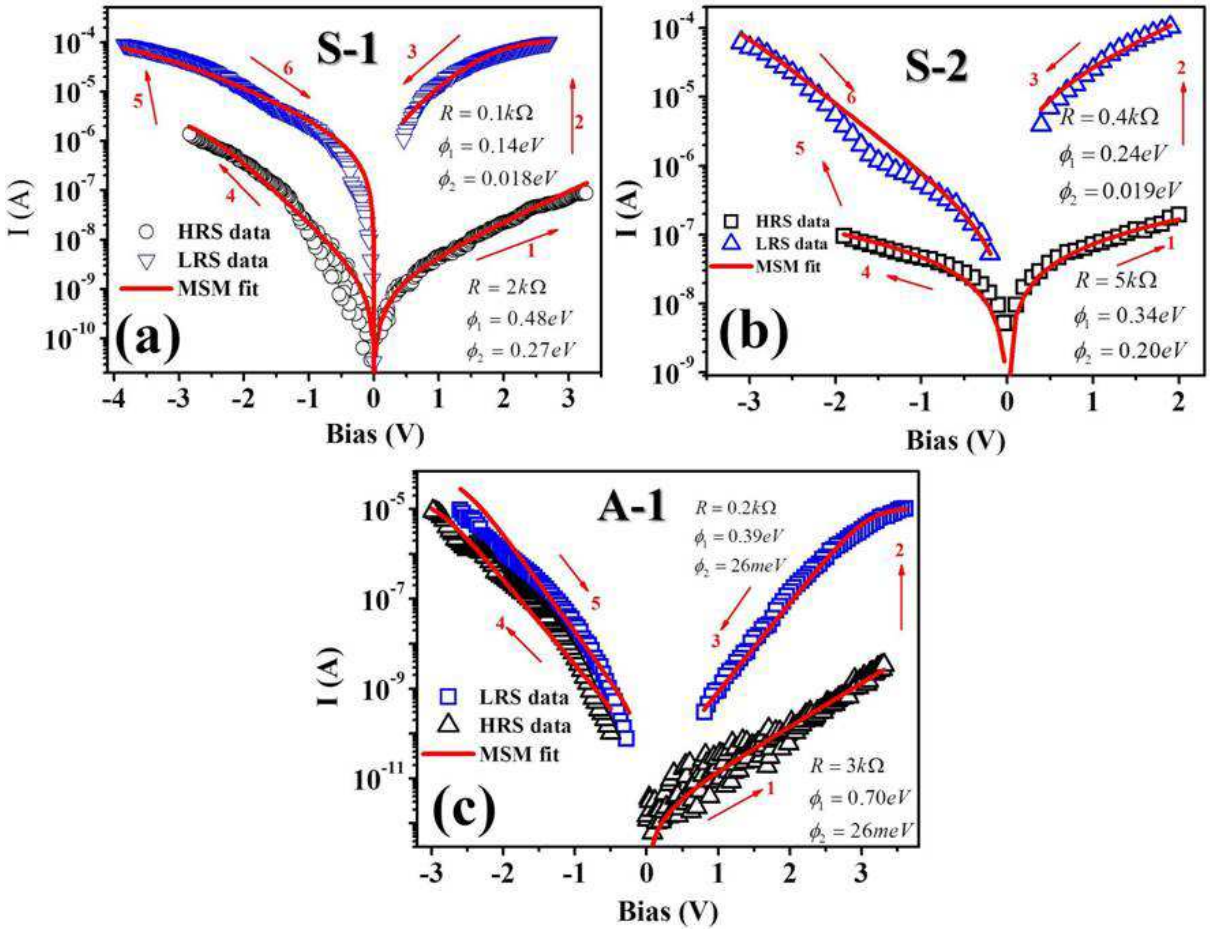

Figure 5.7 Back-to-back Schottky diode MSM fit for ((a) and (b)) symmetric and (c) asymmetric electrode configuration. Here, FEB deposited C-Pt acts as metal (M) and Cu:TCNQ NW as semiconductor (S). M-S junctions act as Schottky contact.

Fig. 5.7, the model fits the data well. Table 5.2 give the relevant fit parameters and table 5.3 gives ON/OFF resistance ratio of different sample measured.

Table 5.2 MSM fitted parameters in HRS and LRS for different devices

Device	HRS				LRS			
	R (kΩ)	ρ_{HRS} (Ω−cm)	ϕ_1 (eV)	ϕ_2 (eV)	R (kΩ)	ρ_{LRS} (Ω−cm)	ϕ_1 (eV)	ϕ_2 (eV)
S-1	2	8.5×10^{-4}	0.48	0.27	0.1	4.25×10^{-5}	0.14	0.018
S-2	5	6.63×10^{-4}	0.34	0.20	0.4	5.3×10^{-5}	0.24	0.019
A-1	3	6.07×10^{-4}	0.702	0.026	0.2	4.05×10^{-5}	0.39	0.026

The following points may be noted:

Table 5.3 OFF/ON resistance ration from fitted parameter.

Device	R (kΩ)		OFF/ON
	HRS (OFF)	LHS (ON)	Ratio
S-1	2	0.1	20
S-2	5	0.4	5
A-1	3	0.2	15

(a) It appears that there is a change in resistance/resistivity of the NWs after switching, although the extent of change may vary.

(b) The ρ_{RHS} of the NWs in all the three devices in HRS lie in the range 0.6 - 0.85 m$\Omega-$cm. After switching (in LRS) ρ_{LHS} lie in the range 40 - 53 $\mu\Omega-$cm. Such a value of resistivity in LRS is what one observes in high resistance metallic systems (like alloys of transition metals). The value of ρ in LRS has quantitative uncertainties, arising from the fit. We will discuss this issue later on.

(c) It is gratifying that the ρ in LRS and HRS being rather similar in the three samples, show reproducibility of the NW fabrication.

(d) The large change in resistance that occurs on switching is much larger than that can arise from change in the resistance of the materials. This establishes essential role of the contact. In Table 5.4 we show the change in contact resistance (R_c) at the HRS and LRS at the point of switching. R_c as defined has total contribution of both contacts. But, one of them being forward bias, R_c will be dominated by the reverse bias contact.

Table 5.4 Contact resistance (R_c) at HRS and LRS at the point of switching

Device	HRS	LHS	Ratio	Switching ratio	
	R_c (Ω)	R_c (Ω)		+ve polarity	-ve polarity
S-1	3.14×10^7	3.35×10^4	$\sim 0.94 \times 10^3$	$\sim 10^3$	$< 10^1$
S-2	1.3×10^6	3.6×10^4	$\sim 3.6 \times 10^1$	~ 36	~ 500
A-1	1.099×10^9	3.49×10^4	$\sim 3.15 \times 10^4$	$\sim 3.3 \times 10^3$	-

It can be seen that jump of device current at switching largely arises from drop in contact resistance for both polarity of the applied bias. R_c will be polarity dependent.

There are quantitative differences in the the actual value of the ON/OFF ratio obtained from current through the device at the switching and that observed from the R_c. This is expected as given from the simple nature of the MSM model that has been used to extract the contact resistances.

The contact barrier heights undergo significant changes on switching. From Table 5.2 and 5.4, it can be seen that the barrier heights in the HRS are substantial and they reduce in the LRS by a large amount and consistently one of the junction becomes almost ohmic with $\phi < 0.02$ eV which is lower than the room temperature energy (~ 0.025 eV). Such reduction of barrier value at reverse polarity of applied bias indicates the signature of metallic channel formation at that junction.

Table 5.5 Contribution of barriers in switching

Device	HRS		LRS		Change in switching for exponential	
	$\phi_1/k_\beta T$	$\phi_2/k_\beta T$	$\phi_1/k_\beta T$	$\phi_2/k_\beta T$	$e^{-\frac{\Delta\phi_1}{k_\beta T}}$	$e^{-\frac{\Delta\phi_2}{k_\beta T}}$
S-1	18.45	10.55	5.3	0.7	5.14×10^5	1.89×10^4
S-2	13.2	7.8	9.26	0.74	5.14×10^1	1.52×10^3
A-1	27	1	15	1	1.62×10^5	1

(f) The use of the above model is only approximate and it overestimates the contact contribution leading to inaccuracy in the determination of the sample resistance. This is because, the sample resistance being a small part of the total 2-probe resistance, almost all the voltage drop occurs at the contacts. This makes the estimation of resistance and hence the resistivity particularly inaccurate in the LRS.

To find the extent in inaccuracy, we have generated a series of I-V curves where we kept the junction parameters unchanged and fit them by varying sample resistance. From the calculated curves along with data are shown in Fig. 5.8. The range of values of sample resistances for which one get reasonable fit are marked in Table 5.6. From this we note the extent of uncertainty in the sample resistance.

Table 5.6 Parameters for generated I-V curves

Device	HRS			LRS		
	R (kΩ)	ϕ_1 (eV)	ϕ_2 (eV)	R (kΩ)	ϕ_1 (eV)	ϕ_2 (eV)
S-1	2	0.48	0.27	0.1	0.48	0.27
S-2	5	0.34	0.20	0.4	0.34	0.20
A-1	3	0.702	0.026	0.2	0.702	0.026

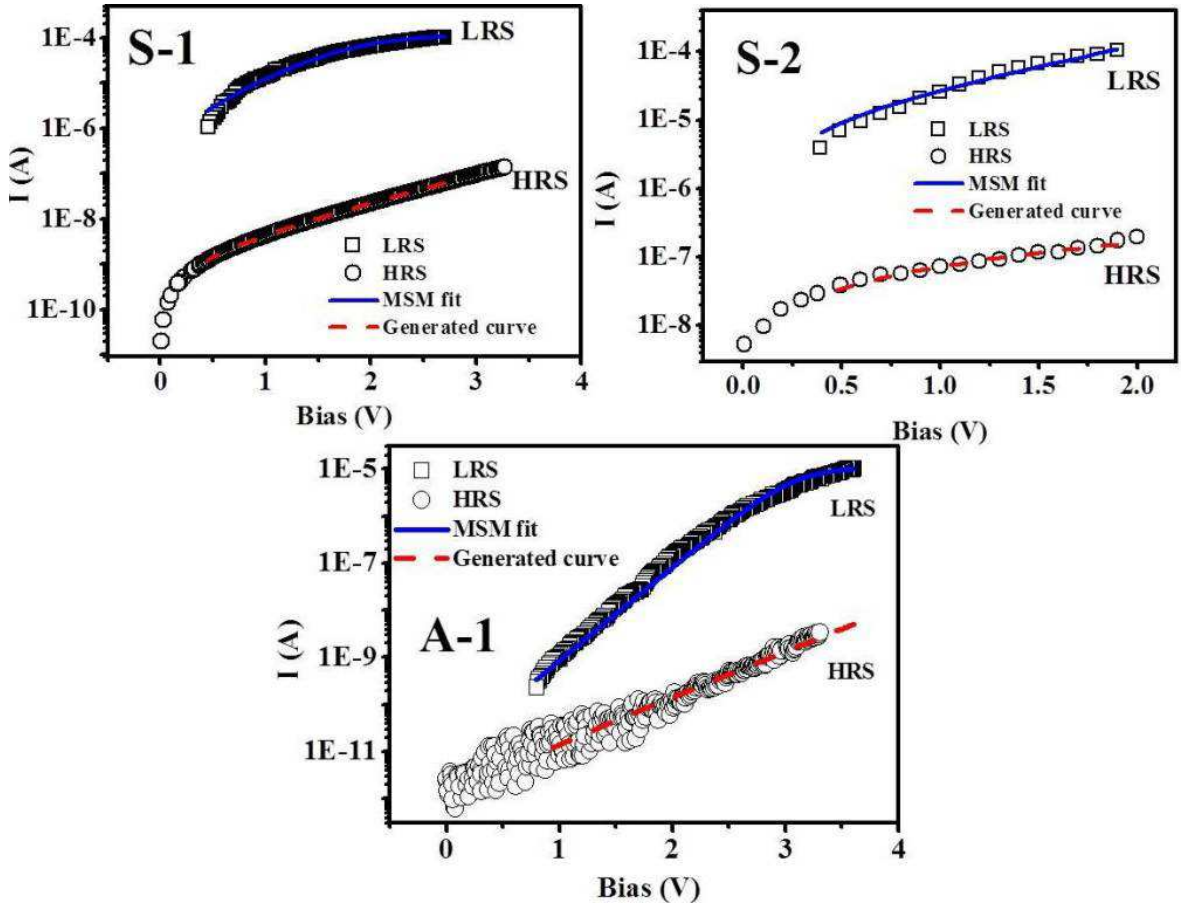

Figure 5.8 MSM fit where junction reduction takes place (blue solid line). Generated I-V curves keeping the junction parameters unchanged and using sample resistance (red dotted curve).

5.7 Phenomenological model of switching

The model analysis above shows that the contacts plays the dominant role in the switching. Previous experiments on bipolar switching also explored this issue, however, without any model based analy-

sis [110]. The MSM model presented above is a rough model that brings out the importance of the contact resistance. In this section, we develop a simple model of the contact based on diffusion of ions which reproduces the observed features. This will present a qualitative scenario of the unipolar switching. We follow-up with a phenomenological model based on rate equations. The model/scenario depicted below draws its motivation from earlier qualitative models proposed for bipolar switching, in which redox reaction leads to filament formation (Cu-filament) at contacts that take part in switching process. In our model we also suggest that the contact barrier is reduced by such filament formation/alignment which is the cause of switching. In contrast to earlier reported bipolar switching devices which had asymmetric type contacts, we observe switching also in devices with symmetric type contacts. In our suggested model we also note that Cu:TCNQ NW is semiconducting in nature (n-type) where transport takes place by hopping through localized state (see chapter 4 on conductivities). The suggested model is given in Fig. 5.9.

The applied bias makes one junction forward biased and the other reversed biased. The two contacts are somewhat differed physically due to variation in the nature of the Pt-carbon composite. Here, charge transport occurs by tunneling through localized metallic regions that include the Cu filaments. In the reversed biased junction (negatively biased) the Cu^+ get aligned in filament by the field leading to enhancement of tunnel rate in turn reduces the potential barrier facilitating current transport and switching. In the numerical part of the model this is taken as a rate constant and a bias dependent function $f(V)$ that control the switching. In the body of NW the transport occurs by hopping through localized state (1d-VRH) that also express by a rate constant as shown below. This scenario that the tunneling rate of carriers at contact region controls the "effective barrier"(ϕ) in the MSM model, can explain the change in ϕ at the contacts during switching.

During measurement across MSM device, one junction stay in forward bias condition (+ve biased junction) and another is in reverse bias condition (-ve biased junction). In this system, Cu:TCNQ NW acts as source of copper ions. When sufficient bias ($V>V_{SET}$) is applied across the NW, Cu^+ ions migrate towards -ve polarity junction and form filament like structure between NW and C-Pt electrodes junction with -ve polarity. At the same time, +ve polarity junction barrier also reduces due to forward bias action. Combination of these two effects result in sharp jump in current at $V \geq V_{SET}$. Process in schematically illustrated in Fig. 5.9. Same results are obtained from MSM fit (Table 5.2). These

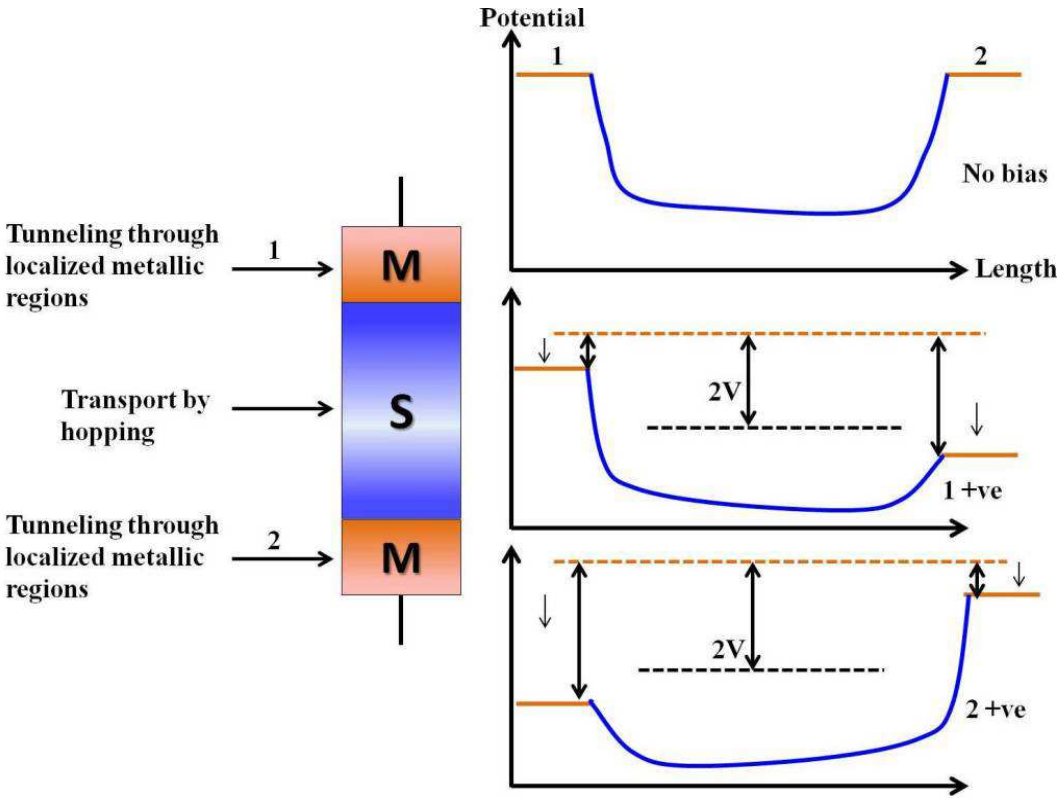

Figure 5.9 (Left frame) Schematic of MSM structure. (Right frame) Band diagram of MSM structure in absence and presence of applied bias across the MSM structure. Applied bias reduces the barrier height in both junction. In positive biased junction, barrier height reduces due to forward bias and in negative biased junction barrier height reduces significantly due to metallic filament formation.

filaments mediate the charge transfers from electrode to Cu:TCNQ NW. Based on the experimental facts, we also assume that after application of certain voltage to the electrodes some filaments get formed/aligned and hence tunnelling probability increases. All the filament alignment and disruption processes are schematically represented in Fig. 5.10 when MS junction '2' is negatively biased and another MS junction '1' is positively biased . Initially the system was in HRS. When +ve bias is applied across junction '1', barrier height across that junction reduces due to forward bias action and that in junction '2' barrier height will reduce due to formation/alignment of Cu atoms towards the -vely biased Pt electrodes. With increasing bias current increases (schematic 'a'). Further increase of bias cause Cu ions to align themselves towards the -vely biased C-Pt electrodes which increases tunneling probability in between NW and C-Pt (schematic 'b'). When applied bias $V \geq V_{SET}$, all the Cu filaments get aligned towards the Pt electrodes and form Cu filament bridge between NW and top/bottom domain (schematic

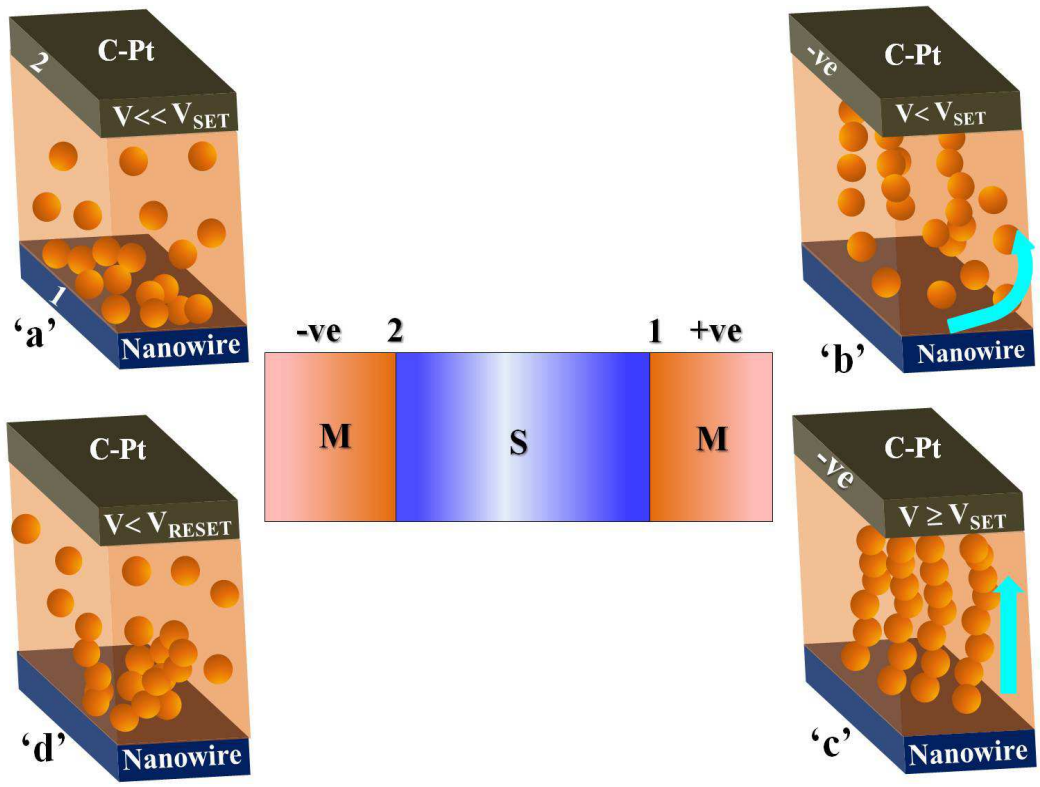

Figure 5.10 Illustration of filament alignment process in between NW and C-Pt electrode when C-Pt electrode is in reversed bias i.e. state '2' is -vely biased. (a) First, Cu ions are aligned randomly. (b) With increasing bias Cu-filaments are getting aligned towards the electrodes to get switched to LRS for $V = V_{SET}$. (c) At $V \geq V_{SET}$ all the Cu-filaments are aligned towards the electrode creating tunneling probability to its extremum and resulting switch in current. Again with reducing bias current decreases. (d) At low bias $V \leq V_{RESET}$ Cu-filaments ruptures due to thermal energy.

'c') which effectively reduces the barrier height and increases the tunneling rates significantly resulting sudden jump or sharp enhancement in current. Again, reduction of bias reduces the current and when bias reduces to V_{RESET}, aligned Cu-filaments are disrupted due to thermal energy or energy state mismatch of NW and top/bottom domain in -ve junction and also barrier height increases in +ve junction, which reduces current to low value (schematic 'd') and bring back the system to HRS. On the other hand, barrier height at junction '1' increases when same process occurs for other polarity of applied bias. In reverse bias, ON/OFF resistance ratio value is low as shown in Fig. 5.5. This may be due to reduces contact area of electrode with NW which effect number of energy states and also the tunneling rate.

For the device A-1 unipolar switching is observed (Fig. 5.6(b)) only when NW-electrode junction

anchored with Pt is negatively biased and this happens also due to filament alignment and disruption with applied bias by changing tunneling rates of carrier between NWs and electrodes resulting in field induced barrier height reduction. But, no switching is observed when junction of growth end of A-1 is negatively biased as this junction is Ohmic and thus carriers get easy path of conduction leading to almost linear conduction with higher current value.

We have also performed numerical analysis to build a model in support of our phenomenological consideration. Our model is motivated by experimental data and reported facts of formation of insulating medium containing non-percolating metallic domains at edges of Cu:TCNQ, metallic clusters, or metallic filaments etc. sandwiched between nano wire and metal electrodes [114, 115]. Our model consider a device with semiconducting charge transfer salts (Cu:TCNQ) having excess copper sandwiched between two electrodes separated by top and bottom domains around the interface of the corresponding electrodes as schematically represented in Fig. 5.11. In this model central domain i.e. NW is connected to metal electrodes via top and bottom domains. In this system, Cu:TCNQ NW acts as source of copper ions which form filament like structure. These filaments mediate the charge transfers from electrode to Cu:TCNQ NW. Nanowire device contains Cu ions, carbon, and metallic clusters in between NW and electrode interface, those are originated during NW growth and also during Pt deposition. The probability of charge transfer from metal electrodes to NW via intermediate top and bottom domain states depend on parameters such as the tunnelling rates Γ which depend on the overlap of electronic wave functions in two systems, the number of states in the domains N and their occupations n. The carriers i.e. electrons move around by hopping between domains as well as between a domain and an electrode, only when bias is applied. Number of states in the domains increases exponentially with their physical size. The tunnelling rates will depend on availability of sites and also on proximity of metallic domains. Therefore it should also depend on the special arrangement of the Cu-filaments. Let us assume that all the Cu-filaments are identical and transport through them have same tunnelling rate.

We solve the model by numerical analysis of carrier transport. As the tunnelling rates depend on overlap of carrier wave functions, the number of states in the domains and their occupations, then, the

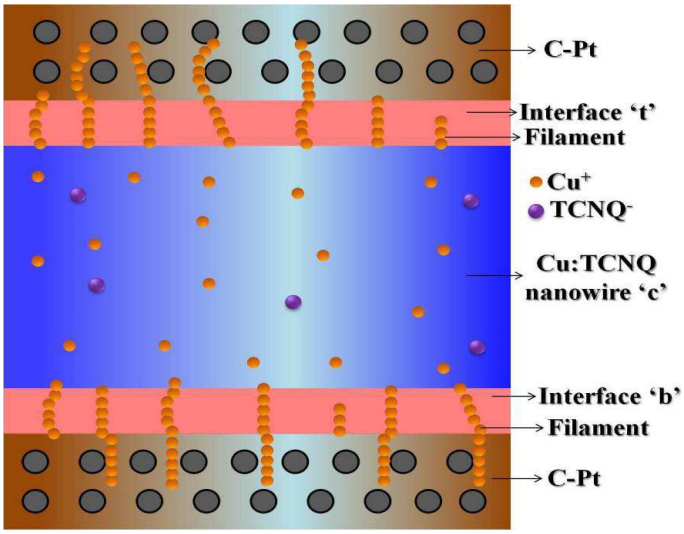

Figure 5.11 A pictorial representation of the model is shown. Cu:TCNQ NW is sandwiched between to two electrodes made up of FEB deposited C-Pt, separated by two interface region where filament formation occurs. The upper part of filament is called top 't' and lower is bottom 'b'. Central part is Cu:TCNQ material and called centre 'c'. Cu:TCNQ NW acts as source of Cu ions.

rate equations for simplest model for the system can be as

$$\begin{aligned} \frac{dn^b}{dt} &= [\Gamma^{E1-b}\frac{N_{E1}}{2}(1-n^b) - \Gamma^{b-c}n^b N_c(1-n^c)]\,f(V) \\ \frac{dn^c}{dt} &= [\Gamma^{b-c}N_b n^b(1-n^c) - \Gamma^{c-t}n^c N_t(1-n^t)]\,f(V) \\ \frac{dn^t}{dt} &= [\Gamma^{c-t}N_c n^c(1-n^t) - \Gamma^{t-E2}n^t\frac{N_{E2}}{2}]\,f(V) \end{aligned} \tag{5.3}$$

Where n^b,n^c and n^t are occupation of bottom, center (NW) and top respect.Γ^{E1-b}, Γ^{b-c}, Γ^{c-t} and Γ^{t-E2} and are the tunnelling rate from electrode to bottom, bottom to center, center to top and top to electrode respectively. For transport through the NW part we do use the rate constant Γ, which is a hopping rate. N_t, N_c, N_b are total number of states in top, center and bottom domains respectively. Here we assumed that the process of charge transport is through localized state although $f(V)$ represents the dependence of the transition probabilities between the two subsystems, like *Pt* to *b* or *b* to *c* etc, on the given external voltage V. $f(V)$ may have very complex form. For the sake of simplicity, form of $f(V)$ is $f(V) = sinhKV$. The function $f(V)$ reflects the dependence of probabilities on the applied external voltage. Note that we take $f(0) = 0$ i.e. in absence of bias there is no current. The occupation of central part (Cu:TCNQ) does not change significantly. This has also been established by the MSM fit that the resistance of the NW does not play a significant role in switching. Therefore, we can assume n^c almost

constant. Assuming that the number of Cu-filaments is same in top and bottom as initial condition, then the above rate equation can be rewritten as

$$\begin{aligned}
\frac{dn^b}{dt} &= [\Gamma^{E1-b}\frac{N_{E1}}{2}(1-n^b) - \Gamma^{b-c}n^b N_c(1-n^c)]\,f(V) \\
\frac{dn^c}{dt} &= \Gamma^{b-c}N_b[n^b(1-n^c) - n^c(1-n^t)]\,f(V) \\
\frac{dn^t}{dt} &= [\Gamma^{c-t}N_c n^c(1-n^t) - \Gamma^{t-E2}n^t\frac{N_{E2}}{2}]\,f(V)
\end{aligned} \tag{5.4}$$

n^b and n^t are related by simple relations. The current can be defined as $\frac{dn^x}{dt}N^x$, where 'x' is 'b', 'c' or 't'. Now, let us rewrite equn, (6.2) as

$$\begin{aligned}
\frac{dn^b}{dt} &= C_1[\frac{(1-n^b)}{2} - r_b n^b(1-n^c)]\,f(V) \\
\frac{dn^c}{dt} &= \Gamma^{b-c}N_b[n^b(1-n^c) - n^c(1-n^t)]\,f(V) \\
\frac{dn^t}{dt} &= C_2[r_t n^c(1-n^t) - \frac{n^t}{2}]\,f(V)
\end{aligned} \tag{5.5}$$

where, $C_1 = \Gamma^{E1-b}N_{E1}$, $r_b = \frac{\Gamma^{b-c}}{\Gamma^{E1-b}}\frac{N_c}{N_{E1}}$ and $r_t = \frac{\Gamma^{c-t}}{\Gamma^{t-E2}}\frac{N_c}{N_{E2}}$. We notice that C just rescales the amplitude of the current where as r controls the ratio of flow of electron in the material.

We solve these equations numerically. From Eqn.5.5, we can see that sudden change of r or C leads to sudden jump in the current. In this case, the sudden change of r may be attributed due to addition of more aligned channels or Cu-filaments to have higher tunnelling rate. In the MSM model this is equivalent to drastic reduction in the barrier potential. Here, we will try to model our experimental results qualitatively. The $I-V$ curve from analytical results are shown in Fig. 5.12 for two different electrode configurations which is similar to our experimental results shown in Fig. 5.5 and Fig. 5.6. We assume that the Cu filaments (n^b and n^t) and electrodes are half filled and n_c =0.48. We take, $\Gamma^{E1-b}N_{E1}$ =10^{-8}, $r^b = r^t$ =10, K1 =K2 =0.04 and jump in r is 60 times of its initial value at V =3.3 and reduced by approximately 56 times near V =0.33. On negative voltage, we start with r ∼300 and it changes by 2 times at V =-3.3V. This can be attributed to the realignment of the Cu-filaments and therefore, there is jump in the Current. During simulating for the device A-1 we notice that electrodes have quite large effect on the $I-V$ curve. To model this material, we assume that the Cu filaments (n^b and n^t) and electrodes are half filled and n^c =0.48. We take N_{E1} =10^{-8}, $r^b = r^t$ =5 , K1 =K2 =0.58 which is almost 11 times higher than type 1 electrode where both side of electrodes are Pt. The jump

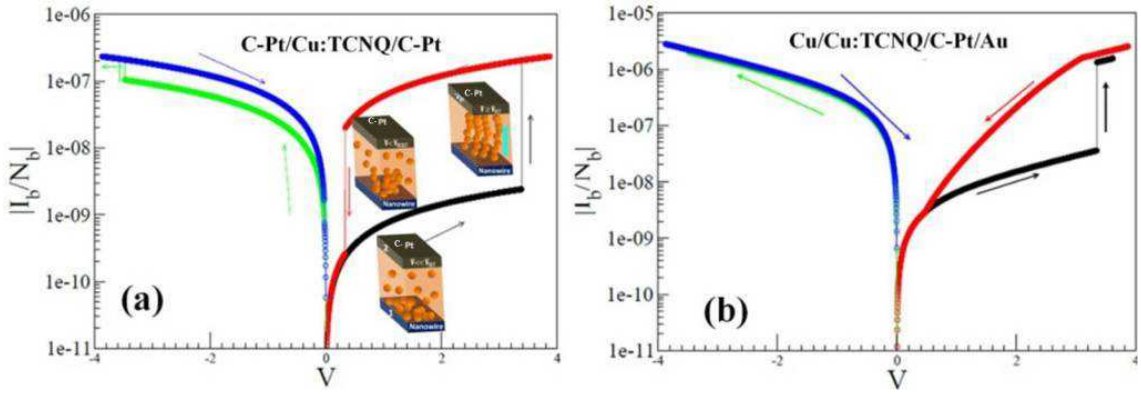

Figure 5.12 Simulated results using phenomenological model. (a) Log $|I|-V$ curves of a single NW of Cu:TCNQ connected with FEB deposited Pt in C-Pt/Cu:TCNQ/C-Pt configuration, load resistor R=10 kΩ in air. (b) Log $|I|-V$ curves of two parallely connected NWs of Cu:TCNQ in Cu/Cu:TCNQ/C-Pt configuration measured in air.

in r is 30 times of its initial value at $V \sim$3.3 V and jump by a factor of 1.4 at 3.7 V. While decreasing V, we notice that the experimental curve sharply decreases for type 1 electrode. This effect may be attributed to V dependence of tunnelling rate. We have assumed a function which can be written as $\Gamma^{b-c} = \Gamma^{b-c}[1 - \frac{1}{1+exp(-\alpha(V_s - V))}]$, where α indicates that how strongly the tunnelling rates changes with V and V_s is proportional to potential height of the system. We have used α=5.2 for our calculations. We also notice that $V_{RESET} \sim$0.5V the current is same as in the beginning. On negative voltage, we start with r =210 and there is a jump in r at V_{SET} =3.3 V. We notice that $I-V$ curve have two jumps for the asymmetric electrode device A-1 on the positive V which may be because of energy alignment or Cu-filaments get realigned and Γ increases. Thus, the switching depends on nature of electrodes as we can see this from both experiment as well as simulated results.

All the Cu:TCNQ NW devices reported in the past by different groups showing bipolar switching were having electrodes of pure metal or oxide metal which forms Cu filament from NW to electrode by redox reaction and brings the system from HRS to LRS and this oxide layer is responsible for bipolar switching [30]. Switching mechanism in our device configuration is somewhat different from the other reported devices showing bipolar switching. In our device to connect the NW with FEB deposited Pt we are using Methylcyclopentadienyl platinum trimethyl $(CH_3)_3(CH_3C_5H_4)$ Pt as precursor is not a pure metal. Thus, during Pt deposition some defect states and metal clusters are created in the interface of NW and metal electrodes. For our electrode configuration at lower bias small current is for

migration of very few charge carriers. As applied voltage reaches the threshold value (V_{SET}), there may be alignment of Cu filament occurs between electrodes and NWs or energy states between top/bottom electrode and NW matches. Both the effect cause sudden increase of tunneling probability and the system goes from HRS to LRS. In LRS tunneling probability remains constant and decrease in voltage reduce the current. As voltage is decreased below the threshold value (V_{RESET}) aligned Cu filaments are getting misaligned due to thermal excitation or energy mismatch occurs between Cu:TCNQ and top/bottom electrode. Same mechanism is applicable in resistive switching for opposite polarity of applied bias. Thus, electrode configuration takes an important part in resistive switching. Nature of electrodes, types of resistive switching and theoretical model enlightening the experimental results make the article distinct from the other reported device of switching in Cu:TCNQ NW.

5.8 Conclusion

In conclusions, we have observed unipolar electrical RS switching in a single NW of Cu:TCNQ with symmetric (C-Pt/Cu:TCNQ/C-Pt) and asymmetric (Cu/Cu:TCNQ/C-Pt) electrode configuration. Both the device shows reproducible electrical switching and memory effect with high on-off resistance ratio ($\sim 10^3$) and at lower threshold voltage. We emphasize that there are very few reports of resistive switching in single Cu:TCNQ NW. This is also the first report of unipolar switching in this material. We have presented a phenomenological model that explains the experimental results of resistive switching. This model may provide useful guidance in this active and promising area of research. The model proposed here is based on two aspects: (a) that the switching phenomena is predominantly controlled by the change at the contact which we establish through a simple MSM type device model and (b) that the transport through the contact region as well as through the body of the NW is localized in nature controlled by hopping/tunneling type process. We obtain semiquantitative agreement with the experimental data.

Chapter 6

Opto-electronic effect in Cu:TCNQ nanowire

In this chapter, we have described the opto-electronic transport measurement on Cu:TCNQ NW, both in array and single, having diameter down to 30*nm. The material shows zero bias photo-current* $\sim 10^5$ *order higher compared to dark-current and also a very high photo-responsivity of* $\sim 10^5 A/W$ *for a applied bias of* $1V$ *in a single NW of length* $\sim$ 200*nm and diameter* 30*nm. We have also explained that the possible reason of current enhancement is due to photo-carrier generation inside the NW along with a barrier height reduction under illumination.*

6.1 Introduction

In recent years, a variety of semiconductor NWs have been synthesized and used as basic building blocks for the development of electronic and optoelectronic nanodevices [117, 118, 119, 120, 122, 123]. These include NWs of inorganic semiconducting materials [117, 118, 119], carbon nanotubes [124], oxide NWs [120], core shell NWs [125], polymeric NWs [126], as well as some organic molecules [127]. These reports showed that it is possible to make photo devices based on a single NW, which can show substantial photo-response. We report here photo-responsive behaviour of a single and array of NW of Cu:TCNQ. The principal motivations for doing this investigation on Cu:TCNQ NW are as follows: first, although there are past reports of resistive state switching in Cu:TCNQ films using high power

laser illumination [8, 128], there is no report of investigation of reversible photoconductivity in this material. The material is expected to exhibit large photoconductive response because it shows laser induced resistive state switching. Secondly, the past studies were done in thin film form and it is expected that the NW will show enhanced photoresponsivity [118, 129]. We indeed see an enhancement of 3 orders of magnitude in photoresponsivity in NW array and even 5 orders in a single NW compared to films. Lastly, the charge transfer complex Cu:TCNQ has attracted considerable recent attention as it exhibits bias driven electrical resistive state switching with memory. This makes the material attractive for making MEMRISTOR (memory resistor) and non-volatile RAM [3]. The present report of large photo-response in Cu:TCNQ NWs, thus, adds an opto-electronic element to the existing electronic switching property and raises the possibility of optoelectronic control to a MEMRISTOR device.

6.2 Operating Principles of Opto-electronic Device

Most optical semiconductor devices are optoelectronic pn-junction devices, such as laser diodes [130], light-emitting diodes [131], and photodiodes [132]. The main interest in the field of optoelectronic devices has shifted from device physics and operation principles to device applications. That is why we require a wide range of knowledge related to optoelectronic semiconductor devices. These opto-electronic pn-junction devices performance depends on the type of pn-junction and nature of semiconducting materials.

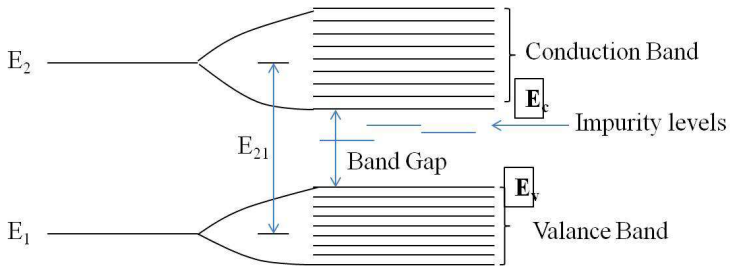

Figure 6.1 Schematic of band diagram of semiconductor.

The valence band and conduction band of semiconducting materials are separated by a distance known as band of the semiconductor. There exists some impurity levels in between valence and conduction band due to imperfections or defects in the materials. Figure 6.1 schematically illustrates the energy levels that might be associated with optically induced transition in both an isolated atom and in

a semiconductor solid.

Many opto-electronic phenomena observed in photo-active semiconductor can be described in terms of some basic concepts involving electron activity in semiconductors. These includes optical absorption by which free carriers are created, electrical transport by which free carriers contribute to the electrical conductivity of the materials, and the capture of free carriers either by recombination or trapping. All the effects are illustrated in Fig. 6.2. Intrinsic optical absorption in Fig. 6.2(a) corre-

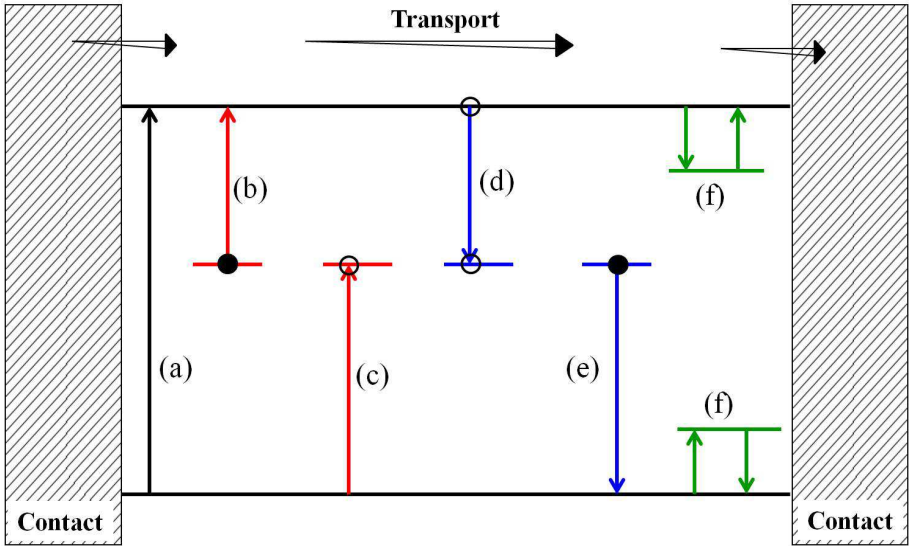

Figure 6.2 Major transitions and phenomena associated with opto-electronic effects in homogeneous semiconductors. (a) intrinsic absorption, (b) and (c) extrinsic absorption, (d) and (e) capture and recombination, (f) trapping and detrapping.[Reprinted with permission from [133]. Copyright (1992) Cambridge University Press.]

sponds to the raising of an electron from valence band to conduction bans due to absorption of photon energy illuminated on the materials. Extrinsic optical absorption corresponds to the raising of an electron from imperfection to conduction band or from valance band to imperfection as in Fig. 6.2(b) and (c) respectively. A captured carrier at an imperfection may do the following two things: (i) recombine with a carrier with the opposite type as in Fig. 6.2(d) and (e), or (ii) thermally reexcited to the nearest energy band before recombination occurs. In the latter case it is referred to as trap, and the capture and release processes are called trapping and detrapping. Fig. 6.2(f) shows such trapping and detrapping situation. This processes control the extent of photoconduction as well as photoconduction dynamics (time dependent).

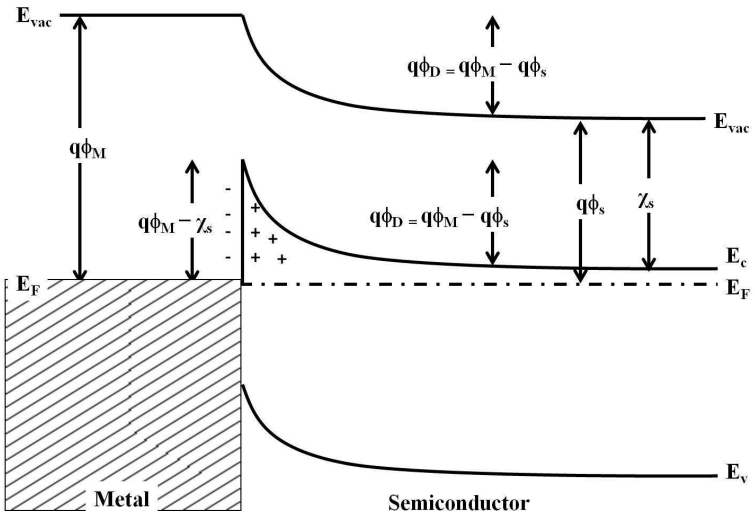

Figure 6.3 A Schottky barrier blocking contact between a metal and n-type semiconductor, formed when workfunction of metal is larger than that of semiconductor. [Reprinted with permission from [133]. Copyright (1992) Cambridge University Press.]

6.2.1 Electrical Contacts

The physical situation of electrical current flow under illumination also involves the effect of contacts. Effect of electrical contacts between a metal and a semiconductor under illumination can be described in terms of different classes of behaviour like: (a) ohmic contact - able to fill up carriers created by photoexcitation when they are drawn out of the material by an applied electric field. (b) blocking contacts - unable to fill up carriers created by photoexcitation when they are drawn out of the material by an applied electric field. Current varies less than linearly with applied bias and become saturated. A typical blocking contact to an n-type semiconductor is shown in Fig. 6.4. Such contact is also called a rectifying contact or non-ohmic contact or a Schottky barrier. The quantity $q\phi_D$ is the energy difference between the workfunction of metal ($q\phi_M$) and semiconductor ($q\phi_s$), where ϕ_D is diffusion potential. Now, barrier height experienced by an electron in moving for metal to semiconductor is $\phi = q\phi_M - \chi_s$, where χ_s is electron afinity of the semiconductor. Thus, barrier height is larger than $q\phi_D$ by an amount $E_c - E_F$, E_c and E_F being energy of bottom of conduction band and Fermi level respectively.

The work performed during the course of this thesis are with NW devices having both blocking/Schottky contact or combination of ohmic and Schottky contact. As discussed in chapter-3, NW device fabricated with *top-down* approach have Schottky contacts and *bottom-up* approach have one

contact Schottky and another Ohmic (growth end of the NW). If voltage difference is applied across such a blocking contact, current will depend on the polarity of applied voltage. If metal electrode is positive, energy levels of the semiconductor are raised and more electron will flow into the metal. Considering a NW is connected with two blocking contact, then current flow in such a device can be expressed as [113]: [Although the equation has already been stated in chapter 5, here we reproduce the same for convenience.]

$$I(V) = I_0 \exp\left(\frac{qV'}{\eta kT} - 1\right) \frac{\exp\left(\frac{-q(\phi_1+\phi_2)}{kT}\right)}{\exp\left(\frac{-q\phi_2}{kT}\right) + \exp\left(\frac{-q\phi_1}{kT}\right)\exp\left(\frac{qV'}{\eta kT}\right)} \tag{6.1}$$

where, where, $V' = V - IR$, R being the series resistance, and ϕ_1 and ϕ_2 are the barrier heights associated with two contacts (M's) in forward and reverse bias respectively, k being Boltzmann constant and η is ideality factor of a diode. I_0 is current flow across the metal-semiconductor interface by thermionic emission in both direction leads to a form for I_0 as

$$I_0 = A^* T^2 exp\left(\frac{-\phi}{kT}\right) \tag{6.2}$$

ϕ being barrier height in the metal-semiconductor interface and T is temperature. Illumination can reduce barrier height ($\phi's$) by carrier generation, leading to photo-current enhancement.

6.2.2 Photoconductive Gain

Photoconductive gain (G) is number of carriers generated to the number of photons incident on the sample [134], which is directly related to lifetime and transit time of photo-generated carrier.

$$G = \frac{N_{carrier}}{N_{photon}} = \frac{\tau}{\tau_t} = \frac{\mu V}{l^2}\tau \tag{6.3}$$

where, τ in lifetime of the generated carrier,τ_t is transit time of photo-generated carrier, μ is mobility of carrier, V is bias applied across the sample and l is length of the sample.

6.2.3 Responsivity

Responsivity ($\Re$) is defined as the amount of photo-current generated due to unit power falling on the sample (electrical output to optical input in an opto-electronic device) and is represented as fol-

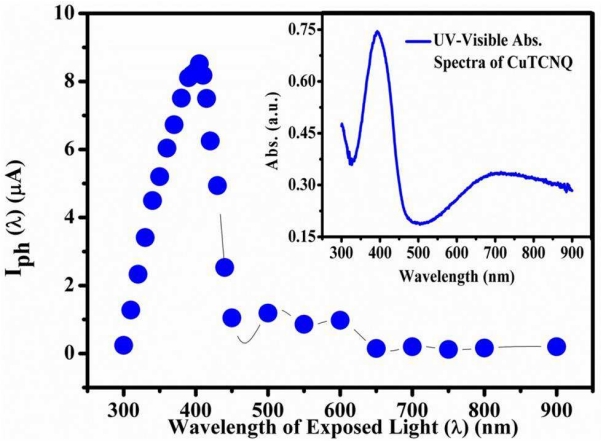

Figure 6.4 Photo-current of a single NW as a function of wavelength. Inset shows the absorption spectra of NWs as a function of wavelength.

lows [135]:

$$\Re = \frac{I_{ph}}{P_{sample}} = \frac{q\eta}{h\nu}G \tag{6.4}$$

Thus, from equn. (4.3) and (4.4), prolonging life time of carrier, reduced transit time of photon and shorted length enhances the photoconductive gain and hence responsivity of a NW.

6.2.4 Spectral response of photoresponsivity

To produce photocurrent, light must be absorbed in the process of creating free carriers by either intrinsic and extrinsic optical absorption. Therefore, there is a close correlation between optical absorption vs excitation wavelength to the photocurrent vs excitation wavelength. Sharper is the spectra more defined will be the band gap energy. Broad absorption spectra indicates the distribution of trap states around fermi level E_F. Fig. 6.4 shows photocurrent as a function excitation wavelength for a single NW of Cu:TCNQ, whereas inset shows the absorption spectra of the corresponding.

6.3 Photoresponsive behaviour of Cu:TCNQ NW array

Opto-electronic measurement was performed first on a Cu:TCNQ NW array ($\sim$80 NWs in number) device (with asymmetric electrode configuration) of average diameter of $\sim$30 nm grown on two prefabricated electrodes of separation 1.7μm with bottom-up approach as shown in Fig. 6.5(a). The asymmetry in contacts occurs because wires were made to grow preferentially from one electrode

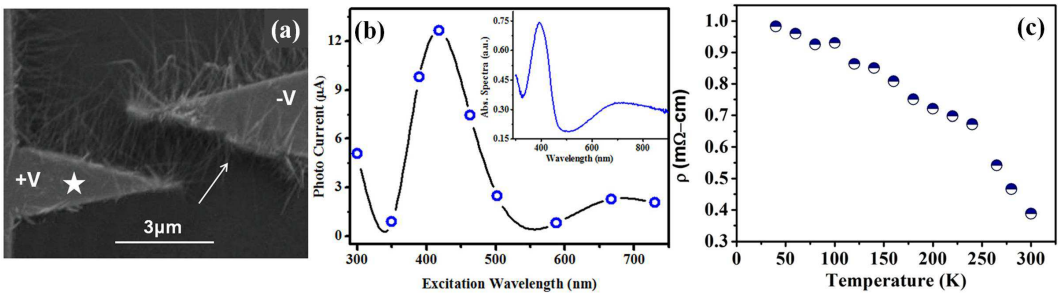

Figure 6.5 (a)Top view SEM image of a Cu:TCNQ nanobridge device. The electrode from which growth starts is marked by star and direction of growth is marked by arrow.(b)Photo-current of NW array at constant bias of 3 Volt as a function of wavelength. Inset shows the absorption spectra of NWs as a function of wavelength.(c) Temperature dependent resistivity of the NW array measured separately in dark.

of the bridge and terminate on the other. The electrode, from which growth starts (marked as star in Fig. 6.5(a)), was selected by choosing the angle of orientation of the substrate during growth. The direction of growth is marked with arrow in Fig. 6.5(a). All the experiment performed in this work were taken at an illumination of $\lambda = 405$nm because the photoresponse shows a peak at this wavelength as shown in Fig. 6.5(b). This links the photo-response to the process of fundamental carrier generation in the material. Separate studies on an ensemble of NWs show that the absorption reaches a peak around this wavelength as shown in the inset of Fig. 6.5(b). Fig. 6.5(c) represents the resistivity curve of Cu:TCNQ NW device representing semiconducting nature of the material.

The spectral dependence of the photo-current ($I_{Ph}(\lambda)$) in Fig. 6.5(b) was taken in the wavelength range 300-750 nm with applying bias of $V = 3$ V. The spectral response of the data shows a peak around $\lambda = 405$ nm. To check whether the spectral response has a relation to the absorption, we measure later indeed. The absorption data are taken by two methods. One method is by dispersing the NWs in ethanol by ultrasonication and taking data with the dispersing medium, and other method is by dispersing the NWs on a polished quartz plate and then allow the dispersing medium to evaporate. In both cases the normalized absorption was found to be similar with a maximum at around the same λ (≈ 405 nm) as shown in inset of Fig. 6.5(b). Comparison with the absorption and the optical response ($I_{Ph}(\lambda)$) curves shows that the optical response is indeed caused by the absorption of the light in the Cu:TCNQ NW predominantly at the peak absorption range, while at longer wavelength the response is at least an order less. The observed photo-response is related to creation of carriers (electron-hole pairs) at the

absorption peak. It is generally believed that on illumination the light is absorbed by the TCNQ moiety which leads to creation of neutral TCNQ and the absorption peak in Cu:TCNQ arises mainly from neutral (anion radical) TCNQ ($TCNQ^{-1}$) [136]. If that indeed is the case, there is creation of electron from the TCNQ anion radical.

Fig. 6.6 shows a typical $I-V$ data taken on such a nanobridge device (Fig. 6.5(a)) at dark and also under continuous illumination of wavelength $\lambda = 405$nm with optical power density $p_{opt} = 6.6x10^6 \mathrm{W/m^2}$. The $I-V$ data of such a device is not symmetric which arises due to asymmetric contacts which we quantify below. The dark as well as illuminated $I-V$ data have been analysed considering the device as metal-insulator-metal (MSM) structure, where Cu electrodes act as metal electrodes and Cu:TCNQ NWs as semiconductor. The current through the device has two components: a zero bias photocurrent $I_{Ph}(V=0)$ and a bias dependent current $I(V)$. The zero bias photo-current $I_{Ph}(V=0)$ is measured separately. The bias dependent current $I(V)$ both in dark and under illumination through the MSM device is fitted using equation (4.1) with a model of two back-to-back Schottky diodes, connected by a series resistance R, representing the resistance of the NWs between the two electrodes. ϕ_1 and ϕ_2 are barrier heights of the two contacts with forward and reverse bias respectively. Thermionic emission current I_0 does not change on illumination i.e. enhancement of current under illumination is independent of thermionic emission. The bias dependent $I-V$ obtained from the equation above has been added to experimentally observe zero bias photocurrent $I_{Ph}(V=0)$ to obtain the total device current I in the device. If the two M contacts in the MSM structure are identical ($\phi_1 = \phi_2$), then the $I-V$ curves will be symmetric. However, unequal barrier heights ($\phi_1 \neq \phi_2$) at the two contacts will lead to asymmetric $I-V$ curves as observed. A simple schematic of the barriers and the MSM device model used in the analysis are given in the inset of Fig. 6.6. From the fit of the experimental $I-V$ data using Eq. (4.1) we obtain $\phi_1 = 5 \pm 2$meV and $\phi_2 = 200 \pm 2$meV in the dark with NW resistance, $R = 8.0 \pm 0.1\mathrm{k\Omega}$. (Note: The parameters are obtained from the best fit to experimental data and the fit procedure gives the parameters uniquely. Variation of resistance or barrier values beyond the error limits leads to perceptible deviation of the fit from the experimental data.) The observed barrier height (ϕ_1) is rather small in the NW electrode junction. The low barrier indicates that the contact is almost ohmic, representating growth end of the NW device marked with star in Fig. 6.5(a). At other end where NWs make contact to the electrode after growth, the barrier height (ϕ_2) is larger. From the fitted value of the series resistance

R in dark, we have calculated the resistivity $\sim 0.34 m\Omega$cm, which matches well with the experimental resistivity data ($\sim 0.38 m\Omega$cm) measured separately in dark as shown in Fig. 6.5(c).

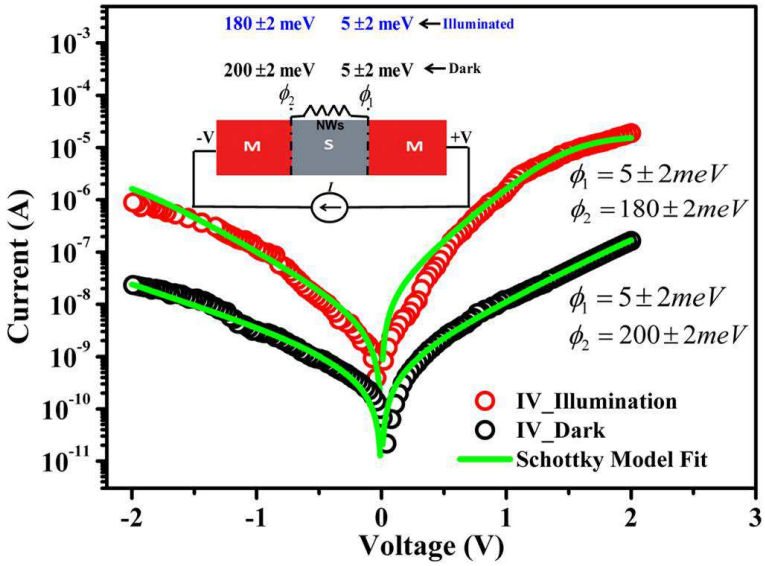

Figure 6.6 I-V curves in dark (black circle) and under illumination (red circle) of Cu:TCNQ NW array. Wavelength of illumination $\lambda = 405$nm with power density $p_{opt} = 6.6 \times 10^6 \text{W/m}^2$. Solid green curve is fit to the MSM device model. The barrier heights ϕ_1 and ϕ_2 obtained from the fit are $\phi_1 = 5 \pm 2$meV and $\phi_2 = 200 \pm 2$meV in dark and $\phi_1 = 5 \pm 2$meV and $\phi_2 = 180 \pm 2$meV under illumination. The inset shows the schematic of barriers at contacts.

On illumination at 405 nm, the barrier heights change marginally along with change of NWs resistance R. While ϕ_1 remains unchanged and there is a small lowering of ϕ_2 from 200 ± 2meV to 180 ± 2meV. On illumination, the main change occurs for the series resistance (R) that shows a significant reduction. The value of the series resistance under illumination $R = 1.0 \pm 0.1 \text{k}\Omega$ as obtained from the fit. This is an order lower than the value of R in the dark. The suppression of the series resistance R is due to the photoconductivity in the NWs between the two contacts. In this context, it is noted that in many NW based photodetectors (working as MSM device), the response under illumination can arise from the photoconductivity of the NW and also from significant lowering of the barrier under illumination [137, 138]. In the NW arrays grown directly on Cu electrodes, we find that the barrier being low, the contribution arising from lowering of barrier is also low and most of the response arises from the photoconductivity nature of the wire.

The material also showed zero bias photocurrent i.e. even if bias was not applied across the NW device, it produced current only by illuminating with light. Fig. 6.7 represents the photo-response of

the array of NWs at zero bias, taken at a wavelength $\lambda = 405$nm at different incident powers using a mechanical chopper (frequency 130 Hz). In zero bias, the dark current was below the instrumental limit of detection which is 0.5 pA. Thus, we may consider dark current $I_d < 0.5$ pA. As can be seen in Fig. 6.7, the current under illumination $I_{ill} \approx 8$ nA at an illumination power density $p_{opt} = 6.6 \times 10^6$ W/m^2. Thus, at zero bias, photocurrent gain $(I_{ill} - I_d)/I_d$ is at least $\sim 10^4$. This gain is much higher than the gain obtained in thin film of Cu:TCNQ NW [43]. There is no persistent photo-current as the dark current is fully recovered when the illumination is turned off. The photoresponse time shown in Fig. 6.7 is limited by the speed of the mechanical chopper. The absence of any reported zero bias response in Cu:TCNQ films is likely due to much larger electrode separation than the carrier recombination length.

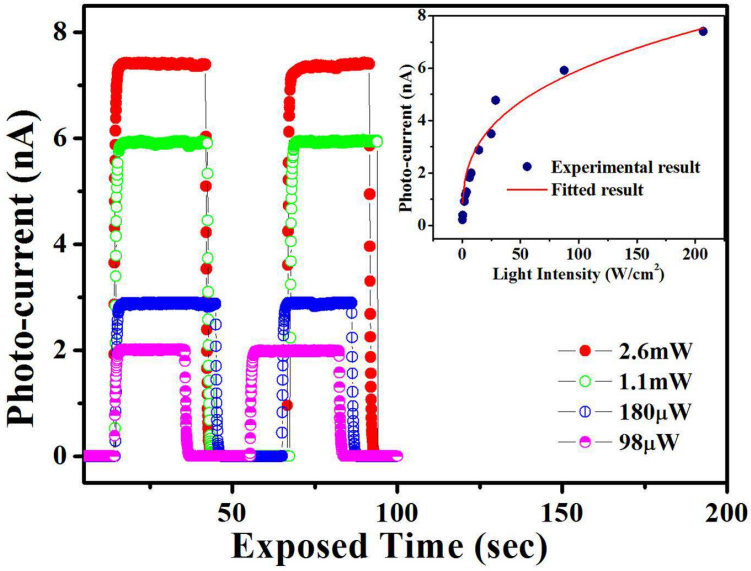

Figure 6.7 Reversible zero bias photoresponse $I_{Ph}(V = 0)$ of Cu:TCNQ nanobridge device under an illumination at wavelength 405 nm with varying power density. Inset shows dependence of zero bias photocurrent on the incident optical power density P_{opt}.

The zero bias photo-current $I_{Ph}(V = 0)$ increases with the incident optical power density P_{opt} as shown in the inset of Fig. 6.7. It was found to have dependence of photocurrent on optical power as

$$I_{Ph}(V = 0) \propto P_{opt}^{\gamma} \tag{6.5}$$

From the fit, we find $\gamma \approx 0.15$. The exponent γ depends on the process of electron-hole generation under illumination, trapping, and recombination of the carriers within the NW array [139]. The fractional exponent γ has been observed in a number of crystalline as well as amorphous photoconductors [120,

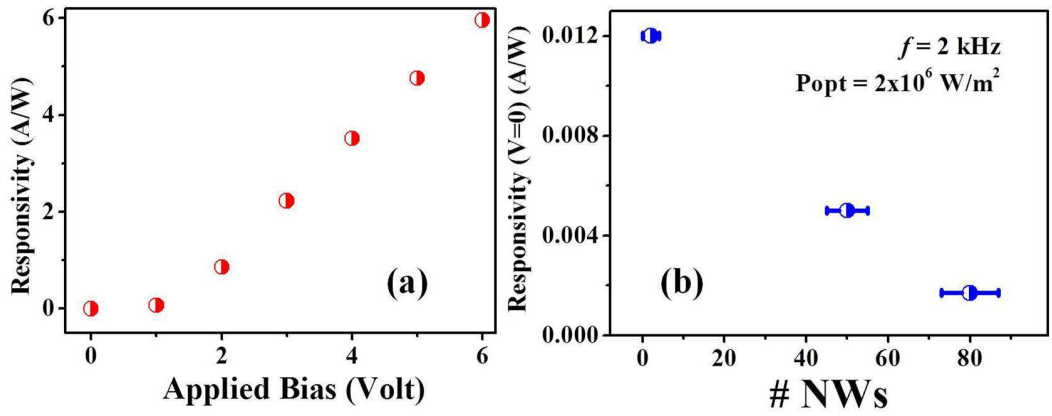

Figure 6.8 (a) Responsivity as a function of applied bias and (b)Zero bias responsivity as a function of no. of illuminated NWs bridging the electrodes.

139]. It has been explained due to existence of localized traps near the band edges that controls the process of recombination and the resulting in photocurrent [139]. The value of γ depends on the energy distribution of the localized states. In a specific model [139] for localized states near the conduction band edge (E_c), if they are distributed with an exponential dependence so that the density of states is given as $g(E) = g(E_c)e^{\frac{E-E_c}{E_1}}$, where $g(E)$ and $g(E_c)$ are densities of states at energies E and E_c, respectively, and E_1 is a characteristic energy scale, the exponent $\gamma \approx \frac{E_1}{E_1+k_\beta T}$. From the observed value of γ; we find $E_1 \approx 4.6$ meV, which is more or less same as our fitted result $\phi_1 \approx 5$ meV.

The responsivity, $\Re$ as defined in equation (4.4), depends on NWs' potoresponsive nature as well as P_{sample}, where P_{sample} is the power absorbed by the NWs of the array. We assume that all the power falling on the surface of the NW array is absorbed so that the total power $P_{sample} = P_{opt}AN$, N being the number of the NW in a particular device and A is the average area of each NW. This underestimates the responsivity because not all the power incident on the NWs is absorbed. Due to sub-linear dependence of the photo-current on the optical power (see Eq. 4.5), the zero bias responsivity $\Re(V = 0)$ was found to be decreased with increasing illumination power. $\Re(V = 0)$ at low power ($P_{opt} = 7.8 \times 10^4$ W/m^2) was 2.3 mA/W and it decreased to 0.3 mA/W at $P_{opt} = 2.0 \times 10^6$ W/m^2. However, application of bias enhances the responsivity $\Re$ significantly. At $V = 2.0$ V, $\Re = 1$ A/W. The variation of responsivity with bias is shown in Fig. 6.8(a). For bias $V > 2.0$ V, $\Re$ was found to have linear dependence on V and it reaches $\Re = 6$ A/W at 6.0 V. The device can be operated upto 10.0 V without damage. The variation of $\Re$ with number of NW was also stated in Fig. 6.8(b), where $\Re$ decreases linearly with increasing

number of NW of same length in a device due to increase in N as well as effective area A of NW. Although this linear dependence of $\Re$ on NW number is an over estimation due to limited no. of data points.

Thus, respossivity can be increased by decreasing the no. of NW along with radius, which reduces the power falling on the sample. Another way to increase the responsivity is to reduce photo-generated carrier transit time τ_t (see Eqn. 6.3). This can be possible by the reduction of NW length or the distance between collection electrodes. In the next section, we will discuss the photoresponsive behaviour in a single NW of reduced length.

The fact that the responsivity increased significantly when one has a single NW (Fig. 6.8(b)), modified us to work on a single NW photo-detector.

6.4 Photoresponse in a single Cu:TCNQ nanowire

In the previous section, we have observed that charge transfer complex Cu:TCNQ NW exhibit photoresponsive behaviour irrespective of its electrical switching property. In this section, we will discuss opto-electronic results obtained from a single NW of Cu:TCNQ. These reports showed that it was possible to make photo devices based on a single NW, which can show substantial photo-response. One of the reported data on Si NW observed generation of substantial photocurrent even at zero applied bias [140]. This gives possibility of making a solar cell as well as unbiased photo detectors. In some of the inorganic NWs like ZnO [120], the reported resoponsivity, can reach a value of 10^5 A/Watt under an applied bias of 1.0 V. The high $\Re$ detectors ($\Re > 10^4$ A/Watt) for single photon detection are made using avalanche diodes [141], single NWs p-n junction type photodetectors [135] or from superconductive films [142]. In this paper we report a photodetector made from a single NWs of charge transfer complex Cu:TCNQ that can reach a responsivity 8×10^4 A/Watt, well in excess of 10^4 A/Watt, at a low bias of 1.0 V.

Four probe single NW device of diameter ~ 30 nm in Fig. 6.9(a) was fabricated using *top-down* approach as already discussed in *Chapter 3*. Opto-electronic measurement has been performed on this device in dark and under continuous illumination of wavelength $\lambda = 405$ nm as schematically represented in Fig. 6.9(b). Illuminated light of $\lambda = 405$ nm has been selected for measurements as the

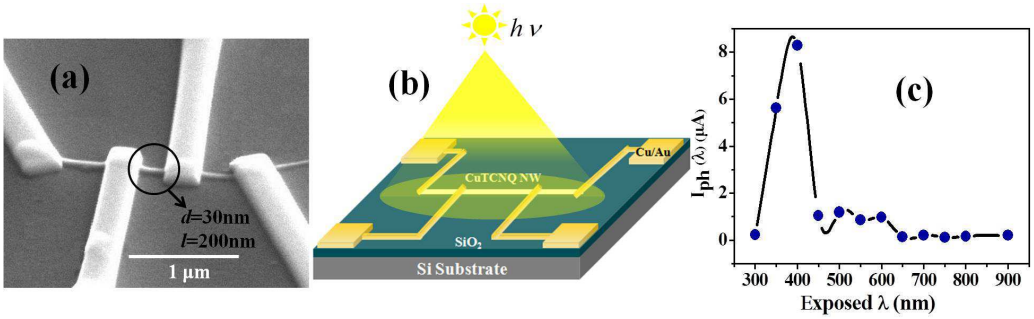

Figure 6.9 (a) SEM image of single nW device of diameter 30 nm and distance between two inner probe is $\sim$ 200 nm which determines the length of the NW used for opto-electronic measurement. (b) Schematic representation of illuminated sample. (c) Photocurrent (I_{ph}) spectral response of the single NW device kept at a constant bias of 0.5 V

material gives maximum response at this wavelength as shown in Fig. 6.9(c).

6.4.1 Spectral dependence

In Fig. 6.10(a) we have shown the photo-response of the device at zero bias $I_{ph}(v=0)$, taken at a wavelength $\lambda = 405$ nm at different incident powers ranging from 98μW to 2.6 mW using lock-in-amplifier as already described in experimental technique section in Chapter 3. Fig. 6.10(b) represents the photocurrent at different power density for constant chopper frequency of 2 kHz. The power density at the largest power corresponds to 2×10^6 W/m^2. At that illumination power density, the single NW device shows a large enhancement of the current to 120 nA. The dark current at zero bias was below the detection limit (0.5 pA) of lock-in-Amplifier. The enhancement of photo-current over dark is thus $\geq 1.2\times10^5$ as shown in inset of Fig. 6.10(b). For a constant illuminated power (2.6 mW) photocurrent increases with chopper frequency and saturates after 2 kHz as shown in Fig. 6.10(c). So, the zero bias measurement has been performed with constant chopper frequency of 2 kHz to get maximum response.

The zero bias photo current, $I_{ph}(V=0)$ with the optical power density P_{opt} as shown in Fig. 6.10(b) was found to have dependence $I_{ph}(V=0) \propto P_{opt}^{\gamma}$,where the exponent $\gamma \approx 0.3-0.4$ for a number of devices tested. Due to the sub-linear dependence of $I_{ph}(V=0)$ on optical power density P_{opt},$\Re(V=0)$ decreases as P_{opt} increases. In general, the power dependence of the photo-current depends on the distribution of trap states around the Fermi level (E_F). For systems with traps distributed uniformly with energy around the E_F, $\gamma \approx 1$ [139]. However, for many photoconductors (in bulk form) $\gamma \approx 1-0.5$

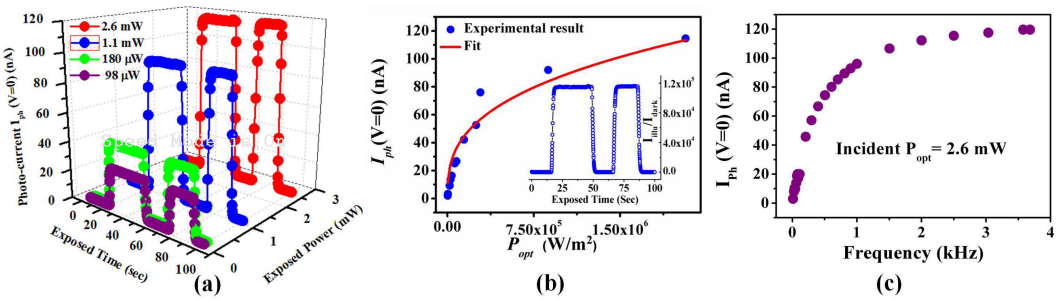

Figure 6.10 (a) Reversible zero bias photoresponse $I_{Ph}(V=0)$ of Cu:TCNQ single device under an illumination at wavelength 405 nm with varying power density. (b) Dependence of $I_{Ph}(V=0)$ on the incident optical power density P_{opt}. (Inset) Ratio of illuminated current over dark showing current gain at zero bias is $\sim 10^5$. (c) Chopper frequency dependence of $I_{Ph}(V=0)$

showing a non-uniform distribution of trap states around E_F [133]. In NW arrays as well as single NW [118, 143], the typical exponent was found to be $\gamma \approx 0.3-0.5$. It thus appears that in NWs the traps have a broad distribution of energy around E_F. The large carrier generation rate in a confined volume is expected to increase the non-geminate recombination cross-section and reduce γ.

6.4.2 Zero bias photoresponse

For the device under test (DUT), the NW has a diameter $d = 30$ nm, with the length l between electrodes used for optoelectronic measurement ≈ 200 nm. Assuming the NW absorbs all around and over the whole length l between the electrodes, an optical power density of $P_{opt} = 1$ W/m^2 corresponds to 1.9×10^{-14} W absorbed by the sample (P_{sample}) between two electrodes. Since the absolute value of the absorbance is not known this is the maximum power absorbed by the sample. The value of P_{sample} is thus an overestimation. For $P_{opt} = 2 \times 10^6$ W/m^2 the responsivity at zero bias $\Re(V=0) \equiv \dfrac{I_{Ph}(V=0)}{P_{sample}} \approx 3$ AW^{-1}. The above estimate of the $\Re(V=0)$ is made with the assumption that all the optical power that falls on the wire is absorbed. As pointed out before this overestimates the value of sample P_{sample} and thus is a lower bound on $\Re(V=0)$. This is more than that seen in GaN NW [144] [$\Re(V=0)0.1$ AW^{-1}] that shows one of the highest recorded zero bias responsivity and much higher than that seen in Si single NW [140] [$\Re(V=0)0.6$ mAW^{-1}].

6.4.3 Bias dependent photoresponse

Application of bias enhances the responsivity $\Re$ significantly. The $I-V$ data on the device in dark and under continuous illumination ($P_{sample} \leq 1.24\times10^{-7}$ Watt, $\lambda = 405$ nm) is shown in Fig. 6.11. The measured $\Re(V) \approx 8\times10^{4}(4\times10^{3})$ AW^{-1} for an applied bias of $V = 1$V (-1V) which is due to photoresponsive behaviour of Cu:TCNQ as well as reduction in barrier height at the metal-NW interface as obtained from MSM fit.

The observed ultra large responsivity of Cu:TCNQ NWs based MSM device can arise from contributions of three factors elaborated below. Two of these factors depend on the photoconductive response of the NW and the third on the MSM device configuration. Semiconductor NWs with diameter < 100 nm generally show very large photoconductive gain,G [134] already defined earlier as $G \equiv \frac{I_{Ph}}{qF}$, I_{Ph} is the photo-current generated due to absorbed photon flux F. As from equation (4.3) G also depends on carrier life time τ and photon transit time τ_t through the device. Large $G \gg 1$ can occur due to one or more of the following reasons. Existence of surface states lead to formation of depletion region near the surface that gives rise to built-in field which effectively breaks the photo generated electron-hole pair. The strong lateral field can trap the holes (for n-type conductors), thus prolonging the photocarrier (electron) life time (τ). Secondly, close proximity of the electrodes can reduce the carrier transit time (τ_t) leading to large enhancement of the photoconductive gain G. Since, G is directly related to $\Re$ (from equation (4.3) and (4.4)), increase in G increases responsivity, $\Re$ of a device. The reduction of the device length scale by reducing electrode separation ($\sim$ 200 nm) is thus one of the causes that enhance $\Re$.

In addition to the above, a third and rather effective way to enhance gain in the device under consideration originates because it is configured as a MSM device. In MSM devices the Schottky barriers at the junctions can get reduced by the photo-generated carriers [137, 145]. This causes a large enhancement of the photo-current I_{Ph}, which in turn leads to a large enhancement of $\Re$. For the device used here, under illumination, the barrier height is reduced ~ 0.1eV and resistance changes from 1.0kΩ to 0.03 kΩ as shown in Table 6.1. Reduction in barrier height and resistance are obtained after fitting the $I-V$ curves in dark and under illumination (Fig. 6.11) using Eqn. (6.1) under the framework of model of back-to-back Schottky diode that is used to model MSM devices [138]. Fitted

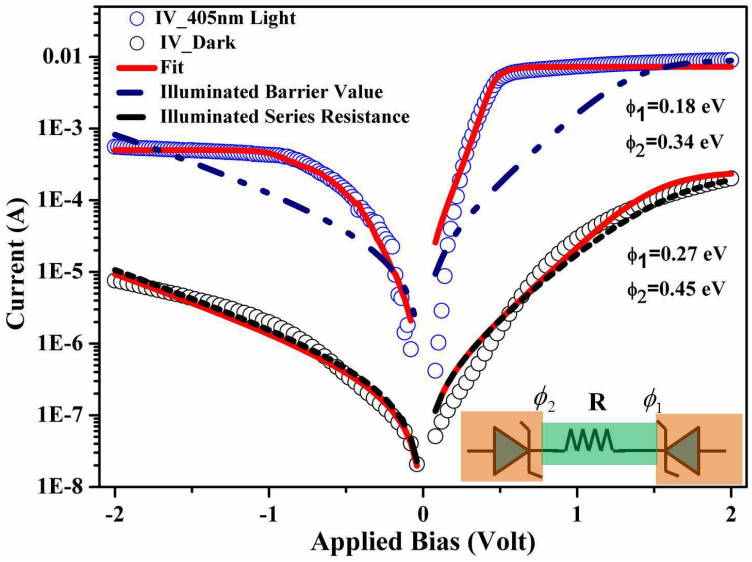

Figure 6.11 $I-V$ curves in dark (black circle) and under illumination (blue circle) of a single Cu:TCNQ NW MSM device. Wavelength of illumination is 405 nm. Solid red curve is fit to the MSM model. The dashed-dotted curve and dashed curve are calculated $I-V$ curves using the same MSM model with (i) dark value of series resistance but barrier height values with illumination and (ii) illuminated value of the series resistance value but dark barrier values respectively. (inset) Schematic of MSM model.

curves are shown in Fig. 6.11 (red line). All the fit parameters for both the dark and under illumination are tabulated in Table 6.1. The suppression of the series resistance R is due to the photoconductivity in the NW between the two contacts. Thus, large enhancement of the device current is a combined contribution of both barrier height reduction and photoconductivity in the NW. It is observed (Table 6.1) that on illumination, the barrier heights change to lower value, $\phi_1 \approx 0.18$ eV and $\phi_2 \approx 0.34$eV and the resistance of the NWs reduces to R = 0.03 kΩ. Both the barrier heights are thus reduced by nearly the same amount of $\Delta\phi \approx 0.1$ eV on illumination.

Table 6.1 MSM fitted parameters of $I-V$ in Dark and under illumination

Conditions	ϕ_1 **(eV)**	ϕ_2 **(eV)**	**R (kΩ)**
Dark	0.27	0.45	1.0
Illuminated	0.18	0.34	0.3

An estimation of the lowering of barrier height due to photo-generated carriers is given below. The photosensitivity, S which is defined as $S = \frac{(\sigma_{ph} - \sigma_{dark})}{\sigma_{dark}}$, where σ_{ph} is the conductivity under

illumination and σ_{dark} is that in dark. We have calculated in NW, S is ≈ 33. Considering that the change in the conductivity due to the illumination ($\Delta\sigma = \sigma_{ph} - \sigma_{dark}$) of the NW is solely due to the change in the carrier density (Δn), without any change in mobility, we can get a measure of the change in carrier density $\frac{\Delta n}{n_0} \approx 33$ under illumination. This change in the carrier concentration Δn would lead to a change in the chemical potential which will lower the Schottky barrier [142]. The lowering of the Schottky barrier would thus be $\Delta\phi \approx \frac{k_\beta T}{q} ln\left(\frac{n_0+\Delta n}{n_0}\right)$. Using $\frac{\Delta n}{n_0} \approx 33$, at room temperature, we obtain $\Delta\phi \approx 0.09$ eV. This is very close to the actual lowering observed in both the barriers ($\Delta\phi_1 \approx 0.09$ eV and $\Delta\phi_2 \approx 0.11$). This is clear evidence that the photo-carriers generated by illumination in the NW reach the junction region and lower the barriers.

In a MSM device, the photocurrent through the device depends on the light induced barrier reduction in the contact region [137]. It had been shown that in MSM type devices made on NWs, one can obtain lowering of barrier, if large number of carriers are created or diffuse into the contact region due to illumination [138, 124]. Control of contact barrier by electrical gate controlled charge injection has been recently utilized in Si NW devices [146]. Lowering of interfacial barriers on illumination at the metal-semiconductor junction in polymer field effect transistors, have been investigated using optical excitation directed in the electrode region without optically perturbing the channel [147]. Even charge generated in piezo-electric ZnO NW was found to lower the barrier [145]. The analysis of the $I-V$ data presented above shows substantial lowering of barriers at the two M-contacts under illumination. The extra carriers generated optically, that lead to photoconduction enhancement, however, diffuse to the barrier region leading to lowering of the Schottky barrier. A recent experiment on CdS NW MSM device, using near-field scanning microscope and localized excitation, has shown that such indeed is the case that most of the photo-response arises at the reverse biased MS junction [146, 148] which leads our experimental results. Table 6.2 pointed out the responsivity value for different NW devices under comparable bias and compared with the responsivity of single Cu:TCNQ NW device.

From parameters of different devices in Table 6.2 it is clear that excluding photoresponsive property of the material, reduced diameter also enhances the responsivity of a NW device.

Table 6.2 Comparative study of photo-responsivity for different NWs

NW/NWs	**Diameter (nm)**	**Responsivity (A/W^{-1})**	**Bias (V)**	Ref
ZnS	200	0.12	5	[149]
InP	200	0.3	5	[150]
In_2Se_3	80	89	3	[151]
V_2O_5	100	482	1	[152]
GaN	80	2×10^3	1	[144]
Si	80	$\sim 10^4$	1	[121]
ZnO	60	$\sim 10^5$	1	[120]
Cu:TCNQ	30	8×10^4	1	This work

6.5 Role of contact and contact modification on photo-response in Cu:TCNQ

We have observed Cu:TCNQ as photoresponsive material and discover a shorter length single NW as ultra large responsivity photodetector. Irrespective of the material property, we will now discuss the role of contact on photo-response and how one can modify the contact to increase the response further. For that we have taken a single NW device, which is combination of Ohmic and Schottky contact, made by *bottom-up* approach and measured current in dark and under illumination. After modification of Schottky contact, measurement has been performed again to figure out the role of contact in photo-response. Fig. 6.12 shows the SEM image of the device before and after modification of the contact stated as $S-1$ and $S-2$ respectively.

The $I-V$ data in dark as shown in Fig. 6.13 is for the device before and after modification of the blocking contact. Growth end of the NW acts as Ohmic contact and free end of the NW touching the other Au electrode acts as Schottky type. It has been observed that after anchoring (capping the Cu:TCNQ/Au contact with FEB deposited Pt) there is an enhancement of the device current. This enhancement mainly arises from the reduction of the barrier height at the blocking contact as the analysis shown below. The $I-V$ data is analyzed in the frame work of MSM configuration where the Cu and the Au electrodes connecting the NW act as the metal (M) electrodes and Cu:TCNQ NW is the semiconductor. The bias dependent current through the device is fitted to the model of two back to back

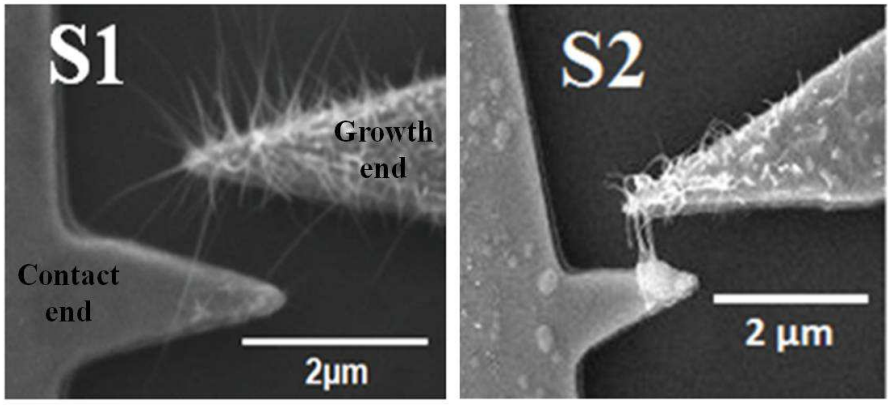

Figure 6.12 SEM images of (a)as synthesized single NW device of diameter $\sim$ 30 nm and length $\sim 1\mu$m (restricted by inter electrode spacing) having one contact Ohmic and other Schottky type, and (b) after Schottky contact modification by FEB deposited Pt

Schottky diodes (Egn. (6.1)) connected by a series resistance R, which mainly represents the resistance due to the portion of the NW between the electrodes. As shown in Fig. 6.13, ϕ_1 and ϕ_2 are the barrier heights associated with Ohmic and Schottky contact respectively when Ohmic contact is in positive bias, R is resistance of the NW. Fitted parameters sre tabulated below: Solid lines through the data in

Table 6.3 MSM fitted parameters of $I-V$ in dark before and after contact modification

Conditions	ϕ_1 **(meV)**	ϕ_2 **(meV)**	**R (kΩ)**
Pre-anchoring	27	200	5.0
Post-anchoring	26	180	6.0

Fig. 6.13 show the fit to the $I-V$ curves. As a validation of the model we find that the value of R obtained from the model fit is close to the value calculated from the independently measured 4-probe resistivity of the NW. Low enough value of ϕ_1 ($\phi_1 \approx 27$ meV) at room temperature indicated the contact is Ohmic, whereas ϕ_2 is quite higher ($\phi_2 \approx 200$ meV) as the NW just touches the surface of Au electrodes and act as Schottky type contact. Asymmetric $I-V$ is due to difference in barrier height at two contact ends of the NW. This asymmetry in $I-V$ reduces after anchoring the free end of the NW with FEB deposited Pt, which is due to blocking contact barrier height reduction ($\phi_2 \approx 180$ meV) after contact modification as shown in table 6.3. The resistance of the NW R changes somewhat during the capping process and increases by 20 % (6.0 kΩ).

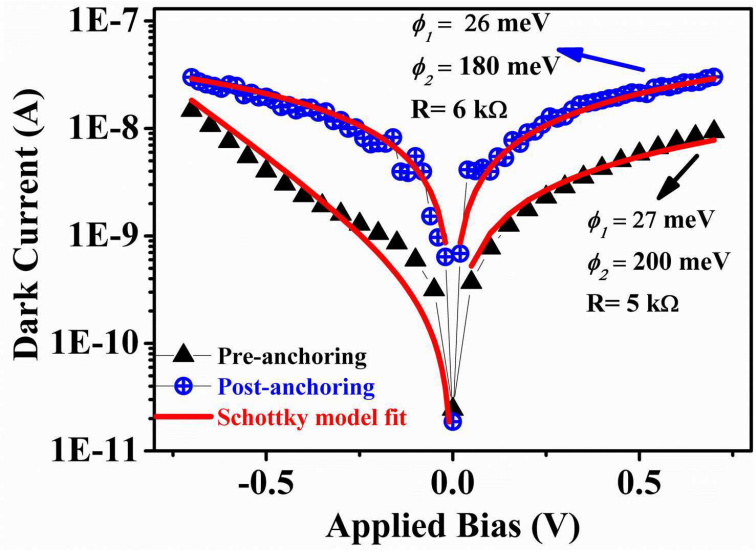

Figure 6.13 $I-V$ of single NW device in dark before (triangle) and after (circle) contact modification.

The effect of the contact and the contact modification on the photoresponse was investigated. In Fig. 6.14(a), we show the results of measurement of the photoresponse for zero bias (applied bias $V=0$). The zero bias photoresponse, which is dominated by contact barriers, is enhanced significantly in device $S2$ due to the capping by Pt. Photocurrent as a function of bias for both the cases (pre and post anchored) is shown in Fig. 6.14(b). The current shown is the total device current measured, which under illumination is marked as I_{ill} while that under dark is the dark current I_{dark}. (The bias dependence of the of the ratio I_{ill}/I_{dark} is shown in inset of Fig. 6.14(b) for the two devices.) The photocurrent $I_{Ph}(V)$ at an applied bias V is defined as difference of the current under illumination I_{ill} and the dark current I_{dark} at a given bias ($I_{Ph} \equiv I_{ill} - I_{dark}$). There is no external field at zero bias and photogenerated carriers reach the electrodes without any recombination. This is possibly because of the close proximity of the electrodes $\sim 1\mu$m, which is smaller than or of the order of the typical recombination length in such materials.

The enhancement of the photocurrent after the barrier modification mainly occurs at the low bias as one can see in Fig. 6.14. This is expected because at higher bias the device current is restricted by the wire resistance due to finite voltage drop across it. In the low bias region, the device current is mainly junction limited being controlled by the barrier height. This can also be seen in the inset of Fig. 6.14(b), where we plot the ratio I_{ill}/I_{dark} as a function of the bias. It can be seen that at higher bias ($|V| \geq 0.5$

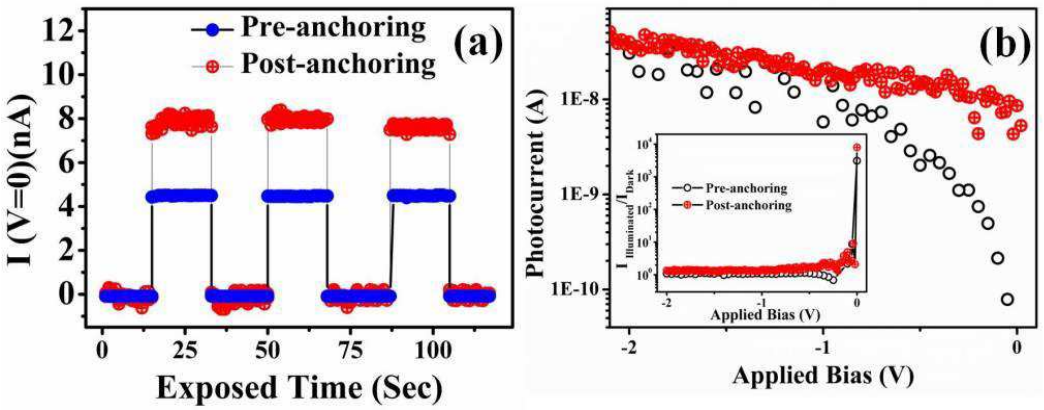

Figure 6.14 (a) Zero bias photocurrent (applied bias $V = 0$) of the NW devices before (solid circle) and after (plus circle) Schottky contact modification. (b) Bias dependence of the photo current $I_{Ph} = I_{ill} - I_{dark}$ as a function of reverse bias. The inset shows the bias dependence of the ratio I_{ill}/I_{dark}. (Wavelength of illuminated light, $\lambda = 405$ nm)

V) the effect of barrier modification shrink down as effect of the illumination also diminishes.

From the measured $I-V$ curve under illumination, using Eqn. (4.1), we could deduce the barrier height modifications produced by the illumination. Both the barrier heights change to lower values. For instance for device $S1$,$\phi_1 \approx 20$ meV and $\phi_2 \approx 160$ meV and the resistance of the NWs reduces to R=0.9kΩ under illumination. The change in barrier heights on illumination are $\Delta\phi_1 \approx 7$ meV and $\Delta\phi_2 \approx 40$ meV with a reduction in resistance by a factor of $1/5$ due to photoconductivity. The photosensitivity S can be evaluated from the change in resistance and for the device $S1$, $S = 4.6$. After modification of contact, in $S2$, the barrier height $\phi_2 \approx 130$ meV under illumination, corresponding to a change of $\Delta\phi_2 \approx 50$ meV. The change in $\Delta\phi_1$ meV is similar to that in $S1$. Under illumination in $S2$ NW resistance reduces from R=6.0kΩ to R=0.5kΩ leading to a photosensitivity $S = 11$.

The enhancement of the total photocurrent in the single NWs MSM device has contributions of illumination-induced reduction of the barrier at the junction, as well as photoconductive reduction of the series resistance of the wire which gives us a measure of the photosensitivity S. In the present device the lowering of the barrier at the contact under illumination is a major reason for the photo response, which in turn accentuates the effect of the photoconductivity. As a result the barrier modification leads to a change in current in the device. Importantly, the barrier modification has a large effect on the zero bias photocurrent $I_{Ph}(V = 0)$ as can be seen from Fig. 6.14(a). The enhancement of the photo current can be nearly 2 orders for $V = 0$. The change in the photoconductivity being much less, it

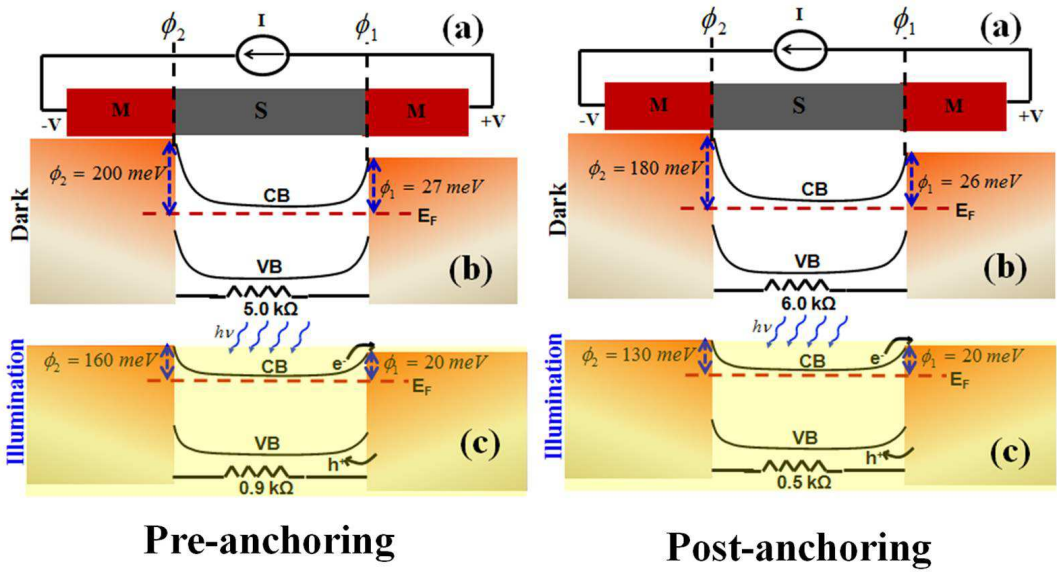

Figure 6.15 Comparative study of the parameters for NW MSM devices before (left) and after (right) Pt deposition: (a) Schematic structure with barrier heights derived from model with illumination and in dark; (b) Band bending of the conduction band in dark and (c) Band bending under illumination. Relevant barrier heights as well as the resistances of the strand of the NWs for the two devices are shown as derived from the model in dark and under illumination.

is the modification of the contact by the FEB deposited Pt which causes this large change. All the measurements are done at low bias so that the NW is under safe region of electric field below the phase change threshold during the measurements [23]. The lowering of barrier on illumination occurs due to diffusion of photo-generated carrier into the contact region. We have calculated change in barrier height, $\Delta\phi$ from change in carrier concentration under illumination $S = \frac{\Delta n}{n_0}$, for $S2$ which is 43 meV for $\Delta\phi_1$ and 62 meV $\Delta\phi_2$. This is somewhat larger but close to the observed change of $\Delta\phi_2 \approx 50$ meV. The Cu contact being Ohmic with a low enough barrier, there is a negligible change in the barrier height.

In both the devices studied we find clear signature of photocurrent at zero bias that is substantially larger than the dark current and the current critically depends on the barrier height and the nature of the contact. The observation of zero bias current in both the devices ($S1$ and $S2$) points to a common origin. The existence of such a current depends on the field due to the built-in potential that exists near the contacts. If the electrode separation is more than the depletion width, there will be no axial field in the middle of the NW in absence of an applied bias. In this case the photo-generated carriers will not reach the electrodes. However, in our case the electrode separation being small it is likely that it is

less than the total of depletion widths at the contact regions. This will give rise to a built-in field which will collect the carriers. If the two junctions are symmetrical then the net current at zero bias will be zero. However, existence of asymmetric junctions at the two ends will ensure a non-zero net current. Another mechanism that also contributes to the transport of photo-generated carriers in MSM junction is tunnelling through the barrier at the junction [153]. This is prevalent when the photon energy $h\nu$ is much greater than the barrier height ϕ, which is adequately satisfied in our case. Existence of such a tunneling of the photo-electron at the junction can thus be another source of the photocurrent at zero bias. The nature of the contact is thus a critical parameter for collection of charge and results in a zero bias current. It is then justified that the barrier modification by FEB deposited Pt that modifies the barrier height will affect this process. The barrier height reduction due to the capping of the contact will thus enhance the photo current. The physical process that leads to the dominant role of the contact and the contact modification can be best summarized by the schematic band diagram shown in Fig. 6.15. The figure shows the barriers, the depletion regions, changes in these parameters in dark and under illumination in both the devices that lead to the changed response on modification of the contact.

6.6 Conclusion

In summary, we have reported bias dependent as well as zero bias photoresponse in an array of Cu:TCNQ NWs fabricated as nanobridge devices. Photoresponse is enhanced in a single NW with shorted length (200nm) reaching a responsivity value of $\sim 10^5$ A/W with the enhancement of zero bias photocurrent over dark current is $\geq 10^5$. Bias dependent current in dark and under illumination is fitted with MSM Schottky diode model. Enhancement of current under illumination is explained under light induced carrier generation in the NW and reduction of barrier height at the MS junction. Role of contact and contact modification on photo-response in Cu:TCNQ NW has also been discussed.

Chapter 7

Summary and Concluding remarks

In this final chapter, we summarize important observations of this thesis work and discuss the scope for future investigations. We have spent lot of time in developing high vacuum evaporation chamber for *insitu* NW synthesis, experimental techniques such as e-beam lithography, electric field assisted direct growth between pre-fabricated electrodes, controlled growth of thinner diameter NW (as small as 10 nm) and were extensively used during the work. Important observation during this thesis work is pointed out bellow:

7.1 Growth

◯ We have synthesized Cu:TCNQ NW both by physical vapour deposition and chemical methods. NWs are also grown within prefabricated electrodes, whose specing defines the length of the NWs. Nanowire diameter were also controlled by evaporation rate of TCNQ, thickness and temperature of Cu film during growth. We have grown NW of diameter ranging from 10 nm to $>$ 100 nm. Even we are able to grow successfully a NW of diameter 10 nm and length 200 nm.

◯ We also observed the effect of electric field on NW diameter applied between two electrodes during growth. The NW diameter decreases with increasing field and the possible reason for it has been investigated by COMSOL Multiphysics simulation. It has been found that NW growth under field is a balance of two forces (electrostatic and dielectrophoretic force).

◯ As grown NWs are characterizes by X-RD, SEM, TEM, FTIR, and Raman spectroscopy. Nanowires

are found to be Phase-I (tetragonal) and Phase-II (monoclinic) in crystal structure. Charge transfer between Cu and TCNQ was (50 - 60)% which is enhanced to 81 % by transferring extra charge from graphitic oxide to Cu:TCNQ. All the experiment performed in this thesis work are performed with Phase-I in crystal structure.

7.2 Electronic properties

◯ We have investigated the temperature and bias dependent electrical transport properties of array as well as single NW of Cu:TCNQ, laterally connecting two electrodes ($\sim 1\mu$m gap) with and without the presence of external electric field applied between the electrodes during growth. We have found that application of the electric field during vapor phase growth can be a very viable tool to enhance/modify the conductivity of NWs. The electrical conductance of the NWs (measured) down to 40K shows a strong non-linear conductance which has a well defined threshold for T$\leq$ 100K. The non-linear conductance was found to follow a modified Zener tunneling model proposed for CDW transport. Such an observation was not made before and opens up the possibility of new investigation of CDW in this system.

◯ The application of the field during growth enhances significantly the linear as well as non-linear part of the conductance of NWs grown in presence of field. Zero field grown NW have conductance is in insulating regime, but field grown NWs reach conductance value close to the insulator-metal transition boundary (G = $\frac{h}{e^2}$).

◯ We proposed a scenario for the field growth condition where the applied field helps diffusion of Cu ions from Cu to the growing face leading to enhanced charge transfer leading to enhanced linear conductivity. The field applied during growth has been proposed to improve the stacking of the TCNQ moiety leading to enhancement of conductance and also change in parameters of the non-linear conduction. Though the experiment has been done in context of a charge transfer complex NW, the concept may have applicability in growth of other semiconducting NWs also.

◯ We have presented a phenomenological model that explains the experimental results of resistive switching and performed numerical analysis to build a model in evidence of our phenomenological consideration. Non-percolating metallic domains such as dopants, vacancies at edges of Cu:TCNQ,

metallic clusters, or metallic filaments sandwiched between NW and metal electrodes formed metallic channel at voltage greater than threshold voltage and bring the system from high to low resistive state. At reduced bias, thermal agitation disrupt the metallic channel and bring back the system to its high resistive state.

◯ This model may provide useful guidance in this active and promising area of research. The model proposed is based on two aspects: (a) the switching phenomena is predominantly controlled by the change at the contact which we establish through a simple MSM type device model and (b) the transport through the contact region as well as through the body of the NW is localized in nature controlled by hopping/tunneling type process. We obtain semiquantitative agreement with the experimental data

7.3 Opto-electronic properties

◯ For the first time, we have observed that the charge transfer complex material which is mainly known for its electrical switching property also show good optoelectronic property. We have measured $I-V$ on array and single NW of Cu:TCNQ in dark and under illumination and it shows excellent opto-electronic effect. Large amount of measurable photo-current can be achieved even without applying any bias.

◯ We got zero-bias responsivity of the order of few mA/W in NW arrays while around 3 A/W for single NW, which is the highest zero-bias responsivity till date. In the single NW device, we have achieved $\sim 10^5$ A/Watt responsivity for a applied bias of 1 volt, which is a good sign to use the device as single photon detector.

◯ This excellent opto-electronic effect is mainly due to photo generated carrier and reduction of barrier height due to illumination. It also depends on carrier life time and transit time through the device. Existence of surface states lead to formation of depletion region near the surface that gives rise to built-in field which effectively breaks the photo generated electron-hole pair. The strong lateral field can trap the holes (for n-type conductors), thus prolonging the photocarrier (electron) life time. Secondly, close proximity of the electrodes can reduce the carrier transit time leading to large enhancement of the photoconductive gain and consequently responsivity. Another effective way to

increase photoconductive gain is Metal-Semiconductor-Metal (MSM) type devices where a Schottky barrier at the junction can get reduced by the photo-generated carriers leading to large enhancement of the photo-current.

◯ The present report of a very large photo-response, thus adds an opto-electronic element to the existing electronic switching property and raises the possibility of an opto-electronic control to a MEMRISTOR device. This is thus a unique property of a photodetector made from Cu:TCNQ NW.

7.4 Scope for future work

◯ In the NW fabrication front, it will be a great challenge to reduce diameter and length as small as possible so that quantum phenomena can be observed.

◯ Nature of channel formed during switching can be estimated by measuring resistivity of the NW before and after switching i.e. in high and low resistive state.

◯ Although we have proposed a phenomenological model with numerical analysis of metallic channel formation to explain unipolar switching, there is no experimental evidence of it. It will be a challenging work to grow NW in a electronically transparent membrane and observe the metallic channel in switched state under TEM.

◯ Photoconductive gain should be increased in lower diameter NW and for shorter length. To investigate the quantitative dependence of photocurrent on length and diameter of NW one can perform opto-electronic measurement on (a) NW with constant length and varying diameter and (b) constant diameter with varying length.

◯ Conductance of Cu:TCNQ can be increased by induced charge by using it as FET device. Also fractional amount of charge being transferred between Cu and TCNQ during growth, more charge can be transferred to Cu:TCNQ directly from a material of having higher ionization potential like GO. It will be a challenging work to enhance the conductance of Cu:TCNQ by induced charge as well as by direct transfer of charge to it as Cu:TCNQ is a charge transfer complex material.

◯ We have already been observed that Cu:TCNQ single NW acts as ultra-high responsivity material which is due to photo-responsive behavior of the material as well as illuminated barrier reduction. Our next target will be to separate out these two effect by NSOM (near-field scanning optical mi-

croscopy) in a single Cu:TCNQ NW. This will allow us for the surface inspection with high spatial, spectral and temporal resolving power.

◯ Although we have observed the presence of CDW (charge density wave) in Cu:TCNQ NW at low temperature, we need a details investigation on that. We will do further rigorous study on structural and electrical transport in Cu:TCNQ.

Appendix A

Effect of graphitic oxide on conductance of Cu:TCNQ

We have demonstrated a simple method to increase the conductance of Cu:TCNQ nanowire using graphitic oxide. Conductance of chemically grown Cu:TCNQ nanowire film is increased by ~ 10 *times, whereas enhancement in a PVD grown single NW is* $> 10^2$ *order. Increase in conductance is due to electronic charge transfer from graphitic oxide to Cu:TCNQ which is supported by FTIR spectra.*

A.1 Introduction

In last few years, chemically modified graphene (CMG) has been studied in the context of many applications such as polymer composites, energy-related materials, sensors, field-effect transistors (FET) and biomedical applications, due to its excellent electrical, mechanical, and thermal properties [154, 155]. Graphitic Oxide (GO) which is obtained by chemical oxidation of graphene, is electrically insulator due to their disrupted sp^2 bonding network. GO films are especially attractive because their aromatic conjugated domains and reactive functional groups allow the films to be modified by different functional organic and inorganic material via covalent or non-covalent bonding [156, 157]. Thus, it is possible to tune the structural, optical and electrical properties of GO according to the application needs. On the other hand, organic material 7,7,8,8-Tetracyanoquinodimethane (TCNQ) is an excellent electron acceptor with a wide diversity of electron donating materials like Cu, Ag to form

$Cu^{+}TCNQ^{-}$, $Ag^{+}TCNQ^{-}$ metal-organic compounds [8, 158].

Hsu et al [159] already used Graphene/TCNQ alternative multilayer sheet as conducting anodes for making solar cells where carrier density and mobility of the combined sheet increases. Flexible electronic and opto-electronic materials had been proposed by Zhang et al with reduced graphene oxide (rGO) sandwiched by a high density metal nanoparticles (Cu and Ag) combined with organic molecule of TCNQ [160]. But, there is no report on change in electrical property of Cu:TCNQ if this charge transfer complex material is induced by GO. In this report we have investigated a simple method to enhance the electrical conductance of Cu:TCNQ nanorod film and a single Cu:TCNQ nanowire by just applying a film of GO on Cu:TCNQ nanorod/nanowire surface. We show that charge transfer between GO and Cu:TCNQ take place which leads to change in the conductivity of Cu:TCNQ film.

A.2 Experimental results

Enhancement in conductance due to addition of GO is observed both in chemically synthesized nanorod film as well as PVD grown single nanowire of Cu:TCNQ. Experimental outcome of each case has been discussed below:

A.2.1 Enhancement in chemically grown Cu:TCNQ nanorod film

In this section, we have reported the effect of GO on conductance in chemically grown Cu:TCNQ nanorod film. Nanorod film was synthesized by dipping Cu coated film into homogeneous solution of TCNQ in acetonitrile. For controlled and selective growth of Cu:TCNQ complex, after deposition of Cu film on an insulating glass substrate, masking has been done on the Cu film, followed by Au deposition on top of masked Cu-coated substrate. This allow selective exposure of Cu film to react with TCNQ when immersed into the solution. Thus, inplane configuration of the fabricated device will be Cu-Au/Cu:TCNQ/Cu-Au as illustrated in step (5) of Fig. A.1. This device has been used to to measure I-V without GO. Au electrodes are then covered with insulating PMMA polymer resist to avoid direct contact of GO with electrodes, so that no current will pass through GO when it is dispersed on top of surface of Cu:TCNQ nanorod film as shown in step (7) of Fig. A.1. All the deposition and growth process is schematically illustrated in Fig. A.1. Device of the nanorod film is illustrated

schematically in Fig. A.2(a). Two interface regions of Au/Cu:TCNQ was covered with PMMA resist to avoid short circuit of GO with Au electrodes. SEM image of the device and magnified SEM image before and after GO deposition on film surface is shown in Fig. A.2(b). Electrical measurements

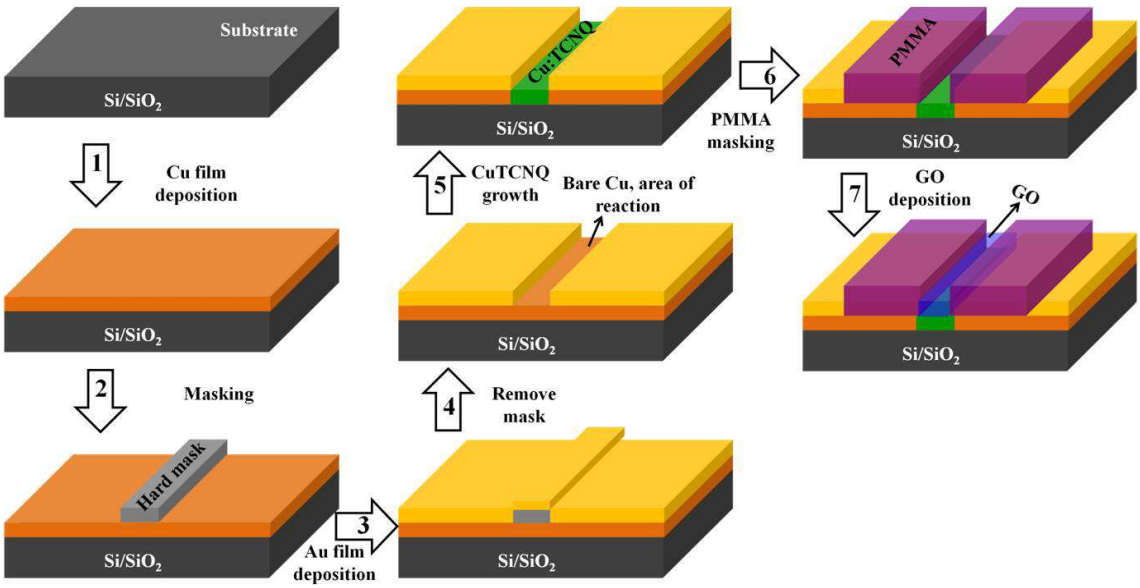

Figure A.1 Schematic representation of selective growth of Cu:TCNQ nanorod film and GO deposition by partial masking with PMMA.

were performed on Cu:TCNQ nanorod film using a source-meter with current resolution of 1 pA. Measurements were done to check that there were no substantial contributions from contact resistance. All the measurements were performed in dark and in ambient atmosphere at room temperature. As expected, excellent electrical properties were observed for the Cu:TCNQ nanorod films. We performed electrical I-V measurements on the film of organic charge transfer complex Cu:TCNQ nanorods with two different conditions: without and with GO deposition on nanorod film. Fig. A.2(c) represents the I-V of the device taken before (circle) and after (star) depositing GO. Almost linear I-V curves (see inset of Fig. A.2(c)) represent that the contacts (Cu/Au) are ohmic contacts. The figure clearly represents that due to deposition of GO conductivity of the device is increased by 10 times over Cu:TCNQ nanorods without GO. The extent of charge transfer can be controlled by controlling charge transfer on Cu:TCNQ and GO reduction which is explained elaborately in discussion section.

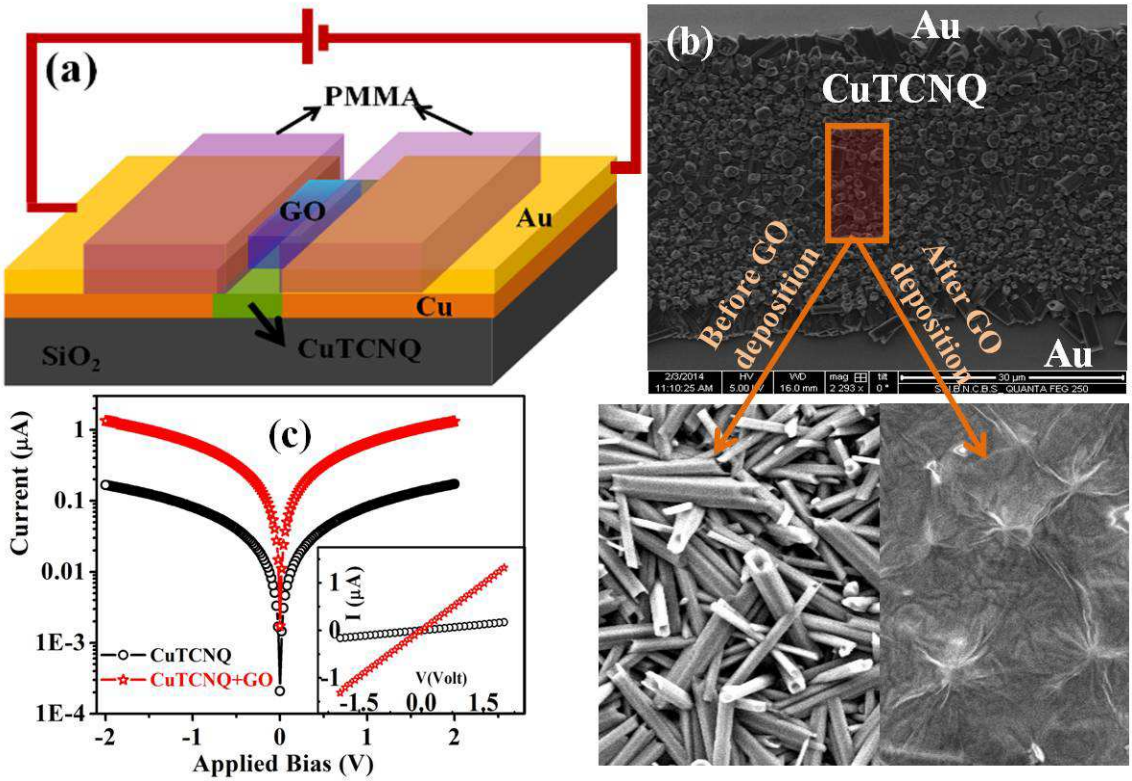

Figure A.2 (a) Schematic representation for chemically grown nanorod film device. PMMA covers the Au electrode from contact with GO. (b) SEM image of the device and magnified SEM image before and after GO deposition on film surface used for measurements. (c) I-V of chemically grown Cu:TCNQ nanorod film before (circles) and after (stars) GO deposition. Inset shows the corresponding linear plot.

A.2.2 Enhancement in PVD grown Cu:TCNQ single nanowire

The same experiments was done on single Cu:TCNQ nanowire device (D-2) connected with FEB deposited Pt (Fig. A.3). Electrical measurement has been performed on that device in dark without GO deposition on the surface of nanowire as shown in Fig. A.3(c) (circle). I-V has also been performed after deposition of GO on top of NW surface. Better way to selectively deposit GO on top surface of the NW is by covering the device with PMMA resist and removing the resist only from the NW surface region by e-beam exposure. But this process is not suitable for such a small dimension NW, as it need to go very high magnification during e-beam exposure. At such a high magnification range high energetic E-beam can destroy the metal-organic Cu:TCNQ NW, which hampers the selective deposition of GO on NW surface. And that is the reason why GO has been deposited on NW surface as well as contact electrodes without masking it (Fig. A.3(a)). In this configuration, to get the effect of

GO on NW conduction, one has to be confirmed that GO does not take place in conduction. Electrical measurement results before (circle) and after (star) GO deposition was shown in Fig. A.3(c). In this case enhancement in conductance is 3.3×10^2 i.e. two order higher compared to the normal nanowire conductance without GO. To confirm whether GO make any substantial contribution to conduction or not we have performed an experiment as discussed below.

A device has been made where nanorods are grown vertically on Au film. Electrical measurement has been performed on this vertical nanowire by conducting probe AFM (Atomic Force Microscopy) measurements as illustrated schematically in Fig. A.3(a). An SEM image of vertical nanorods grown by

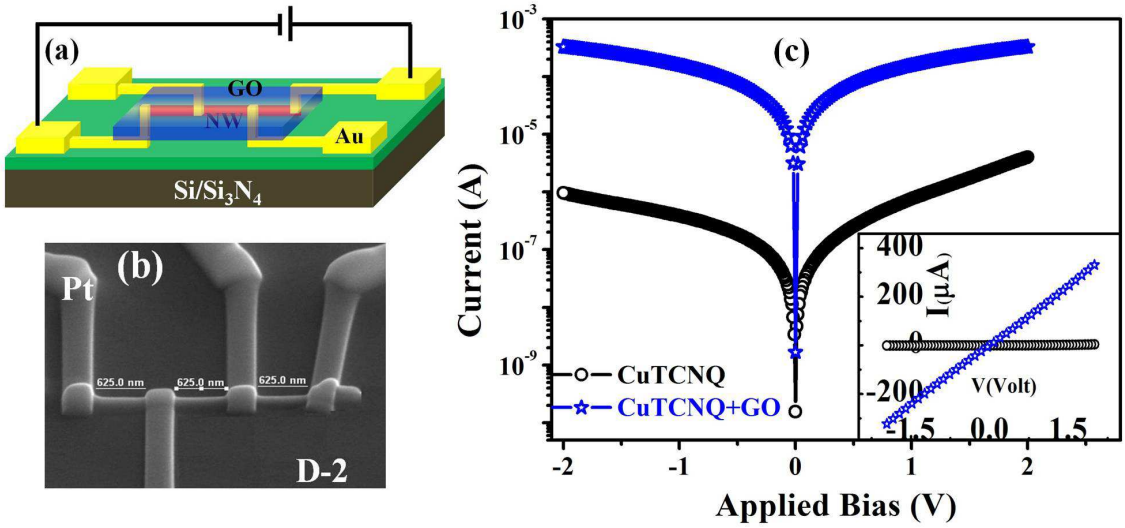

Figure A.3 (a) Schematic and (b) SEM image of the single nanowire device used for measurements. (c) I-V of PVD grown Single Cu:TCNQ nanowire before (circles) and after (stars) GO deposition. Inset shows the corresponding linear plot.

chemical method is shown in Fig. A.4(b), whereas inset of Inset of Fig. A.4(b) shows magnified image of such a vertical nanorods of $\sim 3\mu$m length and 600nm diameter used for measurements. Fig. A.4(c) also shows the AFM image of the nanorod. For conducting probe AFM measurement, Au film, the base of Cu:TCNQ nanorod is grounded and bias is applied on conducting Pt/Ir AFM tip (Fig. A.4(a)). The nanowire shows an excellent I-V curve as shown in Fig. A.4(d) as expected. After that, GO was dispersed on top surface of the nanorod and same electrical measurement has been performed after GO deposition. An AFM image of the nanorod after GO deposition is shown in inset of Fig. A.4(c). In this configuration AFM tip is now being in contact with the insulating GO, the tip is not receiving any signal from the NW as shown in inset of Fig. A.4(d). This experiment confirms that current couldn't follow

the path through GO film and all current is passing through the nanowire only. Thus, enhancement of current in single nanowire as shown in Fig. A.4(b) is due to addition of GO layer onto the surface of Cu:TCNQ.

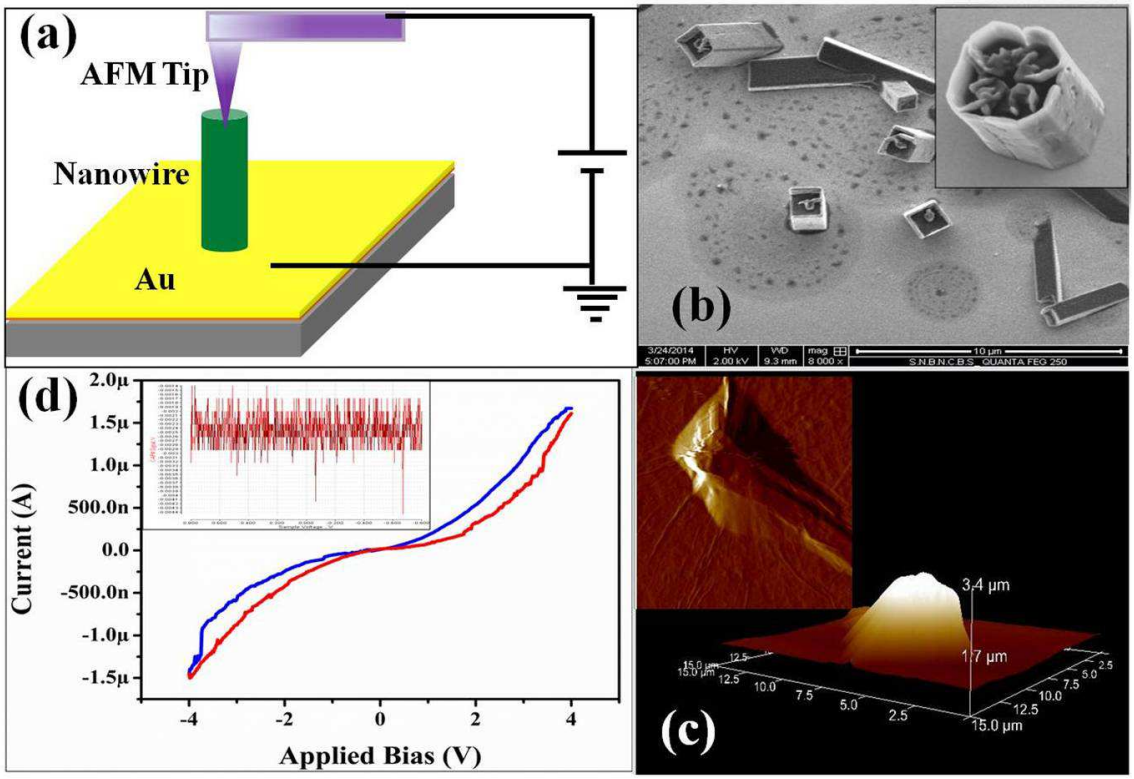

Figure A.4 (a) Schematic representation of a single nanowire conducting probe AFM measurement. (b) SEM image of vertically grown Cu:TCNQ chemical nanorods on Cu/Au film. Inset shows magnified image of one such nanorod. (c) AFM image of one chemical nanorod. Inset represents AFM image of the same nanorods after GO dispersion.

A.3 Discussion

The proposed explanation of the observed conductance enhancement is the charge transfer of electrons from GO to Cu:TCNQ. This explanation was validated by measuring the charge transfer that can be done using FTIR spectroscopic measurements. TCNQ is a well known electron acceptor material. Electron donor Cu reacts with TCNQ and transfers fractional amount of charge to TCNQ and forms Cu:TCNQ. It has been known that Cu:TCNQ or TCNQ is more electronegative than GO [157, 159]. When Cu:TCNQ forms it has partial charge transfer from Cu and there is scope for further charge

transfer. When GO is dispersed on Cu:TCNQ nanorods, electronegative TCNQ takes charge from GO.

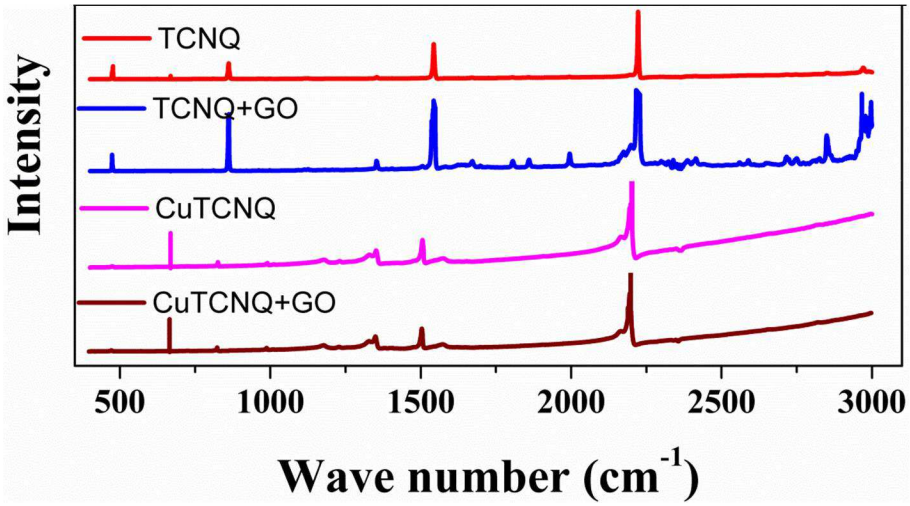

Figure A.5 FTIR spectroscopic results of TCNQ and Cu:TCNQ before and after addition of GO.

Fig. A.5 shows the FTIR spectra derived from different materials prepared with KBr as pellet material which is used as background, while TABLE A1 summarizes the data obtained from these experiments. Electronegative material TCNQ, where the cationic charge is fractional, distributed over an aromatic donor molecule and screened by the conduction electrons, has C≡N stretching band at 2228 cm^{-1} [161]. After reaction with Cu, C≡N stretching band is shifted to 2201 cm^{-1} confirming Cu:TCNQ formation. To calculate the degree of charge transfer (Z) in metal-TCNQ salts we have chosen nitrile stretching mode because that occurs at a frequency overlapping the strong electronic absorption in most conducting TCNQ salts. Amount of charge transferred from Cu to TCNQ is ~ 0.60 as calculated using reference of Chappell et. al. [11]. After depositing GO onto Cu:TCNQ nanorods

Table A.1 Degree of charge transfer from shift of C≡N stretching mode

Materials	C≡N stretching mode (cm^{-1})	Shift (cm^{-1})	Z
TCNQ	2228	-	-
TCNQ with GO	2220	8	0.16
Cu:TCNQ	2201	27	0.60
Cu:TCNQ with GO	2192	36	0.81

C≡N stretching mode is slightly shifted to 2192 cm^{-1} and corresponding degree of charge transfer for this shift is ~ 0.81. Thus, due to addition of GO, charge transferred to Cu:TCNQ is increased. The change in Z=0.21. This enhances its conductivity that is consistent with our experimental result shown in Fig. A.5. This enhancement in charge carrier concentration occurs due to transfer of electronic charge from GO to TCNQ as one can see from Fig. A.5, where C≡N stretching mode at 2228 cm^{-1} in neutral TCNQ is shifted to 2220 cm^{-1} when GO is added to it and corresponding degree of charge transfer is ~ 0.16 as stated in Table A.1. The degree of charge transfer (0.16) is thus comparable to the $\Delta Z \approx 0.21$, same for Cu:TCNQ case. Thus, shift in C≡N stretching mode due to addition of GO is same for TCNQ (2228 $cm^{-1} \rightarrow$ 2220 cm^{-1}) and Cu:TCNQ (2201 $cm^{-1} \rightarrow$ 2192 cm^{-1}) which confirms the charge transfer from GO to TCNQ for both cases.

A.4 Conclusion

We have demonstrated a simple method to increase the conductance of chemically grown Cu:TCNQ nanorod film as well as PVD grown single nanowire using graphitic oxide. Conductance of chemically Cu:TCNQ nanowire film is increased by ~ 10 times, whereas enhancement in a PVD grown single NW is $> 10^2$ order. This increase in conductance after addition of GO is due to charge transfer from GO to Cu:TCNQ film and hence increase of carrier concentration in Cu:TCNQ film which is confirmed from FTIR data. Amount of charge transfer from GO to Cu:TCNQ is approximately same as from GO to TCNQ. Thus, electrical conductance of Cu:TCNQ can be tuned by graphitic oxide even though GO is an insulator.

Appendix B

Charge induced conductance enhancement in single Cu:TCNQ nanowire

Field-effect transistors (FETs) based on organic semiconductors have been extensively investigated for the recent decade, in which realizing high-mobility, low-power, and fast-switching devices has been a central subject to take the best advantage of their simple and low-cost production processes. For this purpose, the material combination in the layered structure of organic FETs is being intensively studied because the interfacial phenomena are crucial in determining their device performances. Electronic transport, opto-electronic effect and switching phenomena observed in Cu:TCNQ nanowire has already been discussed. There are few other processes to tune or enhance the conductance in Cu:TCNQ nanowire by applying field during growth; applying threshold bias across the nanowire; or transferring charge from a donor material (Graphitic Oxide) with higher ionization energy to a compound with less ionization energy (Cu:TCNQ) etc. Cu:TCNQ nanowire conductance can also be enhanced by induced charge in the nanowire. These can be done by floating gate MOSFET (FG-MOSFET) and electric double layer FET. Experimental outcome from each process are described below:

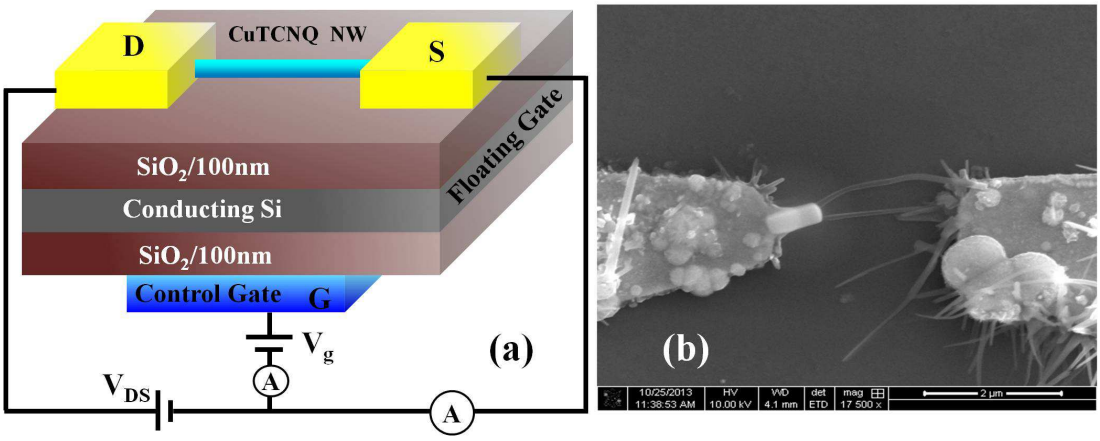

Figure B.1 Schematic of floating gate FET structure of a single nanowire. (b) SEM image of the single Cu:TCNQ nanowire device of diameter 70 nm used to measure floating gate FET effect.

B.1 Conductance enhancement by floating back gate MOSFET (FG-MOSFET)

We have used conducting Si sandwiched by two SiO_2 (100 nm thickness) layer as a floating gate. Here,insulating SiO_2 layer acts as gate dielectric layer. Cu:TCNQ nanowire device is made on one surface of the substrate containing the SiO_2 layer. Au deposited opposite to another surface of the substrate containing SiO_2 layer and used as control gate. Schematic of the device is shown in Fig. B.1(a). SEM image of the single nanowire device of diameter $\sim$ 70 nm used to make single nanowire FET is shown in Fig. B.1(b). Conducting Si used as floating gate is surrounded by insulating SiO_2 layer and being electrically isolated from the surrounding, charge induced in floating gate remains constant for a long time. Double dielectric layer also reduces leakage current through the device.

The transfer characteristic for a FG-MOSFET can be determined experimentally, keeping drain-source voltage, V_{DS} constant and measuring drain current, I_{DS} for various values of gate-source voltage, V_g. The transfer characteristic relates drain current (I_{DS}) response to the input gate-source driving voltage (V_g). Since the gate terminal is electrically isolated from the remaining terminals (drain, source, and nanowire), the gate current should be essentially zero, so that gate current is not part of device characteristics. The transfer characteristic curve can locate the gate voltage at which the transistor passes current and leaves the OFF-state. The characteristic curve plotted between gate-source voltage,

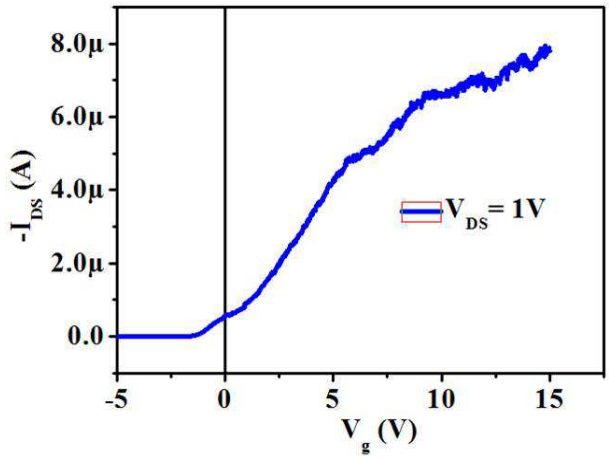

Figure B.2 Transfer characteristic of the FG-MOSFET single nanowire device.

V_g and drain current, I_{DS} for a constant $V_{DS} = 1$ Volt is illustrated in Fig. B.2. From the transfer characteristic curve, it is observed that current enhances for positive bias of gate-source voltage. So, we have measured current I_{DS} as a function of source-drain voltage V_{DS} through the device for different positive gate voltage. From the transfer characteristic curve, OFF-state current for the device is $\sim 0.5\mu$A. Output or drain characteristic curve i.e. I_D vs. V_{DS} for constant V_g which can be used either in enhancement mode or depletion mode are depicted in Fig. B.3(a). Thus, for a positive value of the gate-source voltage, current through the device increases as expected from transfer characteristic curve as can be seen in Fig. B.2. Whereas negative value of gate-source voltage depleted or reduced the drain-source current as shown by dotted curve in Fig. B.3. We have also plotted leakage current through the dielectric layer from source to gate in Fig. B.3(b) which is negligible compared to device current. This enhancement of current for positive gate bias is due to charge induced in the nanowire as illustrated schematically in Fig. B.3(c). When positive voltage is applied across the back control-gate, electrons will accumulate below the gate oxide layer. Due to capacitive effect, oxide layer will induce electron in conducting Si floating gate followed by hole induction in the oxide layer near the floating gate surface. This oxide layer also acts as dielectric and induces positive charge due to capacitive action. This positive charges are confined in a thin region, called channel, extends all over the way through the nanowire from source to drain as shown in Fig. B.3(c). When a negative bias is applied to the drain with respect to the source, positive charges in the channel drift towards the drain. Thus a current will flow from source to drain. With increasing $+V_g$ number of induced positive carrier in the

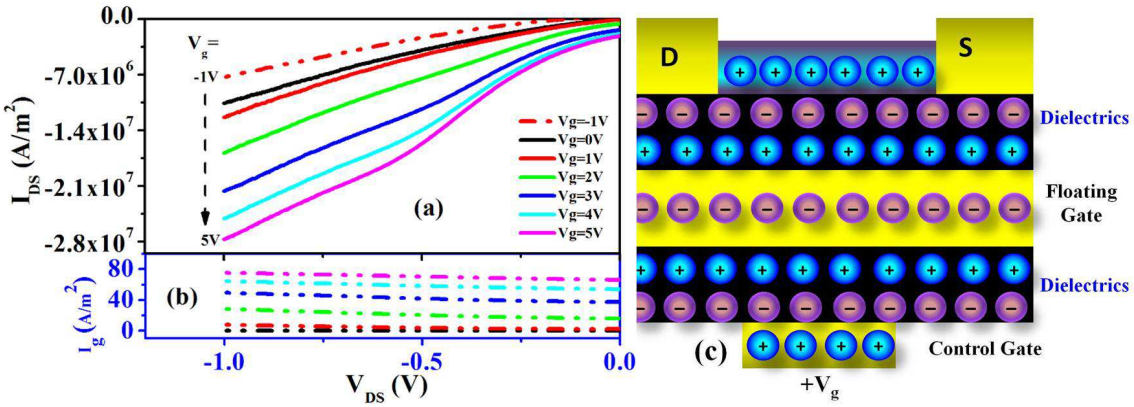

Figure B.3 (a) Output characteristic curve of the FG-MOSFET single nanowire device, (b) leakage current corresponding to the gate voltage, ∼6 order lower than I_{DS} current density. (c) Schematic of induced charge in the nanowire due to positive gate bias.

nanowire increases and device current also increases as experimentally obtained in Fig. B.3(a). Thus, induced charge in FG-MOSFET configuration increases conductance of Cu:TCNQ nanowire.

B.2 Conductance enhancement by electric double layer FET (EDL-FET)

Charge carrier control is a key issue in the development of electronic functions of semiconductive materials. Beyond the simple enhancement of conductivity, high charge carrier accumulation can realize various phenomena, such as chemical reaction, phase transition, magnetic ordering, and superconductivity. Electric double layers (EDLs), formed at solid-electrolyte interfaces, induce extremely large electric fields. The ionic liquids have attracted much attention, their utilization as a gate dielectric material is a new trend in the history of the EDL-FETs. Since the electrolyte solutions of organic solvents and water are volatile and unstable in air, it is hard to maintain them at a constant concentration. In contrast, the ionic liquids are free from these difficulties, and their low molecular weights and high polarizabilities make them much more conductive than conventional electrolytes. Studies on the use of EDL-FETs in ionic-liquid gate dielectrics were initiated in 2007 in experiments using an inorganic semiconductor [162], which was insoluble and robust even in ionic-liquids. The first report on ionic-liquid EDL-FETs of organic semiconductors appeared in 2008 [163]. Use of ionic-liquid results in a high charge carrier accumulation in the solid, much more effectively than solid dielectric materials. In this section, we describe recent developments in the field-effect transistors (FETs) with gate dielectrics

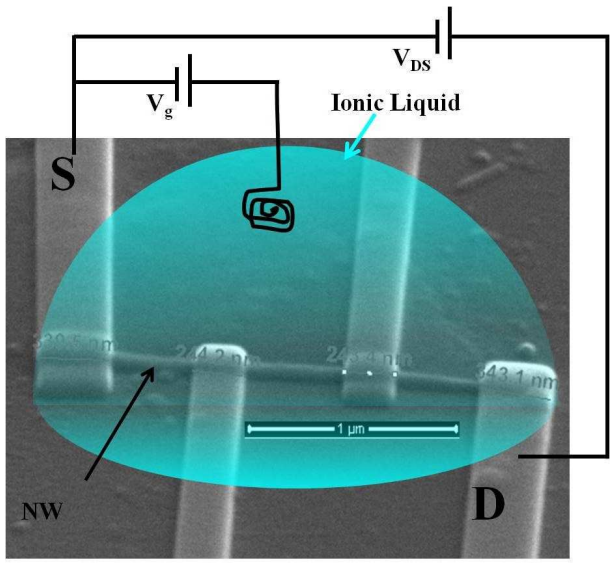

Figure B.4 EDL-FET configuration of a single nanowire of diameter $\sim$ 100 nm. PEO:$LiClO_4$=10:1 is used as gate dielectric.

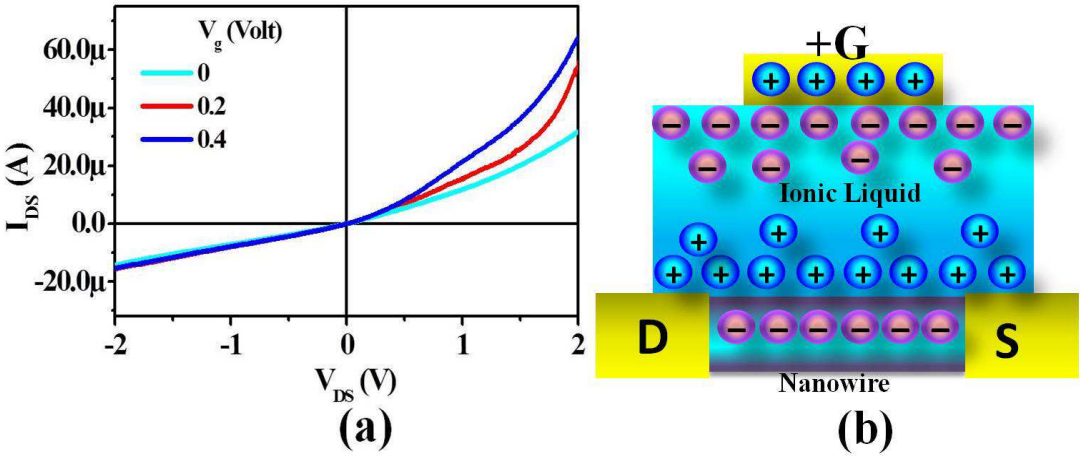

Figure B.5 (a) Output characteristic curve of the EDL-FET single nanowire device. (c) Schematic of induced charge in the nanowire due to positive gate bias.

of ionic liquids, which have attracted much attention due to their wide electrochemical windows, low vapor pressures, and high chemical and physical stability. Here, capacitive effect of ionic liquid is used to enhance the performance of transistor. In this section we have tried to improve the conductance of Cu:TCNQ by induced charge using PEO:$LiClO_4$ (10:1) as gate electrolyte.

We have connected a single nanowire by four probe with FEB deposited Pt. Among them One probe is used as source, one is as drain. Ionic liquid (PEO:$LiClO_4$=10:1) is put on top of the nanowire and use as gate dielectric. Positive bias is applied on the dielectric as gate voltage. SEM image with

ionic-liquid schematic is shown in Fig. B.4.

Source-drain current as a function of V_{DS} for different constant V_g is shown in Fig. B.5(a). Enhancement in I_{DS} is observed due to application of positive V_g. When positive bias is applied across the gate metal electrode anions accumulate near the surface of gate metal-electrodes and due to capacitive effect cations will store far from the anions i.e. near nanowire. This accumulation of cations near nanowire induces negative charge in the nanowire and increases the carrier density of the nanowire, resulting in enhancement of current through the device. Charge induction process is schematically illustrated in Fig. B.5(b). Although, the change in current in EDL-FET is higher compared to FG-MOSFET for lower value of applied gate voltage.

B.3 Conclusion

Thus, we have enhances the conduction of Cu:TCNQ nanowire by induced charge inside the nanowire. Charge induction in the nanowire is performed by floating gate FET and by electric double layer FET. The EDL-FET method is an excellent methodology to achieve high charge injection at solid/liquid interfaces, and enables the development of flexible devices and their low-power operation.

Bibliography

[1] Book: 'Nanowires Science and Technology', Edited by Nicoleta Lupu, ISBN 978-953-7619-89-3, Publisher: InTech, 2010.

[2] H. Alves, Anna S. Molinari, H. Xie, Alberto F. Morpurgo, *Nature Materials*, **7**, 574-580 (2008).

[3] R. Muller, S. D. Jonge, K. Myny, D. J. Wouters, J. Genoe, P. Heremans, *Appl. Phys. Lett.*, **89**, 223501 (2006).

[4] J C Scott and L D Bozano, *Advanced Materials*, **19**, 1452 (2007).

[5] R. J. Warmack, T. A. Callcott and H. C. Schweinler, *Appl. Phys. Lett.*, **24**, 635 (1974).

[6] Y. Tomkiewicz, A. R. Taranko, and J. B. Torrance, *Phys. Rev. B*, **15**, 1017 (1977)

[7] T. Linker and M. Schmittel, Wiley - VCH, 1998.

[8] R. S. Potember, T. O. Poehler, and D. O. Cowan, *Appl. Phys. Lett.*, **34**, 405 (1979).

[9] L. R. Melby, R. J. Harder,W. R. Hertler,W. Mahler, R. E. Benson, and W. E. Mochel, *JACS*, **84**, 3374, (1962).

[10] R. E. Long, R. A. Sparks, and K. N. Trueblood, *Acta Crystallographica*, **18**, 935 (1965).

[11] R. A. Heintz, H. Zhao, X. Ouyang, G. Grandinetti, J. Cowen, and K. R. Dunbar, *Inorg. Chem.*, **38**, 144-156 (1999).

[12] C. A. Fernandez, P. C. Martin, T. Schaef, M. E. Bowden, P. K. Thallapally, L. Dang, W. Xu, X. Chen , B. P. McGrail; *Scientific Report*, **4**, 06114 (2014).

[13] R.Muller, S. Jonge, K.Myny, D.J.Wouters, J.Genoe, P.Heremans, *Solid State Electron.*, **50**, 601(2006).

[14] M. Hanack and G. Pawlowski, *Die Naturwissenschaften*, **69**(6) 266-275 (1982).

[15] D. Shorokhov and Ahmed H. Zewail; *Phys. Chem. Chem. Phys.*, **97**, 2879-2893(2008).

[16] Z. Gu, H. Wu, and Y. Wei and J. Liu, *J. Phys. Chem.*, **10**, 2543-2545 (1993).

[17] Z. Zhou, K. Xiao, R. Jin, D. Mandrus, Jing Tao, D. B. Geohegan, and S. Pennycook, *Appl. Phys. Lett.*, **90**, 193115 (2007).

[18] R. Muller, R Naulaerts, J Billen, J. Janoe, P Heremans; *Appl. Phys. Lett.*, **90**, 063503 (2007).

[19] L. Venkataraman, Y. S. Hong, and P. Kim, *Phys. Rev. Lett.*, **96**, 076601 (2006).

[20] A. N. Aleshin, H. J. Lee, Y. W. Park, and K. Akagi; *Phys. Rev. Lett.*, **93**, 196601 (2004).

[21] M. Colle, M. Buchel, and D. de Leeuw, *Org. Electron.* **7**, 305 (2006).

[22] Yaling Liu, H. Li, D. Tu, Z. Ji, C. Wang, Q. Tang, M. Liu, W. Hu, Y. Liu, and D. Zhu, *J. Am. Chem. Soc.*, **128**, 12917-12922 (2006)

[23] K. B. Zheng, H. T. Shen, C. N. Ye, J. L. Li, D. L. Sun and G. R. Chen, *Nano-Micro Lett.*, **1**(1), 23-26 (2009).

[24] N. Lopez, H. Zhao, A. Ota, Andrey V. Prosvirin, Eric W. Reinheimer, and Kim R. Dunbar, *Adv. Mater.*, **22**, 986-989 (2010).

[25] N. Knorr, A. Bamedi, Z. Karipidou, R. Wirtz, M. Sarpasan, S. Rosselli, and G. Nelles, *J. Appl. Phys.*, **114**, 124510 (2013).

[26] J. Billen, R. Muller, J. Genoe and P. Heremans, *Proceed. 2nd Int. Conf. Mem. Technol and Des.*, **135** (2007).

[27] H. Shen, K. Zheng, J. Li, D. Sun and G. Chen, *Nanotechnology*, **19**, 015305 (2008).

[28] K. Xiao, I. N. Ivanoy, A. A. Puretzky, Z. Q. Liu, D. B. Geohegan, *Adv. Mater.*, **18**, 2184 (2006).

[29] Okamoto, T. Komatsu, Y. Iwasa, T. Koda, Y. Tokura, S. Koshihara, T. Mitani, and G. Saito, *Synth. Met.* **27**, 8189 (1988).

[30] D. Deleruyelle, C. Muller, J. Amouroux, and R. Muller; *Appl. Phys. Lett*, **96**, 263504-3 (2010).

[31] Z. Y. Fan, X. L. Mo, G. R. Chen, J. G. Lu, *Adv.Mater.Sci.*, **7**, 72-75 (2003).

[32] L. Ren, L. Fu, Y. Liu, S. Chen, and Z. Liu, *Adv. Mater.*, **21**, 4742-4746 (2009).

[33] R Muller, C Krebs, L Goux, D J Wouters, P Heremans, S Spiga and M Fanciulli, *IEEE Electron Device Letters*, **30**, 620 (2009).

[34] B. Mukherjee, M. Mukherjee, Jae-eun Park, and S. Pyo, *J. Phys. Chem. C*, **114**, 567-571 (2010).

[35] J. Billen, S. Steudel, R. Muller, J. Genoe, and P. Heremans; *Appl. Phys. Lett.*, **91**, 263507 (2007).

[36] J.G. Simmons and R.R. Verderber; *Proc. Roy. Soc. A*, **301**, 77-102, (1967).

[37] A. Sawa, T. Fujii, M. Kawasaki, and Y. Tokura; *Appl. Phys. Lett.*, **88**, 232112 (2006).

[38] R. Waser; *Nanoelectronics and Information Technology*, Wiley - VCH, 2003.

[39] J. Maier; *Nature Materials*, **4**, 2005.

[40] M. N. Kozicki, C. Gopalan, M. Balakrishnan, M. Park, and M. Mitkova; *IEEE Proceeding*, 10-17 (2004).

[41] R. S. Potember, T. O. Poehler, and R. C. Benson; *Appl. Phys. Lett.*, **41**, 548 (1982).

[42] T. Kever, U. Bottger, C. Schindler and R. Waser; *Appl. Phys. Lett.*, **91**, 083506 (2007).

[43] N. Gu, C.-W. Yuan, and Y. Wei; *Annual International Conference of the IEEE in Medicine and Biology Society*, **12**, 1803-1804 (1990).

[44] A. Carbone, C. Pennetta and L. Reggiani; *Appl. Phys. Lett.*, **95**, 233303 (2009).

[45] R.C. Hoffman and R.S. potember; *Appl. Optics*, **28**, 1417 (1989).

[46] Ch. Turquat, A. Demolliens, J. Razafindramora, A. Merlen, J-Ch. Valmalette, Ch. Muller, R. Muller, L. Goux, and D. J. Wouters; *IEEE*, p-45-48, 2007.

[47] C. F. Powell, J. H. Oxley, and J. M. Blocher Jr; *Vapor Deposition*; Wiley, New York, 1967.

[48] J. N. Crosby, R. S. Hanley, US Patent, No. US4250210 A, Feb' 1981.

[49] Douglas B. Chrisey (Editor), Graham K. Hubler (Editor), pp. 648. ISBN 0-471-59218-8. Wiley-VCH, May 2003.

[50] H. A. Pohl, *Dielectrophoresis the behavior of neutral matter in nonuniform electric fields.* Cambridge University Press, Cambridge, 1978.

[51] H-X. Ji, J-S. Hu, Y-G. Guo, W-G. Song, and L-J. Wa; *Adv. Mater.* **20**, 4879-4882 (2008).

[52] F. Tian, W. Liu, and C.-R. Wang; *J. Phys. Chem. C*, **11**(24), 8763-8766 (2008).

[53] Peter A. Smith, Christopher D. Nordquist, Thomas N. Jackson, and Theresa S. Mayer; *Appl. Phys. Lett.*, **77**, 1399-1401 (2000).

[54] B. D. Gates; *Nature Nanotech.*, **5**, 484-485 (2010).

[55] Ketan H. Bhatt and Orlin D. Velev; *Langmuir*, **20**, 467-476 (2004).

[56] M. Sakai, M. Nakamura M and K. Kudo K; *Appl. Phys. Lett.*, **90**, 062101 (2007).

[57] T Phanindra Sai and A K Raychaudhuri; *Nanotechnology*, **21**, 045703 (2010).

[58] S. van Dorp, U. F. Keyser, N. H. Dekker, C. Dekker and S. G. Lemay; *Nature Phy.*, **5**, 347-351 (2009).

[59] Hui Liu and Haim H. Bau, *Phys. Fluids*, **16**(5), 1217-1228 (2004).

[60] T. Sun, N. G. Green, and H. Morgan; *Appl. Phy. Lett.*, **92**, 173901 (2008).

[61] S. Nudurupati, N. Aubry and P. Singh; *J. Phys. D: Appl. Phys.*, **39**, 3425-3439 (2006).

[62] A. K. Neufeld, I. Madsen, A. M. Bond, and C. F. Hogan; *Chem. Mater.*, **15**, 3573-3585 (2003).

[63] L. Reimer; *Scanning Electron Microscope: Physics of Image Formation and Microanalysis*, Springer, 1998.

[64] D. benard Williams, C. barry Carter; *Transmission Electron Microscope: A Textbook for Materials Science*, Springer, 1996.

[65] B. D. Cullity, S. R. Stock; *Elements of X-ray Diffraction*, Prentice Hall, 2001.

[66] P. R. Griffiths, J. A. de Haseth; *Fourier Transform Infrared Spectrometry*, Wiley, New York, 1986.

[67] M. B.Inoue, M.Inoue, Q. Fernando, K. W. Nebesny; *J. Phys. Chem.*, **91**, 527 (1987).

[68] W. Pukacki, M. Pawlak, A. Graja, M. Lequan, R. M. Lequan; *Inorg. Chem.*, **26**, 1328 (1987).

[69] J. S. Chappell, A. N. Bloch, W. A. Bryden, M. Maxfield, T. O. Poelher and D. O. Cowan; *J. Am. Chem. Soc.*, **103**, 2442 (1981).

[70] E. I. Kamitsos and W. M. Risen; *J. Chem. Phys.*, **79**, 5808 (1983).

[71] Pt-Rh thermocouple wire, Heatcon Sensors Pvt. Ltd., India.

[72] Lakeshore Cryotronics Inc. 575, Mc Corkle Blvd, Westerville, Ohio, 43082, USA.

[73] http://www.keithley.com

[74] http://www.lakeshore.com

[75] *Nanoelectronics: V.K. Arora; Quantum Engineering of Low-Dimensional Nanoensembles, CRC press*, 2015.

[76] A. Roy , T. Pandey , N. Ravishankar , and A. K. Singh; *J. Phys. Chem. C*, **118**, 18676-18682 (2014).

[77] C. Wang, Yongjie Hu, Charles M. Lieber and S. Sun; *J. Am. Chem. Soc.*, **130**, 8902-8903 (2008).

[78] C. Durkan and M.E. Wallend, *Phy. Rev. B*, **61**, 14215 (2000).

[79] A. Bid, A. Bora, and A. K. Raychaudhuri; *Phy. Rev. B*, **74**, 113415 035426 (2006).

[80] J. E. Fischer, W. Zhou, J. Vavro, M. C. Llaguno, C. Guthy, R. Haggenmueller, M. J. Casavant, D. E. Walters and R. E. Smalley; *J. Appl. Phys.*, **93**, 2157 (2003).

[81] T-In Jeon, K-Ju Kim, C. Kang, S-Jae Oh, J-Hiuk Son, K. Hyeok An, D. Jae Bae, and Young Hee Lee; *Appl. Phys. Lett.*, **80**, 3403 (2002).

[82] Xinyuan Zhao, C. M. Wei, L. Yang, and M. Y. Chou; *Phys. Rev. Lett.*, **92**, 236805 (2004).

[83] J Bardeen; *Phys. Rev. Lett.*, **42**, 1498 (1979).

[84] J Bardeen; *Phys. Rev. Lett.* **45**, 1978 (1980).

[85] R. E. Peierls, *Quantum Theory of Solids*, Clarendon Press, 1955.

[86] M. Schwoerer and Hans Christoph Wolf, *Organic Molecular Solids*, WILEY-VCH, Weinheim (2007).

[87] K. Wang, X. Qian, L. Zhang, Y. Li, and H. Liu; *ACS Appl. Mater. Interfaces*, **5**, 5825 (2013).

[88] R. Basori, K. Das, P. Kumar, K. S. Narayan, A. K. Raychaudhuri; *Optics Express*, **2**, 4944 (2014).

[89] Anthony P. O'Mullane, Nigel Fay, Ayman Nafady, and Alan M. Bond; *J. Am. Chem. Soc.*, **129**, 2066-2073 (2007).

[90] Chuan Zhao, Alan M Bond; *J. Am. Chem. Soc.*, **131**, 4279-4287(2009).

[91] Z. Zhou, R. Jin, G. Eres, A. Subedi, and D. Mandrus, *Appl. Phys. Lett.*, **89**, 133124 (2006).

[92] M J Cohen and A J Heeger; *Phys. Rev. B*, **16**, 688 (1977).

[93] R. Springell, R. C. C. Ward, J. Bouchet, J. Chivall, D. Wermeille, P. S. Normile, S. Langridge, S. W. Zochowski, and G. H. Lander; *Phys. Rev. B*, **89**, 245101 (2014).

[94] P. Goli , J. Khan , D. Wickramaratne , Roger K. Lake , and Alexander A. Balandin; *Nano Lett.*, **12**, 5941-5945 (2012).

[95] T Phanindra Sai and A K Raychaudhuri; *Mater. Res.Soc. Symp. Proc.*, **1058**, JJ05-03 (2008).

[96] A. N. Bloch, R. B. Weisman, and C. M. Varma; *Phys. Rev. Lett.*, **28**, 753 (1972).

[97] M. M. Fogler, S. V. Malinin, and T. Nattermann; *Phys. Rev. Lett.* **97**, 096601 (2006).

[98] L Sneddon, M C Cross and D S Fisher; *Phys. Rev. Lett.*, **49**, 292 (1982).

[99] R. Basori and A. K. Raychaudhuri; Accepted in *IEEE Explore Conference Proceeding* (2014).

[100] Y. Avigal and R. Kalish; *Phys. Lett.*, **78**, 2291 (2001).

[101] J.D. Meindl; *IEEE Transaction on Electron Devices.* ED-**31** (11), 1555-1561 (1984).

[102] *Intel 22nm Technology*. Retrieved 26 July 2014.

[103] J. Lin, O. Cretu, W. Zhou, K. Suenaga, D.Prasai, K. I. Bolotin, N. T. Cuong, M. Otani, S.Okada, A. R. Lupini, J-C. Idrobo, D. Caudel, A. Burger, N. J. Ghimire, J. Yan, D. G. Mandrus, S. J. Pennycook and S. T. Pantelides; *Nature Nanotech.*, **9**, 436-442 (2014).

[104] P. Nukala, R. Agarwal, X. Qian, M. H. Jang, S. Dhara, K. Kumar, A. T. Charlie Johnson, J. Li, and R. Agarwal; *Nano Lett.*, **14**, 2201-2209 (2014).

[105] S. Tappertzhofen, I. Valov, T. Tsuruoka, T. Hasegawa, R. Waser, and M. Aono; *ACS Nano*, **7**, 6396-6402 (2013).

[106] V. Dubost, T. Cren, C. Vaju, L. Cario, B. Corraze, E. Janod, F. Debontridder, and D. Roditchev, *Nano Lett.*, **13**, 3648-3653 (2013).

[107] International Technology Roadmap for Semiconductors, 2011 Edition. Available Online at www.itrs.net

[108] I. G. Baek et al., *Tech. Dig. IEDM*, 587 (2004).

[109] S.M. Sze, D.J. Coleman Jr., A. Loya; 'Current transport in metal-semiconductor-metal (MSM) structures' *Solid-State Electon*, **14**, 1209-1218 (1971).

[110] A. Hefczyc, L. Beckmann, E. Becker, Hans-H. Johannes, and W. Kowalsky; *Phys. Stat. Sol.*, **205** (3), 647-655 (2008).

[111] R. waser and M. Aono; *Nature Materials*, **6**, 833-840 (2007).

[112] M. Menon and D. Srivastava; *Phys. Rev. Lett.* **79**, 4453 (1997).

[113] H. Norde; *J. Appl. Phys.*, **50**, 5052 (1979).

[114] M. J. Rozenberg, I.H. Inoue, and m. J. Sanchez; *Phy. Rev. Lett.*, **92**(17), 178302 (2004).

[115] U. Celano, L. Goux, A. Belmonte, K.Opsomer, A. Franquet, A. Schulze, C. Detavernier, O. Richard, H. Bender, M. Jurczak, and W. Vandervorst; *Nano Lett.*, **14**, 2401-2406 (2014).

[116] T. P. Sai, Thesis titled 'Synthesis and electronic properties of nanowires of charge transfer complexes', 2010

[117] J. Wang, M. S. Gudiksen, X. Duan, Y. Cui, and C. M. Lieber; *Science*, **293**, 1455 (2001).

[118] S.-C. Kung, W. Xing, W. E. van der Veer, F. Yang, K. C. Donavan, M. Cheng, J. C. Hemminger, and R. M. Penner; *ACS Nano*, **5**, 7627 (2011).

[119] R.-S. Chen, S.-W. Wang, Z.-H. Lan, J. T.-H. Tsai, C.-T. Wu, L.-C. Chen, K.-H. Chen, Y.-S. Huang, and C.-C. Chen; *Small*, **4**, 925 (2008).

[120] H. Kind, H. Yan, B. Messer, M. Law, and P. Yang, *Adv. Mater.*, **14**, 158 (2002).

[121] K. Das, S. Mukherjee, S. Manna, S. K. Ray and A. K. Raychaudhuri; *Nanoscale*, **6**, 11232-11239 (2014).

[122] Y. Xia, P. Yang, Y. Sun, Y. Wu, B. Mayers, B. Gates, Y. Yin, F. Kim, and H. Yan, *Adv. Mater.* **15**, 353 (2003).

[123] Z. L. Wang; *Mater. Today*, **7**, 26 (2004).

[124] M. Freitag, Y. Martin, J. A. Misewich, R. Martel, and P. Avouris; *Nano Lett.*, **3**(8), 1067-1071 (2003).

[125] M. Afsal, C. Y. Wang, L. W. Chu, H. Ouyang, and L. J. Chen, *J. Mater. Chem.*, **22**(17), 8420-8425 (2012).

[126] G. A. O'Brien, A. J. Quinn, D. A. Tanner, and G. Redmond; *Adv. Mater.*, **18**(18), 2379-2383 (2006).

[127] X. Zhang, J. Jie, W. Zhang, C. Zhang, L. Luo, Z. He, X. Zhang, W. Zhang, C. Lee, and S. Lee; *Adv. Mater.*, **20**(12), 2427-2432 (2008).

[128] Y. Iwasa, T. Koda, Y. Tokura, S. Koshihsra, N. Iwssawa, and G. Saito; *Appl. Phys. Lett.*, **55**, 2111 (1989).

[129] Y. Takahashi, M. Kanamori, A. Kondoh, H. Minoura, and Y. Ohya; *Jpn. J.Appl. Phys.*, Part 1 **33**, 6611 (1994)

[130] *Semiconductor Laser Diode Technology and Applications*, Edited by D. S. Patil, InTech, 2012.

[131] *Light-Emitting Diodes* , E. Fred Schubert, Cambridge University Press, 2006.

[132] *Photodiodes - From Fundamentals to Applications*, Edited by Ilgu Yun, InTech, 2012.

[133] *Photoelectronic Properties of Semiconductors*, Richard H. Bube, Cambridge University Press 1992.

[134] J. S. Jie, W. J. Zhang, Y. Jiang, X. M. Meng, Y. Q. Li, and S. T. Lee; *Nano Lett.*, **6**(9), 1887-1892 (2006).

[135] A. Zhang, H. Kim, J. Cheng, and Y.-H. Lo; *Nano Lett.*, **10**(6), 2117-2120 (2010).

[136] S.-G. Liu, Y.-Q. Liu, P.-J. Wu, and D.-B. Zhu, *Chem. Mater.*, **8**(12), 2779-2787 (1996).

[137] R. R. Mehta and B. S. Sharma, *J. Appl. Phys.*, **44**, 325 (1973).

[138] T.-Y. Wei, C.-T. Huang, B. J. Hansen, Y.-F. Lin, and L.-J. Chen; *Appl. Phys. Lett.*, **96**, 013508 (2010).

[139] A. Rose, *Concepts in Photoconductivity and Allied Problems* (Krieger,New York, 1978).

[140] Y. Ahn, J. Dunning, J Park; *Nano Lett.*, **5**, 1367-1370 (2005).

[141] G. Bulgarini, M.E. Reimer, M. Hocevar1, E.P.A.M. Bakkers, L.P. Kouwenhoven, and V. Zwiller; *Nature Photonics*, **6**, 455-458 (2012).

[142] G.N. Goltsmana, O. Okunev, G. Chulkova, A. Lipatov, A. Semenov, K. Smirnov, B. Voronov, and A. Dzardanov; *Appl. Phys. Lett.*, **79**, 705-707 (2001).

[143] X. N. Xie, Y. Xie, X. Gao, C. H. Sow, and A. T. S. Wee; *Adv. Mater.*, **21**(29), 3016-3021 (2009).

[144] R. Calarco, M. Marso, T. Richter, A. I. Aykanat, R. Meijers, A. v.d. Hart, T. Stoica, and H. Luth; *Nano Lett.*, **5**(5), 981-984 (2005).

[145] Y. Liu, Q. Yang, Y. Zhang, Z. Yang, and Z. L. Wang; *Adv. Mater.*, **24**(11), 1410-1417 (2012).

[146] A. K. Okyay, C. O. Chui, and K. C. Saraswat; *Appl. Phys. Lett.*, **88**(6), 063506 (2006).

[147] M. Rao and K. S. Narayan, Appl. Phys. Lett. **92**(22), 223308 (2008).

[148] Y. Gu, E.-S. Kwak, J. L. Lensch, J. E. Allen, T. W. Odom, and L. J. Lauhon; *Appl. Phys. Lett.*, **87**(4), 043111 (2005).

[149] X. Fang, Y. Bando, M. Liao, U. K. Gautam, C. Zhi, B. Dierre, B. Liu, T.Zhai, T. Sekiguchi, Y. Koide and D. Golberg; *Adv. Mater.*, **21**, 2034-2039(2009).

[150] V.J. Logeeswaran, A. Sarkar, M.S. Islam, N.P. Kobayashi, J. Straznicky, X. Li, Wei Wu, S. Mathai, M.R.T. Tan, S.-Y. Wang and R.S. Williams, *Appl. Phys. A*, **91**, 1 (2008)

[151] T. Zhai, X. Fang, M. Liao, X. Xu, L. Li, B. Liu, Y. Koide, Y. Ma, J. Yao, Y. Bando and D. Golberg; *ACS Nano*, **4**(3), 1596-1602 (2010).

[152] T. Zhai, H. Liu, H. Li, X. Fang, M. Liao, L. Li, H. Zhou, Y. Koide, Y. Bando, D. Golberg; *Adv. Mater.*, **22**, 2547-2552 (2010).

[153] D. Diesing, M. Merschdorf, A. Thon and W. Pfeiffer; *Appl. Phys.B-Lasers O.*, **78**, 443-446 (2004).

[154] A. K. Geim and K. S. Novoselov; *Nat. Mater.*, **6**, 183-191 (2007).

[155] S. Park and R. S. Ruoff, *Nat. Nanotech.*, **4**, 217-224 (2009).

[156] J. J. Hoagland, X. D. Wang, and K. W. Hipps; *Chem. Mater*, **5**, 54-60 (1993).

[157] C. N. R. Rao and Rakesh Voggu; *Materials Today*, **13**(9), 34-40 (2010).

[158] J. Lu, X. Qu, G. Peleckis, J. F. Boas, A. M. Bond and L. L. Martin; *J. Org. Chem.*, **76**, 10078 (2011).

[159] E. Nossol, A. B. S. Nossol, Si-X. Guo, J.Zhang, Xi-Y. Fang, A. J. G. Zarbin and A. M. Bond; *J. Mater. Chem. C*, **2**, 870-878 (2014).

[160] W S Hummers and R E Offeman; *J. Am. Chem. Soc.*, **80**, 1339 (1958).

[161] W. Hu, B. Gompf, J Pflaum, D. Schweitzer, M. Dressel; *Appl. Phys. Lett*, **84**, 4720-4723 (2004).

[162] Misra, M. McCarthy and A. F. Hebard; *Appl. Phys. Lett.*, **90**, 052905 (2007).

[163] S. Ono, S. Seki, R. Hirahara, Y. Tominari and J. Takeya; *Appl. Phys. Lett.*, **92**, 103313 (2008).